UNIVERSITY OF CALIFORNIA,
IRVINE

Improving projections of sea level contribution from the Greenland ice sheet by modeling calving dynamics

DISSERTATION

submitted in partial satisfaction of the requirements
for the degree of

DOCTOR OF PHILOSOPHY

in Earth System Science

by

Youngmin Choi

Dissertation Committee:
Professor Mathieu Morlighem, Chair
Professor Eric Rignot
Professor Francois Primeau

2020

TABLE OF CONTENTS

LIST OF FIGURES

LIST OF TABLES

ACKNOWLEDGMENTS

First, I would like to express my sincere gratitude to my advisor Dr. Mathieu Morlighem for having me as his first graduate student and giving me this incredible opportunity. During my PhD, he continuously provided great support and guidance and was always willing to assist in any way he could throughout this project.

I would like to thank my dissertation committee members, Dr. Eric Rignot and Dr. Francois Primeau, for providing me great insights and feedback on my work and helping me with this dissertation.

I am grateful to many colleagues from the cryosphere group and the Department of Earth System Science at UCI. I really appreciate a great research environment, support, and inspiration from them.

I thank my entire family for their great support during my PhD and special thanks to my wife Jinsol for supporting me while doing her own PhD. This work would not be possible without her.

The work presented in this dissertation was performed at the University of California, Irvine and funded by the National Science Foundations ARCSS program (1504230), the National Aeronautics and Space Administration Cryospheric Sciences Program (NNX15AD55G), and the NASA Earth and Space Science Fellowship Program (80NSSC17K0409).

Parts of Chapter 4 are reprinted from a publication in The Cryosphere. Parts of Chapter 5 are reprinted with permission from the American Geophysical Union (*Geophysical Research Letters*). I would like to thank all co-authors for their contributions to all papers published and this dissertation.

CURRICULUM VITAE

Youngmin Choi

EDUCATION

Doctor of Philosophy in Earth System Science — **2020**
University of California, Irvine — *Irvine, CA*

Master of Science in Earth System Science — **2017**
University of California, Irvine — *Irvine, CA*

Master of Science in Energy Resources Engineering — **2015**
Seoul National University — *Seoul, Korea*

Bachelor of Science in Civil Engineering — **2013**
Seoul National University — *Seoul, Korea*

RESEARCH EXPERIENCE

Graduate Research Assistant — **2015-2020**
University of California, Irvine — *Irvine, California*

Graduate Research Assistant — **2013-2015**
Seoul National University — *Seoul, Korea*

Research Intern — **2013**
New-Renewable Energy Resource Center — *Seoul, Korea*

TEACHING EXPERIENCE

Teaching Assistant — **2016-2017**
University of California, Irvine — *Irvine, CA*

Teaching Assistant — **2013-2014**
Seoul National University — *Seoul, Korea*

REFEREED JOURNAL PUBLICATIONS

Y. Choi, M. Morlighem, E. Rignot, J. Mouginot, and M. Wood, Modeling the response of Nioghalvfjerdsfjorden and Zachariae Isstrøm glaciers, Greenland, to ocean forcing over the next century, *Geophysical Research Letter*, 2017.

Y. Choi, M. Morlighem, M. Wood, and J. H. Bondzio, Comparison of four calving laws to model Greenland outlet glaciers, *The Cryosphere*, 2018.

M. Morlighem, M. Wood, H. Seroussi, **Y. Choi**, and E. Rignot, Modeling the response of Northwest Greenland to enhanced ocean thermal forcing and subglacial discharge, *The Cryosphere*, 2019.

H. Yu, E. Rignot, H. Seroussi, M. Morlighem, and **Y. Choi**, Impact of iceberg calving on the retreat of Thwaites Glacier, West Antarctica over the next century with different calving laws and ocean thermal forcing Modeling, *Geophysical Research Letter*, 2019.

REFEREED CONFERENCE PUBLICATIONS

Modeling the Northeast Greenland Ice Stream in response to climate forcing — Dec 2016
2016 American Geophysical Union

Modeling ice front dynamics of Greenland outlet glaciers using the level set method — Apr 2017
19th International Conference on Finite Elements in Flow Problems

Understanding calving dynamics of Greenland outlet glaciers by comparing calving laws in a 3D ice sheet model — Dec 2017
2017 American Geophysical Union

Comparison of calving laws for understanding calving dynamics of Greenland outlet glaciers — Jun 2018
2018 International Glaciological Society Symposium

Modeling the response of Greenland outlet glaciers to climatic forcing over the next century — Dec 2018
2018 American Geophysical Union

Modeling the Contribution of the Greenland Ice Sheet to Sea Level over the Next Century — Jul 2019
2019 IUGG General Assembly

Modeling calving dynamics of tidewater glaciers to simulate the future sea-level contribution of Greenland, (invited) — Dec 2019
2019 American Geophysical Union

ABSTRACT OF THE DISSERTATION

Improving projections of sea level contribution from the Greenland ice sheet by modeling calving dynamics

By

Youngmin Choi

Doctor of Philosophy in Earth System Science

University of California, Irvine, 2020

Professor Mathieu Morlighem, Chair

The contribution of the Greenland ice sheet to global sea-level rise has increased rapidly during the last two decades and is currently ~ 0.8 mm/year. As observations show a clear, accelerating increasing trend in both global temperature and ice mass loss from the Greenland ice sheet, how much mass the Greenland ice sheet is going to lose over the next century and beyond is one of the most urgent questions in understanding the implication of climate change. Estimating future ice sheet contributions to sea-level rise is currently an active area of research and numerical ice sheet modeling is our best tool to address this question.

This thesis provides an estimate of sea-level contribution from Greenland with a new generation ice sheet model that fully accounts for changes of 200+ Greenland glaciers. First, we introduce modeling of calving dynamics which is one of the most important processes contributing to mass loss from outlet glaciers around the coast of Greenland. We test and compare calving laws in an ice sheet model and assess which calving law has better predictive abilities for each glacier. We then apply the best calving law to Nioghalvfjerdsfjorden and Zachariae Isstrøm glaciers in northeast Greenland to investigate the response of these fast-changing glaciers to future climate forcing.

We extend our model to the entire Greenland ice sheet to estimate the future sea-level

contribution from Greenland. Compared to previous studies, we calibrate our model at the individual glacier scale with a moving boundary capability to better constrain the retreat of marine-terminating glaciers. We find that the Greenland ice sheet will contribute 79.2 to 167 mm to sea-level between 2007 and 2100 under the most extreme warming scenarios. Our simulations show that discharge from ice dynamics will contribute to the total mass loss from Greenland more than previously estimated, implying that future scientific focus should remain on not only atmospheric processes but also the ice front of marine-terminating glaciers.

Chapter 1

Introduction

Climate change and ice sheets

The average temperature of the Earth has increased by 0.85°C over the past 130 years (Pachauri et al., 2014). This increase in Earth's average temperature has led to an increase in the eustatic component of global sea-level through both enhanced thermal expansion and accelerated melting of glaciers and ice sheets. According to the International Panel for Climate Change (IPCC) report (Pachauri et al., 2014), the global surface temperature will exceed 1.5°C above 1850-1900 by the end of this century due to continued emissions of greenhouse gases for most climate scenarios. Consequently, sea-level will continue to rise at a rate exceeding the observed rate over the past 30 years. Antarctic and Greenland ice sheets are the major components contributing to sea-level rise due to the rapid warming of both the atmosphere and ocean. The contribution of these two ice sheets to global sea-level rise has increased rapidly during the last two decades, observed at a rate of 0.43 mm/yr and 0.27 mm/yr for Greenland and Antarctica, respectively, for the period 1993-2010 (Pachauri et al., 2014). Together, the Greenland and Antarctic ice sheets have the potential to raise sea-level nearly by 64 m if all the ice of ice sheets were to melt, and are projected to lose

between 0.43 m and 0.84 m of sea-level equivalent of ice mass by the end of the century relative to 1986-2005 (Pachauri et al., 2014). A warming climate would not only lead to the addition of large amounts of meltwater into the adjacent oceans but also rapid accelerations in grounded ice discharge. There are many mechanisms changing the dynamics of ice sheets that are poorly understood. To predict how much sea-level will rise due to changes in the ice sheets, it is critical to understand how these ice masses will evolve and interact with other Earth components (e.g., atmosphere and ocean) in the future climate.

Greenland ice sheet

The Greenland ice sheet is the second-largest body of ice on Earth. Its total ice volume is $2.99 \pm 0.02 \times 10^6$ km^3 which corresponds to 7.42 ± 0.05 m of sea-level rise (Morlighem et al., 2017). Greenland is an important component of the Earth system, as it interacts with numerous other climate components. The Greenland ice sheet can lose its mass due primarily to changes in both atmospheric and oceanic temperatures.

Atmospheric warming leads to surface melt of the ice sheet, which accounts for about 50% of mass loss from Greenland (van den Broeke et al., 2016). Meltwater due to atmospheric warming also affects the ice sheet dynamics. The drainage of surface meltwater to the base of the ice sheet lubricates the ice bottom, which accelerates ice flow. This mechanism causes a dynamic thinning of the ice sheet and therefore induces mass loss. In addition, enhanced runoff due to atmospheric warming affects ocean-induced ice melt by increasing subglacial freshwater discharge from the glaciers (e.g. Xu et al., 2013; Rignot et al., 2016; Wood et al., 2018). This leads to the formation of highly buoyant plumes adjacent to the glacier's calving front, further accelerating glacial melt (Slater et al., 2018).

An increase in ocean temperatures has direct effects on over 200 tidewater glaciers around the coast of the Greenland ice sheet because they are connected to the ocean through deep

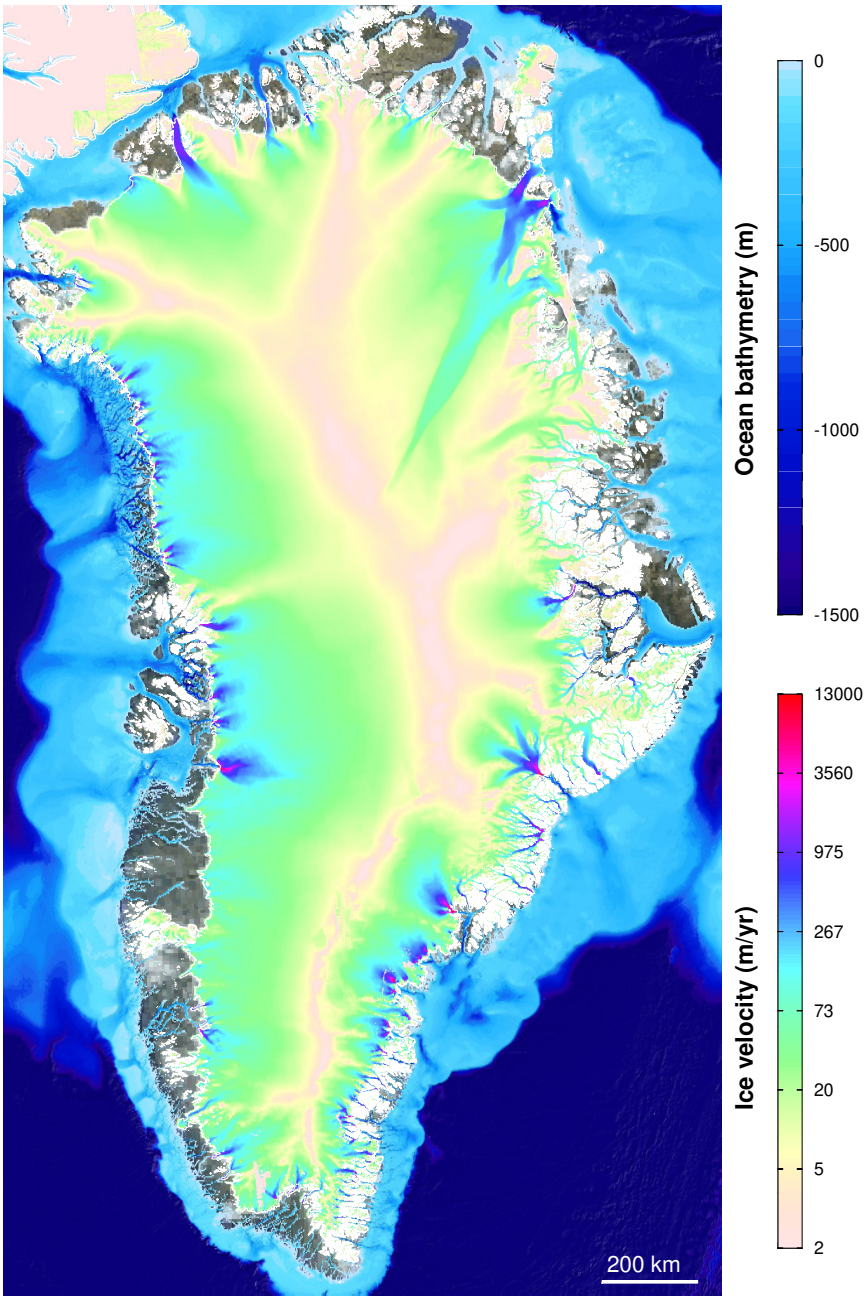

Figure 1.1: Ocean bathymetry around the coast of Greenland (Morlighem et al., 2017) and surface ice velocity (Joughin et al., 2010) of the Greenland ice sheet

and narrow troughs (Fig. 1.1). Ice-ocean interactions of the Greenland ice sheet have gained both scientific and public attention due to the widespread and synchronous acceleration and retreat of tidewater glaciers during a period of ocean warming (Straneo and Heimbach, 2013) (Fig. 1.2). These ice-ocean interactions play a major role in the evolution of Greenland's

ice dynamics since increased ocean temperatures can trigger positive feedbacks between glacier retreat and ice discharge. If warm ocean water enhances ice shelf thinning and ice front/grounding-line retreat, there will be a loss of buttressing that stabilizes upstream grounded ice. This can lead to a significant acceleration of tidewater glaciers, leaving these glaciers prone to future destabilization. This positive feedback is considered the primary driver of today's mass loss in Greenland.

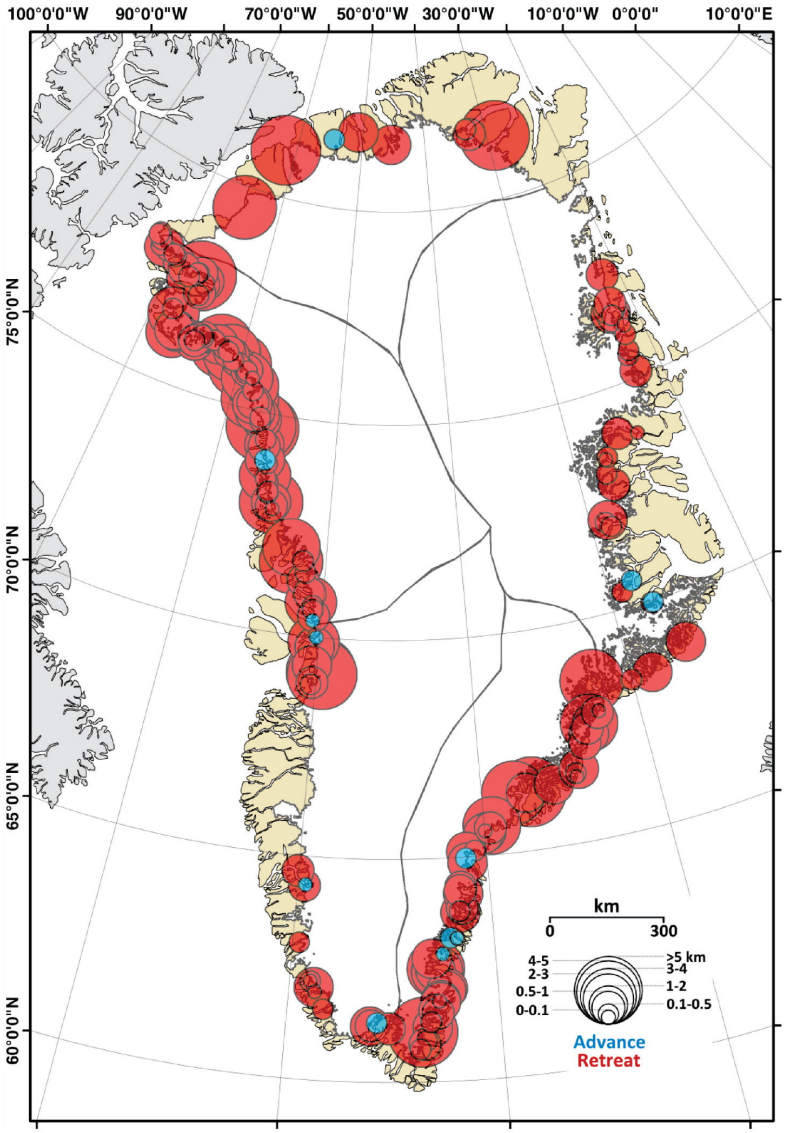

Figure 1.2: Overall change in ice front positions for tidewater glaciers between 2000 and 2010. Figure adapted from Murray et al. (2015)

.

Tidewater glaciers

Marine-terminating glaciers around the Greenland ice sheet have undergone rapid changes over the past decades, as observed by high resolution satellite images (Fig. 1.2). These changes have been widespread almost all over the Greenland ice sheet. However, there also has been significant regional and glacier-to-glacier variability in changes of tidewater glaciers.

In the late 1990s, significant changes were observed in the ice velocity and terminus positions of tidewater glaciers in the southeast region of Greenland (Rignot and Kanagaratnam, 2006). This region underwent more rapid changes between 2000-2005, in which both ice discharge and ice front retreat rates almost doubled (Rignot and Kanagaratnam, 2006). Although the ice velocity began to stabilize and ice front readvances within this region after 2005, continued ice mass loss was observed due to an increase in ice discharge of tidewater glaciers (Mouginot et al., 2019). The northwest region of Greenland, which contains over 70 tidewater glaciers, has also lost a significant amount of ice mass since the 1980s (Mouginot et al., 2019). A majority of this mass loss is due to increases in ice discharge and decreases in the area-integrated surface mass balance after 2005. In contrast to the changes observed in the southeast and northwest regions, glaciers of central west Greenland showed little change in both the terminus position and ice velocity until 2010 (Moon et al., 2012; Seale et al., 2011). However, some glaciers in this region started to accelerate and lose more mass since 2010 with a decrease in surface mass balance (Mouginot et al., 2019). Overall, accelerations in ice front retreat and surface ice velocity from tidewater glaciers have increased Greenland's glacial discharge from 456 Gt/year in 2000 to 555 Gt/year in 2018 (Mouginot et al., 2019).

Despite the regional trend of changes in tidewater glaciers, significant variability exists within each region. For example, while oceanic and atmospheric forcings slowly change with latitude along the coast of northwest Greenland, the pattern of glacier retreat varies dramatically from one glacier to the next (Murray et al., 2015; Wood et al., 2018). Some large glaciers dominate trends in ice discharge of this region even though a third of tidewater glaciers

showed no trend in velocity (Moon et al., 2012). In 2000-2012, approximately half of the observed mass loss from the Greenland ice sheet was associated with only four glaciers: Jakobshavn Isbræ, Kangerlussuaq, Koge Bugt, and Ikertivaq S (Mouginot et al., 2019). Therefore, while we seek an understanding of tidewater glacier dynamics at a regional or ice sheet scale, it is also critical to investigate the changes in individual glaciers.

The retreat of tidewater glaciers is the primary driver of mass loss from Greenland. Ice front retreat typically results from a coupling between the undercutting of warm ocean water and iceberg calving (Fig. 1.3). However, these two processes are poorly constrained since there are no direct observations of the melting or calving process. Although recent advances in plume theory (Jenkins, 2011) and modeling approaches (e.g., Cowton et al., 2015; Xu et al., 2013; Rignot et al., 2016; Benn et al., 2017) provide a better understanding of submarine melting and calving, their links to ice sheet dynamics are still poorly constrained. It is, therefore, important to understand those processes to investigate the changes in tidewater glaciers.

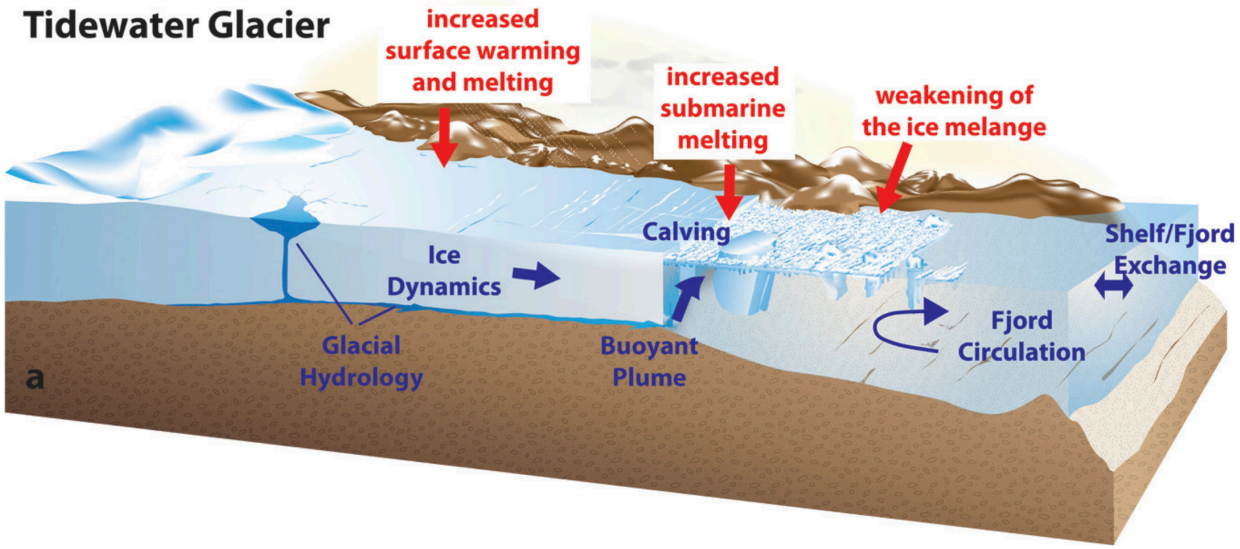

Figure 1.3: Schematic of a tidewater glacier with proposed mechanisms for glacier retreat (red) and key processes that affect these mechanisms (blue). Figure adapted from Straneo et al. (2013)

Ice sheet modeling

With a clear trend of an increase in ice mass loss from the Greenland ice sheet observed, how much mass the Greenland ice sheet is going to lose over the next century and beyond has become one of the most urgent questions in understanding the consequences of climate change. Numerical ice sheet modeling is our best tool to address this question. In this thesis, we use the Ice Sheet System Model (ISSM, Larour et al., 2012). ISSM is a high-resolution, open-source, massively parallelized finite element ice flow model that has been developed by researchers at the Jet Propulsion Laboratory and the University of California, Irvine, CA, USA. It includes various ice flow approximations (e.g., Full-Stokes , Blatter-Pattyn (Blatter, 1995; Pattyn, 2003), Shelfy-stream (MacAyeal, 1989), Shallow ice (Hutter, 1983), and L1L2 (Hindmarsh, 2004)), grounding line and moving boundary capabilities. It also includes data assimilation capability to calculate unknown and poorly constrained parameters. In this thesis, we detail the implementation of additional tools in ISSM that parameterize physical processes that are important in the evolution of Greenland's glaciers in a changing climate system. We focus on calving dynamics and consequent glacial change through ice-ocean interactions. Calving is one of the grand challenges of glaciology and addressing this question will make it possible to improve the reliability and accuracy of projecting the future of the Greenland ice sheet.

Objectives of this thesis

This thesis aims to estimate the contribution of the Greenland ice sheet to global sea-level rise through 2100 using a new generation ice sheet model that fully accounts for ice front changes of individual tidewater glaciers. To model individual tidewater glaciers,

1. We implement ice front calving and ocean melting parameterizations in ISSM.
2. We apply those capabilities on Northeast Greenland to investigate the response of this

region to ocean forcing over the next century.

3. We extend our model to include all tidewater glaciers along the coast of Greenland to investigate their future evolution.

We estimate sea-level rise from the Greenland ice sheet using various climate model scenarios. We force our ice sheet model with forcings taken from several general circulation model outputs from the Coupled Model Intercomparison Project Phase 5 (CMIP5) and Phase 6 (CMIP6).

Chapter 2

Numerical Ice Sheet Modeling

This chapter presents an overview of the mathematical and scientific theories underpinning a numerical ice sheet model. The first section describes ice sheet dynamics described by mass balance and momentum balance. The second section deals with the inversion method to find out unknown properties of ice. The final section describes how the ice sheet model is used for future projections of the ice sheet system and previous studies for projections of Greenland in ice sheet models.

2.1 Ice sheet dynamics

The ice flow can be described by the governing equations derived from mass balance and momentum balance equations.

2.1.1 Mass balance

A local form of mass conservation is derived:

$$\frac{D\rho}{Dt} + \rho \, \nabla \cdot \boldsymbol{v} = 0 \tag{2.1}$$

The density of ice sheet increases with depth. However, the largest density changes occur only in the upper 50 to 100 m of the ice sheet, which typically decreases the average density of the ice column by 1 to 2% (Cuffey and Paterson, 2010). Further below, both thermal expansion and compression change the ice density with depth by at most 1% (Cuffey and Paterson, 2010). For these reasons, the ice in glaciers and ice sheets is considered an incompressible material. For an incompressible material, the mass balance equation is reduced to the continuity equation as:

$$\nabla \cdot \boldsymbol{v} = 0 \tag{2.2}$$

Using the kinematic boundary conditions for the surface and bottom of an ice sheet, we have the evolution of surface elevation described as:

$$\frac{\partial s}{\partial t} + v_x \left(s\right) \frac{\partial s}{\partial x} + v_y \left(s\right) \frac{\partial s}{\partial y} - v_z \left(s\right) = \dot{M}_s \tag{2.3}$$

and the similar boundary condition at the base:

$$\frac{\partial b}{\partial t} + v_x \left(b\right) \frac{\partial b}{\partial x} + v_y \left(b\right) \frac{\partial b}{\partial y} - v_z \left(b\right) = \dot{M}_b \tag{2.4}$$

where s and b are surface elevation and ice base elevation, respectively, v_x, v_y, and v_z are x, y and z components of the velocity, respectively, and $\dot{M}_s$ and $\dot{M}_b$ are accumulation/ablation rate at the ice surface and melting/freezing rate at the ice bottom, respectively.

2.1.2 Momentum balance

Quasi-static equation

The balance of linear momentum is the extension of Newton's second law to a continuous body:

$$\rho \frac{D\boldsymbol{v}}{Dt} = \rho \boldsymbol{g} + \nabla \cdot \boldsymbol{\sigma} \tag{2.5}$$

The gravitational force, $\rho \boldsymbol{g}$, and the Coriolis force, $2\rho\Omega \times \boldsymbol{v}$, are two body forces that act on ice sheets but the Coriolis force is negligible (Greve and Blatter, 2009). The acceleration and inertia term, $\rho \frac{D\boldsymbol{v}}{Dt}$ is also negligible (Reist, 2005), which can reduce the general momentum balance equation above to a 'quasi-static' equation:

$$\nabla \cdot \boldsymbol{\sigma} + \rho\, \boldsymbol{g} = \mathbf{0} \tag{2.6}$$

Constitutive Equation: Glen-Nye flow law

Ice is considered as an incompressible material. For the incompressibility, the Cauchy stress tensor can be decomposed to a deviatoric stress term and a pressure term:

$$\boldsymbol{\sigma} = \boldsymbol{\sigma}' - p\mathbf{I} \tag{2.7}$$

Ice is also commonly assumed perfectly isotropic, which derives a constitutive relation of ice:

$$\boldsymbol{\sigma}' = 2\mu\dot{\boldsymbol{\varepsilon}} \tag{2.8}$$

where μ is ice viscosity and $\dot{\boldsymbol{\varepsilon}}$ is strain rate. Glen's flow law states a relation between the effective strain rate and effective stress of ice (Glen, 1955):

$$\dot{\varepsilon}_e = \left(\frac{\sigma'_e}{B}\right)^n \tag{2.9}$$

where B is a viscosity parameter and n is the stress exponent, empirically derived parameter ranging from 1.5 to 4.2. A value of $n = 3$ is most commonly used in glaciology (Cuffey and Paterson, 2010). Nye (1957) extended Glen's flow law to tensorial form to cover multiaxial states of stress. For isotropic material, the strain rate component is proportional to its corresponding stress component:

$$\dot{\boldsymbol{\varepsilon}} = \lambda \boldsymbol{\sigma}' \tag{2.10}$$

and

$$\dot{\varepsilon}_e = \lambda \sigma'_e \tag{2.11}$$

Combining Eq. 2.11 with Glen's flow law, we obtain:

$$\lambda = \left(\frac{\sigma'^{n-1}_e}{B^n}\right) \tag{2.12}$$

and

$$\dot{\boldsymbol{\varepsilon}} = \left(\frac{\sigma'^{n-1}_e}{B^n}\right) \boldsymbol{\sigma}' \tag{2.13}$$

Eliminating σ'_e, we get:

$$\dot{\boldsymbol{\varepsilon}} = \frac{\dot{\varepsilon}_e^{\frac{n-1}{n}}}{B} \boldsymbol{\sigma}' \tag{2.14}$$

From Eq. 2.8 and Eq. 2.14, the viscosity, μ is derived as:

$$\mu = \frac{B}{2\left(\dot{\varepsilon}_e^{1-\frac{1}{n}}\right)} \tag{2.15}$$

Boundary conditions

To solve the momentum balance equation of ice sheet dynamics, boundary conditions are required (Fig 2.1).

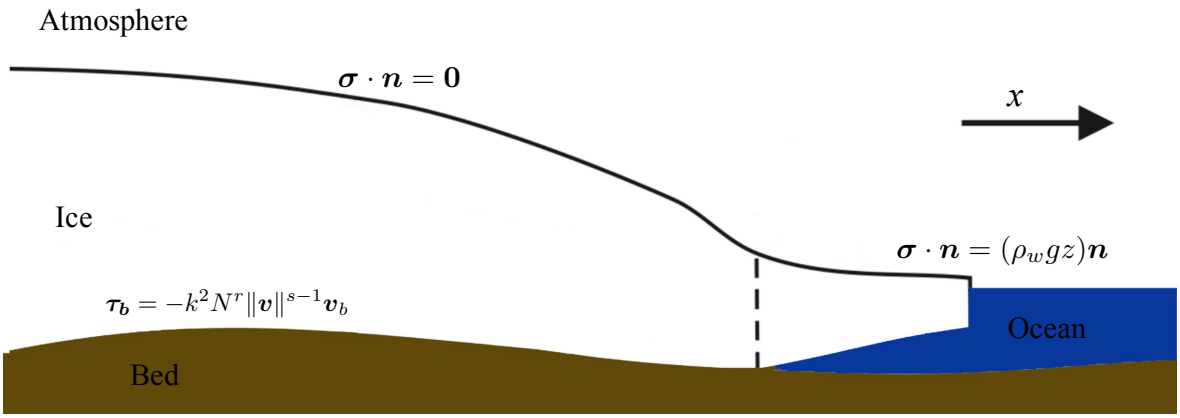

Figure 2.1: Schematic of boundary conditions for the momentum balance equation

Ice-Atmosphere boundary The ice-atmosphere boundary is considered to be a free surface since the atmospheric pressure is negligible compared to the ice lithostatic pressure:

$$\boldsymbol{\sigma} \cdot \boldsymbol{n} = -p_0 \boldsymbol{n} \simeq \mathbf{0} \tag{2.16}$$

where $\boldsymbol{n}$ is the unit normal vector pointing outward.

Ice-Ocean boundary The water pressure, p_w, is applied at the ice-ocean boundary, which linearly increases with ocean depth:

$$\boldsymbol{\sigma} \cdot \boldsymbol{n} = -p_w \boldsymbol{n} = (\rho_w g z)\boldsymbol{n} \tag{2.17}$$

where ρ_w is the density of sea water and z is the water depth.

Ice-Bedrock boundary At the ice-bedrock interface, two boundary conditions are applied. One is a Dirichlet boundary condition which ensures a non-interpenetrating condition between the ice and the bedrock:

$$\boldsymbol{v} \cdot \boldsymbol{n} = \dot{M}_b \tag{2.18}$$

The other one is a Neumann boundary condition which describes basal friction. The basal sliding of glaciers is generally described using a viscous friction law (Cuffey and Paterson, 2010):

$$\|\boldsymbol{v}_b\| = kN^{-q}\|\boldsymbol{\tau}_b\|^p \tag{2.19}$$

- $\boldsymbol{v}_b$ is the velocity component, tangential to the bedrock surface
- $N = g\rho H + \rho_w g z_b$ is the effective pressure at the base, z_b.
- $\boldsymbol{\tau}_b$ is the friction stress component, tangential to the bedrock surface: $\boldsymbol{\tau}_b = \boldsymbol{\sigma} \cdot \boldsymbol{n} - \sigma_{nn}\boldsymbol{n}$
- k, q and p are positive constants

The general form of the friction law can be described as (Weertman, 1957; Budd et al., 1979):

$$\boldsymbol{\tau}_b \quad = \quad -k^2 N^r \|\boldsymbol{v}\|^{s-1}\boldsymbol{v}_b \tag{2.20}$$

where $r = q/p$ and $s = 1/p$. In this thesis, $p = 1, q = 1$ is applied to consider the effective pressure. The basal friction coefficient, k, can be computed through inversion, which will be discussed in more detail in section 2.2.

Full Stokes model

Mass conservation (Eq. 2.2) and momentum balance equations (Eq. 2.6) with an ice constitutive equation (Eq. 2.8) yield the full Stokes equation that can be described in a Cartesian

coordinate system as:

$$\begin{cases} \frac{\partial}{\partial x}\left(2\mu\frac{\partial v_x}{\partial x}\right)+\frac{\partial}{\partial y}\left(\mu\frac{\partial v_x}{\partial y}+\mu\frac{\partial v_y}{\partial x}\right)+\frac{\partial}{\partial z}\left(\mu\frac{\partial v_x}{\partial z}+\mu\frac{\partial v_z}{\partial x}\right)-\frac{\partial p}{\partial x}=0 \\ \frac{\partial}{\partial x}\left(\mu\frac{\partial v_x}{\partial y}+\mu\frac{\partial v_y}{\partial x}\right)+\frac{\partial}{\partial y}\left(2\mu\frac{\partial v_y}{\partial y}\right)+\frac{\partial}{\partial z}\left(\mu\frac{\partial v_y}{\partial z}+\mu\frac{\partial v_z}{\partial y}\right)-\frac{\partial p}{\partial y}=0 \\ \frac{\partial}{\partial x}\left(\mu\frac{\partial v_x}{\partial z}+\mu\frac{\partial v_z}{\partial x}\right)+\frac{\partial}{\partial y}\left(\mu\frac{\partial v_y}{\partial z}+\mu\frac{\partial v_z}{\partial y}\right)+\frac{\partial}{\partial z}\left(2\mu\frac{\partial v_z}{\partial z}\right)-\frac{\partial p}{\partial z}-\rho g=0 \\ \frac{\partial v_x}{\partial x}+\frac{\partial v_y}{\partial y}+\frac{\partial v_z}{\partial z}=0 \end{cases} \tag{2.21}$$

Higher-order model

Because solving the full Stokes equation is computationally expensive, simplified models are widely used in the ice sheet modeling community. The three-dimensional higher-order (HO) model is one of the simplified models that makes the model much less computationally intensive. The two main assumptions are made for this model. First, the horizontal gradients of the vertical velocity are negligible compared to vertical gradients of the horizontal velocity ($\frac{\partial v_z}{\partial x} \ll \frac{\partial v_x}{\partial z}$ and $\frac{\partial v_z}{\partial y} \ll \frac{\partial v_y}{\partial z}$). The second main assumption is that the horizontal gradient of the horizontal shear stress is small compared to the vertical gradient of the vertical stress ($\frac{\partial \sigma_{xz}}{\partial x} \ll \frac{\partial \sigma_{zz}}{\partial z}$ and $\frac{\partial \sigma_{yz}}{\partial y} \ll \frac{\partial \sigma_{zz}}{\partial z}$). With this assumption, the vertical normal stress is equal to the ice overburden pressure, which reduces the vertical component of the momentum balance equation to:

$$\frac{\partial \sigma_{zz}}{\partial z}-\rho g=0 \tag{2.22}$$

Finally, the higher-order model can be described as:

$$\begin{cases} \dfrac{\partial}{\partial x}\left(4\mu\dfrac{\partial v_x}{\partial x}+2\mu\dfrac{\partial v_y}{\partial y}\right)+\dfrac{\partial}{\partial y}\left(\mu\dfrac{\partial v_x}{\partial y}+\mu\dfrac{\partial v_y}{\partial x}\right)+\dfrac{\partial}{\partial z}\left(\mu\dfrac{\partial v_x}{\partial z}\right)=\rho g\dfrac{\partial z_s}{\partial x} \\ \dfrac{\partial}{\partial x}\left(\mu\dfrac{\partial v_x}{\partial y}+\mu\dfrac{\partial v_y}{\partial x}\right)+\dfrac{\partial}{\partial y}\left(4\mu\dfrac{\partial v_y}{\partial y}+2\mu\dfrac{\partial v_x}{\partial x}\right)+\dfrac{\partial}{\partial z}\left(\mu\dfrac{\partial v_y}{\partial z}\right)=\rho g\dfrac{\partial z_s}{\partial y} \\ v_z\left(x,y,z\right)=v_z\left(x,y,z_b\right)-\displaystyle\int_{z_b(x,y)}^{z}\dfrac{\partial v_x}{\partial x}+\dfrac{\partial v_y}{\partial y}dz' \end{cases} \tag{2.23}$$

Shelfy-stream approximation

In addition to the two assumptions made for the higher-order model, the Shelfy stream approximation model (SSA) assumes that the vertical shear is negligible ($\dfrac{\partial v_x}{\partial z}=0$, $\dfrac{\partial v_y}{\partial z}=0$, $\dot{\varepsilon}_{xz}=0$, $\dot{\varepsilon}_{yz}=0$), resulting in a two-dimensional model (Morland and Zainuddin, 1987; MacAyeal, 1989). Under the assumptions described above with flat bed topography, the SSA model can be represented as:

$$\begin{cases} \dfrac{\partial}{\partial x}\left(4H\bar{\mu}\dfrac{\partial v_x}{\partial x}+2H\bar{\mu}\dfrac{\partial v_y}{\partial y}\right)+\dfrac{\partial}{\partial y}\left(H\bar{\mu}\dfrac{\partial v_x}{\partial y}+H\bar{\mu}\dfrac{\partial v_y}{\partial x}\right)=\rho gH\dfrac{\partial z_s}{\partial x}+\alpha^2 v_x \\ \dfrac{\partial}{\partial y}\left(4H\bar{\mu}\dfrac{\partial v_y}{\partial y}+2H\bar{\mu}\dfrac{\partial v_x}{\partial x}\right)+\dfrac{\partial}{\partial x}\left(H\bar{\mu}\dfrac{\partial v_x}{\partial y}+H\bar{\mu}\dfrac{\partial v_y}{\partial x}\right)=\rho gH\dfrac{\partial z_s}{\partial y}+\alpha^2 v_y \end{cases} \tag{2.24}$$

where $\bar{\mu}$ is the depth-averaged ice viscosity and α is the friction coefficient.

Shallow ice approximation

The shallow ice approximation (SIA) is the simplest, therefore the most computationally efficient ice flow model introduced by Hutter (1983). With the assumptions of HO model, the SIA only takes the vertical shear into account, as opposed to the SSA model. The stress components that are not negligible are σ'_{xz} and σ'_{yz}, which simplifies the momentum balance

equation to:

$$\begin{cases} \dfrac{\partial}{\partial z}\left(\mu\dfrac{\partial v_x}{\partial z}\right) = \rho g\dfrac{\partial z_s}{\partial x} \\ \\ \dfrac{\partial}{\partial z}\left(\mu\dfrac{\partial v_y}{\partial z}\right) = \rho g\dfrac{\partial z_s}{\partial y} \end{cases} \tag{2.25}$$

The SIA model is suitable for grounded ice with limited sliding, but not for the fast-changing region on a short time scale (Blatter et al., 2010). Therefore, in this thesis, only HO and SSA models are considered.

2.1.3 Energy balance

Assuming that the heat conduction follows Fourier's law, a local energy conservation equation is derived:

$$\rho\frac{D}{Dt}\left(cT\right) = \nabla\cdot k_{th}\,\nabla T + \Phi \tag{2.26}$$

Assuming ρ, c and k_{th} are constant in time and space (Hooke, 2005), Eq. 2.26 becomes

$$\frac{\partial T}{\partial t} = -\boldsymbol{v}\cdot\nabla T + \frac{k_{th}}{\rho c}\Delta T + \frac{\Phi}{\rho c} \tag{2.27}$$

Boundary conditions

Ice-Atmosphere boundary On the surface of a glacier, the mean annual air temperature is imposed since the ice temperature measured at 10-15 m depth is equal to the mean annual air temperature (Cuffey and Paterson, 2010):

$$T_s = T_a \tag{2.28}$$

This assumption has been widely used in the ice sheet thermal model (e.g., Hulbe and MacAyeal, 1999; Pattyn, 2003; Seroussi et al., 2013).

Ice-Ocean boundary On the ice-ocean boundary, a heat flux, proportional to the temperature difference between the ice shelf and the ocean, is imposed:

$$k_{th}\ \nabla T|_b\ .\boldsymbol{n} \simeq -k_{th}\ \left.\frac{\partial T}{\partial z}\right|_b = -\rho_w c_{pM} \gamma\ (T_b - T_{pmp}) \tag{2.29}$$

With:

- $\boldsymbol{n} = (n_x, n_y, n_z)$ normal vector pointing outward
- c_{pM} mixed layer (Holland and Jenkins, 1999, p5) specific heat capacity (J kg^{-1} K^{-1})
- γ thermal exchange velocity (m s^{-1})
- T_{pmp} pressure melting point (melting point of ice under pressure in K) (Paterson, 1994, p.212)

Ice-Bedrock boundary On the bottom of the grounded ice sheet, the boundary condition is constrained by a geothermal flux, G, and the heat due to basal friction:

$$k_{th}\ \nabla T|_b \cdot \boldsymbol{n} \simeq -k_{th}\ \left.\frac{\partial T}{\partial z}\right|_b = G + \|\boldsymbol{\tau}_b \cdot \boldsymbol{u}_b\| \tag{2.30}$$

2.2 Inverse method in ice sheet modeling

Many ice sheet/glacier properties, such as surface elevation, surface velocity, can be directly measured from in-situ or remotely sensed observations. Other properties, such as basal friction or ice rigidity, are poorly understood because they are not directly measurable.

Some of those properties are critical for ice sheet modeling because they control ice speed. To calculate those properties in ice sheet modeling, the inverse method was introduced by MacAyeal (1992, 1993). The main idea of the inverse method is to infer poorly known parameters using observed properties. In ice sheet modeling, basal friction and ice hardness are two main unknown parameters that can be inferred using inversion.

To infer basal friction or ice hardness, a cost function, $\mathcal{J}$, that measures the misfit between the modeled and the observed surface velocity is calculated. Here, the cost function that consists of three terms is introduced as:

$$\mathcal{J}(\boldsymbol{v}, \alpha) = \gamma_1 \int_{\Gamma_s} \frac{1}{2} \|\boldsymbol{v} - \boldsymbol{v}_{obs}\|^2 \, d\Gamma_s + \gamma_2 \int_{\Gamma_s} \frac{1}{2} \ln \left(\frac{\|\boldsymbol{v}\| + \varepsilon}{\|\boldsymbol{v}_{obs}\| + \varepsilon} \right)^2 d\Gamma_s + \gamma_3 \int_{\Gamma_b} \nabla\alpha \cdot \nabla\alpha \, d\Gamma_b \tag{2.31}$$

where $\boldsymbol{v}$ and $\boldsymbol{v}_{obs}$ are the modeled and observed ice velocity respectively, α is the inferred parameter (basal friction coefficient or ice hardness), ε is the small value to avoid dividing by zero, Γ_s and Γ_b are ice surface and bed, respectively, and γ_1, γ_2 and γ_3 are constants. The first term represents the mean square error, the second term is logarithmic magnitude misfit, and the final term is a regularizing term that penalizes wiggles in the cost function.

With the cost function above, the adjoint method is applied to calculate the gradient to the inferred parameter and a steepest-descent algorithm is applied to finally calculate parameter value. Detailed approaches can be found in many studies (e.g., Morlighem et al., 2010).

2.3 Level-set method

A level-set method, introduced by Osher and Sethian (1988), has been an efficient way to implicitly represent and track the evolution of interfaces in many applications. The main

advantage of this method is to easily deal with changes in topology compared to explicit methods (Osher and Sethian, 1988). Moving boundaries of the ice sheet can be treated using this method (Bondzio et al., 2016). In the level-set method, the contour, or the level-set, φ, is defined to represent the position of ice boundary. The signed distance between the point $\mathbf{x}$ and the ice front is used to partition the model domain into three subdomains: ice domain (Ω), ice-free domain, and ice boundary (Γ) (Fig. 2.2):

$$\begin{cases} \varphi(\mathbf{x}, t) < 0 & \text{if } \mathbf{x} \in \Omega \\ \varphi(\mathbf{x}, t) = 0 & \text{if } \mathbf{x} \in \Gamma \\ \varphi(\mathbf{x}, t) > 0 & \text{if } \mathbf{x} \notin \Omega \end{cases} \tag{2.32}$$

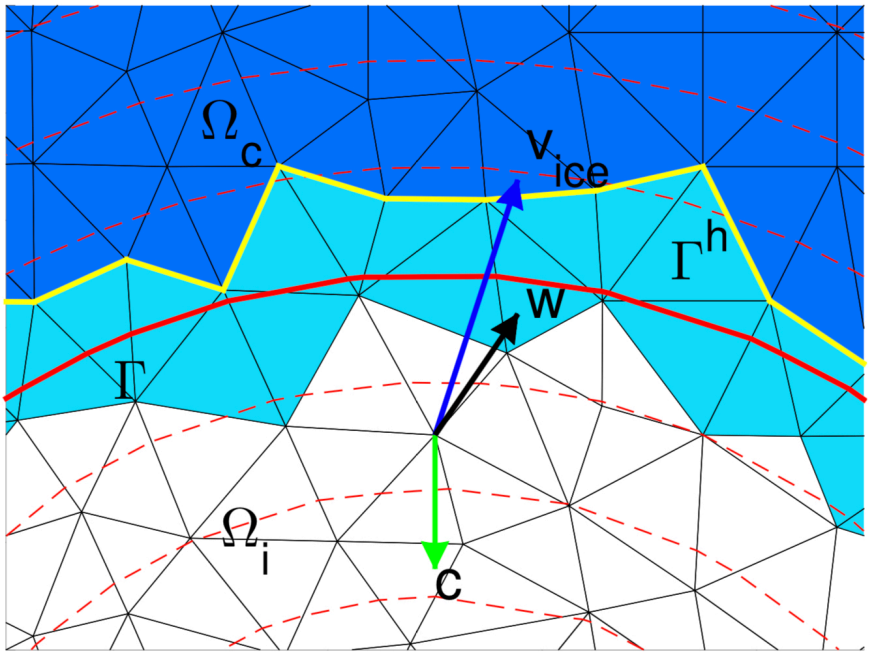

Figure 2.2: Schematic of the numerical ice margin. The red line represents the zero level set and the yellow line represents the numerical calving front. Dark blue triangles are ice-free elements, white ones are ice-filled, and the light blue ones are the front elements. Figure adapted from Bondzio et al. (2016).

At each time step, φ is advected following the level-set equation:

$$\frac{\partial \varphi}{\partial t} + \mathbf{v}_\mathrm{f} \cdot \nabla \varphi = 0 \tag{2.33}$$

where $\mathbf{v}_f$ is the ice front velocity vector. The ice front velocity can be defined by the model user according to the calving/ablation parameterization in the model. Bondzio et al. (2016) provides a detailed description of the implementation of the level-set method in ISSM.

2.4 Modeling the evolution of the ice sheet

2.4.1 Transient solutions

In ISSM, the evolution of the ice sheet can be modeled through a combination of solutions of three conservation laws above and modules that allow the model to be run forward in time. At each time step of the simulation, the following steps are performed in order: thermal solution, stress balance solution, moving front module, and mass transport solution. In this thesis, only HO and SSA model solutions are considered.

Thermal model

It has been shown that changes in temperature of grounded ice do not have a significant influence on ice sheet evolution for century-scale projections (Seroussi et al., 2013). In all simulations of this thesis, the thermal solution is calculated only at the first time step assuming a steady-state and is kept fixed for the entire simulation. The temperature field can be calculated through Eq. 2.27.

Stress balance model

At each time step, the velocity field is calculated through the momentum balance equation constrained by mechanical boundary conditions mentioned in the previous section (2.1). The

computation of the velocity field is non-linear since the viscosity depends on the solution. Therefore, the solving procedure follows an iterative process (Fig. 2.3). The computed velocity field is compared to one from the previous iteration. If the convergence criterion (e.g., $\sim 1\%$) is not fulfilled, viscosity and the basal condition is updated using the velocity of that iteration to compute new velocity.

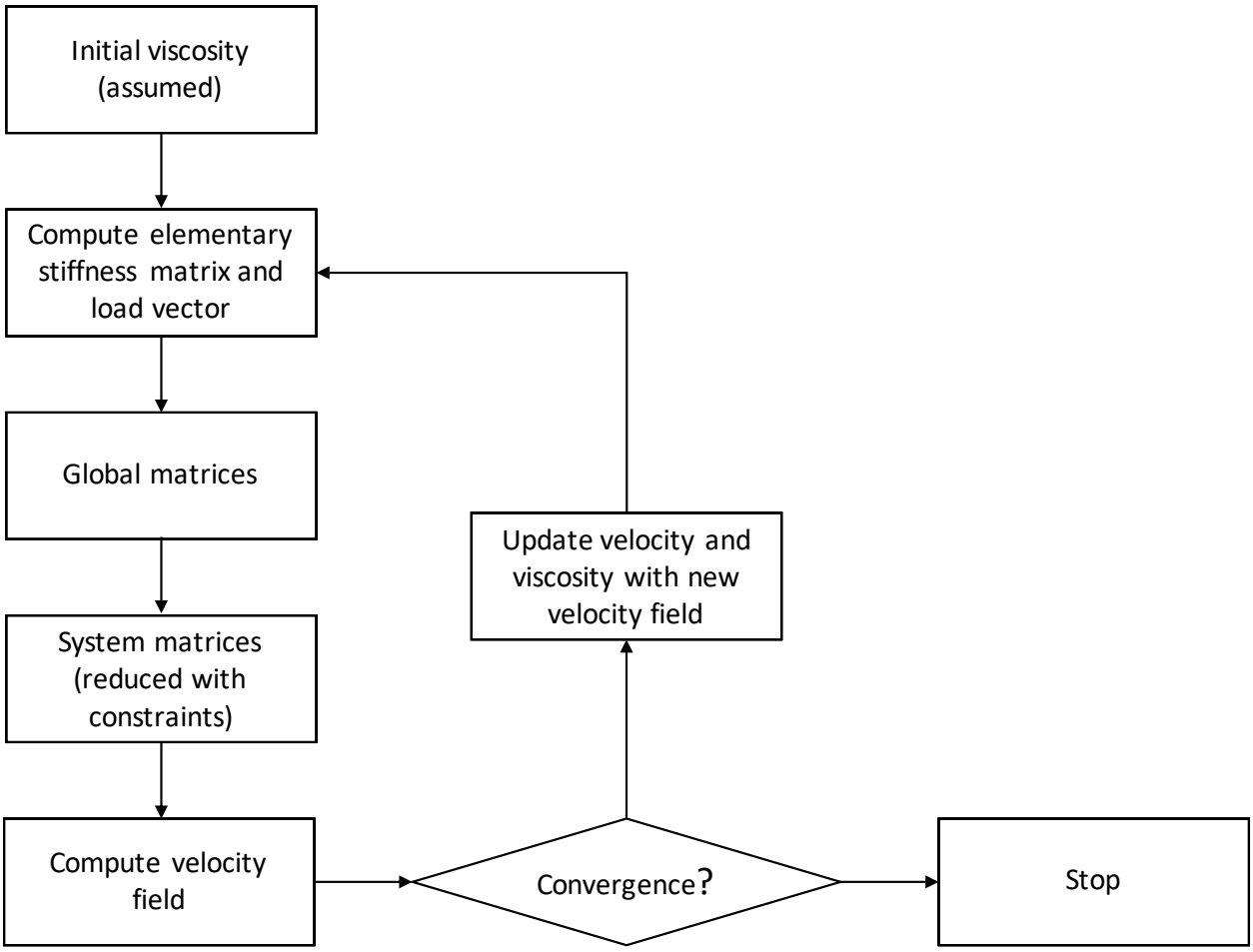

Figure 2.3: Schematic of a non-linear solver used by ISSM

Moving front

The level-set is initialized using a signed distance approach. At each time step, the level-set, φ is advected through the level-set equation (Eq. 2.33). For some model simulations, the level-set is explicitly set to +1 (no ice) or -1 (ice) on each vertex of finite element mesh

depending on constraints. To avoid noise or distortion of level-set over time, φ is reinitialized at every 'user-defined' time step.

Mass transport model

Once the solution of the velocity field is found and the ice domain is updated, the model is run forward in time by updating the geometry of ice through the mass transport equation:

$$\frac{\partial H}{\partial t} + \nabla \cdot H\overline{\boldsymbol{v}} = \dot{M}_s - \dot{M}_b \tag{2.34}$$

where H is ice thickness.

For HO and SSA model, the grounding line position is controlled by hydrostatic equilibrium, which is calculated using the floatation height (H_f):

$$H_f = -\frac{\rho_w}{\rho_i} r \tag{2.35}$$

where ρ_w is the ocean density, ρ_i is the ice density and r is the bedrock elevation (negative if below sea level). Grounding line is located where $H = H_f$.

2.4.2 Previous studies

Over the past two decades, there have been several modeling approaches for projecting future ice mass change of the Greenland ice sheet. Studies focusing on atmosphere assume a passive ice sheet and only simulate changes in surface mass balance (SMB) with general circulation models (Gregory and Huybrechts, 2006) or regional models (Fettweis et al., 2013; van Angelen et al., 2012). These studies did not account for the dynamics of the ice sheet, which might result in conservative estimates. About 60% of the mass loss for the period of

1991-2015 is from increasing surface melt and runoff (Csatho et al., 2014; Enderlin et al., 2014). Estimating a more reliable surface melt is critical for future Greenland projections because surface processes account for a large portion of uncertainty in the ice sheet model projections (Aschwanden et al., 2019). However, patterns of surface melt on Greenland depend on processes (e.g., albedo evolution, surface and basal hydrology, and meltwater buffering by firn) that are complex and challenging to capture (Pachauri et al., 2014). Those processes need to be addressed to help reduce uncertainty for future SMB and ice sheet projections.

Several studies used dynamic ice sheet models using some approximations of the full-Stokes model. Greve (2000) and Huybrechts and de Wolde (1999) used the shallow ice approximation (SIA) to project future changes in Greenland. Later, Nick et al. (2013) used a flowline model for modeling four major outlet glaciers and extrapolated estimates for sea level contribution from the entire Greenland ice sheet. This study provides a first estimate of the contribution to sea level from Greenland that accounts for the effects of dynamic retreat (Nick et al., 2013). However, the model from this study is based on the flowline approach which does not consider several factors such as lateral stresses or buttressing for outlet glaciers, and only simulates four marine terminating glaciers out of 200+ outlet glaciers in Greenland. After Nick et al. (2013), several studies include more complicated physics (higher-order or full-Stokes) for Greenland future projections. Fürst et al. (2015) estimates a future Greenland contribution to sea level using CMIP5 simulation outputs, accounting for SMB and ocean forcing. However, their highest resolution model was 5 km which is not sufficient to capture changes in many tidewater glaciers. More recently, Calov et al. (2018) and Aschwanden et al. (2019) simulate changes in Greenland with a hybrid (SIA/SSA) ice sheet wide model and provide estimates of future sea level contribution based on several climate scenarios. Calov et al. (2018) included subglacial hydrology in their model to better simulate runoff and discharge-driven submarine melt at the ice front. Aschwanden et al. (2019) ran the model at a higher resolution and performed ensemble simulations to quan-

tify the uncertainty in model parameters. Both studies include ice dynamics in a 2D/3D model, incorporating both ocean and atmosphere forcings. Those models, however, were not calibrated to the current changes in ice front positions at the individual glacier scale.

Simulated future sea level contributions of Greenland from recent modeling studies are similar to the upper end of the *'likely'* range reported by the IPCC Fifth Assessment Report (AR5) (Church et al., 2013). Those studies suggest future Greenland mass loss will be dominated by changes in SMB, rather than changes in ice discharge (Church et al., 2013; Goelzer et al., 2016). Although SMB forcing dominated in mass loss over the last two decades (Mouginot et al., 2019) and Greenland projection modeling is most sensitive to uncertainties in the applied climate forcing (Church et al., 2013), it is not clear that recent modeling studies correctly capture the processes that explain the increase in ice discharge from outlet glaciers. The ice-ocean interactions that affect ice discharge need to be included more accurately in the ice sheet model to provide a more reliable future sea level contribution of Greenland, which requires a new generation model.

Chapter 3

Modeling calving dynamics

This chapter focuses on the calving processes of the Greenland ice sheet and how they are represented in numerical models by summarizing the current state of knowledge of calving parameterizations. The first section introduces the calving of Greenland glaciers and the second section introduces calving parameterizations for numerical models. The final section describes the submarine melting processes that link calving and climate and their parameterizations.

3.1 Calving

The calving of icebergs is an important mechanism that controls the dynamics of marine terminating glaciers of Greenland. It accounts for about half of mass loss from Greenland (Enderlin et al., 2014; Rignot and Kanagaratnam, 2006), affecting the entire stress regime of outlet glaciers, which may lead to further retreat and ice flow acceleration (e.g. Gagliardini et al., 2010; Choi et al., 2017). Understanding the exact physical process of calving, however, has been an unsolved problem in glaciology. Benn et al. (2007) provided an overview of the

variety of calving styles and suggested several mechanisms that drive the calving of marine terminating glacier and ice shelves.

Ice velocity typically increases towards the terminus, which leads to an increase in longitudinal stretching of ice near the terminus. The crevasses are formed where the longitudinal strain rate is sufficiently high, which can be promoted by surface melt through "hydrofracture". Many calving models incorporate this stretching based mechanism as their calving criteria. (e.g., Benn et al., 2007; Nick et al., 2010; Morlighem et al., 2016).

The force imbalance between cryostatic and ocean pressure at the terminal face causes tensile stresses at the ice surface through a bending moment to rotate the ice front downward (Reeh, 1968) (Fig. 3.1). Maximum tensile stresses occur at the ice surface roughly one ice thickness away from the terminus. This mechanism typically causes low magnitude and high-frequency calving events, in contrast with the calving of large tabular icebergs driven by crevasse/rift propagation (Benn et al., 2007).

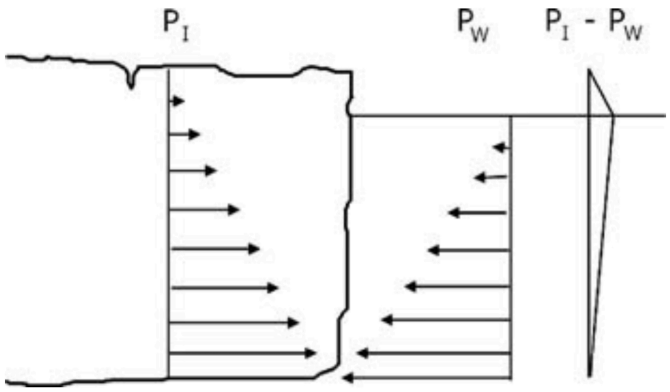

Figure 3.1: Schematic of force imbalance between cryostatic (P_I) and ocean (P_W) pressures. Figure adapted from Benn et al. (2007)

Undercutting of ice front by submarine melting increases the force imbalance at the ice front, which facilitates calving events (Benn et al., 2007). Recently, the effect of undercutting on calving mechanisms has got a lot of attention because submarine melt rates could be significant, especially in tidewater glacier settings where subglacial discharge drives vigorous

upwelling of meltwater. Several studies have shown that many glaciers in west Greenland are highly undercut by submarine melting, and total frontal ablation rates including calving are correlated with sub-surface ocean temperature and subglacial discharge (Rignot et al., 2015; Fried et al., 2015).

Buoyant forces near the ice front may trigger fractures at the ice bottom and promote blocks of ice to calve and rotate from the glacier. Submarine melting facilitates this type of calving by removing ice below the waterline and causing the development of 'an ice foot' or 'a toe', which increases the buoyant force (Wagner et al., 2016). Buoyant-drive calving style occurs at several fast-flowing glaciers in Greenland, such as Helheim Glacier and Jakobshavn Isbræ (James et al., 2014).

Calving is not a single process that can be explained by only one of the mechanisms described above. Iceberg calving can occur in a wide range of environmental settings with a variety of combinations of related processes (**?**). Although the physical complexity and observed variability in calving mechanisms complicate the inclusion of calving in the numerical ice sheet model, it needs to be addressed for more realistic simulation of changes in marine terminating glaciers. The following section introduces calving parameterizations for the ice sheet model that have been proposed and validated.

3.2 Calving parameterizations

In the ice sheet modeling community, several calving laws have been proposed to improve the projections of ice sheet change over the coming decades and reduce the uncertainty in their contribution to sea-level rise. However, most of the proposed parameterizations have been applied only to a specific region and have not been tested on other glaciers, while some others have only been implemented in 1-D flowline or vertical flowband models. The

extremely complicated mechanism of calving, combined with the difficulty of collecting data, makes the dynamic mass loss of glaciers one of the most poorly constrained components to estimating future sea level rise contribution. It is therefore critical to accurately parameterize calving in the ice sheet model to improve the projection of ice sheet changes.

The early attempt to understand calving dynamics focused on empirical relationships between frontal ablation rate and external and/or internal variables. Some studies found a correlation between frontal ablation and water depth (Brown et al., 1982) or terminus position and terminus height threshold (van der Veen, 2002). Other types of calving laws rely on crevasse fracturing processes, in which the terminus position is predicted where surface and basal crevasses exceed a threshold (Benn et al., 2007; Nick et al., 2010). There are also calving laws based on damage mechanics (Pralong and Funk, 2005).

3.2.1 Height-above-buoyancy model

In the height-above-buoyancy model, the position of calving terminus, rather than calving rate, has been taken into account for calving dynamics. The position of the calving front is defined by a floatation criterion. The calving rate, c, is not specified in the level set function but the level set can be set to +1 (ice free) or -1 (ice) following the height-above-buoyancy criterion. The height-above-buoyancy, H_O, is defined as:

$$H_O = (1 + q)\frac{\rho_w}{\rho_i} D_w \tag{3.1}$$

where $q \in [0,1]$ is a fraction, ρ_w and ρ_i are the densities of water and ice, respectively, and D_w is the water depth.

This model performed well in modeling advance and retreat of Columbia Glacier and Hansbreen, a tidewater glacier in Svalbard (Vieli et al., 2002; Benn et al., 2007). In this model,

however, ice shelves cannot be formed, because the model cuts off the glacier terminus before floatation is reached. As a result, the model cannot predict the calving behavior of Antarctic glaciers or ice streams that flow into ice shelves (Benn et al., 2007).

3.2.2 Crevasse-depth calving law

The crevasse-depth calving law is based on the penetration of surface and basal crevasses and the calving front is defined as the point at which surface and basal crevasses exceed a certain threshold. The normal stress responsible for crevasse opening is the resistive stress, R_{xx}, defined as:

$$R_{xx} = 2\left(\frac{\dot{\varepsilon}_{xx}}{A}\right)^{1/n} \tag{3.2}$$

where A is the Glen's law coefficient and $n = 3$ is the flow parameter.

For a surface crevasse, the crevasse penetration depth, d_s, is defined as equation 3.3 including water height in the crevasse, d_w, which allows the crevasse to penetrate deeper (van der Veen, 1998):

$$d_s = \frac{R_{xx}}{\rho_i g} + \frac{\rho_w}{\rho_i} d_w \tag{3.3}$$

where ρ_i and ρ_w are the density of ice and water, respectively.

For a basal crevasse, the penetration height, d_b is estimated from the requirement that net longitudinal stress is zero at that height (Jezek, 1984):

$$d_b = \frac{\rho_i}{\rho_p - \rho_i}\left(\frac{R_{xx}}{\rho_i g} - H_{ab}\right) \tag{3.4}$$

where H_{ab} represents the height above buoyancy, defined as

$$H_{ab} = H - \frac{\rho_p}{\rho_i} D \tag{3.5}$$

where H is full ice thickness and D is the depth of the glacier below sea level.

This model has been successful in reproducing trends of advance and retreat of several major Greenland outlet glaciers (Nick et al., 2012, 2013). It physically links calving to ice dynamics and surface melting by relating the position of ice fronts to crevasse depths. However, in their flowband model, lateral propagations of fractures are not taken into account. Later, Otero et al. (2010) extended the model to a 3D application to account for changes in the direction of crevasse opening stresses. Also, poorly constrained meltwater is used as a control to force this calving model, limiting confidence in predictions.

3.2.3 Kinematic first-order calving law (Eigencalving law)

Levermann et al. (2012) proposed a calving rate, c, proportional to strain rate along and transversal to horizontal flow:

$$c = K \cdot \dot{\epsilon}_{\parallel} \cdot \dot{\epsilon}_{\perp} \tag{3.6}$$

where K is a proportionality constant that captures the material properties relevant for calving.

This calving law could reasonably reproduce the calving trend of large Antarctic ice shelves, including stable fronts as observed and abrupt transitions of calving fronts. However, it does not work for Greenland's outlet glaciers that flow in narrow fjords with nearly parallel walls where the transversal strain rate is close to zero and noisy (Morlighem et al., 2016).

3.2.4 Tensile von Mises stress calving law

Morlighem et al. (2016) proposed a calving law based on tensile von Mises stresses to model calving dynamics of Store Gletscher of Greenland. The calving rate, c, follows the calving law based on tensile von Mises stress, $\tilde{\sigma}$:

$$c = \|\mathbf{v}\| \frac{\tilde{\sigma}}{\sigma_{\max}} \tag{3.7}$$

where $\mathbf{v}$ is ice velocity and $\sigma_{\max}$ is a stress threshold. For incompressible materials and introducing Glen's flow law, the tensile von Mises stress is defined as:

$$\tilde{\sigma} = \sqrt{3}\, B\, \tilde{\dot{\varepsilon}}_e^{1/n} \tag{3.8}$$

where B is the ice viscosity parameter, $\tilde{\dot{\varepsilon}}_e$ is the effective tensile strain rate, and $n = 3$ is Glen's exponent. The compressive deformation is ignored because the tensile strength of ice is considerably smaller than compressive strength (Benn et al., 2007). The effective tensile strain rate is defined as:

$$\tilde{\dot{\varepsilon}}_e^2 = \frac{1}{2}\left(\max\left(0, \dot{\varepsilon}_1\right)^2 + \max\left(0, \dot{\varepsilon}_2\right)^2\right) \tag{3.9}$$

where $\dot{\varepsilon}_1$ and $\dot{\varepsilon}_2$ are the two Eigenvalues of the 2D strain rate tensor, so that only tensile deformation is accounted for (Morlighem et al., 2016).

3.3 Submarine melting

Several mechanisms have been proposed to explain the link between ice front retreat and climate. Recently, submarine melting has been considered the main driver of the Greenland tidewater glacier retreat (Rignot et al., 2010). Submarine melting refers to the melting of ice

by the ocean both under the floating ice shelf and at the vertical calving front of tidewater glaciers. In this thesis, focusing on Greenland tidewater glaciers, submarine melting only refers to frontal melting at glacier termini.

3.3.1 Relationship between submarine melting and calving

Due to the difficulty of the surveying ice fronts, there have been no direct observations of submarine melting and their relations with calving. Instead, several modeling studies have demonstrated how melting at the ice front affects calving dynamics. Submarine melting is generally assumed to increase calving flux by undercutting the ice front. This relation is applied in a simple parameterization of the ice sheet model for Greenland tidewater glaciers (e.g Bondzio et al., 2016; Morlighem et al., 2016; Choi et al., 2017; Todd et al., 2018). Other studies have shown that undercutting has a limited effect on calving rates (Cook et al., 2014; Krug et al., 2014). Ma and Bassis (2019) found both an enhancing and a suppressing effect of frontal melting on calving, depending on the distribution and magnitude of melting. Those studies, however, were limited to steady-state analysis. In this thesis, we assume a simple additive relationship between frontal melting and calving in a time-evolving model to investigate the relative contributions of submarine melt and calving to mass loss of tidewater glaciers.

3.3.2 Submarine melting parameterizations

Some glaciological studies have not separated calving and frontal melting, two ice mass loss processes, by either ignoring submarine melt or parameterizing two processes into a single term as the effective calving rate (Bartholomaus et al., 2013). However, this can introduce significant confusion as recent measurements show that the relative contributions of submarine melt and calving vary from location to location (Enderlin and Howat, 2013;

Rignot et al., 2016). It is therefore important to consider frontal melting separately in the ice sheet model.

Based on the general circulation model and buoyant plume model, water velocity, temperature, and salinity around the calving front can be estimated and they can be converted to a melt rate using a submarine melt rate parameterization (Holland and Jenkins, 1999). Under the most commonly used three-equation parameterization, melt rate increases with both water velocity and temperature, which increases the turbulent transfer of heat. Melt rates also increase weakly with salinity and depth due to the dependence of the melting point on salinity and pressure (Holland and Jenkins, 1999).

Xu et al. (2013) used MITgcm with a modified three-equation formulation to estimate melt rate at the calving front of Store glacier and found a simple relationship between melt rate and other oceanic properties such as subglacial discharge and thermal forcing. They provided simple guidelines for estimating the frontal melt rate along calving fronts of Greenland glaciers (Fig. 3.2).

Rignot et al. (2016) extended the results of Xu et al. (2013) by modeling ocean-induced frontal melt rates using observations of five tidewater glaciers on West Greenland. Ocean-induced melt speeds, q_m, are calculated for various thermal forcing, TF, and subglacial freshwater flux, q_{sg}, and these results are adapted to apply to other glacier geometry as:

$$q_m = (Ahq_{sg}^{\alpha} + B)TF^{\beta} \tag{3.10}$$

where h is the water depth, $A = 3 \times 10^{-4}$ m$^{-\alpha}$ day $^{\alpha-1} \circ$ C $^{-\beta}$, $\alpha = 0.39$, $B = 0.15\ ^{\circ}C^{-\beta}$, and $\beta = 1.18$ (Rignot et al., 2016). Equation 3.10 provides a framework by which the melt rate can be calculated from modeled outputs or observations.

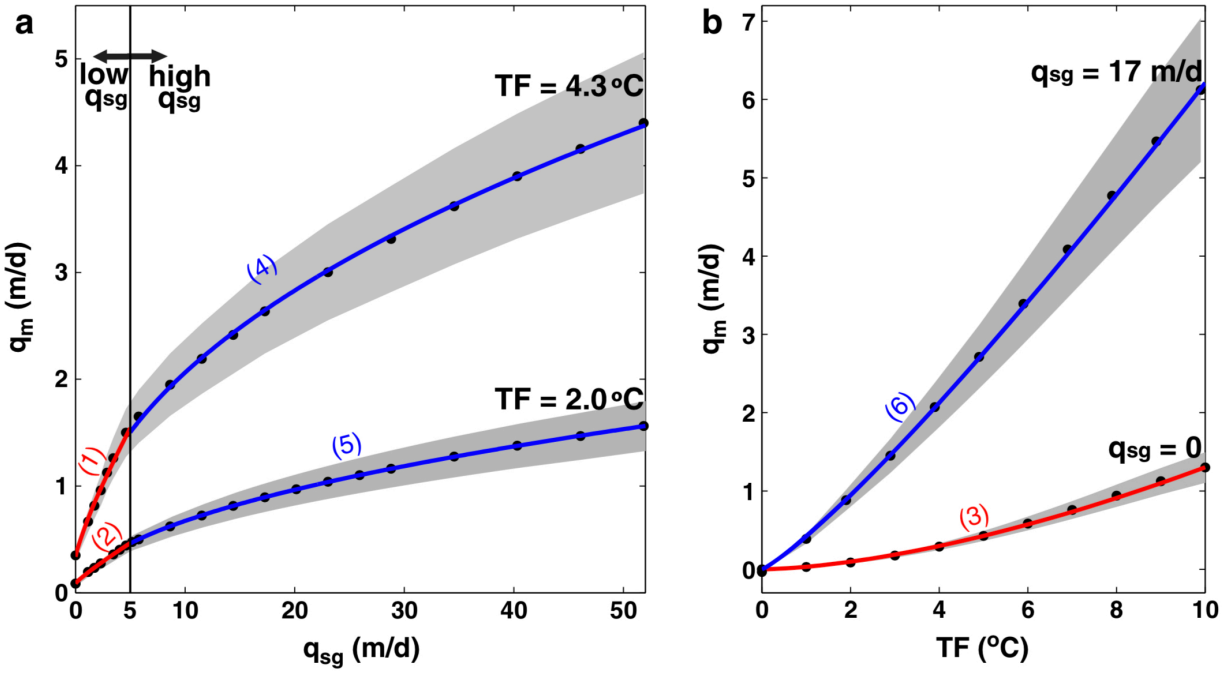

Figure 3.2: (a) Modeled relationship between submarine melt rate q_m and subglacial discharge q_{sg} for two fjord temperature profiles (b) modeled relationship between submarine melt rate q_m and fjord thermal forcing TF for two subglacial discharges. Figures adapted from Xu et al. (2013).

Chapter 4

Comparison of calving laws in ice sheet model

In this chapter, we test and compare several calving laws recently proposed in the literature using the Ice Sheet System Model (ISSM). We test these calving laws on nine tidewater glaciers of Greenland. We compare the modeled ice front evolution to the observed retreat from Landsat data collected over the past 10 years and assess which calving law has better predictive abilities for each glacier.

4.1 Applying calving laws to tidewater glaciers

While all of calving parameterizations proposed in the literatures have been tested on idealized or single, real-world geometries, most of them have not yet been tested on a wide range of glaciers and some of these laws have only been implemented in one-dimensional flowline or vertical flowband models (Vieli and Nick, 2011). The main objective of this chapter is to test and compare some of these calving laws on nine different Greenland outlet glaciers

using a 2D plan-view ice sheet model. Modeling ice front dynamics in a 2D horizontal or 3D model has been shown to be crucial, as the complex three-dimensional shape of the bed topography exerts an important control on the pattern of ice front retreat, which cannot be parameterized in flowline or flowband models (e.g. Morlighem et al., 2016; Choi et al., 2017). We do not include continuum damage models and the linear elastic fracture mechanisms (LEFM) approach in this study because these laws require to model individual calving events, whereas we focus here on laws that provide an "average" calving rate, or a calving front position, without the need to track individual calving events. While these approaches remain extremely useful to derive new parameterizations, their implementation in large scale models is not yet possible due to the level of mesh refinement required to track individual fractures.

We implement and test four different calving laws, namely the height-above-buoyancy criterion (HAB, Vieli et al., 2001), the crevasse-depth calving law (CD, Otero et al., 2010; Benn et al., 2017), the eigencalving law (EC, Levermann et al., 2012) and von Mises tensile stress calving law (VM, Morlighem et al., 2016), and model calving front migration of nine tidewater glaciers of Greenland for which we have a good description of the bed topography (Morlighem et al., 2017). The glaciers of this study are three branches of Upernavik Isstrøm (UI), Helheim glacier, three sectors of Hayes glacier, Kjer, and Sverdrup glaciers (Fig. 4.1). Each of these four calving laws includes a calibration parameter that is manually tuned for each glacier. These parameters are assumed to be constant for each glacier. To calibrate this parameter, we first model the past 10 years (2007-2017) using each calving law and compare the modeled retreat distance to the observed retreat distance. Once a best set of parameters is found, we run the model forward with the current ocean and atmospheric forcings held constant to investigate the impact of the calving laws on forecast simulations. We discuss the differences between results obtained with different calving laws for the hindcast and forecast simulations and the implications thereof for the application of the calving laws to real glacier cases.

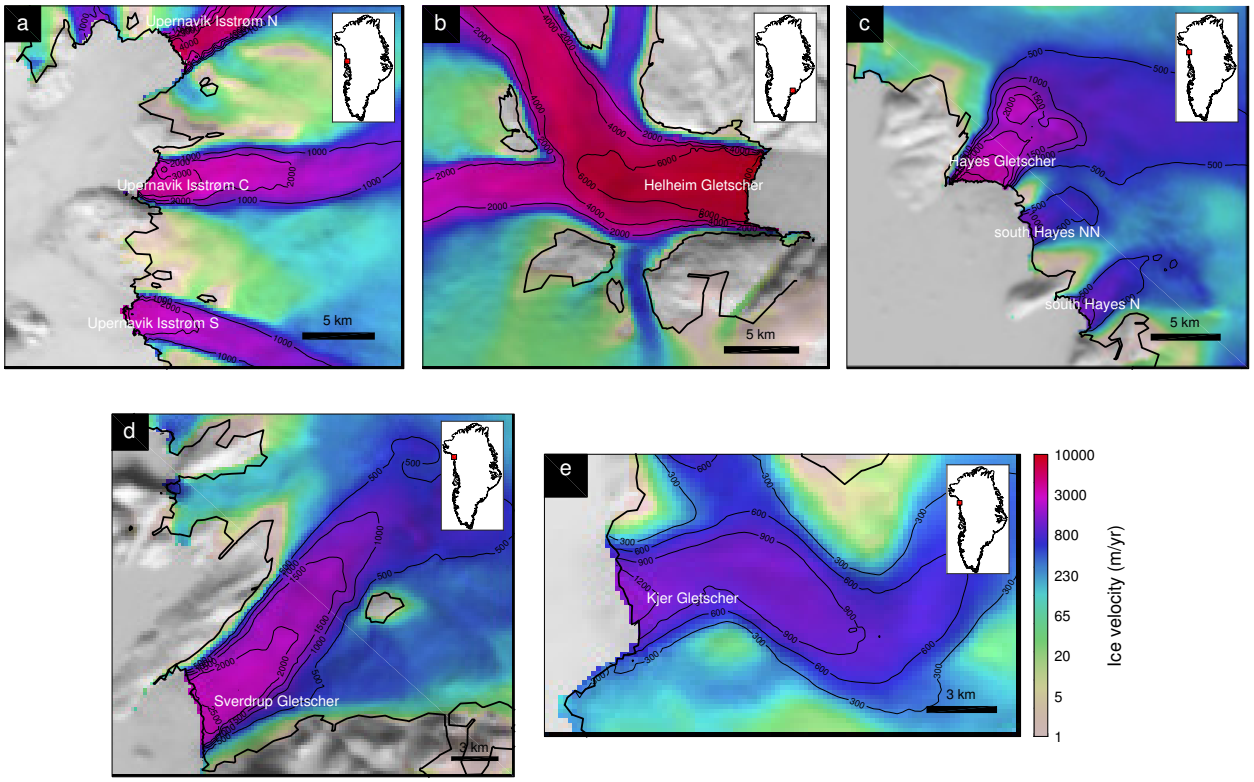

Figure 4.1: Ice surface velocity (black contours) for study glaciers (a) Upernavik Isstrøm (b) Hayes (c) Helheim (d) Sverdrup (e) Kjer. The thick black line is the ice edge.

4.2 Data and Method

We use the Ice Sheet System Model (ISSM, Larour et al., 2012) to implement four calving laws and to model nine glaciers. Our model relies on a Shelfy-Stream Approximation (Morland and Zainuddin, 1987; MacAyeal, 1989), which is suitable for fast outlet glaciers of Greenland (Larour et al., 2012). The mesh resolution varies from 100 m near the ice front to 1000 m inland and the simulations have different time steps that varies between 0.72 days and 7.2 days depending of the glacier in order to satisfy the CFL (Courant-Friedrichs-Lewy) condition (Courant et al., 1928). We use the surface elevation and bed topography data from BedMachine Greenland version 3 (Morlighem et al., 2017). The nominal date of this dataset is 2008, which is close to our starting time of 2007. The surface mass balance (SMB) is from the regional atmospheric model RACMO2.3 (Noël et al., 2015) and is kept constant

during our simulations. We invert for the basal friction to initialize the model, using ice surface velocity derived from satellite observations acquired at a similar period (2008-2009) (Rignot and Mouginot, 2012).

ISSM relies on the level set method (Bondzio et al., 2016) to track the calving front position. We define a level set function, φ, as being positive where there is no ice (inactive) and negative where there is ice (active region) and the calving front is implicitly defined as the zero contour of φ. Here, we implement two types of calving laws: EC and VM provide a calving rate, c, whereas HAB and CD provide a criterion that defines where the ice front is located. These two types of law are implemented differently within the level set framework of ISSM.

When a calving rate is provided, the level set is advected following the velocity of the ice front ($\mathbf{v}_{\text{front}}$) defined as a function of the ice velocity vector, $\mathbf{v}$, calving rate, c, and the melting rate at the calving front, $\dot{M}$:

$$\mathbf{v}_{\text{front}} = \mathbf{v} - \left(c + \dot{M}\right)\mathbf{n} \tag{4.1}$$

where $\mathbf{n}$ is a unit normal vector that points outward from the ice.

EC defines c as proportional to strain rate along ($\epsilon_{\parallel}$) and transversal ($\epsilon_{\perp}$) to horizontal flow (Levermann et al., 2012) (Eq. 3.6). In VM, c is assumed to be proportional to the tensile von Mises stress, $\tilde{\sigma}$, which only accounts for the tensile component of the stress in the horizontal plane (Eq. 3.7). To prevent unrealistic calving rates caused by an abrupt increase in velocity upstream from the ice front, we limit the maximum calving rate to 3 km/yr.

For HAB and CD, we proceed in two steps at each time iteration as they do not provide explicit calving rates, c. First, the ice front is advected following Eq. (4.1) assuming that $c = 0$ and using the appropriate melt rate, $\dot{M}$, which simulates an advance or a retreat of

the calving front without any calving event. The calving front position is then determined by examining where the condition of each law is met. The level set, φ, is explicitly set to +1 (no ice) or -1 (ice) on each vertex of our finite element mesh depending on that condition.

For HAB, the ice front thickness in excess of floatation cannot be less than the fixed height-above-buoyancy threshold, H_O (Vieli et al., 2001) (Eq. 3.1). The fraction $q \in [0, 1]$ of the floatation thickness at the terminus is our calibration parameter. For CD, the calving front is defined as where the surface crevasses reach the waterline or surface and basal crevasses join through the full glacier thickness (Eq. 3.3 - 3.4). The water depth in the crevasse (d_w) is the calibration parameter of this calving law. In this study, we use two different estimations for the crevasse opening stress, σ. First, we use the stress only in the ice-flow direction to estimate σ in which changes in direction are taken into account (Otero et al., 2010). The other estimation for σ is the largest principal component of deviatoric stress tensor to account for tensile stress in any direction (Todd et al., 2018; Benn et al., 2017). We here use the term 'CD1' (flow direction) and 'CD2' (all directions), respectively, to refer to these two estimations for σ.

We use the frontal melt parameterization from Rignot et al. (2016) to estimate $\dot{M}$ in Eq. (4.1). The frontal melt rate, $\dot{M}$, depends on subglacial discharge, q_{sg} and ocean thermal forcing, TF, defined as the difference in temperature between the potential temperature of ocean and the freezing point of seawater (Eq. 3.10). Follwoing Rignot et al. (2012), we use ocean temperature from the Estimating the Circulation and Climate of the Ocean, Phase 2 (ECCO2) project. To estimate subglacial discharge, we integrate the RACMO2.3 runoff field over the drainage basin assuming that surface runoff is the dominant source of subglacial fresh water in summer (Rignot et al., 2016).

We determine each calibration parameter (Table 4.1) by simulating the ice front change between 2007 and 2017 and compare the modeled pattern of retreat to observed retreat. We manually adjust these parameters for each calving law and for each basin to qualitatively

Table 4.1: Chosen calibration parameters. The values in brackets are the range of calibration parameters that produce a qualitatively similar ice front retreat pattern as the chosen calibration parameter

Glaciers	Calving calibration parameter				
	q of HAB $\times 10^{-2}$(unitless)	K of EC $\times 10^{-11}$ (m $\times$ a)	d_w of CD1 (m)	d_w of CD2 (m)	$\sigma_{\max}$ of VM (kPa)
Upernavik N	5.5	82	61	53	825
Upernavik C	0.6	1700	47	25	1400 [1100 1800]
Upernavik S	4 [3 4]	8 [6.5 8.9]	36 [35 36]	25	600 [590 670]
Hayes	9.1	35	45	47 [43 47]	500
Hayes NN	0	400 [160 940]	30 [30 31]	23	1000 [0 3000]
Hayes N	5.8 [4.5 5.9]	1200 [730 2050]	30 [20 40]	20 [18 30]	1000 [430 3000]
Helheim	3.2	103	60	45	900 [890 910]
Sverdrup	35.6	10	44	40	510
Kjer	6.3 [4.8 6.5]	720	39 [38 39]	27	2900 [2660 3000]

best capture the observed variations in ice front position. In order to compare modeled ice front dynamics with observations, we estimate the retreat distance along five flowlines across the calving front of each glacier so that we are able to account for potential asymmetric ice front retreats. We only calculate the retreat distance between 2007 and 2017 and choose the parameters that can produce similar retreat distance for each flowline. We do not take into account the timing of the retreat or advance between 2007 and 2017 when choosing calibration parameters (Fig. 4.2 - 4.4). Based on our calibrated models, we run the models forward until 2100 to investigate and compare the influence of different calving parameterizations on future ice front changes. For better comparison, we keep other factors (e.g., SMB, basal friction) constant in our runs. We also keep our ocean thermal forcing (eq. 3.10) the same as the last year of the hindcast simulation (2016-2017) until the end of our forecast simulations. The simulations are therefore divided into two time intervals: the hindcast period (2007-2017) that we use to calibrate the tuning parameters of the different calving laws, and the forecast time period (2018-2100).

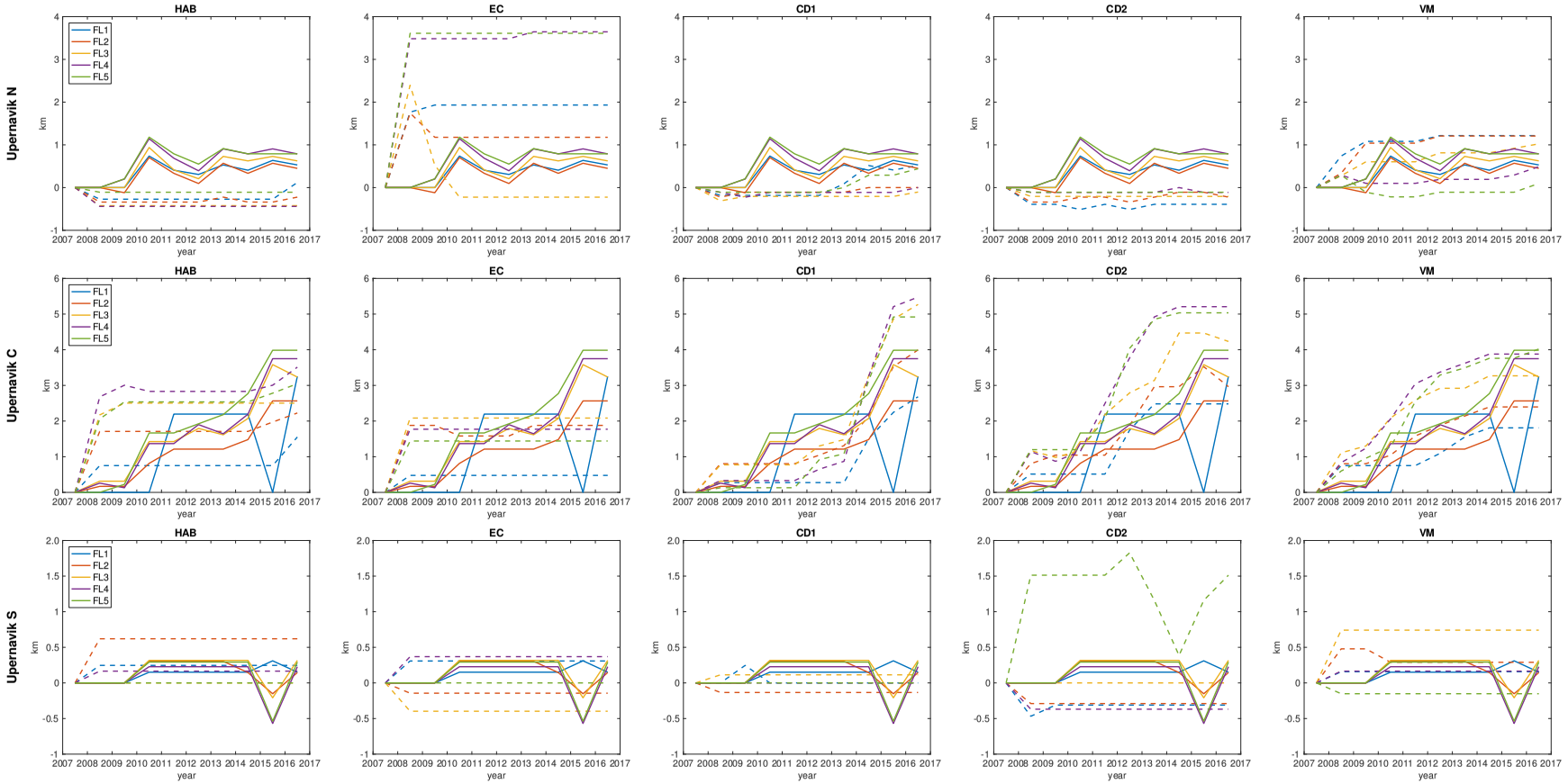

Figure 4.2: Time series of modeled retreat distance (with respect to the calving front initial position in 2007) compared to observed retreat distance for Upernavik Isstrøm. Solid lines indicate the observations and dotted lines represent modeled retreat distance.

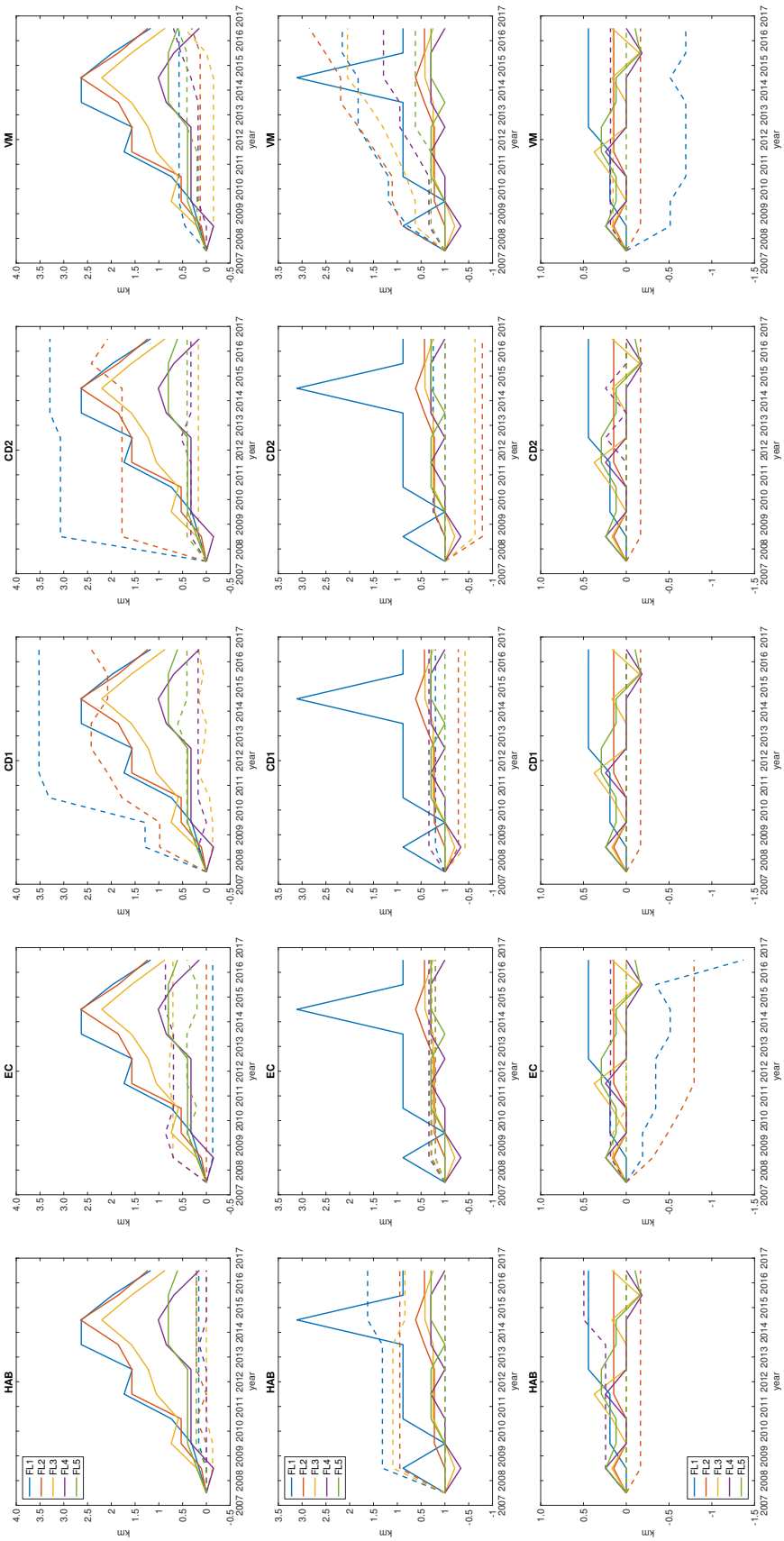

Figure 4.3: Same as Fig. 4.2 but for Hayes Glaciers.

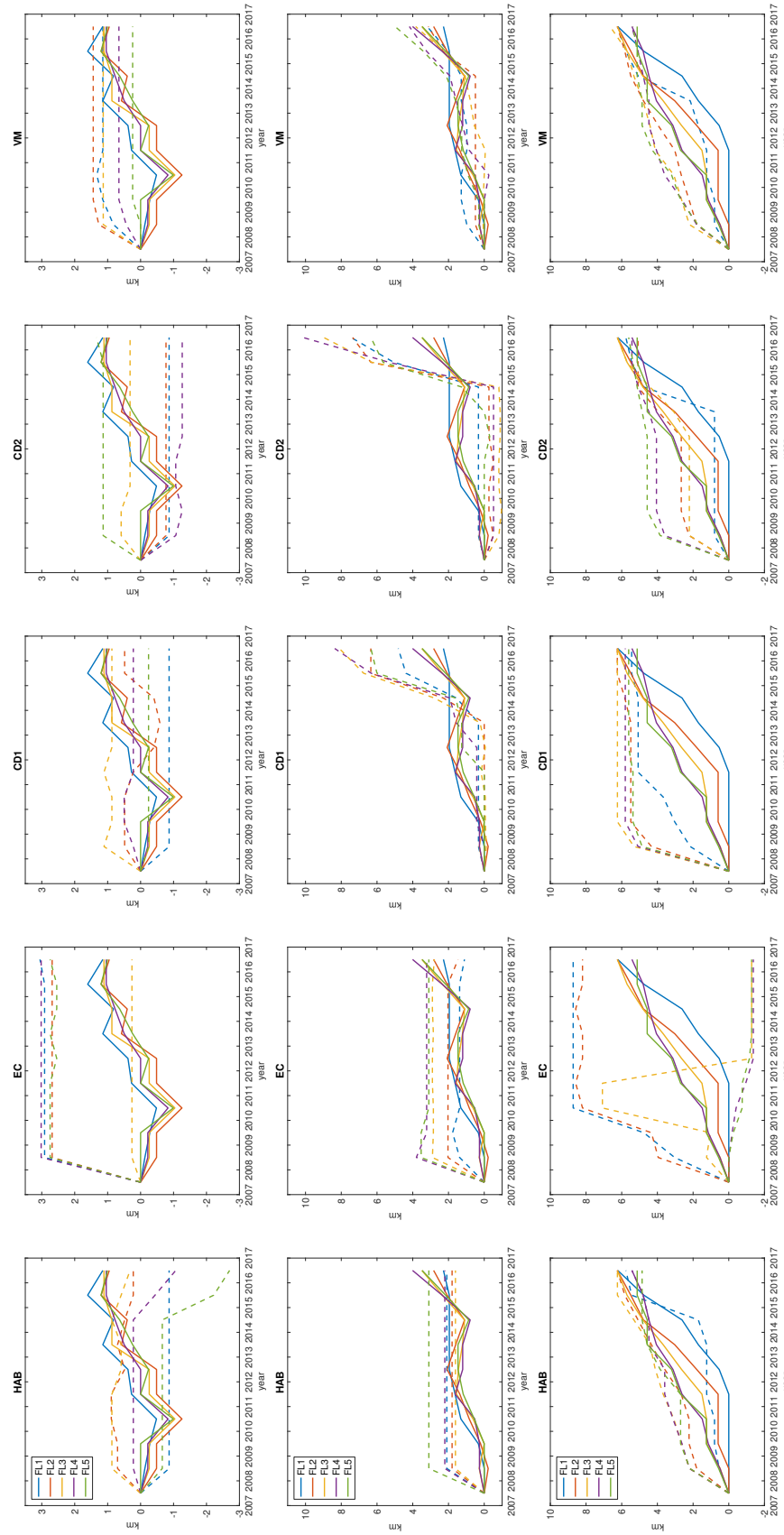

Figure 4.4: Same as Fig. 4.2 but for Helheim, Sverdrup and Kjer glaciers.

4.3 Results

The observed and modeled ice front evolutions in our simulations are shown in Figs. 4.5-4.9. The modeled retreat distances along five flowlines are compared to observed retreat distances in Fig. 4.10. We first notice that, in all cases, the calving laws that model a calving rate (EC and VM) have a smoother calving front than other laws. This results from the numerical implementation of these laws in which it is only required to solve the advection equation of the calving front, and does not rely on a local post processing step that may yield to a more irregular shape of the calving front.

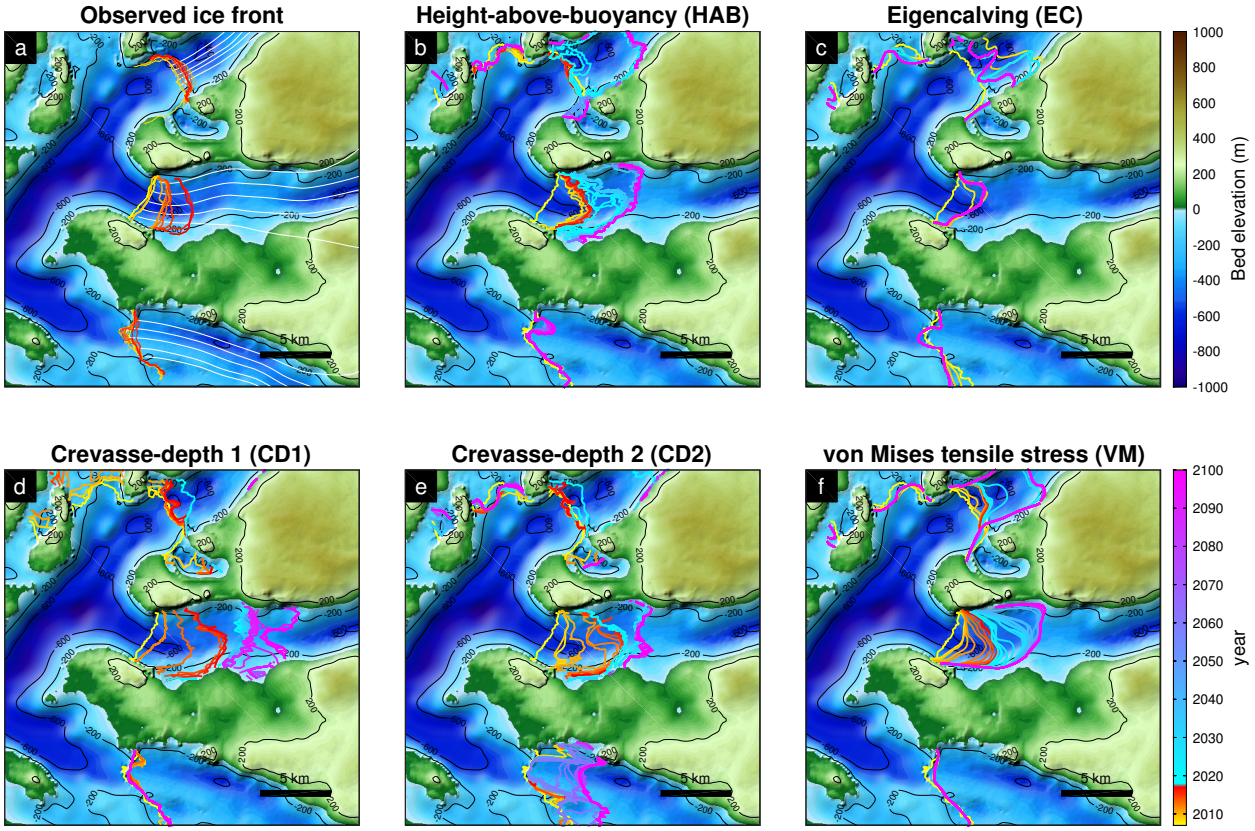

Figure 4.5: (a) The observed ice front positions between 2007-2017 and (b)-(f) modeled ice front positions obtained with different calving laws between 2007-2100 overlaid on the bed topography of Upernavik Isstrøm. The white lines are the flowlines used to calculate retreat or advance distance of ice front.

If we look at individual glaciers, Fig. 4.5a shows the observed pattern of retreat between 2007 and 2017 for the three branches of UI. The northern and southern branches have been rather

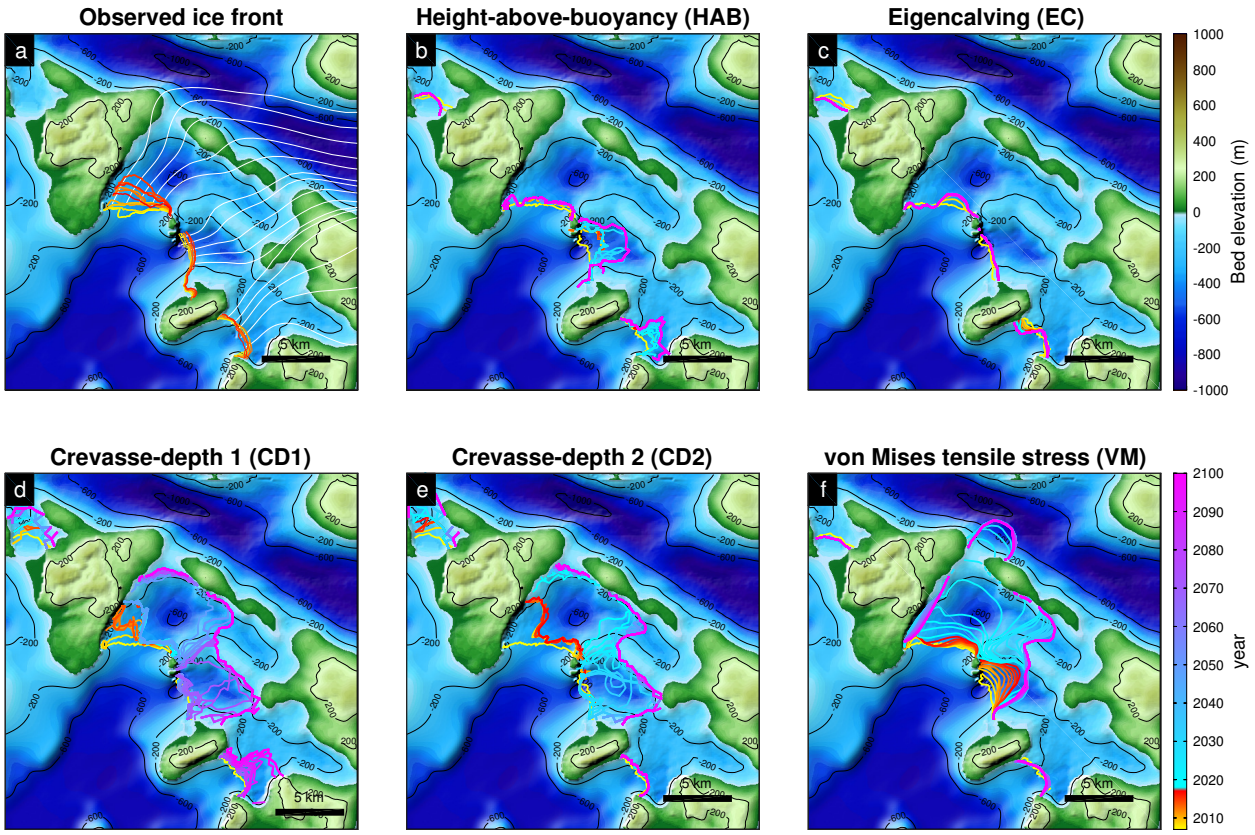

Figure 4.6: Same as Fig. 4.2 but for Hayes Glaciers.

stable over the past 10 years, but the central branch has retreated by 2.6 to 4 km. Figure 4.5b shows the pattern of modeled ice front position between 2007-2017 (hot colors) and 2017-2100 (cold colors) using HAB. We observe that the ice front in the central branch jumps upstream by about 2-3.5 km at the beginning of the simulation and slows down as the bed elevation increases. The ice front starts retreating again after 2017 and stops when it reaches higher ground about 5 km upstream. The modeled northern and southern branches are stable until 2017 and the northern branch retreats significantly to another ridge upstream between 2017-2100. The modeled ice front using EC does not match the observed pattern of ice front retreat well (Fig. 4.5c). This approach causes the calving front to be either remarkably stable or creates an ice front with a strongly irregular shape. Figure 4.5d and 4.5e present the modeled ice front evolution using the CD1 and CD2, respectively. Both models have similar ice front retreat patterns between 2007-2017, and they both overestimate the retreat

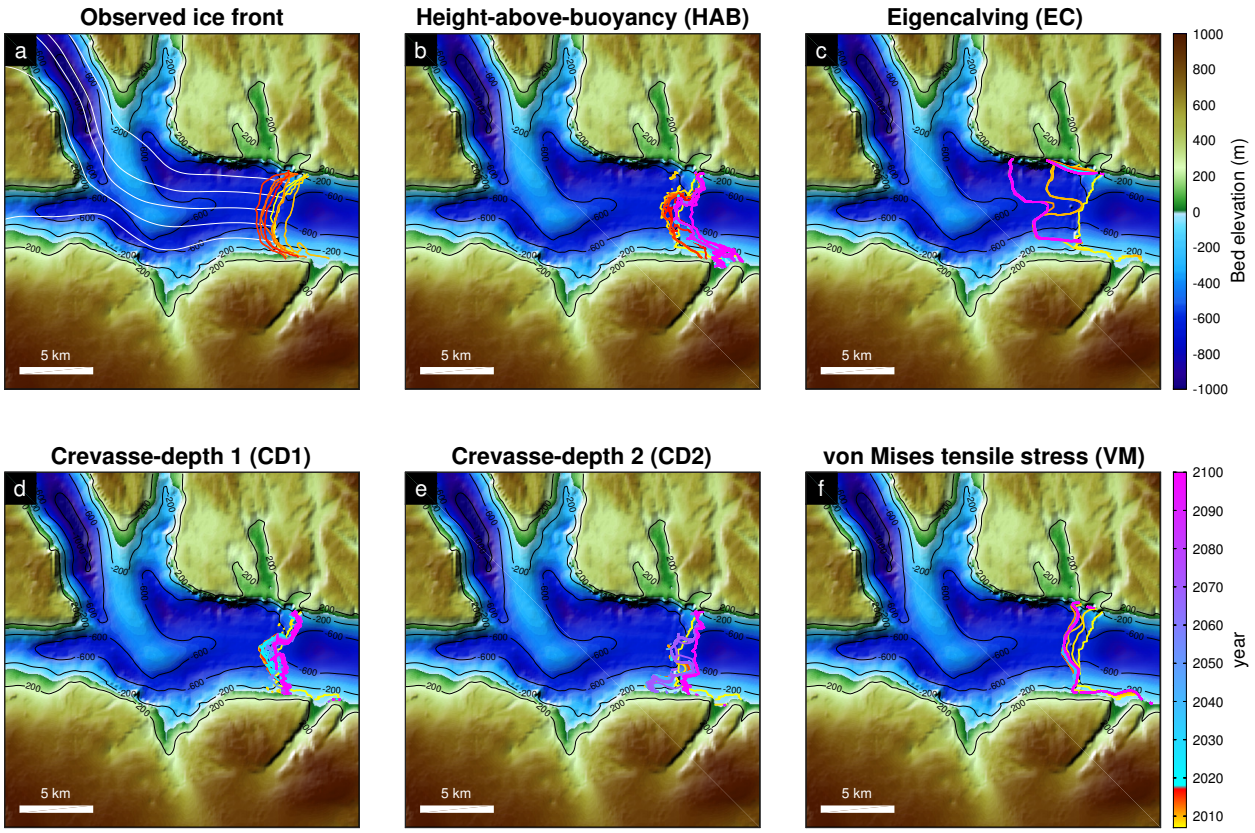

Figure 4.7: Same as Fig. 4.2 but for Helheim glacier.

of the central branch compared to observations (Fig. 4.10). In the forecast simulations, the central branch retreats more when only the flow-direction stress is considered (Fig. 4.5d). However, in both cases, the ice front stops retreating at the same location on a pronounced ridge. The model that relies on VM shows a gradual terminus retreat and stabilizes at the end of 2017 (Fig. 4.5f). After 2017, the retreat behavior is similar to the one with the height-above-buoyancy law. We observe that HAB and VM reproduce the observed changes reasonably well, although they do not capture the exact timing of the 2007-2017 retreat (Fig. 4.5b and 4.5f).

The second region of interest is Hayes glacier. Currently, the three branches of this system rest on a topographic ridge, $\sim$ 300 m below sea level, which is likely responsible for the observed stability in the position of the ice front over the past 10 years (Fig. 4.6a). The ice front of the northern glacier, however, has been retreating by up to 3 km from 2007 to

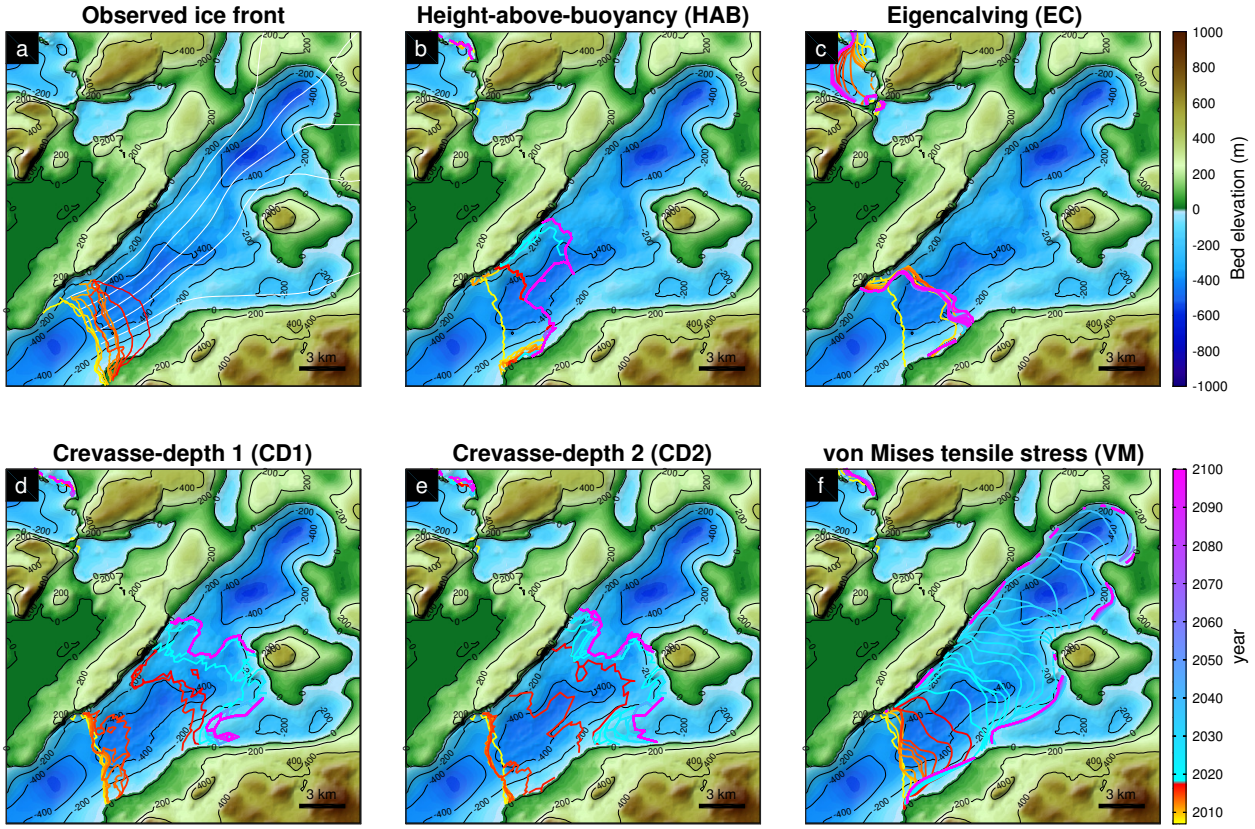

Figure 4.8: Same as Fig. 4.2 but for Sverdrup glacier.

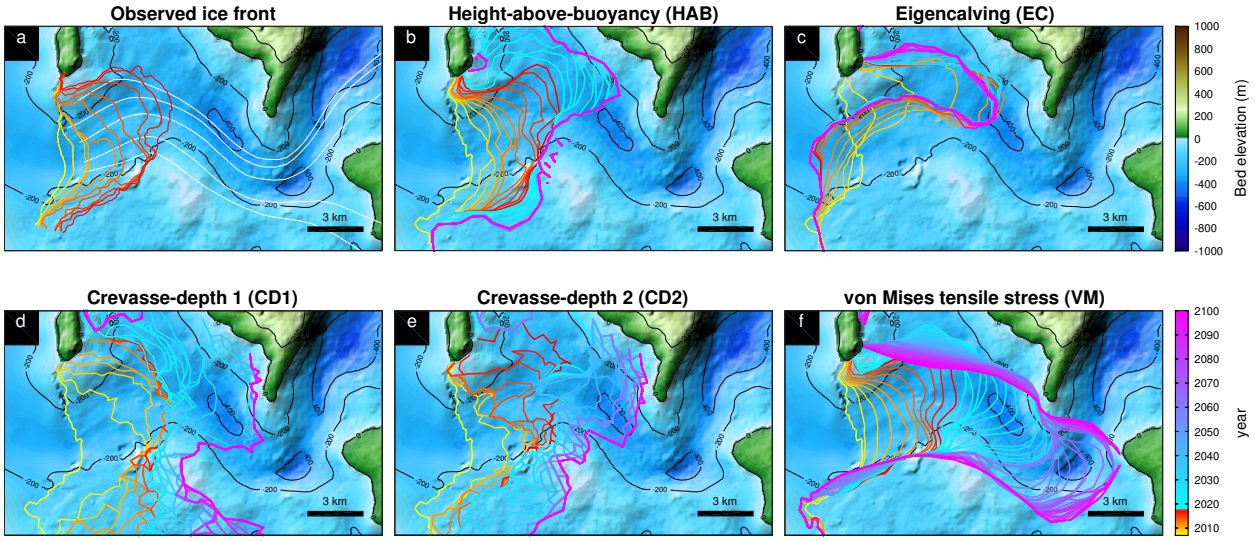

Figure 4.9: Same as Fig. 4.2 but for Kjer glacier.

2014 and readvanced in 2016 and 2017. In this region, HAB produces a stable ice front for the northern (Hayes) and the southern sector (Hayes N) but the central sector (Hayes NN)

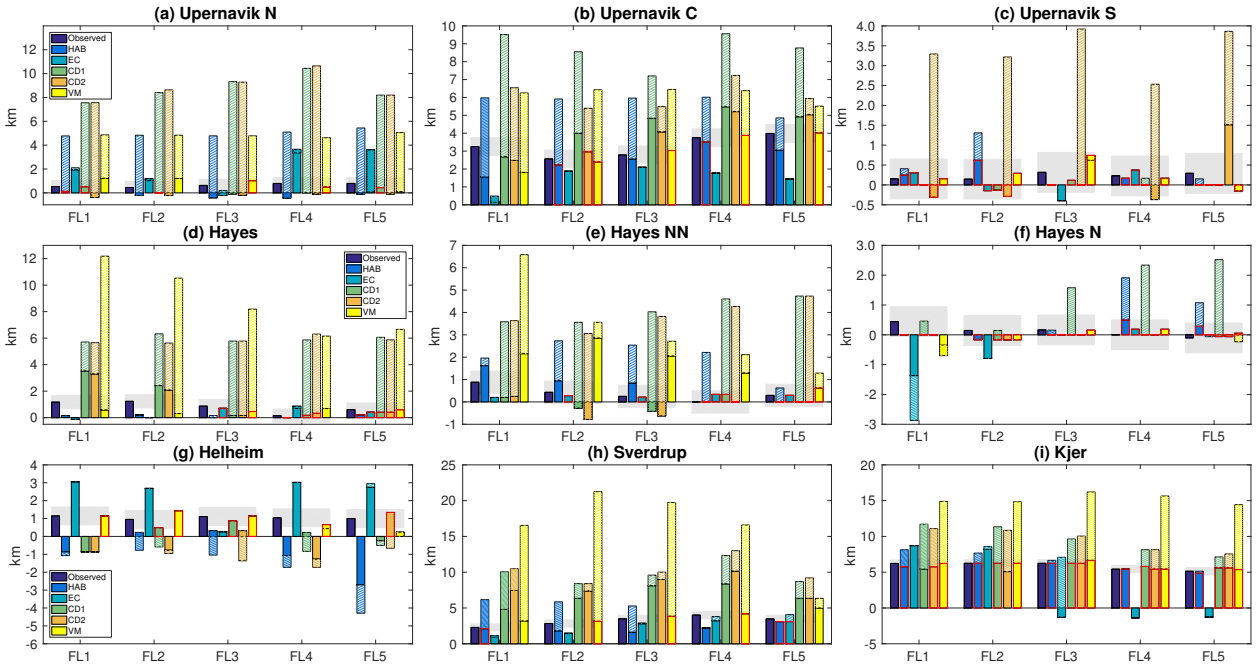

Figure 4.10: Modeled retreat distances (with respect to the calving front initial position in 2007) for different calving laws compared to observed retreat distance for nine study glaciers. The retreat distances between 2007-2017 from each calving law are shown as bar solid colors. The hatched bars are the retreated distances in 2100 for each calving law. Shaded areas represent the range of 500 m from the 2017 observed retreat and the modeled retreats that fall into this range are shown with the red edge.

retreats more than the observations by 0.5-0.7 km (Fig. 4.6b). After 2017, Hayes NN and Hayes N retreat only by a few km and stabilize there until the end of the simulation. The model using EC shows very little change between 2007 and 2100 (Fig. 4.6c). As in the previous region, both the CD1 and CD2 show very similar results (Fig 4.6d and 4.6e). In the hindcast simulation (2007-2017), both models overestimate the retreat at the western part of the northern branch (Hayes). After 2017, Hayes and Hayes NN retreat quickly by 2.2-6 km into an overdeepening in the bed topography. The final positions of the ice front derived from two crevasse-depth laws are 5 km upstream of their initial position on higher ridges further upstream. Figure 4.6f shows the modeled ice front evolution using VM. This model reproduces the stable ice front positions for two sectors (Hayes and Hayes N) but tends to overestimate the retreat for Hayes NN. Although, for the forecast simulation, VM results in more retreat than obtained with other laws for Hayes, the ice front ends up resting on the

same ridges as the ones based on the crevasse-depth laws.

Figure 4.7a shows the observed ice front pattern for Helheim glacier. Since 2007, this glacier has shown a stable ice front evolution, retreating or advancing only by a few km over the past 10 years (Cook et al., 2014). All calving parameterizations, except for EC, result in a stable or a little advanced ice front pattern (Fig. 4.7b-f), and only the VM model reproduces reasonably well the observed retreat distance from 2007 to 2017 for this region (Fig. 4.10g), although it never readvances. The other calving laws do not capture the observed retreat distance or the shape of ice front properly with our ocean parameterization. In the forecast simulations, all model results show an advance or stable pattern of ice front evolutions at the end of 2100. The model with EC results in a significantly different shape of ice front compared to other models (Fig. 4.7c).

From 2007 to 2014, the mean terminus position of Sverdrup glacier (Fig. 4.8a) has been around a small ridge $\sim$ 300 m high. In 2014, the glacier was dislodged from its sill and the glacier started to retreat. The models with HAB and EC show that the ice front jumps to the similar location to 2017 observed ice front (Fig. 4.8b and (c)). The glacier does not retreat much after 2017 in these two models. The two CDs tend to produce more retreat than other parameterizations after the ice front is dislodged from the ridge (Fig. 4.8d and 4.8e). The ice front retreat, after 2017, starts slowing down near another ridge 9 km upstream and the glacier stabilizes there until 2100. Only VM captures the timing of the retreat reasonably right (Fig. 4.8f). After 2017, the forecast simulation shows that ice front retreats up to 4.5 km before slowing down at the second ridge upstream. The ice front then retreats past this ridge quickly and keeps retreating until it reaches a bed above sea level further upstream, where the retreat stops.

The ice front of Kjer glacier has been retreating continuously between 2007-2017 (Fig. 4.9a). All calving parameterizations, except for EC, simulate the observed retreat well (Fig. 4.9b-f and Fig. 4.10i). The forecast simulations, however, show different retreat patterns. HAB

shows relatively less retreat than other models (Fig. 4.9b). The calving front slows down and stabilizes at the location where the direction of trough changes. The calving front from two crevasse-depth parameterizations retreats past this pinning point and stops retreating at the next pinning point where the small ridge is located (Fig. 4.9d and 4.9e). In the model with VM, the retreat rate slows down near this ridge as well. The ice front, however, keeps retreating beyond this ridge and stabilizes on another ridge further upstream (Fig. 4.9f).

4.4 Discussions

Our results show that different calving laws produce different patterns of ice front retreat in both timing and magnitude, despite equal climatic forcing. In the hindcast simulations, we calculate the modeled retreat distance from 2007 to 2017 for a total of 45 flowlines from our study glaciers to investigate which calving law, with the best tuning parameter, better captures the observed ice front changes (Fig. 4.10). We find that overall, VM captures the observed retreat better than other calving laws. For 67% (30 out of 45) of these flowlines, VM reproduce the retreat distance within 500 m from the observations, which we assume to be a reasonable range based on the seasonal variability of ice fronts, error in observations, and model resolution (Howat et al., 2010; Bevan et al., 2012). With HAB, the modeled retreat distance is within 500 m of the observed retreat distance for 53% of the flowlines, while CD1 and CD2 capture the retreat for 51% and 40% of the flowlines. EC reproduces only 31% of the retreat that falls into the 500-m range.

EC was designed to model calving of large-scale floating shelves by including strain rates along and across ice flow (Levermann et al., 2012). Our results show that it does not work well in the case of Greenland fjords, because these glaciers flow along narrow and almost parallel valleys. The transversal strain rate, $\epsilon_{\perp}$, is small and noisy in these valleys, leading to a significantly different pattern of ice front changes with either a remarkably stable (e.g.

Fig. 4.6c) or some complex shape of the modeled ice front (e.g. Fig. 4.5c, 4.7c). The forecast simulations with this calving law also show different retreat patterns compared to other calving laws. While this calving law may be appropriate in the case of unconfined ice shelves, we do not recommend using this calving law for Greenland glaciers.

The two crevasse-depth calving laws are very similar in terms of the ice front retreat patterns they produce. For the regions of fast flow, the maximum principal strain rate is almost the same as the along-flow strain rate, which leads to a similar amount of stress for opening crevasses. We note that for almost all of the glaciers that match the observed retreat, the model is very sensitive to the water depth in crevasses, the calibration parameter, for both laws (Table 4.1). Even a one meter increase in water depth significantly changes the calving rate, and thus the entire glacier dynamics. This behavior has been noticed in other modeling studies (Otero et al., 2017; Cook et al., 2012). Only one glacier (Hayes N) allows to change the water depth by up to ~ 18 m and still reproduces observed ice front pattern. One reason why CDs do not capture the rate of retreat well in the hindcast simulations might also be this high sensitivity to water depth in crevasses. Models relying on this law should be taken with caution because it is hard to constrain the water depth in crevasses. The water depth in crevasses is certainly different from one year to another, and can be significantly affected by changes in surface melting and hydrology of glacier surface for the forecast simulations (e.g., Nick et al., 2013). Todd et al. (2018) applied a CD calving law with 3D full Stokes model and were able to reproduce the seasonal calving variability of Store Glacier without any tuning of water depth in crevasses. For our study glaciers, however, tuning the water depth was necessary to reproduce the observed ice front changes. This either shows that this calving law works well for Store but not for other glaciers without the tuning process, or that full 3D stresses are required to model calving. Further studies need to investigate the stresses from different models and their relationships with water depth in crevasses.

The model results with HAB indicate that this calving law reproduces the final position of

observed calving front well for some glaciers, but does not capture continuous retreat patterns and the timing of retreat between 2007 and 2017. The ice front generally tends to jump to its final position. This may be due to the fact that we keep the height above floatation fraction (q) constant during our simulations. This constant fraction value also explains a relatively limited retreat compared to other calving laws for the forecast simulations. The sensitivity of the model to the parameter q is different for every glaciers (Table 4.1). The glaciers with an ice front that is in shallow water (e.g., Hayes N, Kjer) are less sensitive to the choice of q than the ones with deeper ice front. A wide range of grounding conditions in the study glaciers also explains the wide range of the parameter q between different glaciers. Because determining q is empirical and buoyancy conditions may change through time, this calving law becomes less reliable than other physics-based calving laws for the forecast simulations. Another disadvantage of this law is that it does not allow for the formation of a floating extension, and cannot be applied to ice shelves.

All calving laws implemented in this study rely on parameter tuning for each glacier in order to match observations. However, this tuning process makes it difficult to apply any of these calving laws to glaciers for which we have no observations of ice front change, and it is not clear whether these parameters should be held constant in future simulation or whether they may change. In particular, when the parameters span a wide range between different glaciers, as in HAB or EC, it is hard to constrain these parameters for forecast simulations. Model simulations with these calving laws should be taken with caution.

Our results for forecast simulations suggest that ice front retreat strongly depends on the bed topography. Although different calving laws do not always have the same final positions, the extent of glacier retreat shows a similar pattern: topographic ridges slow down or/and stop the retreat, and retrograde slopes accelerate the retreat, which has been shown in several studies (e.g., Morlighem et al., 2016; Choi et al., 2017). Whether the glaciers continue to retreat beyond these ridges depends on the calving law used and may also depend on the

choice of tuning parameters. For the forecast simulations, it is not clear whether the tuning coefficients of the calving laws should be kept constant, as we did here. Some parameters potentially vary depending on future changes in external climate forcings or ice properties. These changes may affect the final locations where glaciers eventually stabilize. However, the bed topography still plays a crucial role in determining stable positions of ice fronts and the general pattern of retreat before the glaciers stabilize.

The results for Helheim glacier are very similar for all calving laws, and none of them captures the pattern of ice front migration perfectly. In the forecast simulations, the modeled ice front slightly advances until 2100 for all calving laws. This ice front advance is mostly caused by the ocean thermal forcing data used in the forecast simulations. The thermal forcing has been slightly decreasing after 2012 and a relatively cold water is applied to our forecast simulations, which leads to a similar advance of ice front for all calving law simulations. However, according to the bed topography of this region, this glacier might potentially retreat upstream if the ocean temperature increases, which may trigger more frequent calving events.

Ocean forcing is one of the limitations of this study: the frontal melt rate is simply parameterized. The ocean parameterization does not take into account ocean circulation within the fjords, which could cause localized melt higher or lower than the parameterization. We need to account for these ocean processes that may affect melt rate and could potentially vary the retreat rate of ice front. We also assume that calving front remains vertical and the melt is applied uniformly along the calving face (Choi et al., 2017). Future studies should include more detailed ocean physics and coupling to better calibrate our calving laws and improve results.

Based on our results, we recommend using the von Mises stress calving law (VM) for modeling centennial changes in Greenland tidewater glaciers within a 2D plan-view or 3D models. This calving law captures the observed pattern of retreat and rate of retreat better than

other calving laws, and does allow for the formation of a floating extension. VM does not, however, necessarily capture specific modes of calving as it is only based on horizontal tensile stresses, which may be a reason why it does not always capture the pattern of ice front migration perfectly. The strong correlation between calving rate and ice velocity produces reasonable calving rates but whether these relationships hold for forecast simulations needs further investigation. Another disadvantage of this law is that it strongly depends on the stress threshold, σ_{max}, that needs to be calibrated. Some modeled glaciers (e.g., Helheim, Sverdrup, Kjer) are very sensitive to σ_{max}, in which case a ~ 50 kPa change significantly affects the calving dynamics of these glaciers (Table 4.1). As a result, the modeled ice front dynamics is dependent on this one single value that we keep constant through time and uniform in space, which adds uncertainty to model projections. It is therefore critical to further validate the stress threshold and improve this law by accounting for other modes of calving, or to develop new parameterizations. Current research based on discrete element models (e.g, Benn et al., 2017) or on damage mechanics (Duddu et al., 2013) may help the community derive these new parameterizations.

Chapter 5

Modeling the response of Northeast Greenland to ocean forcing

Dynamic thinning of marine terminating glaciers along coastal Greenland accounts for a large portion of mass loss from the Greenland ice sheet (e.g. Pritchard et al., 2009). As glacier termini are exposed to warmer ocean currents and enhanced subglacial water discharge, ocean-induced melt at calving faces and under floating ice increases, which may lead to glacier retreat and ice flow acceleration (Jenkins, 2011; Holland et al., 2008). Assessing the vulnerability of individual glaciers to ocean forcing along the coast of Greenland is necessary to determine the regions that are most likely to change in the coming decades. In this chapter, we model the response of two glaciers in Northeast Greenland (Nioghalvfjerdsfjorden (79North) and Zachariae Isstrm (ZI)) to ocean forcing to investigate their evolution over the coming decades.

5.1 Northeast Greenland

Nioghalvfjerdsfjorden (79North) and Zachariae Isstrøm (ZI) are two major marine terminating glaciers of the NorthEast Greenland Ice Sheet region (NEGIS), that drain about 12% of the Greenland ice sheet surface area (Rignot and Mouginot, 2012) and have the potential to raise sea level by 1.1 m (Mouginot et al., 2015). 79North glacier forms a long (80 km) floating tongue confined in a wide (20 km) valley (Khan et al., 2014; Mouginot et al., 2015) (Fig. 5.1). It exhibits high flow speeds ($\sim$ 1.4 km/year) near the grounding line and slows down near its terminus because of the presence of several nunataks. The bed is 600 m deep at the grounding line and reaches a depth of 900 m below sea level under the floating tongue (Mayer et al., 2000). The bathymetry rises to 200 m below sea level near the ice front (Mouginot et al., 2015). ZI is more exposed to the ocean, with an almost 30-km-wide ice front that is not protected by islands or ice rises. Its velocity was 2 km/year near its floating calving front in 2015. The seafloor is almost 900 m deep under the remnant part of its floating ice tongue, and gradually rises inland for 30 km upstream where a $\sim$ 200 m-high ridge is formed. Inland of this ridge, the bed remains between 300 and 500 m below sea level (Fig. 5.1).

The calving front of ZI has retreated 7-9 km between 2009 and 2014 (Mouginot et al., 2015). The rate of grounding-line retreat increased from 230 m/year to 875 m/year after 2011. The ice surface velocity tripled compared to 2000-2012 and the thinning rate doubled from 2.5 $\pm$0.1 m/year to 5.1 $\pm$0.3 m/year during 1999-2014. These changes led to an increase in ice discharge of about 50%, from 10.3 $\pm$1.2 Gt/year in 1976 to 15.4 $\pm$1.7 Gt/year in 2015 (Mouginot et al., 2015). ZI has lost almost all of its ice tongue and only 5% of the ice shelf remains compared to 2002. 79North glacier has not experienced such dramatic changes, but its ice shelf near the grounding line lost 30% of its thickness from 1999 to 2014, which led to an increase in ice discharge by 8% during 1976-2015 (Mouginot et al., 2015).

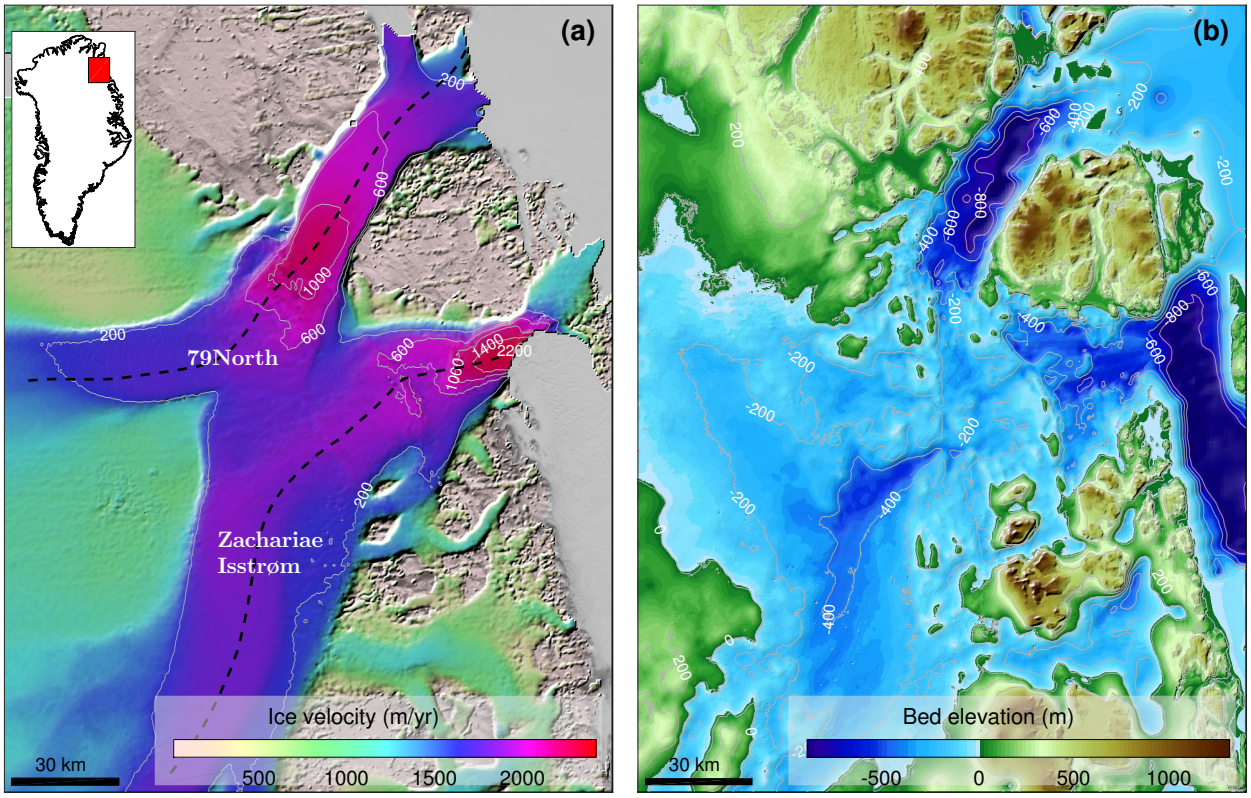

Figure 5.1: (a) Ice surface velocity from 2008 to 2009 (Mouginot et al., 2015). The dashed black lines show the flow lines used in Fig. 5.8. (b) bed topography inferred from mass conservation (Morlighem et al., 2014).

In situ measurements show that the mean temperature of Atlantic Water (AW), transported from the North Atlantic toward the Arctic Ocean, has increased by 1°C over the last decade (Holliday et al., 2008; Mouginot et al., 2015). Although more observations are needed to investigate its transport, warm AW has been observed at the 79North ice shelf (Wilson and Straneo, 2015). Recent studies suggest that AW may be responsible for the fast retreat of the calving front of ZI and enhanced basal melting under the ice shelf of 79North (Mouginot et al., 2015; Khan et al., 2014). It is therefore essential to address the effect of ocean thermal forcing on the dynamics of this region.

Currently, the role of ocean forcing in these observed changes is not well understood, and it remains unclear whether NEGIS will continue to accelerate and retreat over the coming decades. Here we model NEGIS using a three dimensional (3D) ice sheet numerical model

to improve our understanding of this region and investigate its sensitivity to ocean forcings. First, we model the past 6 years of NEGIS to calibrate our calving law (Morlighem et al., 2016); we then make projections based on different ice/ocean interactions scenarios. We discuss the impact of ocean forcing on ice dynamics of each glacier and conclude on the potential future contribution of NEGIS to sea level rise.

5.2 Data and Method

We use the Ice Sheet System Model (ISSM, Larour et al., 2012) to model 79North and ZI glaciers. We rely on a 3D higher-order model (HO, Blatter, 1995; Pattyn, 2003), with sub-element grounding line parameterization (Seroussi et al., 2014a) and level set-based moving boundaries (Bondzio et al., 2016). We use an edge-based anisotropic mesh optimization method (BAMG) by Frey (2001) and Hecht (2006) based on the Hessian of observed surface velocity, which adapts the mesh resolution to minimize the misfit between the measured velocity and its piecewise linear representation in a triangular mesh. Generally speaking, this yields to a mesh that has a higher resolution (more refined) over faster flowing region and close to shear margins, and a lower resolution (coarser) over slower moving region. In addition, we constrain the mesh size in the vicinity of the grounding line to 200 m to capture the retreat of the grounding line more precisely (Seroussi et al., 2014b). The horizontal mesh resolution varies between 200 m in the vicinity of the grounding line and 10 km inland (Fig. 5.2), and is vertically extruded in 12 layers.

To initialize the model, we infer the basal friction coefficients under grounded ice and ice viscosity parameters on floating ice through inversions following Morlighem et al. (2013) based on 2008-2009 surface velocities derived from Landsat and satellite interferometry (Mouginot et al., 2015) (Fig.5.3 and Fig.5.4) (e.g., MacAyeal, 1992; Larour et al., 2012; Morlighem et al., 2010, 2013). To avoid having to invert for both ice rigidity and basal sliding at the

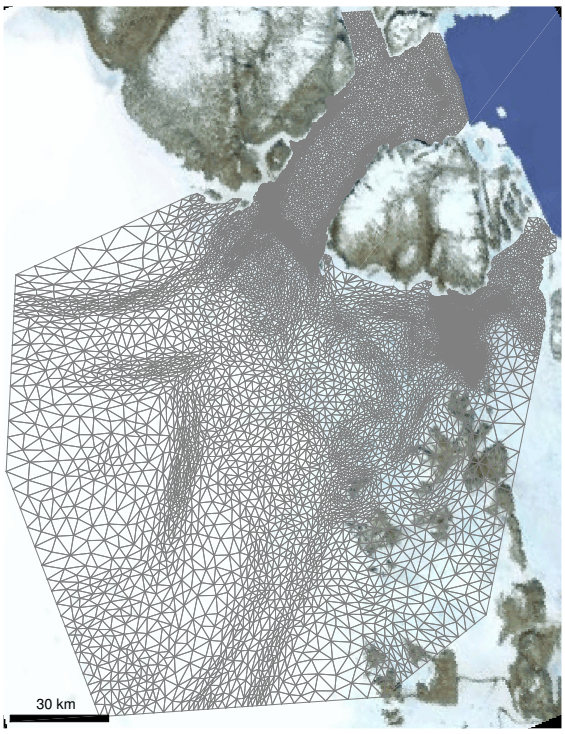

Figure 5.2: The horizontal mesh of Northeast Greenland overlaid on a Google map image

same place, we apply an inversion of ice rigidity to floating ice only and assume that ice rigidity of grounded ice is a constant value equivalent to a temperature of $-10°$C using the table provided by Cuffey and Paterson (2010).

We apply basal friction under grounded ice (Fig. 5.3). The ice hardness (B) or friction coefficient (α) is retrieved by solving an inverse problem, where a cost function ($\mathcal{J}$) that measures the misfit between the modeled ($\mathbf{v}$) and the observed surface velocities ($\mathbf{v}_{obs}$) is minimized. The cost function is defined as:

$$\begin{aligned} \mathcal{J}(\mathbf{v},\alpha) &= \gamma_1 \int_{\Gamma_s} \frac{1}{2}\|\mathbf{v}-\mathbf{v}_{obs}\|^2 \, d\Gamma_s + \gamma_2 \int_{\Gamma_s} \frac{1}{2}\ln\left(\frac{\|\mathbf{v}\|+\varepsilon}{\|\mathbf{v}_{obs}\|+\varepsilon}\right)^2 d\Gamma_s \\ &+ \gamma_3 \int_{\Gamma_b} \nabla\alpha \cdot \nabla\alpha \, d\Gamma_b \end{aligned} \tag{5.1}$$

where ε is a minimum velocity to avoid singularities and Γ_s and Γ_b are ice surface and bed, respectively. The first term is the mean square error, the second term represents a relative misfit of velocities, and the third term is a regularization that smooths the solution. We use $\gamma_1 = 2000$, $\gamma_2 = 40$ and $\gamma_3 = 8 \times 10^{-7}$ to get the best fit of modeled velocity.

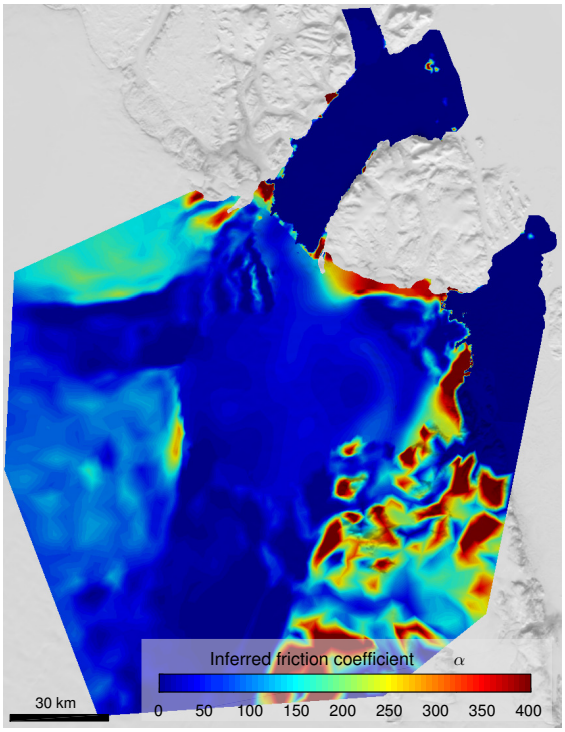

Figure 5.3: Inferred basal friction coefficient α $(\mathrm{m}\times\mathrm{s})^{-1/2}$

These inferred fields are assumed to be constant during the simulations. The bed and surface topography are from BedMachine Greenland version 3 (Morlighem et al., 2014). We force the model using the surface mass balance (SMB) from the regional atmospheric model RACMO2.3 (Lenaerts et al., 2012). We assume constant SMB during the future simulations. All of our simulations start in 2008 and run for 100 years under different ocean forcings described below, using a time step of 7.3 days which satisfies the CFL (Courant-Friedrichs-Lewy) condition.

We model calving front dynamics in the 3D model by relying on the level set method and assuming that the calving front remains vertical (Bondzio et al., 2016; Morlighem et al.,

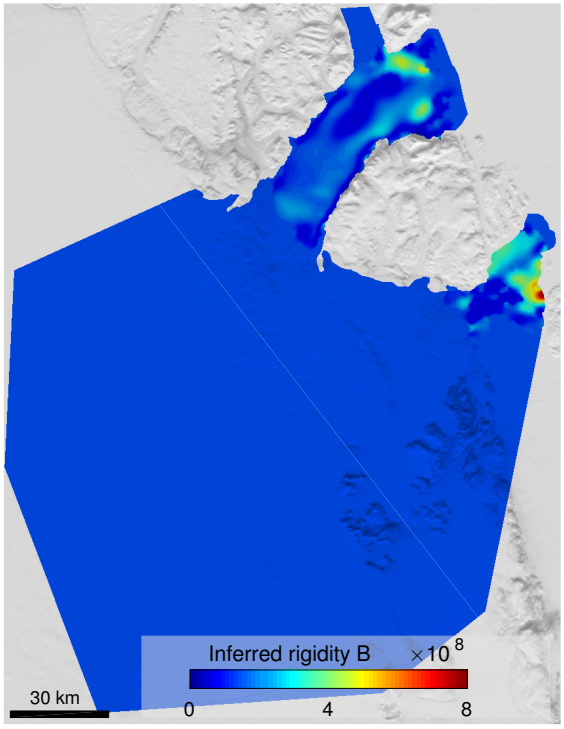

Figure 5.4: Inferred rigidity B Pa/s$^{(1/n)}$

2016). At each time step, the ice front moves at a velocity following Eq. 4.1.

We apply the von Mises tensile stress calving law (VM) introduced in the previous chapter. To calibrate the stress threshold, we run the model from 2008 to 2014 with $\sigma_{\max}$ varying from 100 kPa to 1.5 MPa. We compare the modeled ice front evolution to Landsat derived data and find a best match with $\sigma_{\max} = 1$ MPa for grounded ice, which is the same value as the one used in Morlighem et al. (2016), and is consistent with ice tensile strength measurements (Petrovic, 2003), and $\sigma_{\max} = 150$ kPa on floating ice (Fig. 5.5). We attribute the lowering in the stress threshold over floating ice to crevassing and damage, which generally form at the grounding line and weaken the ice, lowering its resistance to tensile stresses.

We ignore the frontal melt-rates of floating termini due to its shallow depth and relatively cold water near the ocean surface. Yet, frontal melting needs to be accounted for once the glacier loses its floating extension and becomes a tidewater glacier. Once the terminus of the glacier is grounded, the calving face becomes exposed to strong melt-rates due to

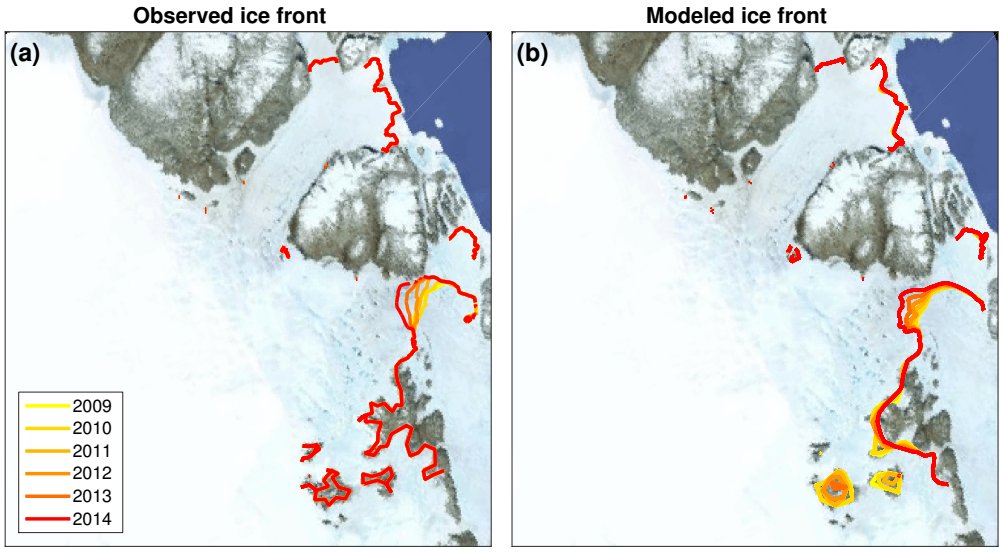

Figure 5.5: (a) Observed and (b) modeled ice front evolutions during 2009-2014 with the stress threshold of $\sigma_{\max} = 1$ MPa for grounded ice and 150 kPa for floating ice. The gray and black lines show 2011 and 2014 modeled grounding lines, respectively.

subglacial freshwater discharge (Straneo et al., 2010; Jenkins et al., 2010; Xu et al., 2012, 2013). Following Morlighem et al. (2016), the melt rate at the ice front, $\dot{M}$, is parameterized using a sine function to represent a seasonal variability, with a maximum melt rate, $\dot{M}_{\max}$, in the summer and no melt in the winter:

$$\dot{M} = \dot{M}_{\max} \frac{(1 + \sin(2\pi t))}{2} \tag{5.2}$$

This melt is applied uniformly along the calving face where it is grounded and where the glacier base is deeper than 300 m below sea level to account for the depth of warm AW (Straneo et al., 2010). For the control experiment, we do not apply frontal melting. However, we apply and increase the maximum summer melt-rates to investigate the sensitivity of glaciers to frontal melting in our sensitivity experiments.

We also need to model basal melting under ice shelves. In this study, we use a simple parameterization to model basal melting following Favier et al. (2014). In this parameterization, basal melting rates increase linearly with depth between the top-water (-100 m) and

the deep-water elevation (-450 m). No basal melting is applied if the bottom of ice shelf is greater than the top-water elevation, and the highest melt rate, 30 m/year, is applied below the deep-water elevation. We calibrate these parameters by comparing the parameterized spatial pattern of basal melt-rates to the one derived from the depth-integrated mass conservation equation:

$$\frac{\partial H}{\partial t} + \nabla \cdot H\bar{v} = \dot{M}_s - \dot{M}_b \tag{5.3}$$

where H is ice thickness, $\bar{v}$ is the depth-averaged velocity, $\dot{M}_s$ is the accumulation/ablation rate at the ice surface, and $\dot{M}_b$ is the melting/freezing rate at the bottom of glacier.

The simple parameterization mimics the spatial pattern of basal melt-rates derived from mass conservation (Fig. 5.6). The highest melt rate (30 m/yr) is also in a good agreement with values from Mouginot et al. (2015). The model with this parameterization reproduces a pattern of grounding line retreat that is in good agreement with observations (Fig. 5.7). For our forcing experiments, we change the maximum basal melt-rate at depth to assess the response of glaciers to ocean forcings.

Based on our model calibrated with the past 6 years of observations, we run the model forward over next 100 years to see if the grounding line retreat of 79North and ice front retreat of ZI continue without any further forcings. Then, to test the sensitivity of NEGIS to ocean forcings, we set up two sets of experiments to test the response of the glaciers to basal melting of floating extensions and frontal melting of grounded termini. In each experiment, we increase ocean forcing parameters to determine the threshold necessary to trigger dramatic changes, so that we assess how vulnerable this region is to an increase in ocean forcing in the future.

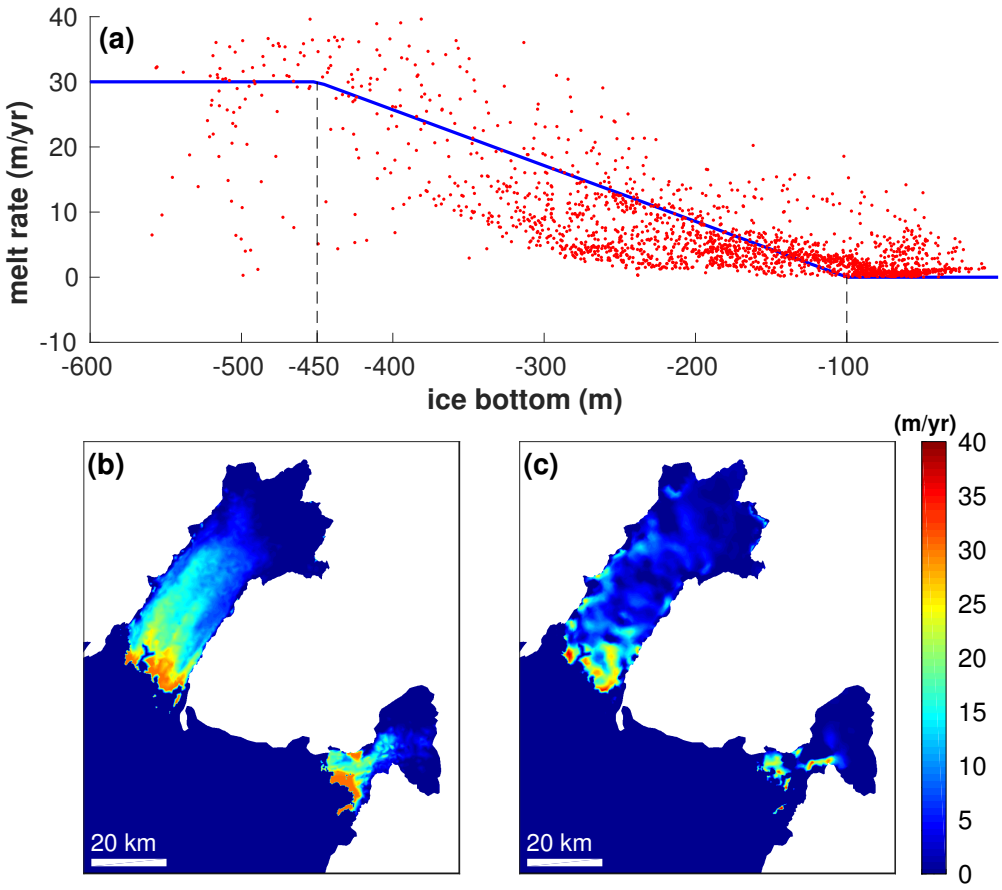

Figure 5.6: (a) Melting distributions for a simple parameterization (blue) and the melt rate values from the mass conservation equation (red dots), and the spatial pattern of basal melt-rates from (b) the simple parameterization and (c) the mass conservation equation

5.3 Results

The control experiment with unperturbed melt-rates (Fig. 5.8) shows that 79North does not change significantly, with only a marginal advance in ice front position. The grounding-line retreats inland about 7-8 km compared to its current position but stops migrating when it reaches higher ground (Fig. 5.1) after 80 years. Although 79North does not retreat significantly during the simulation, the ice shelf velocity increases in response to thinning, and this acceleration propagates up to 150 km upstream (Fig. 5.8b). The ice front of ZI, on the other hand, continues to retreat steadily and loses its floating extension after 70 years, becoming a grounded tidewater glacier. The ice front stabilizes after 70 years 30 km

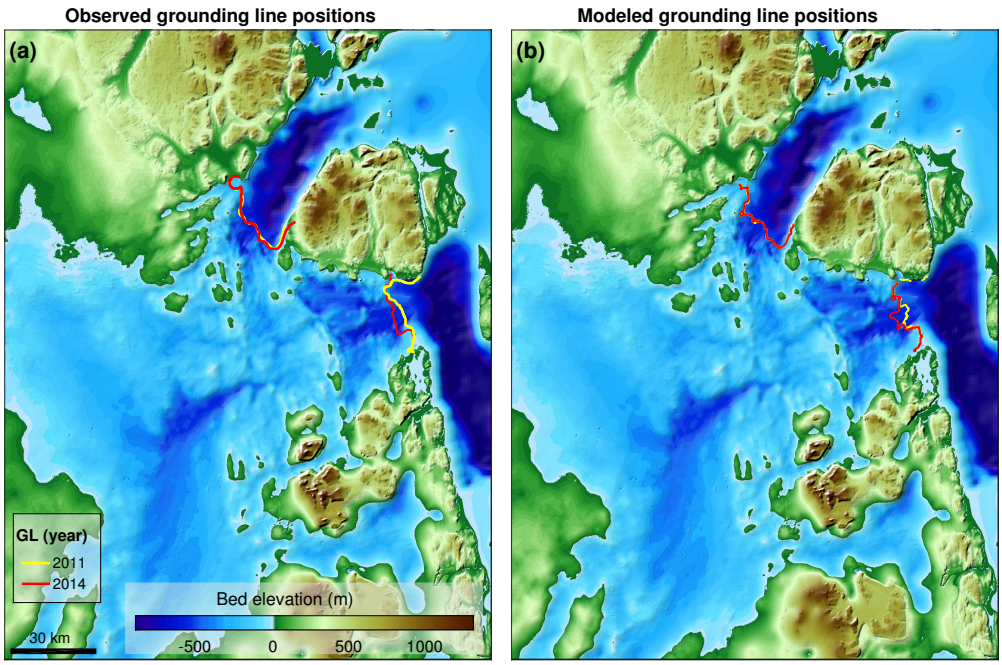

Figure 5.7: (a) Observed and (b) modeled grounding line positions in year 2011 and 2014 with the simple parameterization for basal melting.

upstream, where a 200-m step in bed topography prevents further retreat. ZI also speeds up near the terminus as it retreats, but the velocity stabilizes as the ice front reaches this topographic ridge. Combined, the two glaciers lose about 1,110 km^3 of their volume above floatation (VAF) over the course of the simulation, equivalent to 2.8 mm of sea level rise.

In our first set of sensitivity experiments, we increase the maximum ice-shelf basal melt-rates from 30 m/year up to 90 m/year without frontal melting. In all cases, the pattern of ice front and grounding line retreats are similar to the control experiment with the basal melt-rates modulating the rate of retreat (Fig. 5.9a and 5.9b). In all scenarios, the ice front of 79North remains stable with the same amount of grounding line migration as the one of the control experiment. Notably, the increase in basal melting induces an acceleration of its ice shelf, especially near the grounding line, which causes a local increase in the driving stress, but the glacier nonetheless remains stable. For ZI glacier, higher basal melt-rates accelerate the retreat rate of its calving front and grounding line, but do not considerably affect their final positions. The ice front stabilizes at a similar position as the one of the control experiment.

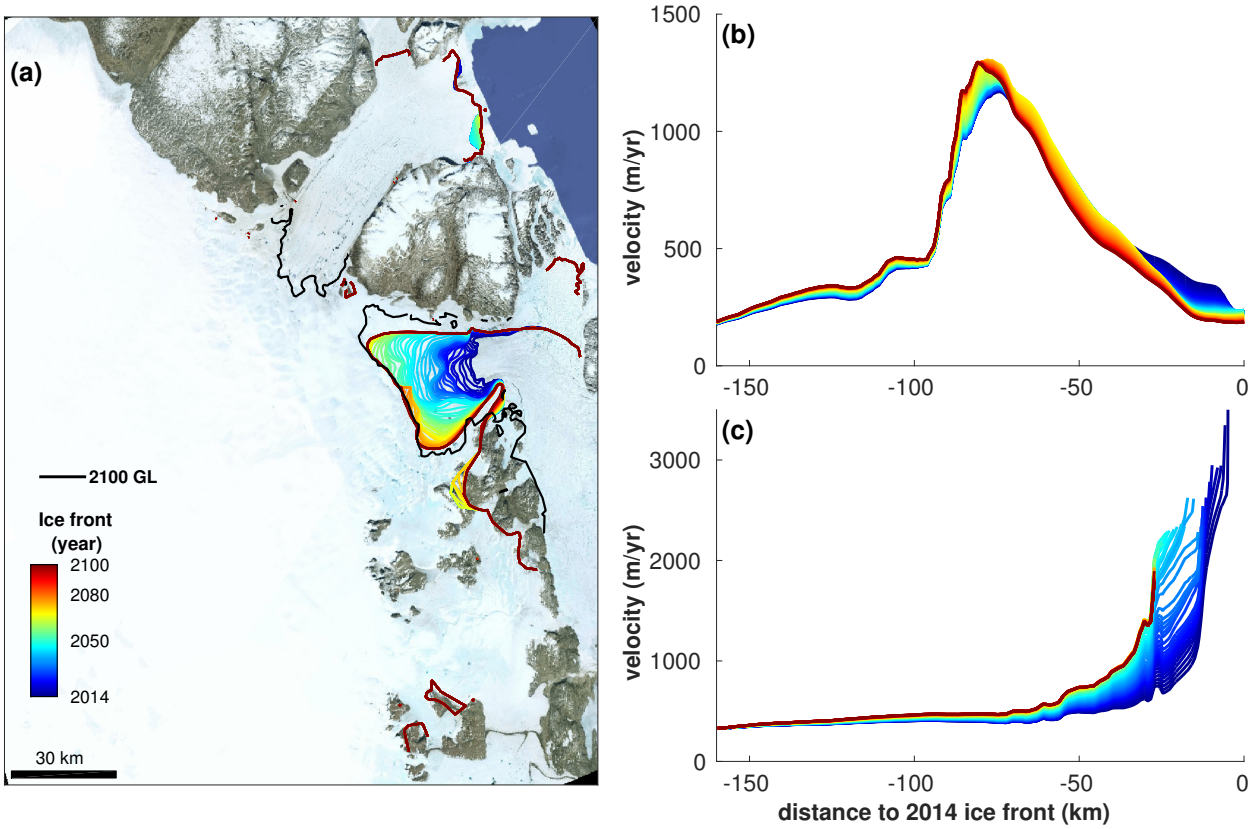

Figure 5.8: (a) Modeled ice front positions from 2014 to 2100 and modeled 2100 grounding line overlaid on a Google Earth image, and modeled ice velocity of (b) 79North and (c) ZI from 2014 to 2100 along the flow line shown in Fig. 5.1a.

Its velocity near the ice front is also similar to the control experiment in all cases. The loss of VAF from two glaciers is slightly larger: 1,200-1,250 km^3 over the coming century (Fig. 5.10).

In our second set of experiments, we investigate the response of the system to increased frontal melting at the grounding termini (Fig. 5.9c and 5.9d). Since the ice front of 79North is floating, it is not sensitive to these experiments. The future of ZI, on the other hand, is strongly dependent on these frontal melt rates: the speed of ice front retreat increases with the summer maximum melt-rate, $\dot{M}_{\max}$. We increase $\dot{M}_{\max}$ from 0 m/day with increments of 1 m/day leaving basal melt-rates at the same value as the control experiment. For all melt-rates below 6 m/day, the ice front of ZI does not retreat beyond the 200-m step during the simulations. A 6 m/day maximum frontal melt rate is necessary for the model to be

dislodged from this step over the course of the century. Under this scenario, the glacier retreats faster and remains stable for about 25 years on this ridge. After 25 years, however, the northern part of the glacier continues to retreat and destabilizes the southern part of the glacier. The glacier is dislodged from the step and starts a fast retreat inland where the bed topography is retrograde. During the simulation, the velocities dramatically increase over the entire region in response to ice front retreat, and the VAF would decreases by about 6,400 km^3, which would raise global sea level by 16.2 mm by 2100 (Fig. 5.10).

To estimate ocean thermal forcing needed to reach 6 m/day of frontal melting, we use ocean temperature from the Estimating the Circulation and Climate of the Ocean, Phase 2 (ECCO2) project (Rignot et al., 2012, 2016). To sample the ECCO2 models, we take a domain on the continental shelf outside of Zachariae's fjord (Fig. 5.11). We integrate thermal forcing over the area of the ice front below 200 m, and average it by the area of the front. On July of 2014, we get 3.23 $°C$ for thermal forcing over the area of Zachariae Isstrøm ice front (Fig. 5.12). To calculate basin-wide subglacial discharge (Q_{sg} $[m^3/d]$), we integrate the RACMO2.3 runoff field over the drainage basin assuming that surface runoff is the dominant source of subglacial fresh water in summer (Rignot et al., 2016) (Fig. 5.12). Using Eq. 3.10 and model-derived Q_{sg} and TF, we calculate how much of an increase in Q_{sg} and TF is required to obtain the threshold of 6 m/day or other frontal melt-rates (Fig. 5.13).

5.4 Discussions

The model suggests that 79North remains relatively stable under all forcing scenarios. ZI, however, retreats steadily about 30 km upstream and loses its floating extension, even with the ocean forcing turned off (i.e. no melt applied at the base or at the front, Fig. 5.14). These results confirm the analyses of Khan et al. (2014) and Mouginot et al. (2015): ZI will

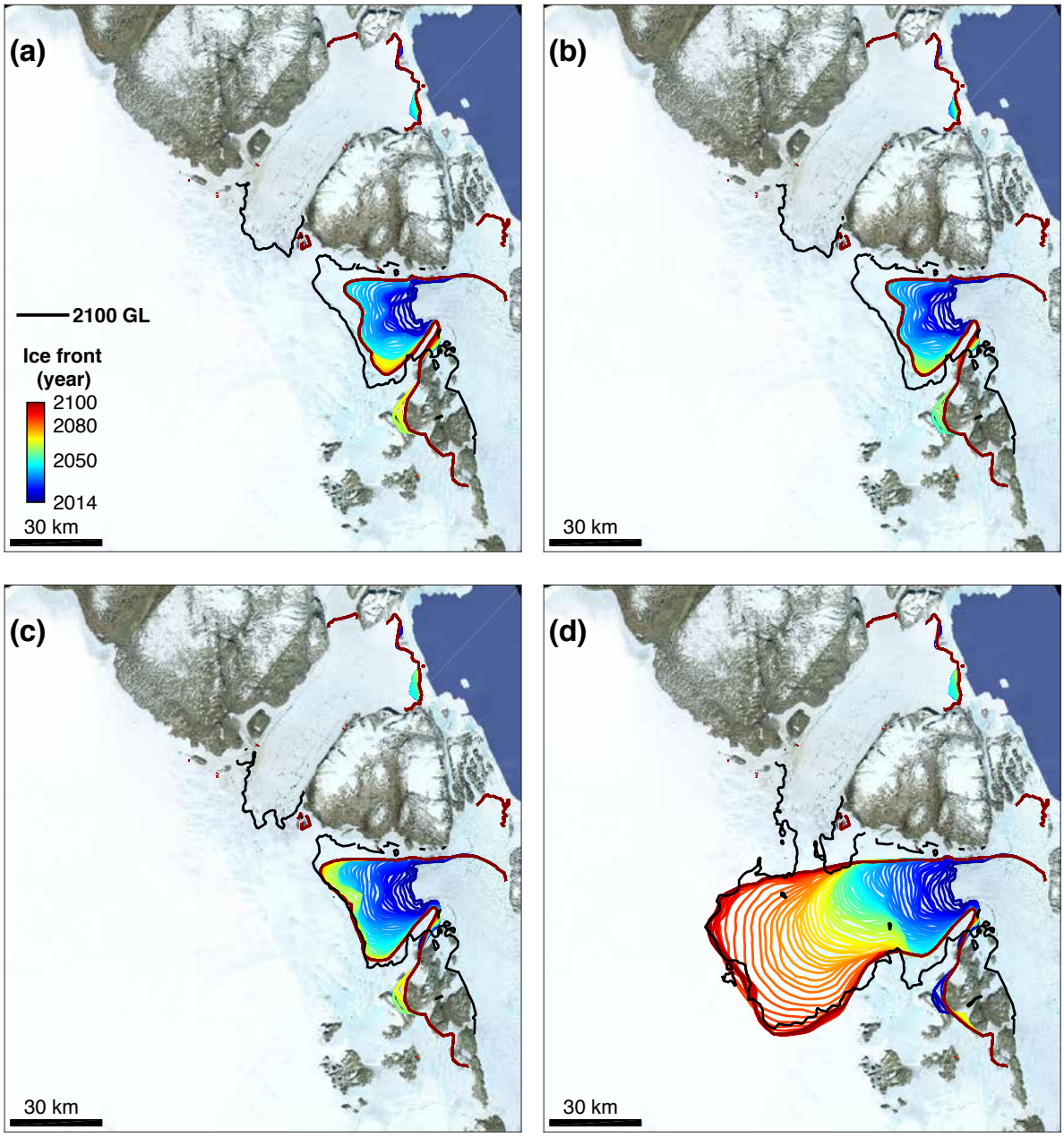

Figure 5.9: Modeled ice front positions between 2014 and 2100 and modeled 2100 grounding-line under different melting scenarios overlaid on a Google Earth image. (a) maximum basal melt of 60 m/year, (b) maximum basal melt of 90 m/year, (c) maximum summer frontal melt of 3 m/day, and (d) maximum summer frontal melt of 6 m/day.

become a grounded tidewater glacier as a result of the complete collapse of its floating part. A pronounced step in the bed topography about 30 km upstream stabilizes the ice front and prevents further retreat of the glacier. To dislodge the glacier from this ridge over the course of the coming century, our model suggests that the maximum summer melt at the

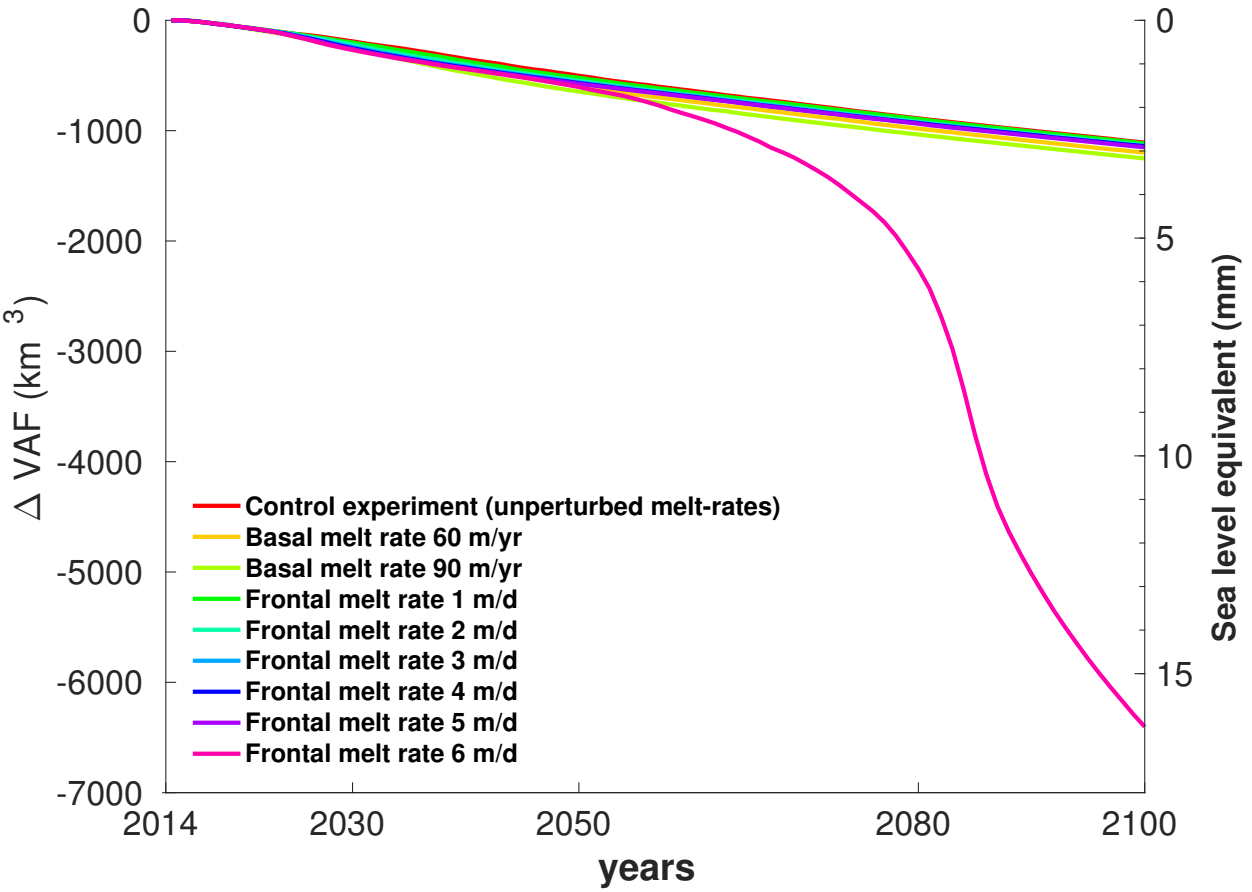

Figure 5.10: Changes in ice volume above floatation (VAF) of two glaciers and their sea level equivalent between 2014 and 2100 under different melting scenarios

ice front must reach 6 m/day. This melting rate would require an increase of 0.8-3.0°C in ocean thermal forcing, together with an increase in subglacial discharge by a factor of 2 to 10 within this century (Fig. 5.13) (Xu et al., 2013; Rignot et al., 2012; Holland et al., 2008; Rignot et al., 2016; Fettweis et al., 2013). While significant, these changes remain within the range of possible scenarios in this region (Yin et al., 2011; Straneo et al., 2013; Fettweis et al., 2013).

In the sensitivity experiments, in which frontal melting is applied to grounded termini, we find that ZI glacier is more sensitive to frontal melting than basal melting. Although an increase in basal melting does not considerably affect calving dynamics, frontal melting causes faster retreat, which further increases ice surface velocity and destabilizes the glacier.

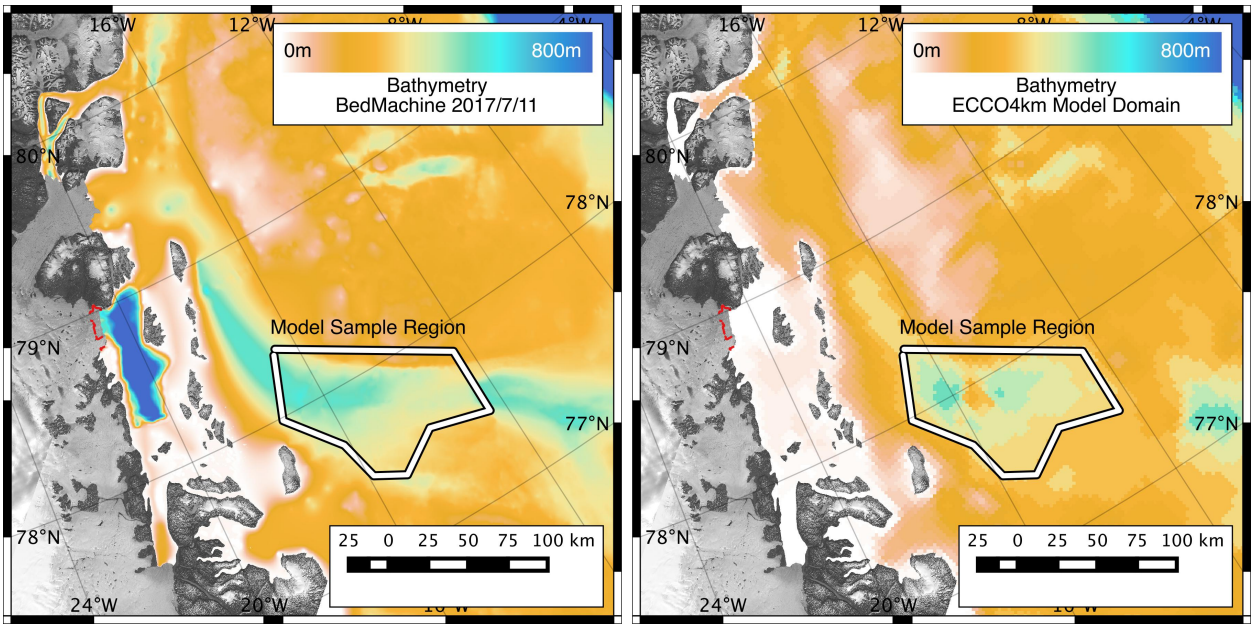

Figure 5.11: ECCO2 model domain (right) in comparison with bathymetry from BedMachine (left) with the grounding line of Zachariae plotted in red. Panchromatic imagery represents all locations where the bed elevation is above sea level and there is land ice (i.e. the extent of the ice for Zachariae is the ice front).

Fast ice front retreat substantially increases ice velocity at the termini and that acceleration propagates upstream over the entire model domain.

Our results show that the bed topography plays a critical role in determining stable positions of grounding lines and ice fronts in response to increased melt rates, which confirms the conclusions of earlier studies (e.g., Weertman, 1974; Schoof, 2007; Pattyn et al., 2013; Morlighem et al., 2016). The ice fronts and grounding lines of 79North and ZI stop retreating once they reach a step in the bed topography. Since the bed topography controls the glacier retreat and basal melting pattern, it is therefore critical to have an accurate bed topography, especially including small ridges or depressions, to understand the glacier behavior and make reliable projections.

The two glaciers have a different response to enhanced ocean forcings mainly because their geometrical settings are different. Near the calving front of 79North, nunataks act as pinning points and stabilize the ice front, which is not undergoing significant tensile forces (Favier

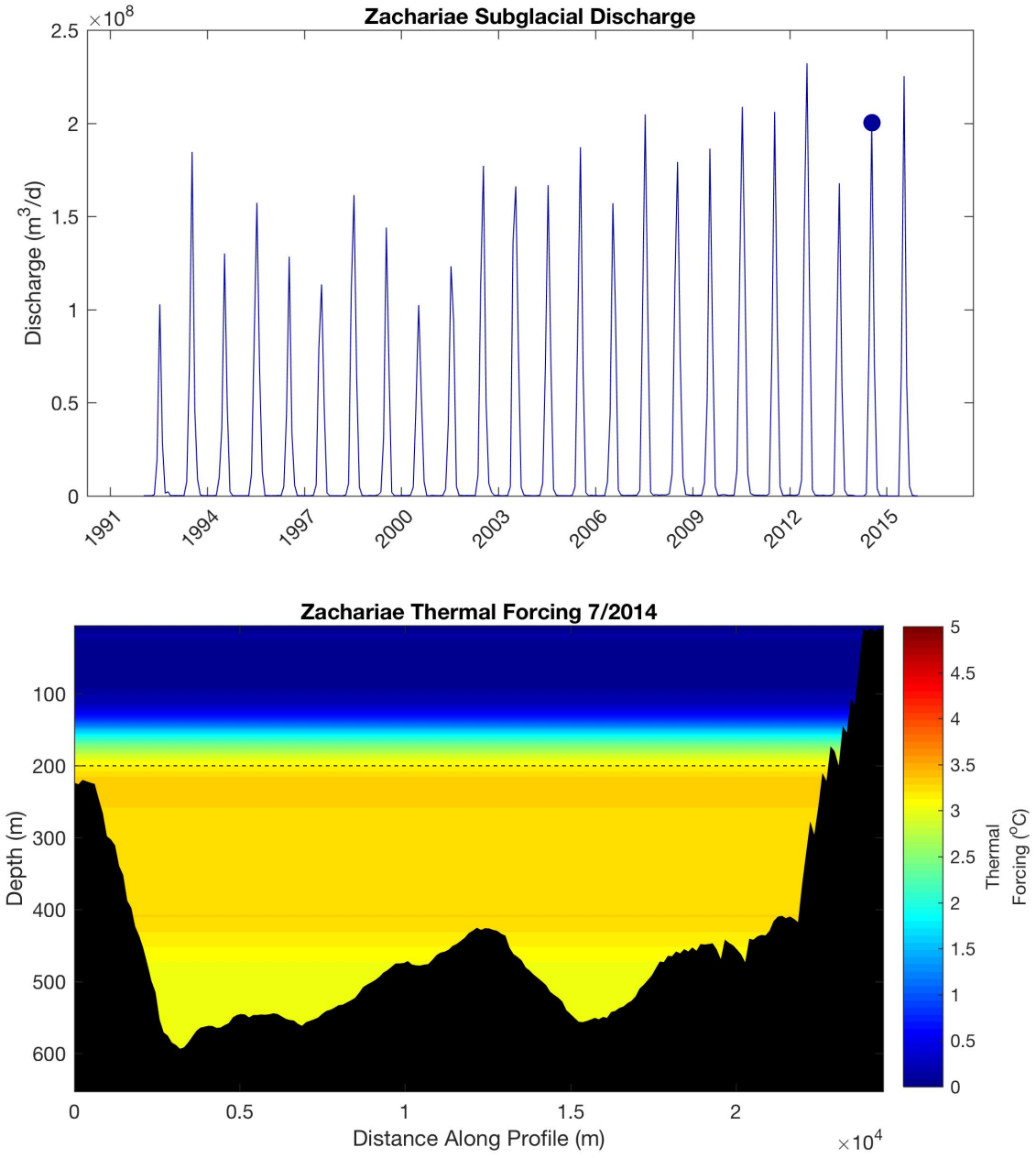

Figure 5.12: Subglacial discharge of Zachariae Isstrøm and estimated thermal forcing over the area of the ice front. The blue dot (upper) represents subglacial discharge of year 2014.

et al., 2016). On the other hand, the terminus of ZI does not have any pinning point and is exposed to ocean water. Tensile stresses are therefore stronger at the calving face, and the glacier is more susceptible to retreat, according to our calving law. Additionally, the bed slope near the current grounding line slows down the retreat of 79North while ZI could retreat about 30 km along the deep seafloor until it reaches a ridge in the bed topography.

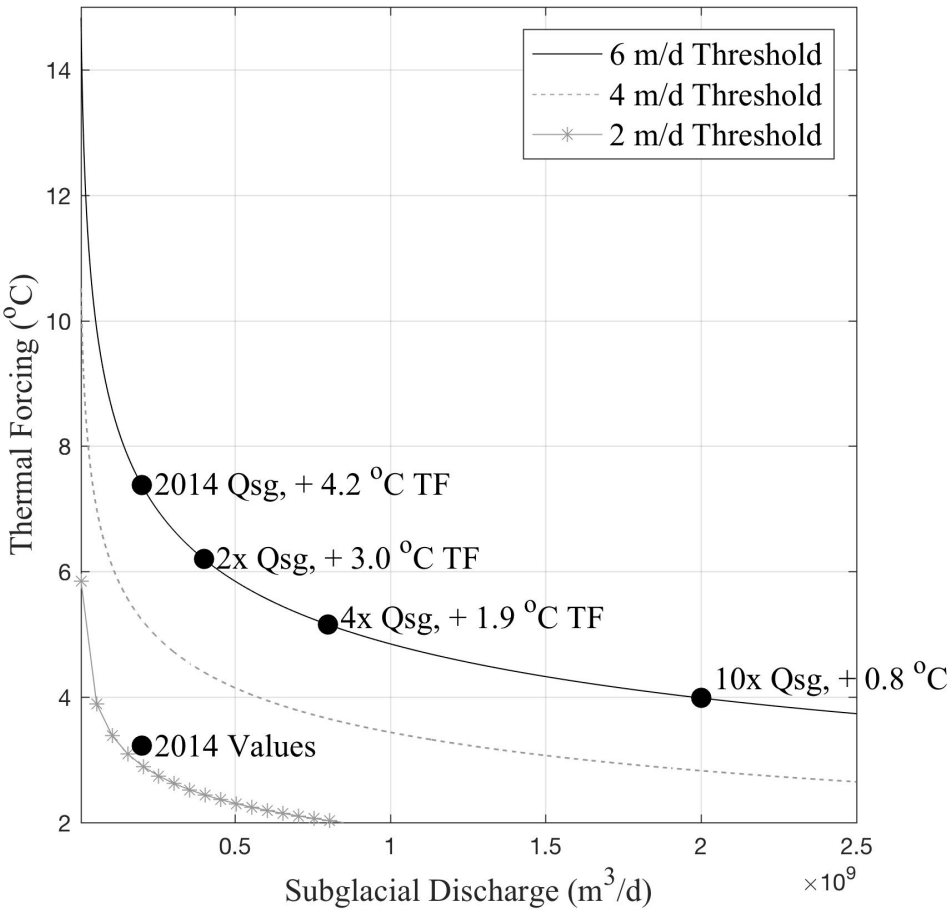

Figure 5.13: The model-derived subglacial discharge and thermal forcing for 2014 (summer) in comparison to the melt rate curves (Eq. 3.10) deduced for Zachariae.

It is important to notice that ZI glacier is already in a stage of retreat and will continue to lose mass until it reaches a new state of equilibrium, 30 km upstream from the current calving front position. The glacier will continue to retreat for 70 years even with no further ocean forcing, or faster for stronger ocean forcings. Our sensitivity study shows that ice mass loss from this region is not sensitive to ocean forcings unless the melt-rate along the calving front increases to 6 m/day, at which point the glacier retreats beyond its stabilizing ridge rapidly in a region of retrograde bed (Fig. 5.10). Ice mass loss from the unperturbed experiment is considered as a committed loss due to the current state of NEGIS (Goldberg et al., 2015; Price et al., 2011), and this is the minimum contribution of this region to global

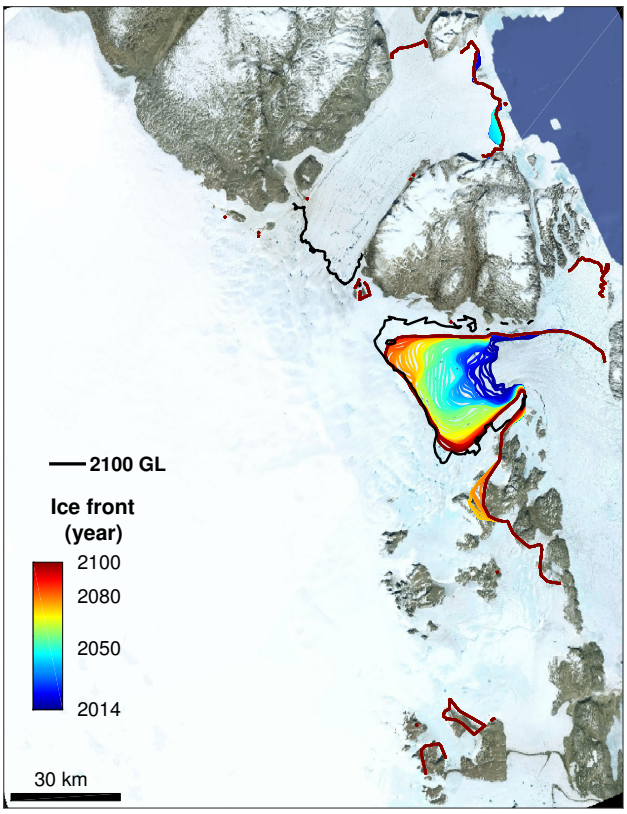

Figure 5.14: Modeled ice front positions from 2014 to 2100 and modeled 2100 grounding-line with the ocean forcing turned off (i.e. no melt applied at the base or at the front).

sea level by 2100. While the grounding line and ice velocity are stable once the ice reaches its stabilizing sill, the glacier does not reach steadystate (Fig. 5.10) and still loses mass over the entire duration of the simulation. It is therefore not clear whether or when the glacier will eventually retreat further inland on a longer time scale.

In this study, we apply a simple parameterization in order to model frontal melt-rates. In reality, summer frontal melt-rates are 2-3 times higher compared to winter depending on subglacial water discharge and thermal forcing (Rignot et al., 2016), which hardly makes the seasonal variability sinusoidal. To better model frontal melting, we need to modulate melt-rates by subglacial discharge, thermal forcing and water depth. In this study, however, we simplify the seasonal variability using a sine function and only increase the maximum melt-rates for the sensitivity experiments, as we do not have ocean temperature data in front

of ZI glacier.

Another limitation of this study is the basal melting under the floating ice tongue, which is based on a depth-dependent parameterization. Although the model with this method reproduces a pattern of grounding line retreat that is in good agreement with observations, it does not account for changes in amplitude or specific spatial patterns. Basal melt-rates vary with time and space depending on the shape of the sub-ice shelf cavity, ice/ocean interactions and ocean water circulation (Wilson and Straneo, 2015). To reproduce basal melting more accurately, ocean circulation models with an accurate bathymetry is essential. We also do not account here for some physical processes that may enhance the retreat rate, such as the effect of surface runoff on crevasse propagation, damage and calving. These processes could potentially decrease the threshold of 6 m/day, as it has been shown that meltwater runoff could be multiplied by a factor of 10 by the end of the century (Fettweis et al., 2013) and the effect of runoff on ice discharge remains poorly known.

Chapter 6

Contribution of the Greenland ice sheet to sea level over the next century with a new generation model

About half of the recent mass loss of Greenland is primarily due to the thinning and retreat of marine terminating glaciers along the coast (van den Broeke et al., 2016). It has been shown that these changes are closely related to regional climate change, especially the ocean thermal forcing, which enhances calving, leading to glacier acceleration and increased ice discharge. How much mass the Greenland ice sheet is going to lose over the next century in response to climate warming remains unclear due to the challenges of capturing all marine terminating glaciers of Greenland at the required resolution. In this chapter, we estimate the future sea level contribution of the Greenland ice sheet using an ice-sheet wide high resolution model that fully accounts for the changes in ice front of individual marine terminating glaciers.

6.1 Modeling the Greenland ice sheet

The Greenland ice sheet has been losing mass over the last two decades (Mouginot et al., 2019) and is currently contributing to sea level at a rate of ~ 0.8 mm/yr (van den Broeke et al., 2016; Forsberg et al., 2017; Rietbroek et al., 2016). Although the increase in melting at the ice sheet surface accounts for a large portion of this mass loss, glacier dynamics have played a stronger role than surface melting during the last 46 years (Mouginot et al., 2019; Enderlin et al., 2014). As marine terminating glaciers are exposed to the warmer ocean and enhanced subglacial discharge, ocean-induced undercutting at glacier termini and melting under floating ice have increased, which leads to glacier retreat and ice flow acceleration (Holland et al., 2008; Jenkins, 2011; Wood et al., 2018), thereby increasing the overall ice discharge. Glacier dynamics will continue to play a significant role in the mass loss as the ocean temperatures are likely to increase in the future. To estimate future changes in Greenland more reliably, therefore, a numerical model with the ability to accurately capture the behavior of outlet glaciers is necessary.

Several studies have been dedicated to projecting the future sea level contribution of Greenland with a focus on outlet glaciers dynamics (Nick et al., 2013; Fürst et al., 2015; Calov et al., 2018; Aschwanden et al., 2019). While these studies model changes in surface mass balance (SMB) relatively well, they either generally use a coarse model grid resolution or simplified physics, and do not calibrate their models at the individual glacier scale. Many studies do not have the required spatial and temporal resolution to model individual marine terminating glaciers of Greenland, even though the dynamics of these outlet glaciers need to be accurately captured in order to provide realistic and robust estimates of present and future discharge of the ice sheet. The models with a coarse resolution or simplified physics result in conservative estimates (Nick et al., 2013; Calov et al., 2018) as the response of outlet glaciers to climate change remains weak. In these projections, the future contribution of Greenland to sea level is almost entirely controlled by changes in SMB, and the effect of

the ocean remains comparatively small (Aschwanden et al., 2019), which is not consistent with current observations (Mouginot et al., 2019). Although some studies relied on higher horizontal model resolution (e.g., ∼400 m) to include individual outlet glaciers, these models were not calibrated to capture the current changes of these glaciers. Poorly calibrated models may result in under- or over-estimation of ice discharge for hindcast and forecast simulations.

Here, we model the response of more than 200 marine terminating glaciers of Greenland to oceanic and atmospheric forcing to investigate their future evolution using an ice-sheet wide model with a spatial resolution of 200 m around the coast (Fig. 6.1). We calibrate this high-resolution model by relying on data collected since 2007. After the model initialization, we run the model forward until today and only calibrate the calving parameterization within each glacier drainage basin so that the model is consistent with observed velocities, changes in ice front positions and thinning rates. This process allows to capture both the current state of the ice sheet but also its current trends, which significantly increases its reliability for short term projections. This approach has been used in a recent study (Morlighem et al., 2019b) but has not been applied at the scale of the entire ice sheet. We use here a 3D high-order model (HO) (Blatter, 1995; Pattyn, 2003) to account for both membrane stresses and vertical shear, which is adequate to model both fast outlet glaciers and the slower moving regions inland of the ice sheet within a unified formulation. We simulate the future sea-level contribution of Greenland until 2100 using different general circulation models (GCMs) outputs from Coupled Model Intercomparison Project Phase 5 (CMIP5) and Phase 6 (CMIP6), which were selected by Ice Sheet Model Intercomparison Project for CMIP6 (ISMIP6) (Goelzer et al., submitted). Contrary to the data provided by ISMIP6, we use a temporal resolution of one month for these climatic forcings instead of a year in order to capture the seasonal cycle in SMB and ocean temperatures.

6.2 Method

Model setup

We use the Ice Sheet System Model (ISSM) (Larour et al., 2012) to model Greenland tidewater glaciers. Our model is based on 3-D higher-order approximation (Blatter, 1995; Pattyn et al., 2013), with subelement grounding line parameterizations (Seroussi et al., 2014a) and level set-based moving boundaries (Bondzio et al., 2016). The horizontal mesh resolution varies from 200 m to 20 km depending on observed surface velocity. The mesh is vertically extruded into 4 layers which are sufficient for the model without a transient thermal field (Cuzzone et al., 2018).

We divide the entire Greenland ice sheet into six domains (Fig. 6.1) to reduce the computational cost for entire simulations. For each domain, we perform the same model initialization approach. The bed and surface topography are from BedMachine Greenland version 3 (Morlighem et al., 2014). To initialize the model, we infer the basal friction coefficients under grounded ice and ice viscosity parameters on floating ice through inversions following (Morlighem et al., 2013) based on 2007-2008 surface velocities (Joughin et al., 2010). The ice viscosity, μ, is defined by Glen's law (Glen, 1955) (Eq. 2.9). The friction in this study follows Budd friction law with a linear relationship with the effective pressure, N (Budd et al., 1979):

$$\tau_b = -k^2 N \|\boldsymbol{v}\|^{s-1} \boldsymbol{v} \tag{6.1}$$

where k is the friction coefficient. The exponent s represents the relation between velocity and basal friction and is chosen to be 1 in this study. The inferred friction coefficient remains to be constant during all simulations. The modeled velocities for each glacier at an initial state are shown in Appendix A.

Model Calibration

To validate our model, we calibrate the modeled ice fronts to match observed ice front changes. Here, we use the von Mises tensile stress calving law (Morlighem et al., 2016) that provides the calving rate at each time step (Choi et al., 2018). We determine the stress threshold value for each glacier by simulating the ice front changes during the calibration period, between 2007 and 2018, and comparing the modeled retreat distance to observed retreat. We manually adjust the stress threshold for each basin to best capture the observed variations in ice front positions. We limit the range of the stress threshold between 150 kPa and 3,100 kPa following the ice tensile strength measurements (Petrovic, 2003). The calibrated stress thresholds assume to be constant during all simulations.

In the calibration phase, our model captures: the observed velocity, the changes in calving front positions and thinning rates (Appendix A). We also compare the modeled ice mass changes to observed mass changes from Mouginot et al. (2019) to validate our model (Fig. 6.3).

Atmospheric forcings

The ice sheet is forced by the surface mass balance (SMB) of RACMO2.3 monthly data for the hindcast simulations. For the forecast simulations, we use the anomalies of SMB from MAR simulations forced by global climate models (GCMs) with respect to average SMB of the calibration period (2007-2017) (Fettweis et al., 2017) (Eq. 6.2). Since the MAR simulations are performed for fixed ice surface elevation, we correct the surface mass balance following the gradient method described in Helsen et al. (2012) to consider changes in ice surface elevation under future warming scenarios. We apply the gradient method only for the ablation regime since this method is not well defined for the accumulation regime (Helsen et al., 2012; Calov et al., 2018). Here we use MIROC5, CanESM2 and NorESM1 outputs

from CMIP5 and CESM2, CNRM-CM6, CNRM-ESM2 and UKESM1 outputs from CMIP6 that are selected for the Ice Sheet Model Intercomparison Project for CMIP6 (ISMIP6).

$$SMB(t) = SMB^{RACMO}_{2007-2017} + (SMB^{GCM}_{RCP}(t) - SMB^{GCM}_{2007-2017}) + (\frac{\delta SMB}{\delta z} \times \Delta z) \tag{6.2}$$

Oceanic forcings

Oceanic forcings here refers to two ocean melt processes: melting of ice under floating ice shelves and at the calving fronts of tidewater glaciers. For the melting under floating ice of northern glaciers (North and Northeast region), we use the parameterization from Holland and Jenkins (1999):

$$m_{floating} = -\rho_M C_{pM} \gamma_T TF \tag{6.3}$$

where ρ_M is the ocean layer density, C_{pM} is the specific heat capacity of the mixed layer, γ_T is the thermal exchange velocity and TF is the thermal forcing. We also follow the simple parameterization from Favier et al. (2014) to consider changes in the basal melt with ice shelf bottom depth. We assume that basal melting increases linearly with a depth between the top-water and the deep-water elevation. We find the different top-water and deep-water elevations for each model domain. For our simulations, we change the thermal forcing, TF in Eq.(6.3), which, in turn, changes the maximum melt rate at the deep-water elevations.

We use the undercutting parameterization from Rignot et al. (2016) to estimate the melt rate at the nearly-vertical ice front of tidewater glaciers (Eq. 3.10). We use ocean thermal forcing from the Estimating the Circulation and Climate of the Ocean, Phase 2 (ECCO2) project (Rignot et al., 2012) for our calibration simulations. To consider the effect of bed topography on ocean temperature (e.g., depth of sill), we use the same extrapolation approach following Morlighem et al. (2019a). To estimate subglacial discharge for calibration, we integrate the RACMO2.3 runoff field over the drainage basin assuming that surface runoff is the dominant

source of subglacial freshwater in summer (Rignot et al., 2016).

For the future simulations, we apply the anomalies of thermal forcing calculated from ocean temperature and salinity of GCM simulations outputs to the average of thermal forcing for the calibration period (Eq. 6.4). We also apply anomalies of runoff from MAR simulations forced by the corresponding GCM models (Fettweis et al., 2017) to the average subglacial discharge for the calibration period (Eq 6.5).

$$TF(t) = TF^{Calibration}_{2007-2017} + (TF^{GCM}_{RCP}(t) - TF^{GCM}_{2007-2017}) \tag{6.4}$$

$$q_{sg}(t) = q^{RACMO}_{sg2007-2017} + (q^{GCM}_{sgRCP}(t) - q^{GCM}_{sg2007-2017}) \tag{6.5}$$

6.3 Results

Tidewater glaciers

The model includes 215 marine terminating glaciers, among which 6 glaciers located in northern Greenland have a floating ice shelf. Most modeled outlet glaciers are in excellent agreement with observed velocities (see Appendix). Among the 215 marine terminating glaciers of Greenland, 67 have a poorly constrained bed topography, which complicates the calibration. For these glaciers, we keep the ice front fixed in time in order to avoid nonphysical behavior during our simulations. The ice fronts of 115 glaciers are calibrated within 1 km from the observations. Of the 33 glaciers remaining, in which our model could not reproduce the observed retreat within 1 km, the retreat distance of 8 glaciers are overestimated by up to 3.2 km, while the retreat of 25 glaciers are underestimated by up to 24 km. Observed and modeled ice front retreat (in km along a center line) during the calibration period is provided in the Appendix

For each marine terminating glacier, we calculate the changes in ice mass, along with the cumulative SMB and ice discharge until 2100 (Fig. 6.2 and Appendix). Our simulations suggest that many outlet glaciers will continue to experience ice front retreat under future climate scenarios. The pattern of modeled retreat varies significantly from one glacier to the next, which is consistent with observations and previous modeling studies (Moon et al., 2015; Aschwanden et al., 2019). For example, in central Greenland, Eqip Sermia glacier and Jakobshavn Isbræ respond differently to the same climate forcing scenario (Fig. 6.2(b) and (c)). Under MIROC5 RCP8.5 scenario, the mass change of Eqip Sermia glacier is mainly controlled by changes in SMB, while the ice discharge decreases once the ice front stabilizes 5 km upstream of its current position. For Jakobshavn Isbræ, on the other hand, the model suggests that ice discharge will continue to dominate in terms of mass loss over this century, as the ice front continues to retreat within the overdeepening upstream of the current ice front position by 2070, and would then stabilizes 56 km upstream of its current position, where the bed rises again. Note that our model does not capture the recent slowdown of Jakobshavn Isbræ because the thermal forcings that we use here do not include a cooling over the past couple of years (Khazendar et al., 2019). The main factor responsible for these contrasting behaviors between these two glaciers is the bed geometry. The ice front of Eqip Sermia retreats only about 5 km and stabilizes because the bed in this sector is shallow, while Jakobshavn Isbræ's retreat seems irreversible once it starts retreating within its deep trough, where the bed is primarily retrograde.

It has been shown that the bed topography plays a critical role in determining stable positions of ice fronts, which affects an overall trend of ice mass change of glacier (Catania et al., 2018; Wood et al., 2018). For two different glaciers from different regions under the RCP8.5 scenario (Fig. 6.2(c) and (d)), Narsap in southwest Greenland and Kakivfaat in northwest Greenland, the ice discharge initially dominates the changes in mass balance during the first 20-30 years, and then the ice discharge decreases as the ice front stabilizes upstream, which leads to a slowdown of the glacier. After 2060, the SMB starts to significantly decrease

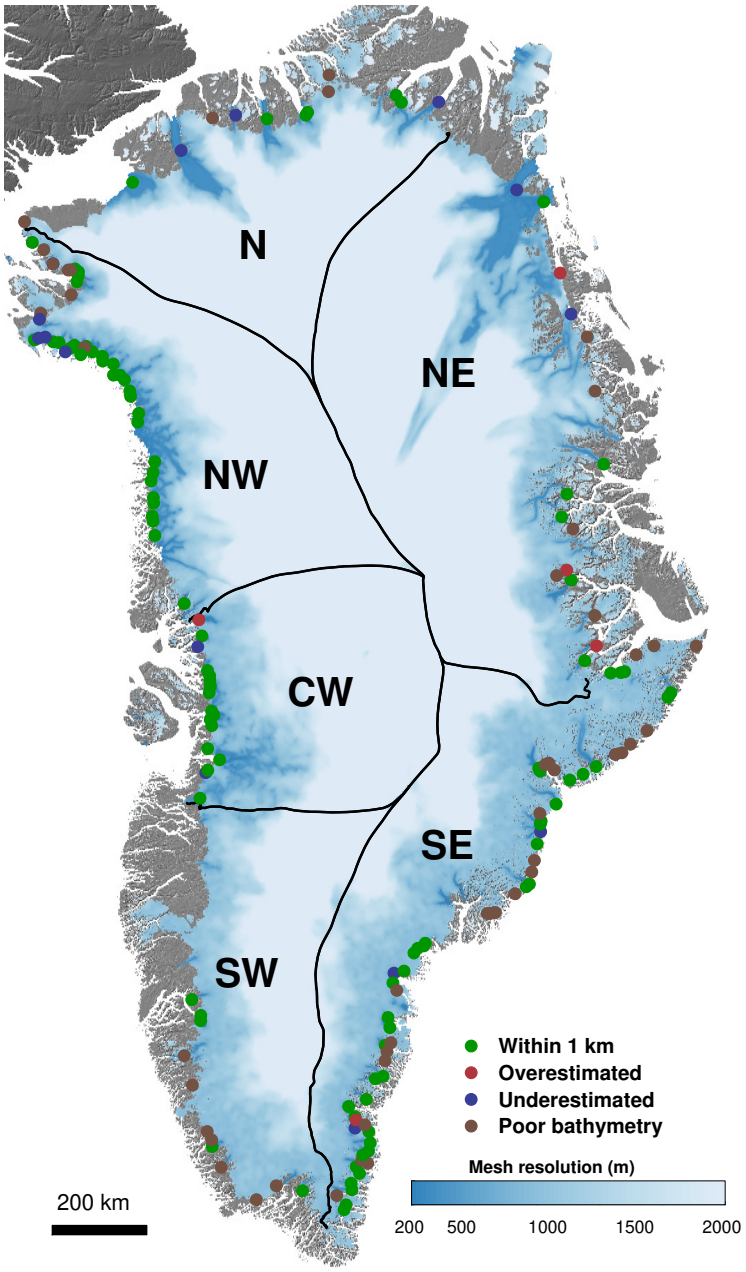

Figure 6.1: Six large regions of the Greenland ice sheet overlaid on the mesh resolution (m) of the model domain. The location of 200 Greenland glaciers represented by circles used to calibrate the model where we distinguish glaciers within 1 km of observations (green), with overestimated retreat (red), underestimated retreat (blue), and poorly-known bathymetry (brown).

and results in glacier mass loss over the last 30 years of the simulation. The primary factor of mass loss therefore changes with time, depending on the retreat and the dynamics of individual glacier. While the extent of the retreat of these two glaciers is different, the

timings of retreat are similar due to the bed topography.

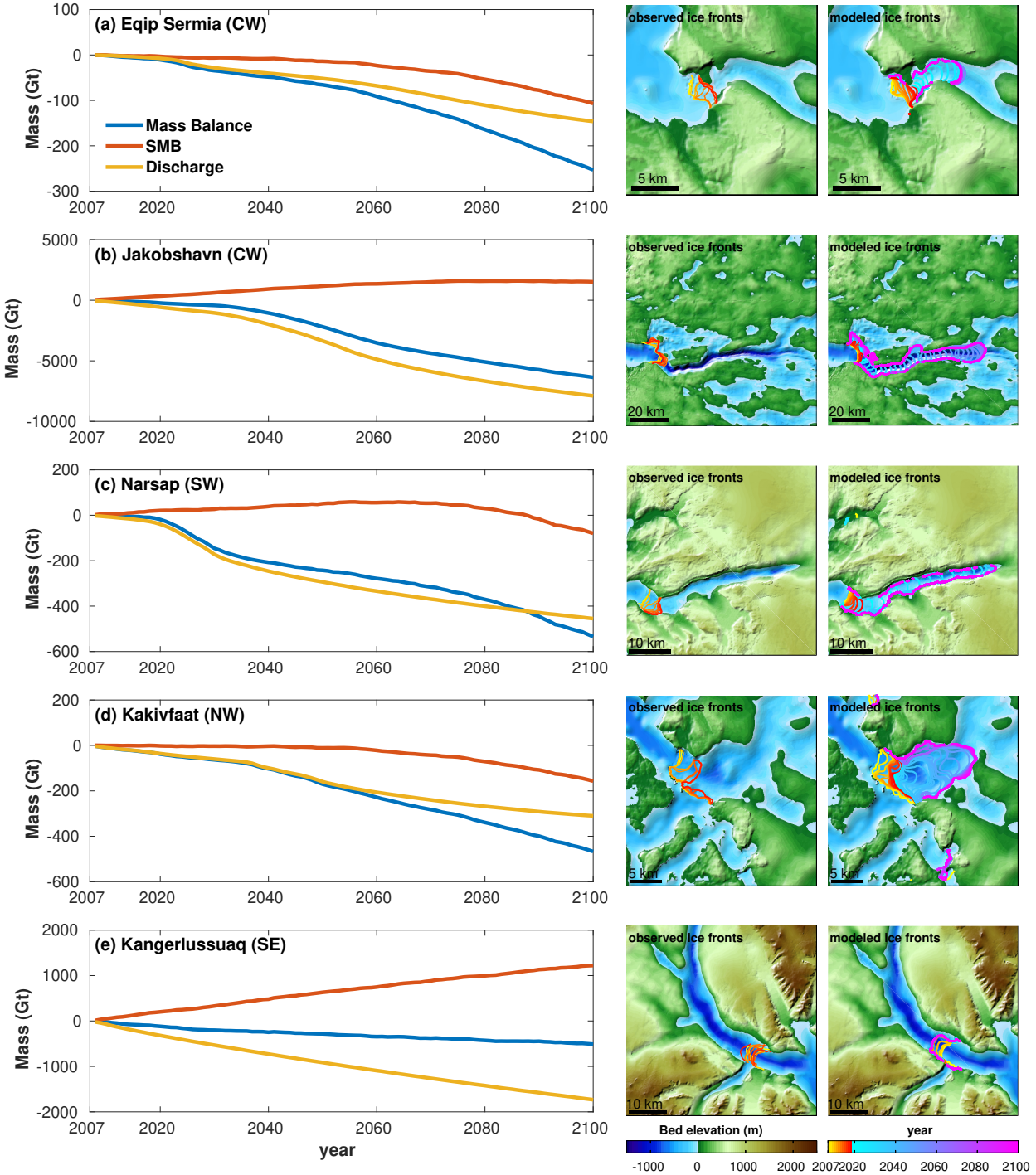

Figure 6.2: Cumulative SMB, ice discharge and changes in ice mass until 2100 (left) and the observed ice front positions between 2007 and 2017 and modeled ice front positions between 2007 and 2100 overlaid on the bed topography of (a) Eqip Sermia, (b) Jakobshavn Isbræ, (c) Narsap, (d) Kakivfaat and (e) Kangerlussuaq glaciers

A deep bed topography does not always lead to glacier retreat, as illustrated by Kangerlussuaq glacier in southeast Greenland under MIROC5 RCP8.5 scenario (Fig. 6.2(e)). This glacier loses mass continuously due to ice discharge, but the SMB remains largely positive over the region, which compensates the mass loss from ice discharge. This positive SMB continues until the end of the simulation and the ice front does not retreat within the deep trough upstream of its current position, which keeps the glacier in nearly balanced in terms of ice mass. The shape of the bed topography provides clues about the potential stability and vulnerability of a given glacier, but several factors such as lateral shear or buttressing may delay or stop the retreat, even within regions of deep bed topography or retrograde bed slopes (Gudmundsson et al., 2012). A numerical model is necessary to determine whether a glacier will retreat or not for a given scenario.

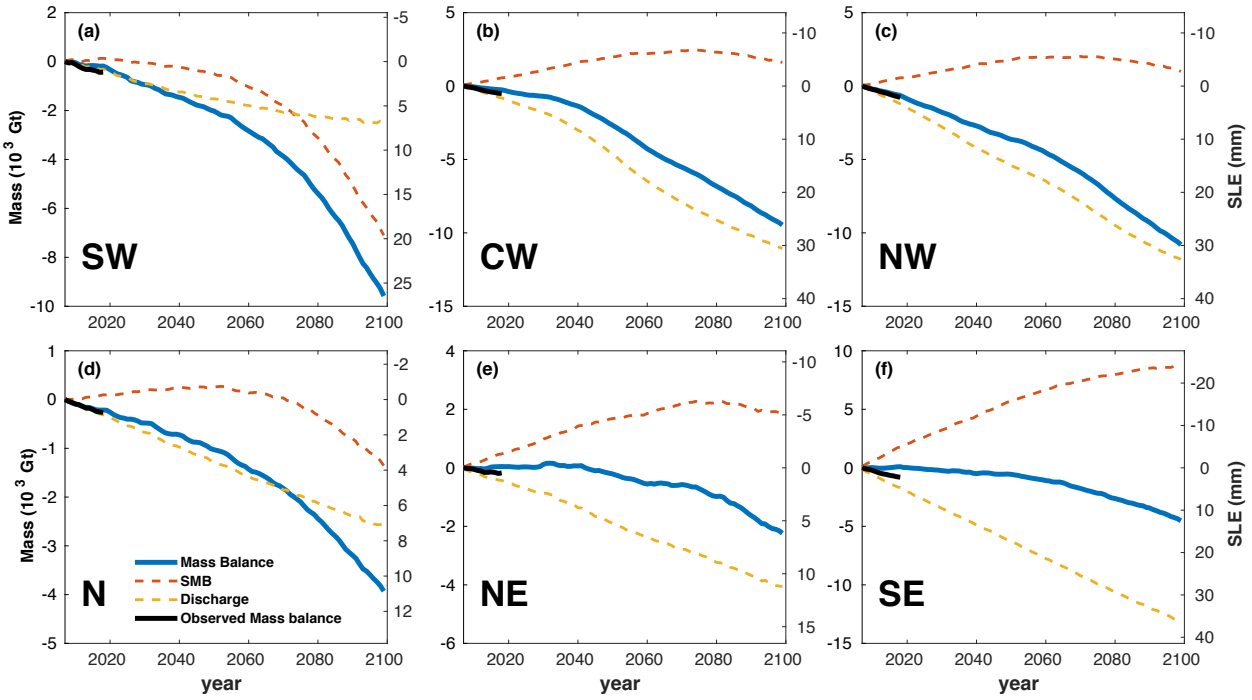

Figure 6.3: Cumulative SMB, ice discharge and changes in ice mass from 2007 to 2100 for the six regions of Greenland under MIROC5 RCP8.5

Regional Changes

We divide Greenland into 6 large regions (Fig. 6.1): (i) southwest (SW), (ii) central west (CW), (iii) northwest (NW), (iv) north (N), (v) northeast (NE), (vi) southeast (SE) and calculate the mass balance, the cumulative SMB and ice discharge for each region over the simulation period (Fig. 6.3). There is a very good agreement between the modeled and estimated trends derived through remote sensing for each region (Mouginot et al., 2019), except for SE. This region still suffers from a poorly constrained bed topography, which is responsible for the weaker agreement between our model and the data, as also shown in previous studies (Aschwanden et al., 2012, 2019). As we keep the ice front of most glaciers in this region fixed due to the poorly constrained bed topography, we are underestimating the mass loss of the SE region.

Fig. 6.3 shows the change in ice mass along with cumulative SMB and ice discharge from 2007 to 2100 for the six different regions of Greenland, forced by MIROC5 under the RCP8.5 scenario. Under this scenario, the SW region would lose a total of 9,581 Gt of ice by 2100, which corresponds to 26.5 mm of sea level contribution. Our results suggest that the primary driver of mass loss in this region is the large decrease in SMB starting in year 2060. The ice discharge from the 15 marine terminating glaciers also decreases after 2060 in response to this decrease in SMB, which reduces the ice flux at the terminus. The CW region would raise sea level by 26.1 mm based on the same simulation. Similarly to SW, the SMB is overall positive until 2060 and then starts to decrease around year 2080. In this region, most of the mass loss is due to the extensive retreat of Jakobshavn Isbræ glacier, which accounts for almost 65% of the entire mass loss of this region. The remaining glaciers of this region lose a total of 3,360 Gt of ice by the end of the century. The NW region has a very similar pattern in terms of mass changes, SMB and ice discharge. This sector would lose 11,334 Gt of ice (31.3 mm sea level equivalent, SLE) until 2100 with ice discharge from over 60 glaciers contributing 67.1% of the total mass loss. The N region would contribute 10.9 mm

to sea level by 2100. While the ice discharge remains approximately constant, the SMB will decrease significantly after 2060, leading to significant mass loss. The NE would lose 2,237 Gt of ice mass (or 6.2 mm SLE) until 2100. Although the SMB remains positive almost over this entire sector until the end of the century, the ice discharge remains higher than the mass gain, which results in a net mass loss at the end of the simulations. The SE shows a similar pattern to the one of NE: while the SE has a positive SMB of 4,521 Gt until 2100, it also loses 141 Gt/year through ice discharge. Although this region shows the largest cumulative ice discharge at the end of the century, a strong positive SMB compensates the mass loss from marine terminating glaciers.

Overall, in all simulations forced by CMIP5 RCP8.5 and CMIP6 ssp585, the model shows that all the sectors of Greenland will continue to lose mass, and the rate of mass loss will increase during this century, including the northern sectors. This mass loss is due to two factors. First the SMB is projected to decrease in most sectors, due to the increase in surface temperature, which leads to higher melting rates at the surface of the ice sheet, and second, due to the sustained or enhanced ice discharge of marine terminating glaciers. This increase in ice discharge remains a major driver of mass loss over the entire time period considered here, except in the SW. In the recent multi-model study of the Ice Sheet Model Intercomparison Project for CMIP6 (ISMIP6) (Goelzer et al., submitted), the SW region is highlighted as the largest contributor to sea level. However, our model shows that the sectors further north of the west coast (i.e.,CW and NW) have a contribution to future sea level rise that is as high as SW, under all scenarios in this study. Most models participating in ISMIP6 either used a parameterized ice front retreat, or a coarse grid resolution, leading to a weak dynamic response of this sector under RCP8.5. Our calibrated model shows, however, that these two sectors remain major contributors to the entire ice mass change over this century.

The Northern sectors of Greenland (N and NE) and SE will also continue to lose mass due to the sustained anomaly in ice discharge along with a decrease in SMB. The simulated sea level

contribution from these regions may be underestimated because of the weaker calibration of the model in this region and the bed topography that remains largely uncertain. Our model does not capture any ice front change for 45 glaciers of these regions, many of which are actually marine terminating glaciers although they are represented as land terminating glaciers in the model due to errors in bed topography. We expect that more glaciers might be susceptible to changes in future ocean conditions, which would affect the ice discharge of this sector. More observations of bed topography are needed to better estimate future changes of these regions.

Sea level contribution from Greenland

Our simulations show that, overall, the Greenland ice sheet contribution to sea level by the end of the century would range from 79.2 mm to 167 mm under RCP8.5 and ssp585 climate forcing scenarios (Fig. 6.4), which is on the high end or exceeds ISMIP6 estimates (Goelzer et al., submitted). Based on the latest CMIP6 ssp585 climate forcings, the simulated Greenland sea level contribution until 2100 ranges from 94 mm to 167 mm, which is at or above the range from CMIP5 RCP8.5 simulations. Based on CMIP5 RCP4.5, the Greenland ice sheet would raise sea level between 54.5 mm and 79.1 mm by the end of this century. Overall, we find that the rate of mass loss will continue to increase and the rate of increase is different between simulations depending on the forcing applied. Interestingly, the simulations forced by CMIP6 ssp585 forcings (CESM2, CNRM-CM6, CNRM-ESM2 and UKESM1-CM6) lose mass at a higher rate after about 2080 compared to the ones forced by CMIP5 RCP8.5 data (MIROC5, CanESM2 and NorESM1), which we attribute to a larger decrease in SMB (Fig. 6.4).

Fig. 6.4 shows the partitioning between ice discharge and SMB that contribute to cumulative mass loss under CMIP5 RCP8.5 (Fig. 6.4(b)) and CMIP6 ssp585 (Fig. 6.4(c)) simulations. The ice loss from ice discharge anomalies continues until 2100 at a similar rate for both

scenarios. SMB anomalies in both scenarios are small until 2050 and then start to decrease significantly around year 2060. Although the importance of changes in SMB increases rapidly, ice discharge will remain a large contributor to the entire mass loss over this century, accounting for 38.9 - 70.3% for CMIP5 RCP8.5 and 22 - 55.6% for CMIP6 ssp585, respectively, in 2100. These estimates are significantly larger than ones from previous studies (Pachauri et al., 2014; Aschwanden et al., 2019; Goelzer et al., submitted), which suggests that future Greenland ice loss will be dominated not only surface processes but dynamic ice discharge to the ocean.

The mass loss from discharge anomalies contributes similar cumulative mass loss under different CMIP5 and CMIP6 models, while the mass loss from SMB varies between models. We attribute this behavior to the fact that many marine terminating glaciers engage in a state of ice front retreat due to ocean warming, and then continue to lose mass, almost regardless of changes in SMB, because the retreat is then primarily dictated by the bed topography. For example, based on both RCP4.5 and RCP8.5 scenarios, Jakobshavn Isbræ glacier continues to retreat along its deep trough about same distance (56 km) at a similar rate once the ice front is dislodged from its current position by the ocean thermal forcing, which leads to a similar overall mass loss for both scenarios. However, this glacier is very sensitive to ocean temperature (Bondzio et al., 2018), implying that future changes in ocean temperature might have a large impact on the stability of the glacier. More sensitivity studies are needed to investigate the threshold necessary to trigger the retreat of this glacier, so that we can better assess how vulnerable this sector is to an increase in ocean forcing in the future.

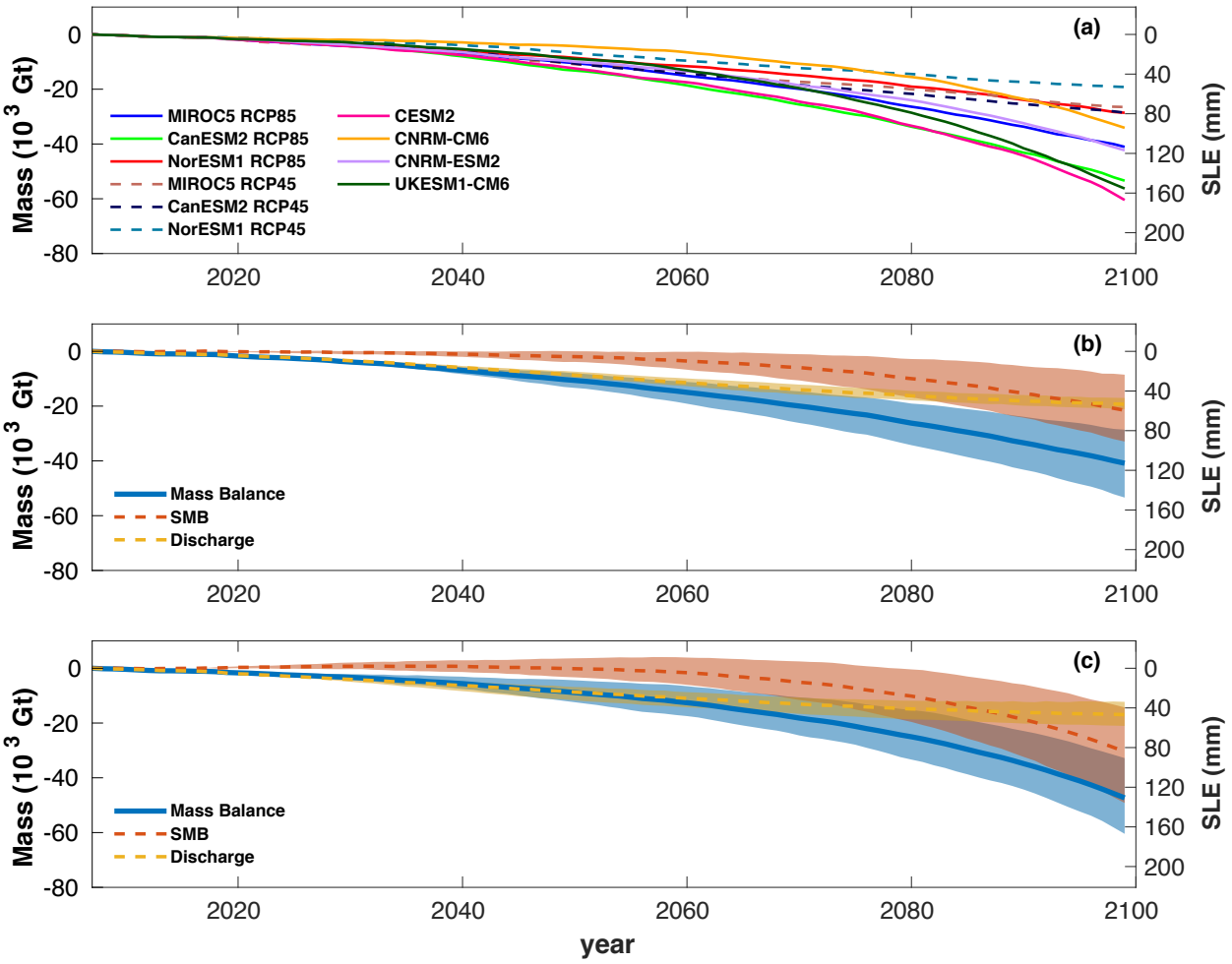

Figure 6.4: (a) Changes in ice mass and corresponding sea level contribution until 2100 for the entire Greenland ice sheet under CMIP5 and CMIP6 outputs. (b), (c) Ensemble of changes in ice mass, partitioning of mass loss between SMB (red) and discharge (yellow) from 2007 to 2100 for entire Greenland based on (b) CMIP5 RCP8.5 and (c) CMIP6 ssp585. The thick lines represent the ensemble means.

Chapter 7

Conclusion

Summary of main results

In this thesis, we estimated the future sea level contribution from Greenland using an ice sheet model that fully accounts for changes in the terminus of individual marine terminating glaciers. First, we introduced the mathematical and scientific theories underpinning a numerical ice sheet model. In addition, we summarized previous studies that have estimated the future evolution of Greenland and determined what needed to be improved upon to better constrain future changes of the ice sheet. This work focused on calving processes, which have been considered the main control on changes in dynamic ice discharge.

In chapter 3 and 4, we introduced calving parameterizations proposed for ice sheet models and compare four calving laws by modeling nine tidewater glaciers of Greenland with a 2-D plan-view ice sheet model. Our simulations show that the von Mises stress calving law (VM) reproduced observations better than other calving laws, although it may not capture all the physics involved in calving events. Other calving laws do not capture the pattern or pace of observed retreat as well as the VM. In forecast simulations, the pattern of ice front retreat is

somewhat similar for most calving laws because of the strong control of the bed topography on ice front dynamics. Based on our results, we recommend using the tensile von Mises stress calving law for predictive ice sheet models.

We applied the von Mises stress calving law to modeling Northeast Greenland glaciers (Nioghalvfjerdsfjorden (79North) and Zachariae Isstrøm (ZI) Glaciers) to assess their response to ocean thermal forcing under different warming scenarios. Under scenarios considered in the study, our model suggests that 79North will not change significantly over the next century, even with a strong increase in basal melt rates. ZI will continue to retreat 30 km upstream and become a grounded tidewater glacier until it reaches a stabilizing $\sim$200 m step in bed topography. Our simulations show that ZI is in a state of unstoppable retreat that does not depend significantly on ocean forcing but is due to its current internal dynamics, which is mainly controlled by the bed topography. This retreat will stop once the ice front reaches this stabilizing ridge in the bed topography. An increase in the frontal melt rate up to 6 m/d in the summer would be necessary to trigger a further retreat inland, and this amount of oceanic forcing, while significant, remains within the range of possible scenarios.

In the last chapter, we extended out the regional model to all glaciers in Greenland to investigate future changes in Greenland. We have simulated the future sea-level contribution of Greenland with a high-resolution model that accounts for the changes in ice front of the individual marine terminating glacier. Under CMIP5 RCP8.5 and CMIP6 ssp585 emission scenarios, Greenland would contribute 79.2 - 167 mm to sea level by 2100, which is higher than current estimates (Goelzer et al., submitted). We find that the ice discharge accounts for 22 to 70.3% of the total mass loss, which is 1.5 to 3 times larger than the estimates from previous studies (Pachauri et al., 2014; Aschwanden et al., 2019; Goelzer et al., submitted). This is attributed to large mass loss from NW and CW region of Greenland, where the extensive retreats of marine terminating glaciers are simulated in our model, which may be sensitive to changes in ocean temperature. Although many glaciers are currently flowing

through a deep, submarine bed topography, the timing for those glaciers to retreat further is different and varies from glacier to glacier, which calls for more research on ice-ocean interaction and iceberg calving.

Perspectives

In this thesis, we used the ice sheet model that improves capturing ice front changes at the outlet glacier termini. However, several processes are still poorly understood and need to be improved upon in ice sheet modeling.

First, new calving parameterizations should be derived to better capture and understand the complex processes involved in calving dynamics. The calving law we tested and used for this thesis depends on one single calibrated parameter that we keep constant through time and uniform in space, which adds uncertainty to model projections. Future studies are needed to validate the calibration parameter and improve the law by accounting for other modes of calving. Current research based on discrete element models (e.g., Benn et al., 2017) or damage mechanics (Duddu et al., 2013) may help the community derive new parameterizations if they overcome the limitation of mesh refinement and computational cost for modeling individual calving events.

Coupled ice-ocean models with hydrology are needed to better reproduce observed submarine melting with feedbacks between the ice sheet and ocean. The melt rates depend on oceanic properties such as subglacial discharge and thermal forcing (Holland and Jenkins, 1999), which, in part, are dependent on basal hydrology and ocean conditions. Different vertical variations in melt rate may affect the shape of the calving front, resulting in different spatial patterns of ice front calving and total ablation rates (Slater et al., 2017). Further investigation is needed to consider more complex processes that occur at the ice-ocean interface.

Another possible improvement is in the representation of basal sliding of the ice sheet. The data assimilation technique applied here to derive the basal drag provides little information about the physical processes contributing to basal sliding. Basal thermal state and basal hydrology are needed in the model to better constrain how the basal drag changes with time. Transient data assimilation with a large dataset of observations will help understanding basal processes and improve our model projections. Additionally, different basal sliding laws should be tested to fill the gap between observations and model results.

Estimating future ice sheet contributions to sea level rise with an ice sheet model heavily depends on data input derived from general circulation models (GCMs), which dominate uncertainties to future Greenland projections. Although reducing uncertainty from GCMs is beyond the scope of this thesis, we can determine which regions are most vulnerable to the warming climate and are most in need of further monitoring and research based on our ice sheet model. We need more sensitivity studies that provide this information and help reduce the uncertainty of future sea level contribution from Greenland.

Bibliography

van Angelen, J. H., J. T. M. Lenaerts, S. Lhermitte, X. Fettweis, P. Kuipers Munneke, M. R. van den Broeke, E. van Meijgaard and C. J. P. P. Smeets. *Sensitivity of Greenland Ice Sheet surface mass balance to surface albedo parameterization: a study with a regional climate model*. Cryosphere, volume 6, no. 5; pages 1175–1186, 2012. doi:10.5194/tc-6-1175-2012.

Aschwanden, A., E. Bueler, C. Khroulev and H. Blatter. *An enthalpy formulation for glaciers and ice sheets*. J. Glaciol., volume 58, no. 209; pages 441–457, 2012. doi: 10.3189/2012JoG11J088.

Aschwanden, A., M. A. Fahnestock, M. Truffer, D. J. Brinkerhoff, R. Hock, K. Khroulev, R. Mottram and S. A. Khan. *Contribution of the Greenland Ice Sheet to sea level over the next millennium*. Science Advances, volume 5, 2019. doi:10.1126/sciadv.aav9396.

Bartholomaus, T. C., C. F. Larsen and S. O'Neel. *Does calving matter? evidence for significant submarine melt*. Earth and Planetary Sci. Lett., volume 380; pages 21–30, October 2013. ISSN 0012-821X. doi:10.1016/j.epsl.2013.08.014.

Benn, D. I., T. Cowton, J. Todd and A. Luckman. *Glacier Calving in Greenland*. Curr Clim Change Rep, volume 3; pages 282–290, 2017. doi:10.1007/s40641-017-0070-1.

Benn, D. I., C. R. Warren and R. H. Mottram. *Calving processes and the dynamics of calving glaciers*. Earth Sci. Rev., volume 82, no. 3-4; pages 143–179, JUN 2007. ISSN 0012-8252. doi:10.1016/j.earscirev.2007.02.002.

Bevan, S. L., A. J. Luckman and T. Murray. *Glacier dynamics over the last quarter of a century at Helheim, Kangerdlugssuaq and 14 other major Greenland outlet glaciers*. Cryosphere, volume 6, no. 5; pages 923–937, 2012. ISSN 1994-0416. doi: 10.5194/tc-6-923-2012.

Blatter, H. *Velocity And Stress-Fields In Grounded Glaciers: A Simple Algorithm For Including Deviatoric Stress Gradients*. J. Glaciol., volume 41, no. 138; pages 333–344, 1995. ISSN 0022-1430.

Blatter, H., G. Greve and A. Abe-ouchi. *A short history of the thermomechanical theory and modelling of glaciers and ice sheets*. Ann. of Glaciol., volume 56 (200); pages 187–194, 2010.

Bondzio, J. H., M. Morlighem, H. Seroussi, M. Wood and J. Mouginot. *Control of ocean temperature on Jakobshavn Isbræ's present and future mass loss*. Geophys. Res. Lett., 2018. doi:10.1029/2018GL079827.

Bondzio, J. H., H. Seroussi, M. Morlighem, T. Kleiner, M. Rückamp, A. Humbert and E. Larour. *Modelling calving front dynamics using a level-set method: application to Jakobshavn Isbræ, West Greenland*. Cryosphere, volume 10, no. 2; pages 497–510, 2016. doi:10.5194/tc-10-497-2016.

van den Broeke, M. R., E. M. Enderlin, I. M. Howat, P. K. Munneke, B. P. Y. Noel, W. J. van de Berg, E. van Meijgaard and B. Wouters. *On the recent contribution of the Greenland ice sheet to sea level change*. Cryosphere, volume 10, no. 5; pages 1933–1946, September 2016. ISSN 1994-0416. doi:10.5194/tc-10-1933-2016.

Brown, C. S., M. F. Meier and A. Post. *Calving speed of Alaska tidewater Glaciers, with application to Columbia Glacier, Alaska*. U.S. Geological Survey Professional Paper, (pages 1258–C. 13pp), 1982. ISSN 10449612.

Budd, W. F., P. L. Keage and N. A. Blundy. *Empirical studies of ice sliding*. J. Glaciol., volume 23; pages 157–170, 1979.

Calov, R., S. Beyer, R. Greve, J. Beckmann, M. Willeit, T. Kleiner, M. Ruckamp, A. Humbert and A. Ganopolski. *Simulation of the future sea level contribution of Greenland with a new glacial system model*. Cryosphere, volume 12; pages 3097–3121, 2018. doi: 10.5194/tc-12-3097-2018.

Catania, G. A., L. A. Stearns, D. A. Sutherland, M. J. Fried, T. C. Bartholomaus, M. Morlighem, E. Shroyer and J. Nash. *Geometric Controls on Tidewater Glacier Retreat in Central Western Greenland*. J. Geophys. Res. - Earth Surface, volume 123, no. 8; pages 2024–2038, 2018. doi:10.1029/2017JF004499.

Choi, Y., M. Morlighem, E. Rignot, J. Mouginot and M. Wood. *Modeling the response of Nioghalvfjerdsfjorden and Zachariae Isstrøm glaciers, Greenland, to ocean forcing over the next century*. Geophys. Res. Lett., volume 44, no. 21; pages 11,071–11,079, 2017. ISSN 1944-8007. doi:10.1002/2017GL075174.

Choi, Y., M. Morlighem, M. Wood and J. H. Bondzio. *Comparison of four calving laws to model Greenland outlet glaciers*. Cryosphere, volume 12, no. 12; pages 3735–3746, 2018. doi:10.5194/tc-12-3735-2018.

Church, J. A., P. U. Clark, A. Cazenave, J. M. Gregory, S. Jevrejeva, A. Levermann, M. A. Merrifield, G. A. Milne, R. S. Nerem, P. D. Nunn, A. J. Payne, W. T. Pfeffer, D. Stammer and A. S. Unnikrishnan. *Climate Change 2013: The Physical Science-BasisChange*, chapter 13, (pages 1137–1216) (Cambridge University Press, Cambridge, United Kingdom and New York, NY, USA, 2013). ISBN ISBN 978-1-107-66182-0. doi: 10.1017/CBO9781107415324.026.

Cook, S., I. C. Rutt, T. Murray, A. Luckman, T. Zwinger, N. Selmes, A. Goldsack and T. D. James. *Modelling environmental influences on calving at Helheim Glacier in eastern Greenland*. Cryosphere, volume 8, no. 3; pages 827–841, 2014. ISSN 1994-0416. doi: 10.5194/tc-8-827-2014.

Cook, S., T. Zwinger, I. C. Rutt, S. O'Neel and T. Murray. *Testing the effect of water in crevasses on a physically based calving model*. Ann. Glaciol., volume 53, no. 60, 1; pages 90–96, 2012. ISSN 0260-3055. doi:10.3189/2012AoG60A107.

Courant, R., K. Friedrichs and H. Lewy. *Über die partiellen Differenzengleichungen der mathematischen Physik*. Mathematische Annalen, volume 100; pages 32–74, 1928. doi: 10.1007/BF01448839.

Cowton, T., D. Slater, A. Sole, D. Goldberg and P. Nienow. *Modeling the impact of glacial runoff on fjord circulation and submarine melt rate using a new subgrid-scale parameterization for glacial plumes*. Journal of Geophysical Research, Oceans, volume 120, no. 2; pages 796–812, February 2015. ISSN 2169-9275. doi:{10.1002/2014JC010324}.

Csatho, B. M., A. F. Schenk, C. J. van der Veen, G. Babonis, K. Duncan, S. Rezvanbehbahani, M. R. van den Broeke, S. B. Simonsen, S. Nagarajan and J. H. van Angelen. *Laser altimetry reveals complex pattern of Greenland Ice Sheet dynamics*. Proc. Natl. Acad. Sci. U.S.A., volume 111, no. 52; pages 18 478–18 483, DEC 30 2014. ISSN 0027-8424. doi:10.1073/pnas.1411680112.

Cuffey, K. M. and W. S. B. Paterson. *The Physics of Glaciers, 4th Edition* (Elsevier, Oxford, 2010).

Cuzzone, J. K., M. Morlighem, E. Larour, N. Schlegel and H. Seroussi. *Implementation of higher-order vertical finite elements in ISSM v4.13. for improved ice sheet flow modeling over paleoclimate timescales*. Geosci. Model Dev., volume 11, no. 5; pages 1683–1694, 2018. doi:10.5194/gmd-11-1683-2018.

Duddu, R., J. N. Bassis and H. Waisman. *A numerical investigation of surface crevasse propagation in glaciers using nonlocal continuum damage mechanics*. Geophys. Res. Lett., volume 40; pages 3064–3068, 2013. ISSN 1944-8007. doi:10.1002/grl.50602.

Enderlin, E. M. and I. M. Howat. *Submarine melt rate estimates for floating termini of Greenland outlet glaciers (2000-2010)*. J. Glaciol., volume 59, no. 213; pages 67–75, 2013. ISSN 0022-1430. doi:10.3189/2013JoG12J049.

Enderlin, E. M., I. M. Howat, S. Jeong, M.-J. Noh, J. H. van Angelen and M. R. van den Broeke. *An improved mass budget for the Greenland ice sheet*. Geophys. Res. Lett., volume 41, no. 3; pages 866–872, 2014. ISSN 1944-8007. doi:10.1002/2013GL059010.

Favier, L., G. Durand, S. L. Cornford, G. H. Gudmundsson, O. Gagliardini, F. Gillet-Chaulet, T. Zwinger, A. J. Payne and A. M. Le Brocq. *Retreat of Pine Island Glacier controlled by marine ice-sheet instability*. Nat. Clim. Change, volume 4; pages 117–121, 2014. doi:10.1038/NCLIMATE2094.

Favier, L., F. Pattyn, S. Berger and R. Drews. *Dynamic influence of pinning points on marine ice-sheet stability: a numerical study in Dronning Maud Land, East Antarctica.* The Cryosphere, volume 10, no. 6; pages 2623–2635, November 2016. ISSN 994-0416. doi:10.5194/tc-10-2623-2016.

Fettweis, X., J. E. Box, C. Agosta, C. Amory, C. Kittel, C. Lang, D. van As, H. Machguth and H. Gallee. *Reconstructions of the 1900-2015 Greenland ice sheet surface mass balance using the regional climate MAR model.* Cryosphere, volume 11, no. 2; pages 1015–1033, April 2017. ISSN 1994-0416. doi:10.5194/tc-11-1015-2017.

Fettweis, X., B. Franco, M. Tedesco, J. H. van Angelen, J. T. M. Lenaerts, M. R. van den Broeke and H. Gallée. *Estimating the Greenland ice sheet surface mass balance contribution to future sea level rise using the regional atmospheric climate model MAR.* Cryosphere, volume 7, no. 2; pages 469–489, 2013. doi:10.5194/tc-7-469-2013.

Forsberg, R., L. Sorensen and S. Simonsen. *Greenland and Antarctica ice sheet mass changes and effects on global sea level.* Surveys in Geophys., volume 38, no. 1, SI; pages 89–104, January 2017. ISSN 0169-3298. doi:10.1007/s10712-016-9398-7.

Frey, P. J. *Yams, A fully Automatic Adaptive Isotropic Surface Remeshing Procedure.* Technical Report RT-0252, INRIA, Rocquencourt, 11 2001.

Fried, M. J., G. A. Catania, T. C. Bartholomaus, D. Duncan, M. Davis, L. A. Stearns, J. Nash, E. Shroyer and D. Sutherland. *Distributed subglacial discharge drives significant submarine melt at a Greenland tidewater glacier.* Geophys. Res. Lett., volume 42, no. 21; pages 9328–9336, 2015. ISSN 1944-8007. doi:10.1002/2015GL065806. 2015GL065806.

Fürst, J. J., H. Goelzer and P. Huybrechts. *Ice-dynamic projections of the Greenland ice sheet in response to atmospheric and oceanic warming.* Cryosphere, volume 9, no. 3; pages 1039–1062, 2015. ISSN 1994-0416. doi:10.5194/tc-9-1039-2015.

Gagliardini, O., G. Durand, T. Zwinger, R. C. A. Hindmarsh and E. Le Meur. *Coupling of ice-shelf melting and buttressing is a key process in ice-sheets dynamics.* Geophys. Res. Lett., volume 37, no. L14501; pages 1–5, JUL 24 2010. ISSN 0094-8276. doi:10.1029/2010GL043334.

Glen, J. W. *The creep of polycrystalline ice.* Proc. R. Soc. A, volume 228, no. 1175; pages 519–538, 1955.

Goelzer, H., S. Nowicki and I. participants. *The future sea-level contribution of the Greenland ice sheet: a multi-model ensemble study of ISMIP6.* The Cryosphere Discuss., submitted.

Goelzer, H., H. P., M.-F. Loutre and T. Fichefet. *Last Interglacial climate and sea-level evolution from a coupled ice sheet-climate model.* Clim. Past., (pages 2195–2213), 2016. doi:10.5194/cp-12-2195-2016.

Goldberg, D. N., P. Heimbach, I. Joughin and B. Smith. *Committed retreat of Smith, Pope, and Kohler Glaciers over the next 30 years inferred by transient model calibration.* Cryosphere, volume 9, no. 6; pages 2429–2446, 2015. doi:10.5194/tc-9-2429-2015.

Gregory, J. M. and P. Huybrechts. *Ice-sheet contributions to future sea-level change*. Phil. Trans R. Soc. A, volume 364, no. 1844; pages 1709–1731, JUL 15 2006. ISSN 1364-503X. doi:10.1098/rsta.2006.1796. Royal-Society Discussion Meeting on Evolution of the antarctic Ice Sheet, London, ENGLAND, OCT 17-18, 2005.

Greve, R. *On the Response of the Greenland Ice Sheet to Greenhouse Climate Change - Springer*. Clim. Chang., volume 46; pages 289–303, 2000.

Greve, R. and H. Blatter. *Dynamics of Ice Sheets and Glaciers*. Advances in Geophysical and Environmental Mechanics and Mathematics (Springer Science & Business Media, 2009). ISBN 978-3-642-03414-5, 1-287 pages. doi:10.1007/978-3-642-03415-2.

Gudmundsson, G. H., J. Krug, G. Durand, L. Favier and O. Gagliardini. *The stability of grounding lines on retrograde slopes*. Cryosphere, volume 6, no. 6; pages 1497–1505, 2012. ISSN 1994-0424. doi:10.5194/tc-6-1497-2012.

Hecht, F. *BAMG: Bi-dimensional Anisotropic Mesh Generator*. Technical report, FreeFem++, 2006.

Helsen, M. M., R. S. W. van de Wal, M. R. van den Broeke, W. J. van de Berg and J. Oerlemans. *Coupling of climate models and ice sheet models by surface mass balance gradients: application to the Greenland Ice Sheet*. Cryosphere, volume 6, no. 2; pages 255–272, 2012. ISSN 1994-0416. doi:10.5194/tc-6-255-2012.

Hindmarsh, R. C. A. *A numerical comparison of approximations to the Stokes equations used in ice sheet and glacier modeling*. J. Geophys. Res., volume 109, no. F1; pages 1–15, MAR 10 2004. ISSN 0148-0227. doi:10.1029/2003JF000065.

Holland, D. M. and A. Jenkins. *Modeling thermodynamic ice-ocean interactions at the base of an ice shelf*. J. Phys. Oceanogr., volume 29, no. 8, Part 1; pages 1787–1800, AUG 1999. ISSN 0022-3670.

Holland, D. M., R. H. Thomas, B. De Young, M. H. Ribergaard and B. Lyberth. *Acceleration of Jakobshavn Isbrae triggered by warm subsurface ocean waters*. Nat. Geosci., volume 1, no. 10; pages 659–664, OCT 2008. ISSN 1752-0894. doi:10.1038/ngeo316.

Holliday, N. P., S. L. Hughes, S. Bacon, A. Beszczynska-Moeller, B. Hansen, A. Lavin, H. Loeng, K. A. Mork, S. Osterhus, T. Sherwin and W. Walczowski. *Reversal of the 1960s to 1990s freshening trend in the northeast North Atlantic and Nordic Seas*. Geophys. Res. Lett., volume 35, no. 3, February 2008. ISSN 0094-8276. doi:10.1029/2007GL032675.

Hooke, R. L. *Principles of Glacier Mechanics* (Cambridge, 2005), 2nd edition, 763 pages.

Howat, I. M., J. E. Box, Y. Ahn, A. Herrington and E. M. McFadden. *Seasonal variability in the dynamics of marine-terminating outlet glaciers in Greenland*. J. Glaciol., volume 56, no. 198; pages 601–613, 2010. ISSN 0022-1430. doi:10.3189/002214310793146232.

Hulbe, C. L. and D. R. MacAyeal. *A new numerical model of coupled inland ice sheet, ice stream, and ice shelf flow and its application to the West Antarctic Ice Sheet.* J. Geophys. Res., volume 104, no. B11; pages 25 349–25 366, NOV 10 1999. ISSN 0148-0227.

Hutter, K. *Theoretical glaciology: material science of ice and the mechanics of glaciers and ice sheets* (D. Reidel Publishing Co, Dordrecht, The Netherlands, 1983), 150 pages.

Huybrechts, P. and J. de Wolde. *The dynamic response of the Greenland and Antarctic ice sheets to multiple-century climatic warming.* J. Clim., volume 12, no. 8, Part 1; pages 2169–2188, AUG 1999. ISSN 0894-8755.

James, T. D., T. Murray, N. Selmes, K. Scharrer and M. OLeary. *Buoyant flexure and basal crevassing in dynamic mass loss at helheim glacier.* Nature Geosci., volume 7, no. 8; pages 593–596, 2014.

Jenkins, A. *Convection-Driven Melting near the Grounding Lines of Ice Shelves and Tidewater Glaciers.* J. Phys. Oceanogr., 2011. doi:10.1175/JPO-D-11-03.1.

Jenkins, A., P. Dutrieux, S. Jacobs, S. McPhail, J. Perrett, A. Webb and D. White. *Observations beneath Pine Island Glacier in West Antarctica and implications for its retreat.* Nat. Geosci., volume 3; pages 468–472, 2010.

Jezek, K. C. *A modified theory of bottom crevasses used as a means for measuring the buttressing effect of ice shelves on inland ice sheets.* J. Geophys. Res., volume 89, no. B3; pages 1925–1931, 1984. ISSN 0148-0227.

Joughin, I., B. E. Smith, I. M. Howat, T. Scambos and T. Moon. *Greenland flow variability from ice-sheet-wide velocity mapping.* J. Glaciol., volume 56; pages 416–430, 2010.

Khan, S. A., K. H. Kjaer, M. Bevis, J. L. Bamber, J. Wahr, K. K. Kjeldsen, A. A. Bjork, N. J. Korsgaard, L. A. Stearns, M. R. van den Broeke, L. Liu, N. K. Larsen and I. S. Muresan. *Sustained mass loss of the northeast Greenland ice sheet triggered by regional warming.* Nat. Clim. Change, volume 4, no. 4; pages 292–299, APR 2014. ISSN 1758-678X. doi:10.1038/NCLIMATE2161.

Khazendar, A., I. G. Fenty, D. Carroll, A. Gardner, C. M. Lee, I. Fukumori, O. Wang, H. Zhang, H. Seroussi, D. Moller, B. P. Y. Noel, M. R. van den Broeke, S. Dinardo and J. Willis. *Interruption of two decades of Jakobshavn Isbrae acceleration and thinning as regional ocean cools.* Nat. Geosci., volume 12; pages 277–283, 2019. doi:10.1038/s41561-019-0329-3.

Krug, J., J. Weiss, O. Gagliardini and G. Durand. *Combining damage and fracture mechanics to model calving.* Cryosphere, volume 8, no. 6; pages 2101–2117, 2014. ISSN 1994-0424. doi:10.5194/tc-8-2101-2014.

Larour, E., H. Seroussi, M. Morlighem and E. Rignot. *Continental scale, high order, high spatial resolution, ice sheet modeling using the Ice Sheet System Model (ISSM).* J. Geophys. Res., volume 117, no. F01022; pages 1–20, Mar 2012. doi:10.1029/2011JF002140.

Lenaerts, J. T. M., M. R. van den Broeke, W. J. van de Berg, E. van Meijgaard and P. K. Munneke. *A new, high-resolution surface mass balance map of Antarctica (1979-2010) based on regional atmospheric climate modeling.* Geophys. Res. Lett., volume 39; pages 1–5, Feb 21 2012. ISSN 0094-8276. doi:10.1029/2011GL050713.

Levermann, A., T. Albrecht, R. Winkelmann, M. A. Martin, M. Haseloff and I. Joughin. *Kinematic first-order calving law implies potential for abrupt ice-shelf retreat.* Cryosphere, volume 6; pages 273–286, 2012.

Ma, Y. and J. N. Bassis. *The effect of submarine melting on calving from marine terminating glaciers.* Journal of Geophysical Research Earth Surface, volume 124, no. 2; pages 334–346, February 2019. ISSN 2169-9003. doi:10.1029/2018JF004820.

MacAyeal, D. R. *Large-scale ice flow over a viscous basal sediment: Theory and application to Ice Stream B, Antarctica.* J. Geophys. Res., volume 94, no. B4; pages 4071–4087, APR 10 1989. ISSN 0148-0227.

MacAyeal, D. R. *The basal stress distribution of Ice Stream E, Antarctica, Inferred by Control Methods.* J. Geophys. Res., volume 97, no. B1; pages 595–603, JAN 10 1992. ISSN 0148-0227.

MacAyeal, D. R. *Binge/Purge oscillations of the Laurentide ice-sheet as a cause of the North-Atlantic's Heinrich events.* Paleoceanography, volume 8, no. 6; pages 775–784, DEC 1993. ISSN 0883-8305.

Mayer, C., N. Reeh, F. Jung-Rothenhausler, P. Huybrechts and H. Oerter. *The subglacial cavity and implied dynamics under Nioghalvfjerdsfjorden Glacier, NE-Greenland.* Geophys. Res. Lett., volume 27, no. 15; pages 2289–2292, Aug 1 2000. ISSN 0094-8276.

Moon, T., I. Joughin and B. Smith. *Seasonal to multiyear variability of glacier surface velocity, terminus position, and sea ice/ice melange in northwest Greenland.* J. Geophys. Res. - Earth Surface, volume 120, no. 5; pages 818–833, MAY 2015. ISSN 2169-9003. doi:10.1002/2015JF003494.

Moon, T., I. Joughin, B. Smith and I. Howat. *21st-Century Evolution of Greenland Outlet Glacier Velocities.* Science, volume 336, no. 6081; pages 576–578, May 4 2012. ISSN 0036-8075. doi:10.1126/science.1219985.

Morland, L. W. and R. Zainuddin. *Plane and radial ice-shelf flow with prescribed temperature profile.* In Veen, C.J. van der, and Oerlemans, J., eds. Dynamics of the West Antarctica Ice Sheet. Proceedings of a Workshop held in Utrecht, May 6-8, 1985. Dordrecht, D. Rediel Publishing Company, volume 117, no. 40; pages 117–140, 1987.

Morlighem, M., J. Bondzio, H. Seroussi, E. Rignot, E. Larour, A. Humbert and S.-A. Rebuffi. *Modeling of Store Gletscher's calving dynamics, West Greenland, in response to ocean thermal forcing.* Geophys. Res. Lett., volume 43, no. 6; pages 2659–2666, 2016. ISSN 1944-8007. doi:10.1002/2016GL067695.

Morlighem, M., E. Rignot, T. Binder, D. Blankenship, R. Drews, G. Eagles, O. Eisen, F. Ferraccioli, P. Fretwell, R. Forsberg, V. Goel, J. S. Greenbaum, G. H. Gudmundsson, J. Guo, V. Helm, C. Hofstede, I. Howat, A. Humbert, W. Jokat, N. B. Karlsson, W. S. Lee, K. Matsuoka, R. Millan, J. Mouginot, J. Paden, F. Pattyn, J. Roberts, S. H. R. Rosier, A. Ruppel, H. Seroussi, B. E. Smith, D. Steinhage, B. Sun, M. R. van den Broeke, T. D. van Ommen, J. M. Van Wessem and D. A. Young. *Deep glacial troughs and stabilizing ridges unveiled beneath the margins of the Antarctic ice sheet*. Nat. Geosci., 2019a. doi: 10.1038/s41561-019-0510-8.

Morlighem, M., E. Rignot, J. Mouginot, H. Seroussi and E. Larour. *High-resolution ice thickness mapping in South Greenland*. Ann. Glaciol., volume 55, no. 67; pages 64–70, 2014. ISSN 0260-3055. doi:10.3189/2014AoG67A088.

Morlighem, M., E. Rignot, H. Seroussi, E. Larour, H. Ben Dhia and D. Aubry. *Spatial patterns of basal drag inferred using control methods from a full-Stokes and simpler models for Pine Island Glacier, West Antarctica*. Geophys. Res. Lett., volume 37, no. L14502; pages 1–6, JUL 2010. doi:10.1029/2010GL043853.

Morlighem, M., H. Seroussi, E. Larour and E. Rignot. *Inversion of basal friction in Antarctica using exact and incomplete adjoints of a higher-order model*. J. Geophys. Res., volume 118, no. 3; pages 1746–1753, SEP 2013. ISSN 2169-9003. doi:10.1002/jgrf.20125.

Morlighem, M., C. N. Williams, E. Rignot, L. An, J. E. Arndt, J. L. Bamber, G. Catania, N. Chauché, J. A. Dowdeswell, B. Dorschel, I. Fenty, K. Hogan, I. Howat, A. Hubbard, M. Jakobsson, T. M. Jordan, K. K. Kjeldsen, R. Millan, L. Mayer, J. Mouginot, B. P. Y. Noël, C. O'Cofaigh, S. Palmer, S. Rysgaard, H. Seroussi, M. J. Siegert, P. Slabon, F. Straneo, M. R. van den Broeke, W. Weinrebe, M. Wood and K. B. Zinglersen. *BedMachine v3: Complete bed topography and ocean bathymetry mapping of Greenland from multi-beam echo sounding combined with mass conservation*. Geophys. Res. Lett., volume 44, no. 21; pages 11,051–11,061, 2017. ISSN 1944-8007. doi:10.1002/2017GL074954. 2017GL074954.

Morlighem, M., M. Wood, H. Seroussi, Y. Choi and E. Rignot. *Modeling the response of northwest Greenland to enhanced ocean thermal forcing and subglacial discharge*. Cryosphere, volume 13; pages 723–734, 2019b. doi:10.5194/tc-13-723-2019.

Mouginot, J., E. Rignot, A. A. Bjørk, M. van den Broeke, R. Millan, M. Morlighem, B. Noël, B. Scheuchl and M. Wood. *Forty-six years of greenland ice sheet mass balance from 1972 to 2018*. Proc. Natl. Acad. Sci., 2019. ISSN 0027-8424. doi:10.1073/pnas.1904242116.

Mouginot, J., E. Rignot, B. Scheuchl, I. Fenty, A. Khazendar, M. Morlighem, A. Buzzi and J. Paden. *Fast retreat of Zachariæ Isstrøm, northeast Greenland*. Science, volume 350, no. 6266; pages 1357–1361, DEC 11 2015. ISSN 0036-8075. doi:10.1126/science.aac7111.

Murray, T., K. Scharrer, N. Selmes, A. D. Booth, T. D. James, S. L. Bevan, J. Bradley, S. Cook, L. C. Llana, Y. Drocourt, L. Dyke, A. Goldsack, A. L. Hughes, A. J. Luckman and J. McGovern. *Extensive retreat of greenland tidewater glaciers, 2000-2010*. Arctic Ant. Alp. Res., volume 47, no. 3; pages 427–447, August 2015. ISSN 1523-0430. doi: 10.1657/AAAR0014-049.

Nick, F. M., A. Luckman, A. Vieli, C. J. Van Der Veen, D. Van As, R. S. W. Van De Wal, F. Pattyn, A. L. Hubbard and D. Floricioiu. *The response of Petermann Glacier, Greenland, to large calving events, and its future stability in the context of atmospheric and oceanic warming*. J. Glaciol., volume 58, no. 208; pages 229–239, 2012. ISSN 00221430.

Nick, F. M., C. J. van der Veen, A. Vieli and D. I. Benn. *A physically based calving model applied to marine outlet glaciers and implications for the glacier dynamics*. J. Glaciol., volume 56, no. 199; pages 781–794, 2010. ISSN 0022-1430.

Nick, F. M., A. Vieli, M. L. Andersen, I. Joughin, A. Payne, T. L. Edwards, F. Pattyn and R. S. W. van de Wal. *Future sea-level rise from Greenland's main outlet glaciers in a warming climate*. Nature, volume 497, no. 7448; pages 235–238, 2013. ISSN 0028-0836. doi:10.1038/nature12068.

Noël, B., W. J. van de Berg, E. van Meijgaard, P. K. Munneke, R. S. W. van de Wal and M. R. van den Broeke. *Evaluation of the updated regional climate model RACMO2.3: summer snowfall impact on the Greenland Ice Sheet*. Cryosphere, volume 9, no. 5; pages 1831–1844, 2015. ISSN 1994-0416. doi:10.5194/tc-9-1831-2015.

Nye, J. F. *Physical properties of crystals: Their representation by tensor and matrices* (Oxford University Press, 1957), first edition. ISBN 9780198511656.

Osher, S. and J. A. Sethian. *Fronts Propagating with Curvature-Dependent Speed - Algorithms Based on Hamilton-Jacobi Formulations*. J. Comput. Phys., volume 79, no. 1; pages 12–49, NOV 1988. ISSN 0021-9991.

Otero, J., F. J. Navarro, J. J. Lapazaran, E. Welty, D. Puczko and R. Finkelnburg. *Modeling the Controls on the Front Position of a Tidewater Glacier in Svalbard*. Front. Earth Sci., volume 5, April 2017. ISSN 2296-6463. doi:10.3389/feart.2017.00029.

Otero, J., F. J. Navarro, C. Martin, M. L. Cuadrado and M. I. Corcuera. *A three-dimensional calving model: numerical experiments on Johnsons Glacier, Livingston Island, Antarctica*. J. Glaciol., volume 56, no. 196; pages 200–214, 2010. ISSN 0022-1430.

Pachauri, R. K., M. R. Allen, V. R. Barros, J. Broome, W. Cramer, R. Christ, J. A. Church, L. Clarke, Q. Dahe, P. Dasgupta, N. K. Dubash, O. Edenhofer, I. Elgizouli, C. B. Field, P. Forster, P. Friedlingstein, J. Fuglestvedt, L. Gomez-Echeverri, S. Hallegatte, G. Hegerl, M. Howden, K. Jiang, B. Jimenez Cisneroz, V. Kattsov, H. Lee, K. J. Mach, J. Marotzke, M. D. Mastrandrea, L. Meyer, J. Minx, Y. Mulugetta, K. O'Brien, M. Oppenheimer, J. J. Pereira, R. Pichs-Madruga, G. K. Plattner, H.-O. Pörtner, S. B. Power, B. Preston, N. H. Ravindranath, A. Reisinger, K. Riahi, M. Rusticucci, R. Scholes, K. Seyboth, Y. Sokona, R. Stavins, T. F. Stocker, P. Tschakert, D. van Vuuren and J. P. van Ypserle. *Climate Change 2014: Synthesis Report. Contribution of Working Groups I, II and III to the Fifth Assessment Report of the Intergovernmental Panel on Climate Change*. EPIC3Geneva, Switzerland, IPCC, 151 p., pp. 151, ISBN: 978-92-9169-143-2, 2014.

Paterson, W. S. B. *The Physics of Glaciers* (Pergamon Press, Oxford, London, New York, 1994), 3rd edition.

Pattyn, F. *A new three-dimensional higher-order thermomechanical ice sheet model: Basic sensitivity, ice stream development, and ice flow across subglacial lakes.* J. Geophys. Res., volume 108, no. B8; pages 1–15, AUG 16 2003. ISSN 0148-0227. doi: 10.1029/2002JB002329.

Pattyn, F., L. Perichon, G. Durand, L. Favier, O. Gagliardini, R. C. A. Hindmarsh, T. Zwinger, T. Albrecht, S. Cornford, D. Docquier, J. Fuerst, D. Goldberg, H. Gudmundsson, A. Humbert, M. Hutten, P. Huybrecht, G. Jouvet, T. Kleiner, E. Larour, D. Martin, M. Morlighem, A. Payne, D. Pollard, M. Ruckamp, O. Rybak, H. Seroussi, M. Thoma and N. Wilkens. *Grounding-line migration in plan-view marine ice-sheet models: results of the ice2sea MISMIP3d intercomparison.* J. Glaciol., volume 59 (215); pages 410–422, 2013. doi:10.3189/2013JoG12J129.

Petrovic, J. J. *Review Mechanical properties of ice and snow.* J. Mater. Sci., volume 38, no. 1; pages 1–6, 2003. ISSN 0022-2461. doi:10.1023/A:1021134128038.

Pralong, A. and M. Funk. *Dynamic damage model of crevasse opening and application to glacier calving.* J. Geophys. Res., volume 110, no. B01309; pages 1–12, 2005. doi: 10.1029/2004JB003104.

Price, S. F., A. J. Payne, I. M. Howat and B. E. Smith. *Committed sea-level rise for the next century from Greenland ice sheet dynamics during the past decade.* P. Natl. Acad. Sci. USA, volume 108, no. 22; pages 8978–8983, 2011.

Pritchard, H. D., R. J. Arthern, D. G. Vaughan and L. A. Edwards. *Extensive dynamic thinning on the margins of the Greenland and Antarctic ice sheets.* Nature, volume 461; pages 971–975, 2009. doi:10.1038/nature08471.

Reeh, N. *On the calving of ice from floating glaciers and ice shelves.* J. Glaciol., volume 7, no. 50; pages 215–232, 1968.

Reist, A. *Mathematical analysis and numerical simulation of the motion of a glacier.* Ph.D. thesis, Ecole Polytechnique Fédérale de Lausanne, 2005.

Rietbroek, R., S.-E. Brunnabend, J. Kusche, J. Schroeter and C. Dahle. *Revisiting the contemporary sea-level budget on global and regional scales.* Proc. Natl. Acad. Sci., volume 113, no. 6; pages 1504–1509, February 2016. ISSN 0027-8424. doi:10.1073/pnas.1519132113.

Rignot, E., I. Fenty, D. Menemenlis and Y. Xu. *Spreading of warm ocean waters around Greenland as a possible cause for glacier acceleration.* Ann. Glaciol., volume 53, no. 60, 2; pages 257–266, 2012. ISSN 0260-3055. doi:10.3189/2012AoG60A136.

Rignot, E., I. Fenty, Y. Xu, C. Cai and C. Kemp. *Undercutting of marine-terminating glaciers in West Greenland.* Geophys. Res. Lett., volume 42, no. 14; pages 5909–5917, JUL 28 2015. ISSN 0094-8276. doi:10.1002/2015GL064236.

Rignot, E. and P. Kanagaratnam. *Changes in the velocity structure of the Greenland ice sheet.* Science, volume 311, no. 5763; pages 986–990, FEB 17 2006. ISSN 0036-8075. doi:10.1126/science.1121381.

Rignot, E., M. Koppes and I. Velicogna. *Rapid submarine melting of the calving faces of West Greenland glaciers*. Nat. Geosci., volume 3, no. 3; pages 187–191, MAR 2010. ISSN 1752-0894. doi:10.1038/NGEO765.

Rignot, E. and J. Mouginot. *Ice flow in Greenland for the International Polar Year 2008-2009*. Geophys. Res. Lett., volume 39, L11501; pages 1–7, JUN 2 2012. doi:10.1029/2012GL051634.

Rignot, E., Y. Xu, D. Menemenlis, J. Mouginot, B. Scheuchl, X. Li, M. Morlighem, H. Seroussi, M. v. den Broeke, I. Fenty, C. Cai, L. An and B. de Fleurian. *Modeling of ocean-induced ice melt rates of five West Greenland glaciers over the past two decades*. Geophys. Res. Lett., volume 43, no. 12; pages 6374–6382, JUN 28 2016. ISSN 0094-8276. doi:10.1002/2016GL068784. 2016GL068784.

Schoof, C. *Ice sheet grounding line dynamics: Steady states, stability, and hysteresis*. J. Geophys. Res., volume 112, no. F03S28; pages 1–19, JUL 14 2007. ISSN 0148-0227. doi:10.1029/2006JF000664.

Seale, A., P. Christoffersen, R. I. Mugford and M. O'Leary. *Ocean forcing of the Greenland Ice Sheet: Calving fronts and patterns of retreat identified by automatic satellite monitoring of eastern outlet glaciers*. J. Geophys. Res., volume 116; pages 1–16, AUG 23 2011. ISSN 0148-0227. doi:10.1029/2010JF001847.

Seroussi, H., M. Morlighem, E. Larour, E. Rignot and A. Khazendar. *Hydrostatic grounding line parameterization in ice sheet models*. Cryosphere, volume 8, no. 6; pages 2075–2087, Nov. 2014a. ISSN 1994-0416. doi:10.5194/tc-8-2075-2014.

Seroussi, H., M. Morlighem, E. Rignot, A. Khazendar, E. Larour and J. Mouginot. *Dependence of century-scale projections of the Greenland ice sheet on its thermal regime*. J. Glaciol., volume 59, no. 218; pages 1024–1034, 2013. ISSN 0022-1430. doi:10.3189/2013JoG13J054.

Seroussi, H., M. Morlighem, E. Rignot, J. Mouginot, E. Larour, M. P. Schodlok and A. Khazendar. *Sensitivity of the dynamics of Pine Island Glacier, West Antarctica, to climate forcing for the next 50 years*. Cryosphere, volume 8, no. 5; pages 1699–1710, 2014b. doi:10.5194/tc-8-1699-2014.

Slater, D., P. Nienow, D. Goldberg, T. Cowton and A. Sole. *A model for tidewater glacier undercutting by submarine melting*. Geophys. Res. Lett., volume 44, no. 5; pages 2360–2368, 2017.

Slater, D. A., F. Straneo, S. B. Das, C. G. Richards, T. J. W. Wagner and P. W. Nienow. *Localized plumes drive front-wide ocean melting ofa Greenlandic tidewaterglacier*. Geophys. Res. Lett., volume 45; pages 12,350–12,358, 2018. doi:10.1029/2018GL080763.

Straneo, F., G. S. Hamilton, D. A. Sutherland, L. A. Stearns, F. Davidson, M. O. Hammill, G. B. Stenson and A. Rosing-Asvid. *Rapid circulation of warm subtropical waters in a major glacial fjord in East Greenland*. Nat. Geosci., volume 3, no. 3; pages 182–186, MAR 2010. ISSN 1752-0894. doi:10.1038/NGEO764.

Straneo, F. and P. Heimbach. *North Atlantic warming and the retreat of Greenland's outlet glaciers*. Nature, volume 504; pages 36–43, 2013. doi:10.1038/nature12854.

Straneo, F., P. Heimbach, O. Sergienko, G. Hamilton, G. Catania, S. Griffies, R. Hallberg, A. Jenkins, I. Joughin, R. Motyka, W. T. Pfeffer, S. F. Price, E. Rignot, T. Scambos, M. Truffer and A. Vieli. *Challenges to Understanding the Dynamic Response of Greenland's Marine Terminating Glaciers to Oceanic and Atmospheric Forcing*. Bull. Amer. Meteorol. Soc., volume 94, no. 8; pages 1131–1144, AUG 2013. ISSN 0003-0007. doi: 10.1175/BAMS-D-12-00100.1.

Todd, J., P. Christoffersen, T. Zwinger, P. Raback, N. Chauché, D. Benn, A. Luckman, J. Ryan, N. Toberg, D. Slater and A. Hubbard. *A Full-Stokes 3-D Calving Model Applied to a Large Greenlandic Glacier*. J. Geophys. Res. - Earth Surface, volume 123, no. 3; pages 410–432, March 2018. ISSN 2169-9003. doi:10.1002/2017JF004349.

van der Veen, C. J. *Fracture mechanics approach to penetration of surface crevasses on glaciers*. Cold Reg. Sci. Technol., volume 27, no. 1; pages 31–47, 1998. ISSN 0165-232X.

van der Veen, C. J. *Calving glaciers*. Prog. Phys. Geogr., volume 26, no. 1; pages 96–122, March 2002. ISSN 0309-1333. doi:10.1191/0309133302pp327ra.

Vieli, A., M. Funk and H. Blatter. *Flow dynamics of tidewater glaciers: a numerical modelling approach*. J. Glaciol., volume 47, no. 159; pages 595–606, 2001. ISSN 0022-1430. doi:10.3189/172756501781831747.

Vieli, A., J. Jania and L. Kolondra. *The retreat of a tidewater glacier: observations and model calculations on Hansbreen, Spitsbergen*. J. Glaciol., volume 48, no. 163; pages 592–600, 2002. ISSN 0022-1430. doi:10.3189/172756502781831089.

Vieli, A. and F. M. Nick. *Understanding and modelling rapid dynamic changes of tidewater outlet glaciers: Issues and implications*. Surv. Geophys., volume 32, no. 4-5; pages 437–458, 2011.

Wagner, T. J., T. D. James, T. Murray and D. Vella. *On the role of buoyant flexure in glacier calving*. Geophys. Res. Lett., volume 43, no. 1; pages 232–240A, 2016.

Weertman, J. *On the sliding of glaciers*. J. Glaciol., volume 3; pages 33–38, March 1957.

Weertman, J. *Stability of the junction of an ice sheet and an ice shelf*. J. Glaciol., volume 13(67); pages 3–11, 1974.

Wilson, N. J. and F. Straneo. *Water exchange between the continental shelf and the cavity beneath Nioghalvfjerdsbrae (79 North Glacier)*. Geophys. Res. Lett., volume 42, no. 18; pages 7648–7654, September 2015. ISSN 0094-8276. doi:10.1002/2015GL064944.

Wood, M., E. Rignot, I. Fenty, D. Menemenlis, R. Millan, M. Morlighem, J. Mouginot and H. Seroussi. *Ocean-induced melt triggers glacier retreat in Northwest Greenland*. Geophys. Res. Lett., volume 45, no. 16; pages 8334–8342, 2018. doi:10.1029/2018GL078024.

Xu, Y., E. Rignot, I. Fenty, D. Menemenlis and M. M. Flexas. *Subaqueous melting of Store Glacier, west Greenland from three-dimensional, high-resolution numerical modeling and ocean observations*. Geophys. Res. Lett., volume 40, no. 17; pages 4648–4653, SEP 16 2013. ISSN 0094-8276. doi:10.1002/grl.50825.

Xu, Y., E. Rignot, D. Menemenlis and M. Koppes. *Numerical experiments on subaqueous melting of Greenland tidewater glaciers in response to ocean warming and enhanced subglacial discharge*. Ann. Glaciol., volume 53, no. 60; pages 229–234, Nov 2012 2012. doi:10.3189/2012AoG60A139.

Yin, J., J. T. Overpeck, S. M. Griffies, A. Hu, J. L. Russell and R. J. Stouffer. *Different magnitudes of projected subsurface ocean warming around Greenland and Antarctica*. Nat. Geosci., volume 4, no. 8; pages 524–528, AUG 2011. ISSN 1752-0894. doi: 10.1038/NGEO1189.

Appendix A

Supporting Information for "Chapter 6. Contribution of the Greenland ice sheet to sea level over the next century with a new generation model"

A.1 Retreat calibration

Table A.1: Observed and modeled ice front retreat (in km along a centerline) during the calibration period (2007-2017) for SW region. Grey represents the glacier that has poorly constrained bed topography, blue shows underestimated retreat and red shows overestimated retreat.

Glacier name	Retreat distance (km) Observed	Modeled
Akullersuup	**-0.251**	**-0.0331**
Avannarleq	x	x
EqalorutsitKangilliit	-0.224	3.41
EqalorutsitKilliit	x	x
EqalorutsitKilliitE	x	x
KangiataNunaata	**-0.472**	**-0.509**
Naajat	x	x
Nakkaasorsuaq	x	x
Narsap	**4.22**	**4.23**
Nigerlikasik	x	x
Qooqqup	**0**	**0.422**
Sermeq	x	x
Sermiligaarsuup	x	x
Sermilik	x	x
Ukaasorsuaq	**0**	**0.187**

Table A.2: Same as Table A.1 but for CW region

Glacier name	Retreat distance (km) Observed	Modeled
Alangorliup	**0**	**0.673**
EqipSermia	**2.09**	**2.11**
Innigia	**5.83**	**5.81**
Jakobshavn (N. branch)	**2.83**	**2.57**
Jakobshavn (S. branch)	**2.355**	**2.701**
Kangerluarsuup	0.806	0.08
Kangerlussuup	**0**	**0.051**
Kangilernata	**1.57**	**1.52**
Kangilleq	**-0.534**	**-0.0642**
Kujalleq	**-0.701**	**-0.787**
Lille	**0.794**	**0.589**
Perlerfiup	**3.07**	**3.32**
RinkIsbrae	0.612	1.62
Saqqarliup	0.842	-0.01
SermeqAvannarleq	**-0.0754**	**-0.011**
SermeqSilarleq	**4.24**	**3.87**
Sermilik	**-0.279**	**-0.252**
Store	**0**	**0.0401**
Ummiammakku	**0.517**	**0.481**

Table A.3: Same as Table A.1 but for NW region

Glacier name	Retreat distance (km) Observed	Modeled
Alison	**3.17**	**3.93**
Bowdoin	1.46	0.0201
Carlos	**0.303**	**-0.118**
CarlosW	x	x
Cornell	**0.78**	**0.78**
CornellN	**0.633**	**0.429**
Dietrisch	x	x
Dietrichson	**1.81**	**1.68**
DockerSmith (N.branch)	**1.42**	**0.731**
DockerSmith (S.branch)	0.927	2.75
DockerSmithW	**0.502**	**1.24**
Farquhar	**0.334**	**0.498**
Gade	**0**	**0.0101**
HaraldMoltke	1.26	-0.325
Hart	x	x
Hayes	1.25	0.204
HayesM	**-0.21**	**0.0413**
HayesN	**-0.157**	**-0.0514**
HayesNN	**0.182**	**0.83**
HayesNorth	**-0.101**	**0.0208**
HayesSS	**2.42**	**2.86**
Heilprin	**0.478**	**0.497**
Helland	1.52	0.418
HellandE	**0.783**	**0.0602**
HellandW	x	x
Hubbard	x	x
Illullip	**1.07**	**0.197**
Issuusarsuit	**0.28**	**1.02**
Kakivfaat	**3.51**	**3.45**
Kjer	**6.61**	**6.5**
KjerN	1.7	0.445
KongOscar	**-0.0101**	**0.0105**
Leidy	x	x
Melville	**0.0828**	**0.0828**
Mohn	**0.895**	**0.231**
MorrisJesup	**0.982**	**-0.0309**
Nansen	**2.85**	**3.01**
NansenS	**0**	**0.531**
Nordenskiold	**4.37**	**4.55**
NordenskioldN	**0.452**	**0.697**
Nunatakassaap	**0**	**-0.02**
OscarN	**2.02**	**1.95**
OscarNN	**0.597**	**0.512**
Qeqertarsuup	**0.918**	**0.854**
RinkGletscher (N.branch)	**0.176**	**0.145**
RinkGletscher (S.branch)	**0.126**	**0.33**
RinkGletscherS	**0**	**0.053**
Savissuaq	4.17	1.19
SavissuaqW	1.24	0.172

SavissuaqWW	1.37	0.309
SavissuaqWWW	0.962	-0.0207
SavissuaqWWWW	**2.25**	**2.13**
Sharp	x	x
Steenstrup	**1.71**	**1.31**
Sverdrup	**3.52**	**3.49**
Tracy	**2.75**	**2.7**
UpernavikIsstromC	**2.95**	**2.82**
UpernavikIsstromN	3.53	1.34
UpernavikIsstromNW	**0.804**	**0.556**
UpernavikIsstromS	**0.293**	**0.246**
UpernavikIsstromSS	**0.896**	**0.633**
UssingBraeer	**0.363**	**0.341**
UssingBraeerN	-0.431	0.845
Verhoeff	x	x
YngvarNielsen	3.49	0.478
YngvarNielsenW	**0.0104**	**0.0104**

Table A.4: Same as Table A.1 but for NO region

Glacier name	Retreat distance (km)	
	Observed	Modeled
Academy	**0**	**0.14**
Adams	x	x
CHOstenfeld	**1.5**	**1.42**
Dodge	x	x
Hagen	0.57	-0.253
Harder	**0.172**	**0**
Humboldt	**2.11**	**2.08**
Jungersen	x	x
MarieSophie	**-0.0601**	**0.201**
Naravana	x	x
Newmann	x	x
Petermann	24.1	0
Ryder	**-0.505**	**-0.291**
Steensby	12.4	-0.153

Table A.5: Same as Table A.1 but for NE region

Glacier name	Retreat distance (km)	
	Observed	Modeled
79North	1.25	-0.0804
Charcot	x	x
DaugaardJensen	**1.62**	**1.7**
Eielson	x	x
FGraae	0.384	2.17
GerarddeGeer	**0**	**0.0825**
Heinkel	x	x
Hisinger	x	x
Jaette	x	x

Kofoed	0.291	2.68
Nordenskiold	x	x
Nunatak	x	x
Rolige	0	1.11
Soranerbraeen	x	x
Storstrommen	4.33	-0.23
Vestfjord	**0.433**	**0.436**
Waltershausen	**0**	**0**
Zachariae	**11.6**	**11.9**

Table A.6: Same as Table A.1 but for SE region

Glacier name	Retreat distance (km) Observed	Modeled
APBernstorff	**0.623**	**0.618**
AnorituupKangerlua	**0.159**	**0.254**
AnorituupKangerluaS	**0**	**0.0212**
Apuseeq	1.27	-0.152
ApuseeqN	x	x
Apuseerajik	1.59	0.0802
Borggraven	x	x
Brede	x	x
Courtauld	x	x
Danell	**0**	**0.0651**
DanellS	**0.584**	**0.561**
DanellSS	**0.394**	**-0.0511**
DanellSSS	x	x
DeceptionOCN	**1.44**	**1.19**
DeceptionOCS	**0.29**	**0.416**
Dendrit	**1.17**	**1.27**
DendritS	**1.49**	**0.742**
Fimbul	x	x
Frederiksborg	**0.298**	**0.294**
Graulv	**0.353**	**0.321**
GraulvE	x	x
GyldenloveN	**1.76**	**1.72**
GyldenloveS	**1.86**	**1.19**
Heimdal	**-0.0101**	**-0.0227**
Helheim	**0.414**	**0.434**
HerlufTrolleN	**-0.184**	**0.131**
HerlufTrolleS	**0.501**	**1.37**
IkertivaqM	**0.173**	**0.848**
IkertivaqN	**0.441**	**0.492**
IkertivaqNN	**1.16**	**0.674**
IkertivaqS	**0.395**	**0.419**
KIVSteenstrup	**0.549**	**0.561**
Kaarale	x	x
Kangerluluk	x	x
Kangerlussuaq	**2.06**	**3.03**
Kangertivala	x	x
Kangertsivala	x	x
KistaDan	**-0.486**	**-0.0709**

KistaDanW	**0.232**	**0.131**
KnudRasmussen	x	x
KnudRasmussenW	x	x
KogeBugtC	1.29	0.338
KogeBugtN	**-0.173**	**-0.0873**
KogeBugtS	**-0.158**	**-0.0105**
KogeBugtSS	x	x
KongChristianIV	**0**	**0.802**
Kronborg	x	x
Kruuse	**0**	**-0.162**
Laube	x	x
LaubeN	x	x
LaubeS	x	x
Maelkevejen	x	x
MaggaDan	**0**	**0.0306**
MogensHeinesenC	0.608	1.63
MogensHeinesenN	**1.56**	**1.55**
MogensHeinesenS	1.92	1.08
MogensHeinesenSS	x	x
MogensHeinesenSSS	**0.351**	**0.343**
Mone	x	x
Nakkaagajik	x	x
NapasorsuaqC	x	x
NapasorsuaqN	**0**	**0.103**
NapasorsuaqS	x	x
NapasorsuaqSS	x	x
Nigertiip	7.54	5.81
Nordfjord	x	x
OstreBorg	x	x
Polaric	**-0.138**	**0.214**
PolaricS	x	x
PuisortoqC	-1.93	-0.56
PuisortoqN	**0.262**	**0.26**
PuisortoqS	**1.34**	**2.32**
Rimfaxe	**-0.303**	**-0.18**
Rosenborg	x	x
Skinfaxe	**0**	**-0.0623**
Sondre	x	x
Sorgenfri	**0.141**	**0.133**
Sortebrae	x	x
Styrte	x	x
Sydbrae	x	x
Thrym	x	x
Tingmiarmiut	**1.55**	**1.6**
TingmiarmiutS	x	x
TorvS	x	x
TorvSS	x	x
Uunartit	2.31	0.127

A.2 Details on glaciers

This section includes details on calibration and future projection result under MIROC5 RCP8.5 for each glacier. (a) observed velocity, (b) modeled velocity, (c) observed thinning rate, (d) modeled thinning rate, (e) cumulative SMB, discharge and mass balance for projection, (f) observed ice fronts, (g) modeled ice fronts between 2007 and 2100. They are sored in the same order as the retreat calibration tables in Appendix A.1.

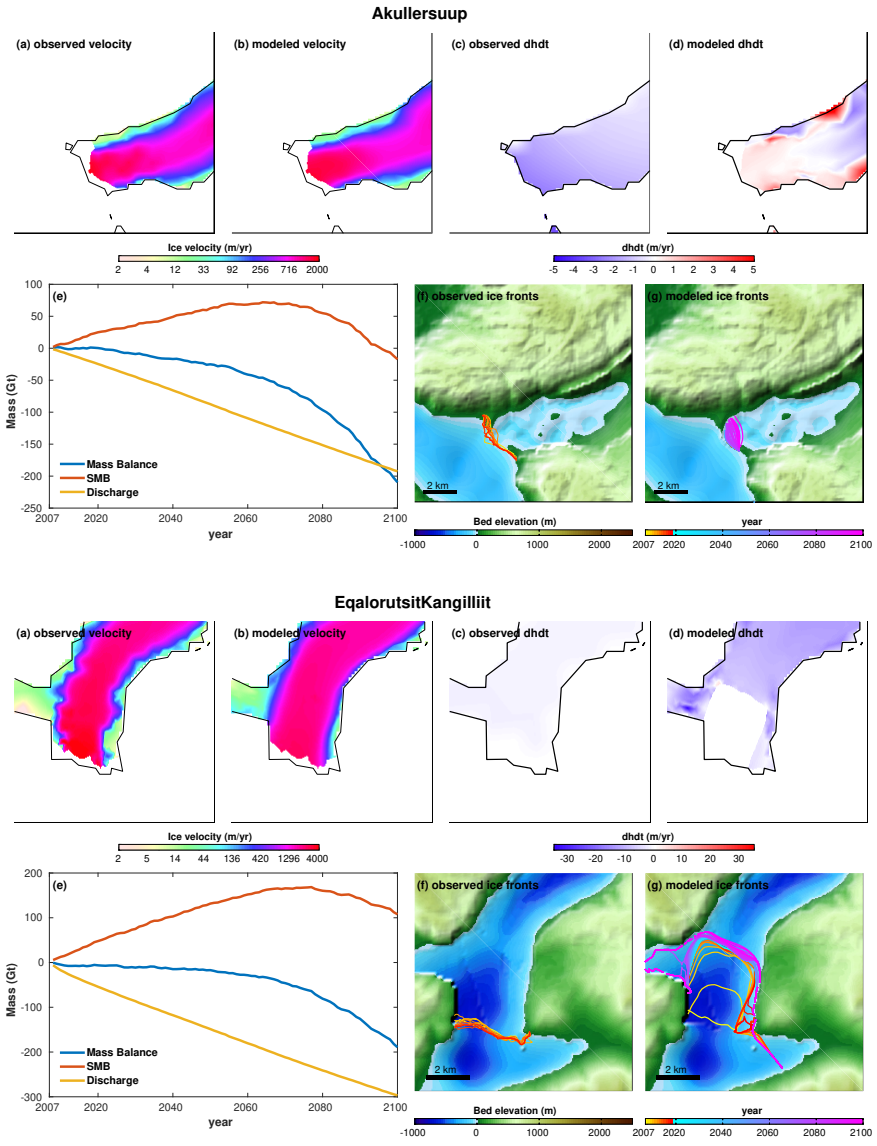
Akullersuup
(a) observed velocity
(b) modeled velocity
(c) observed dhdt
(d) modeled dhdt
Ice velocity (m/yr)
2 4 12 33 92 256 716 2000
dhdt (m/yr)
-5 -4 -3 -2 -1 0 1 2 3 4 5
(e)
Mass (Gt)
Mass Balance
SMB
Discharge
year
(f) observed ice fronts
(g) modeled ice fronts
2 km
Bed elevation (m)
-1000 0 1000 2000
year
2007 2020 2040 2060 2080 2100
EqalorutsitKangilliit
(a) observed velocity
(b) modeled velocity
(c) observed dhdt
(d) modeled dhdt
Ice velocity (m/yr)
2 5 14 44 136 420 1296 4000
dhdt (m/yr)
-30 -20 -10 0 10 20 30
(e)
Mass (Gt)
Mass Balance
SMB
Discharge
year
(f) observed ice fronts
(g) modeled ice fronts
2 km
Bed elevation (m)
-1000 0 1000 2000
year
2007 2020 2040 2060 2080 2100

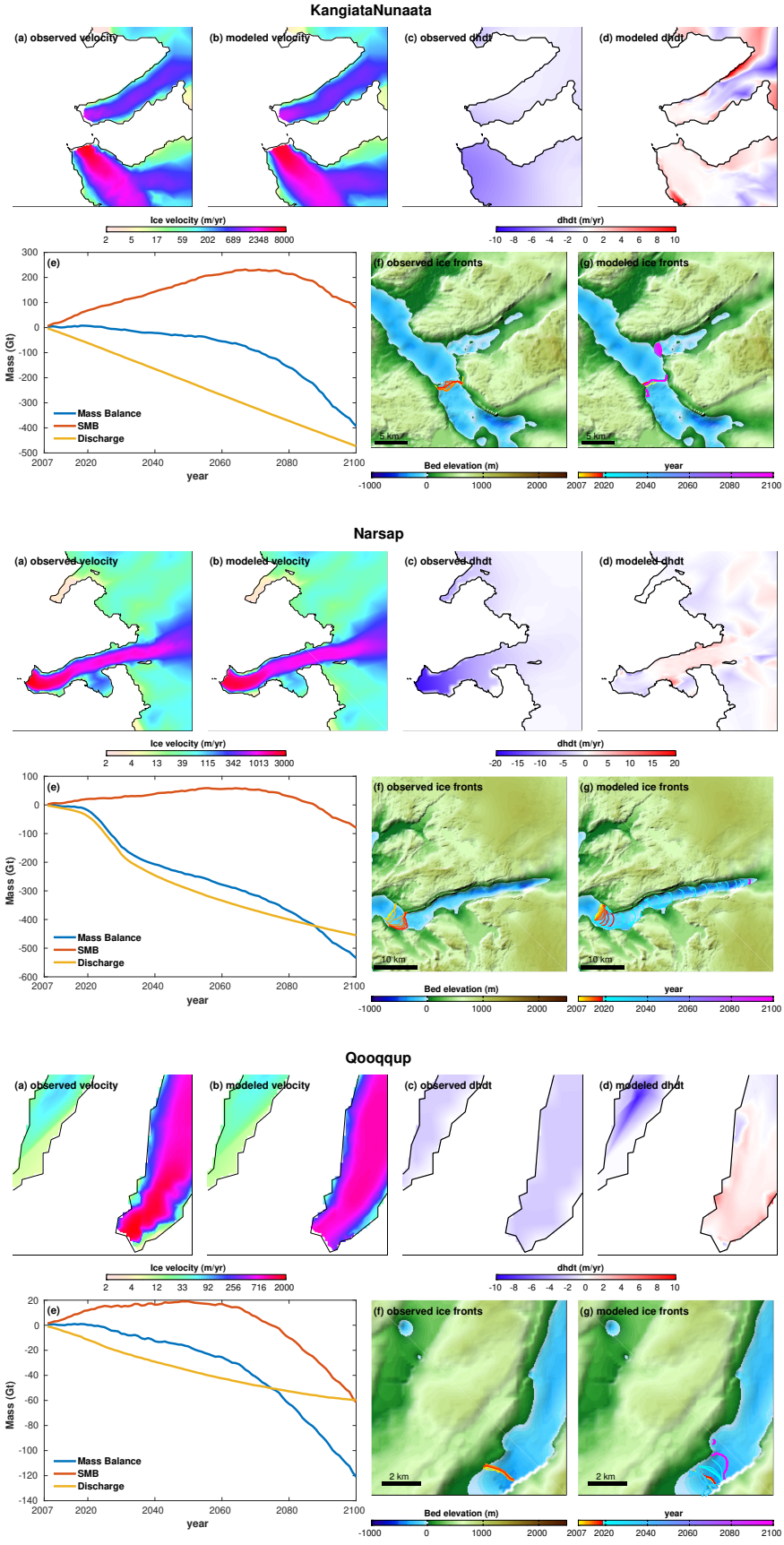
KangiataNunaata
(a) observed velocity
(b) modeled velocity
(c) observed dhdt
(d) modeled dhdt
Ice velocity (m/yr)
2 5 17 59 202 689 2348 8000
dhdt (m/yr)
-10 -8 -6 -4 -2 0 2 4 6 8 10
(e)
Mass (Gt)
Mass Balance
SMB
Discharge
year
(f) observed ice fronts
(g) modeled ice fronts
5 km
Bed elevation (m)
-1000 0 1000 2000
year
2007 2020 2040 2060 2080 2100
Narsap
(a) observed velocity
(b) modeled velocity
(c) observed dhdt
(d) modeled dhdt
Ice velocity (m/yr)
2 4 13 39 115 342 1013 3000
dhdt (m/yr)
-20 -15 -10 -5 0 5 10 15 20
(e)
Mass (Gt)
Mass Balance
SMB
Discharge
year
(f) observed ice fronts
(g) modeled ice fronts
10 km
Bed elevation (m)
-1000 0 1000 2000
year
2007 2020 2040 2060 2080 2100
Qooqqup
(a) observed velocity
(b) modeled velocity
(c) observed dhdt
(d) modeled dhdt
Ice velocity (m/yr)
2 4 12 33 92 256 716 2000
dhdt (m/yr)
-10 -8 -6 -4 -2 0 2 4 6 8 10
(e)
Mass (Gt)
Mass Balance
SMB
Discharge
year
(f) observed ice fronts
(g) modeled ice fronts
2 km
Bed elevation (m)
-1000 0 1000 2000
year
2007 2020 2040 2060 2080 2100

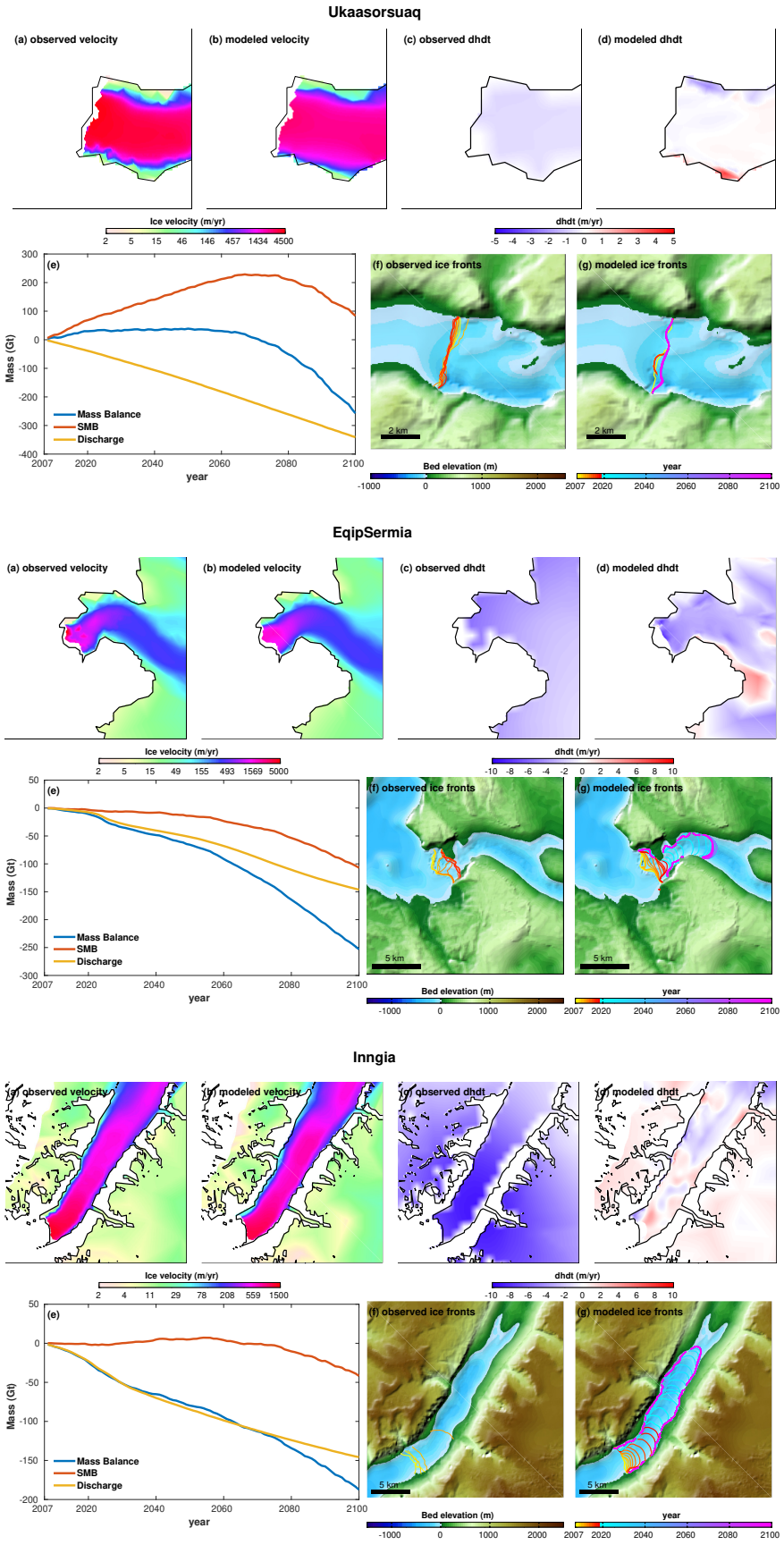
Ukaasorsuaq
(a) observed velocity
(b) modeled velocity
(c) observed dhdt
(d) modeled dhdt
Ice velocity (m/yr)
2 5 15 46 146 457 1434 4500
dhdt (m/yr)
-5 -4 -3 -2 -1 0 1 2 3 4 5
(e)
Mass (Gt)
Mass Balance
SMB
Discharge
year
(f) observed ice fronts
(g) modeled ice fronts
2 km
Bed elevation (m)
-1000 0 1000 2000
year
2007 2020 2040 2060 2080 2100
EqipSermia
(a) observed velocity
(b) modeled velocity
(c) observed dhdt
(d) modeled dhdt
Ice velocity (m/yr)
2 5 15 49 155 493 1569 5000
dhdt (m/yr)
-10 -8 -6 -4 -2 0 2 4 6 8 10
(e)
Mass (Gt)
Mass Balance
SMB
Discharge
year
(f) observed ice fronts
(g) modeled ice fronts
5 km
Bed elevation (m)
-1000 0 1000 2000
year
2007 2020 2040 2060 2080 2100
Inngia
(a) observed velocity
(b) modeled velocity
(c) observed dhdt
(d) modeled dhdt
Ice velocity (m/yr)
2 4 11 29 78 208 559 1500
dhdt (m/yr)
-10 -8 -6 -4 -2 0 2 4 6 8 10
(e)
Mass (Gt)
Mass Balance
SMB
Discharge
year
(f) observed ice fronts
(g) modeled ice fronts
5 km
Bed elevation (m)
-1000 0 1000 2000
year
2007 2020 2040 2060 2080 2100

Jakobshavn

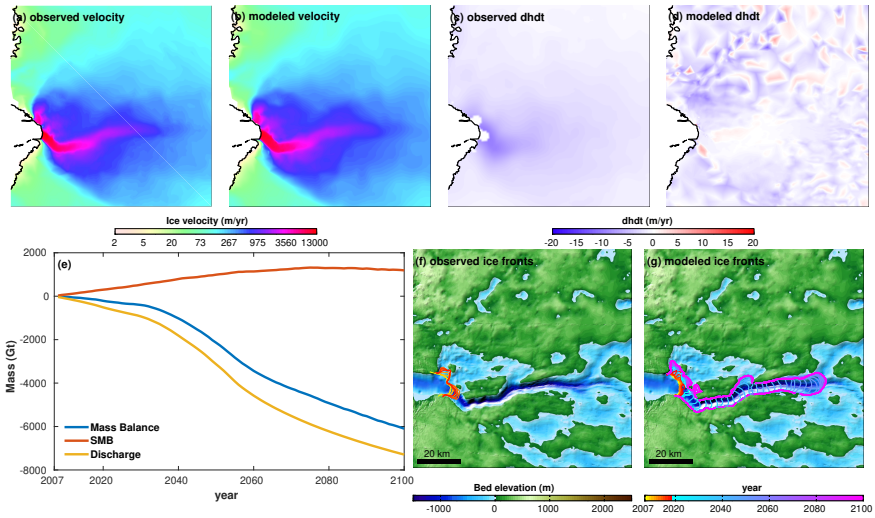

Kangerlussuup

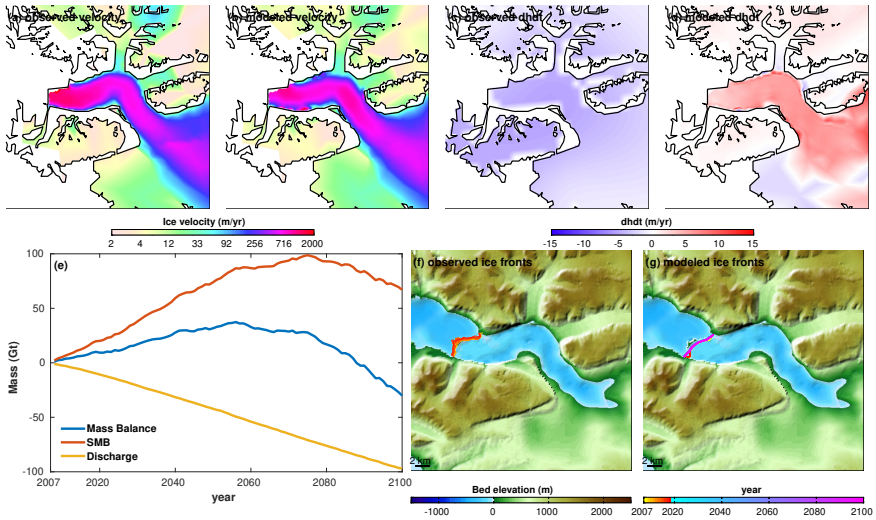

Kangilernata

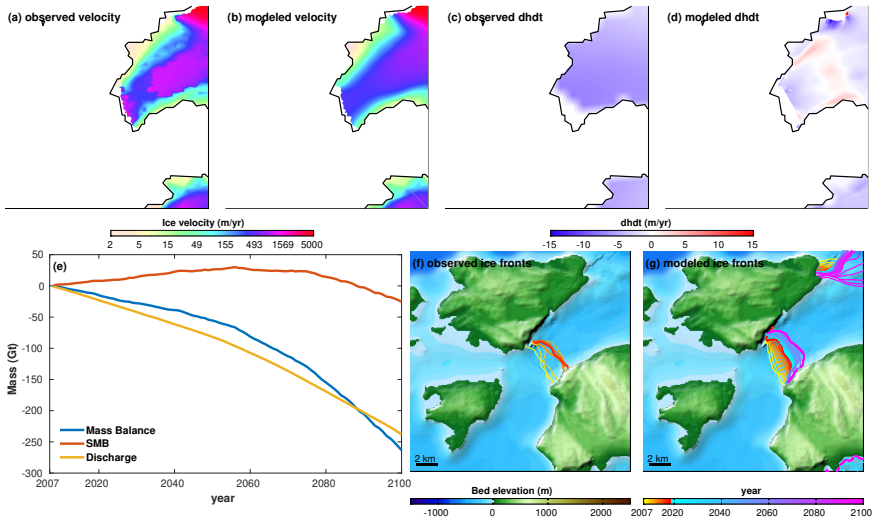

Kangilleq

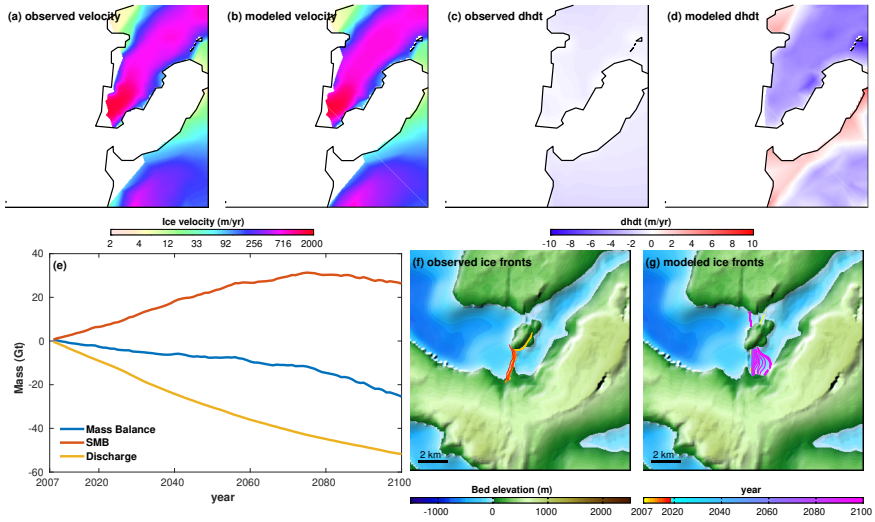

Kujalleq

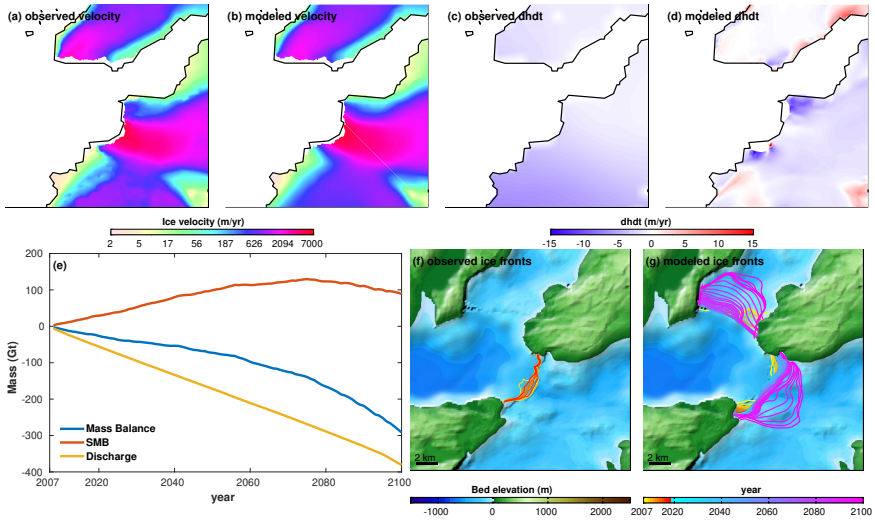

Lille

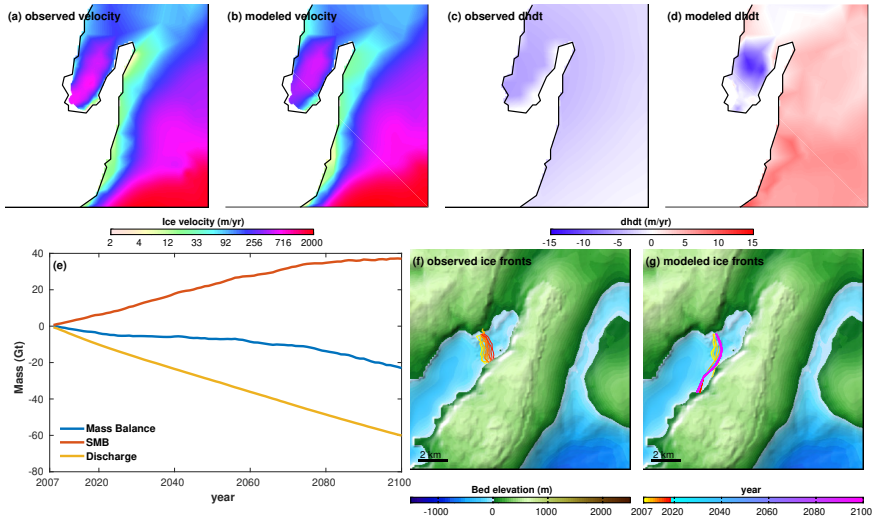

Perlerfiup

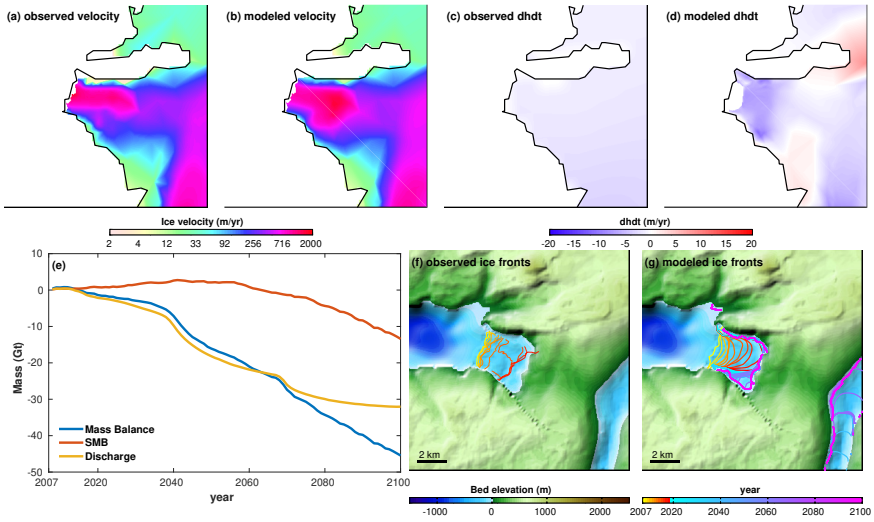

RinkIsbrae

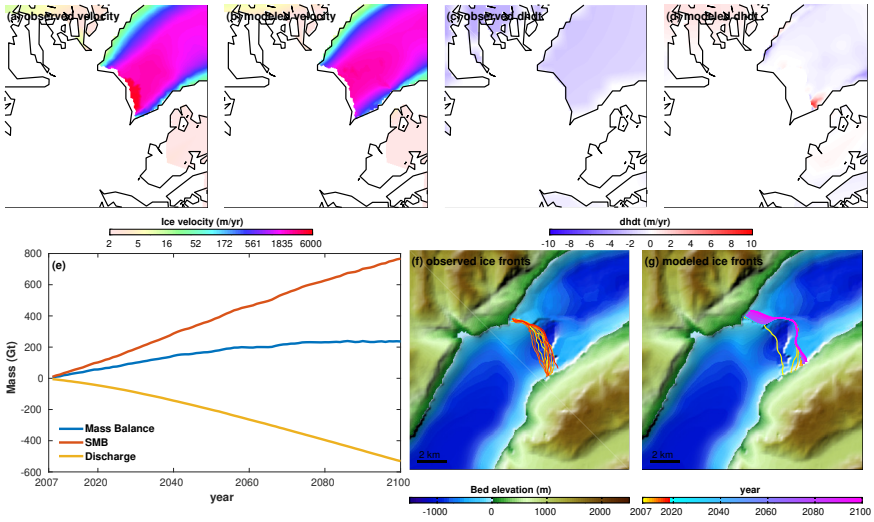

SermeqAvannarleq

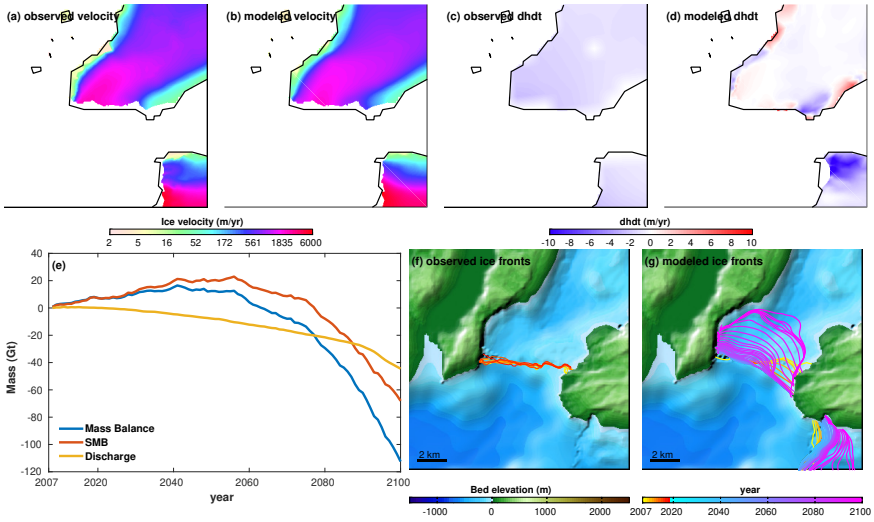

SermeqSilarleq

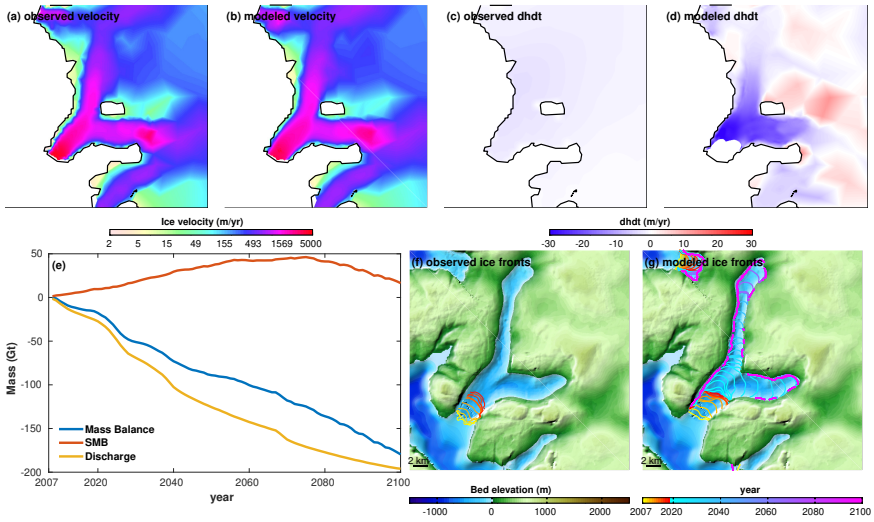

Store

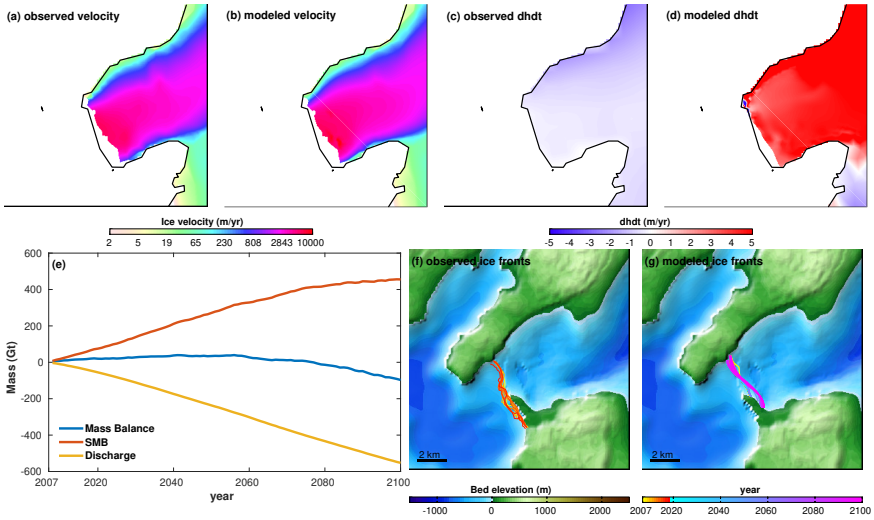

Ummiammakku

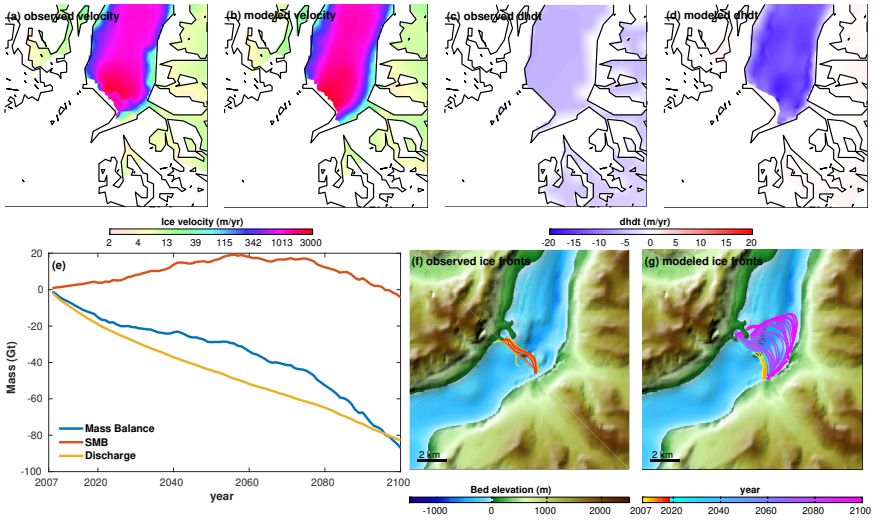

Alison

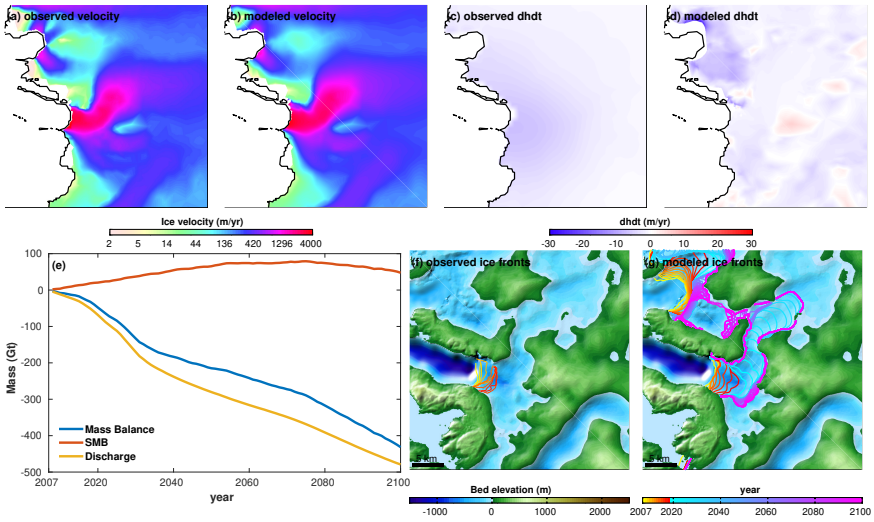

Carlos

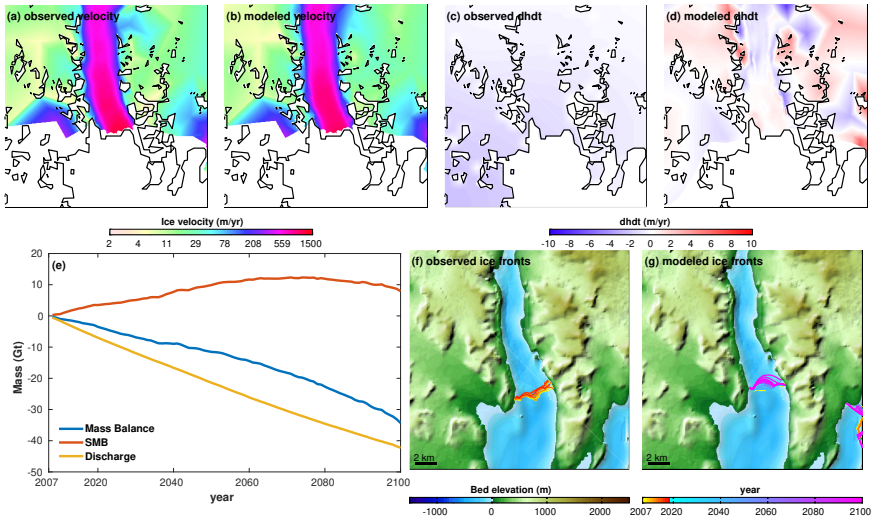

Cornell

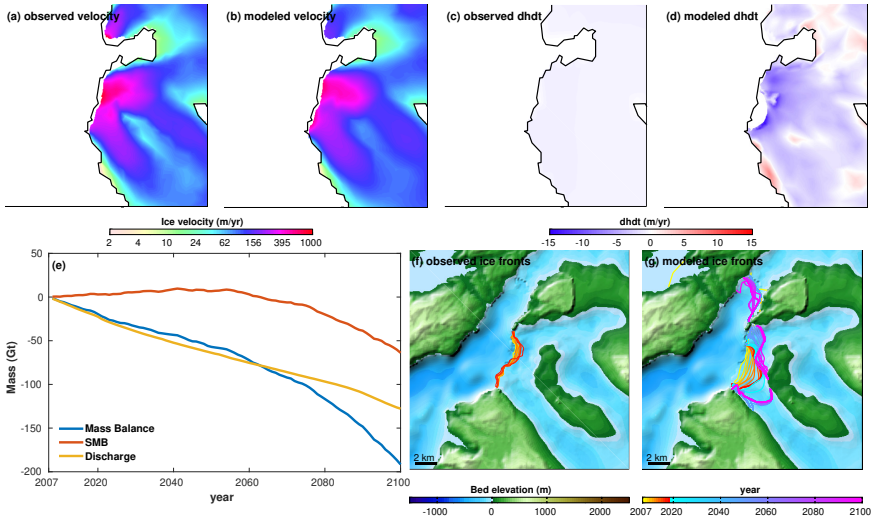

CornellN

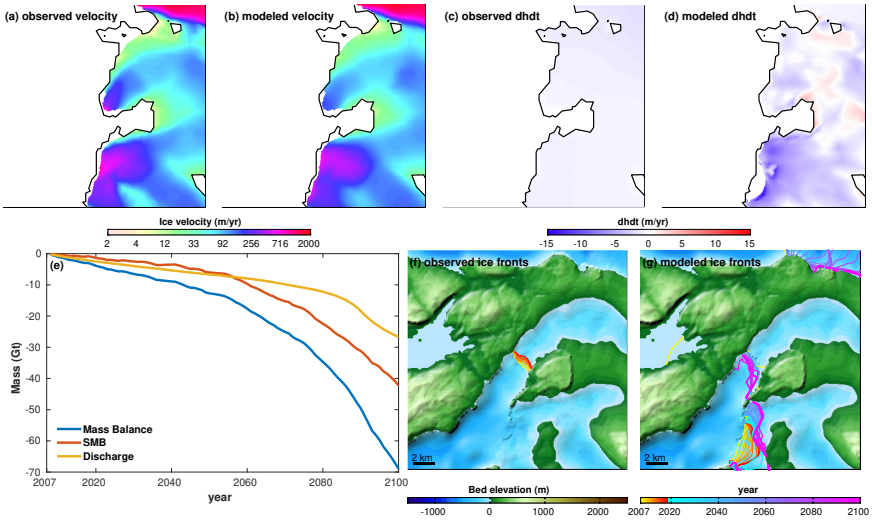

Dietrichson

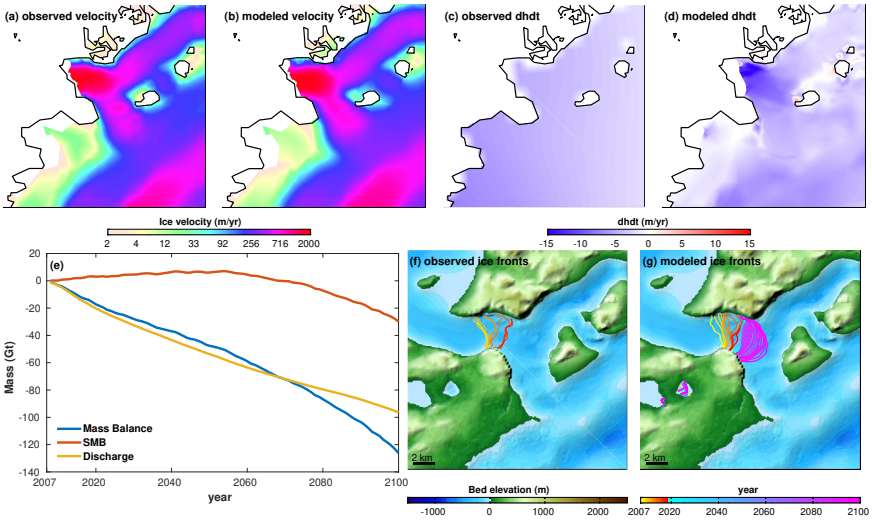

DockerSmith

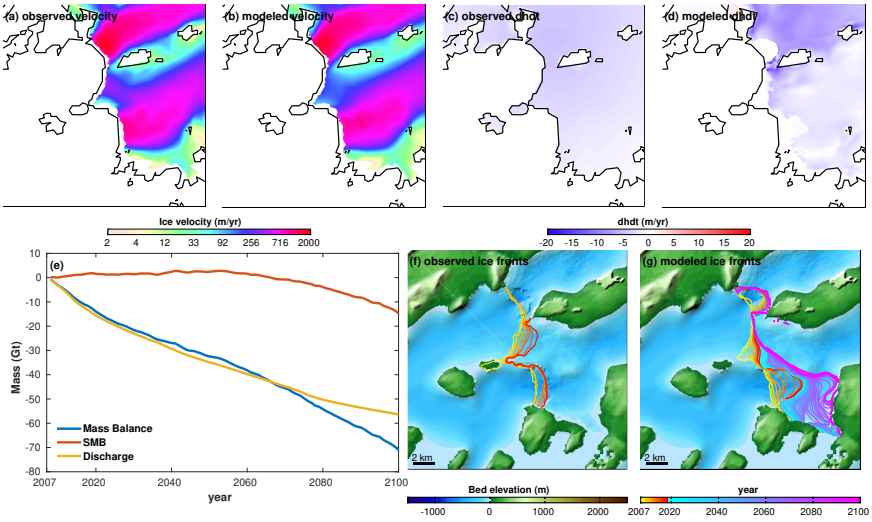

DockerSmithW

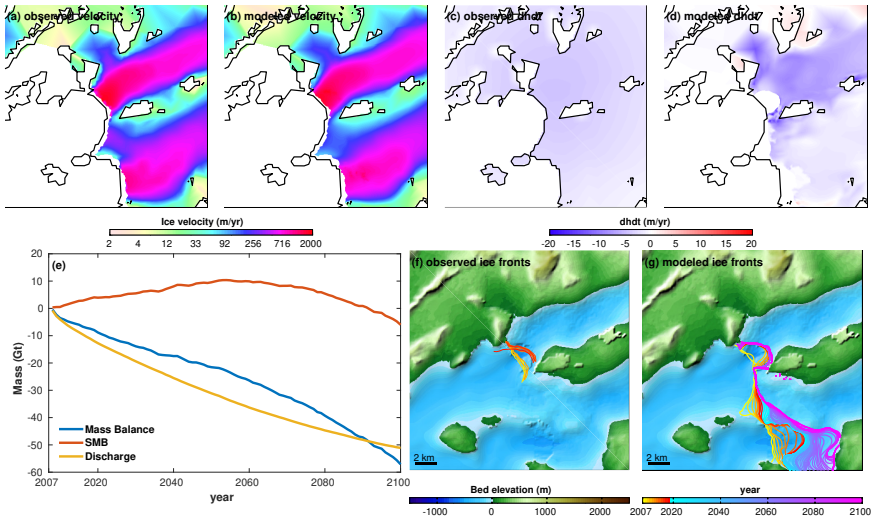

Gade

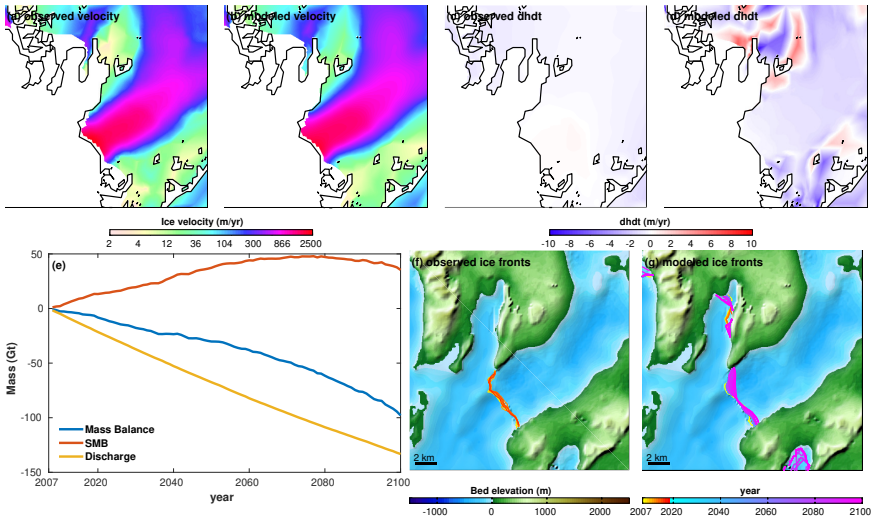

Hayes

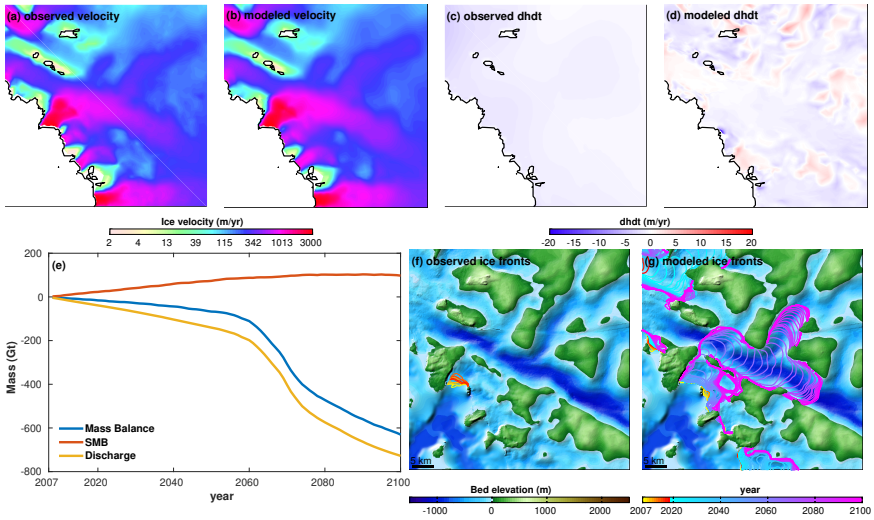

HayesM

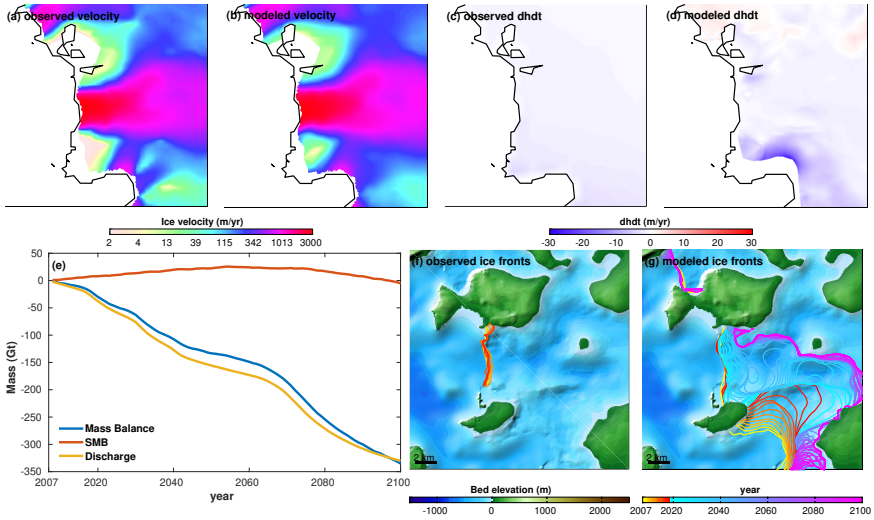

HayesN

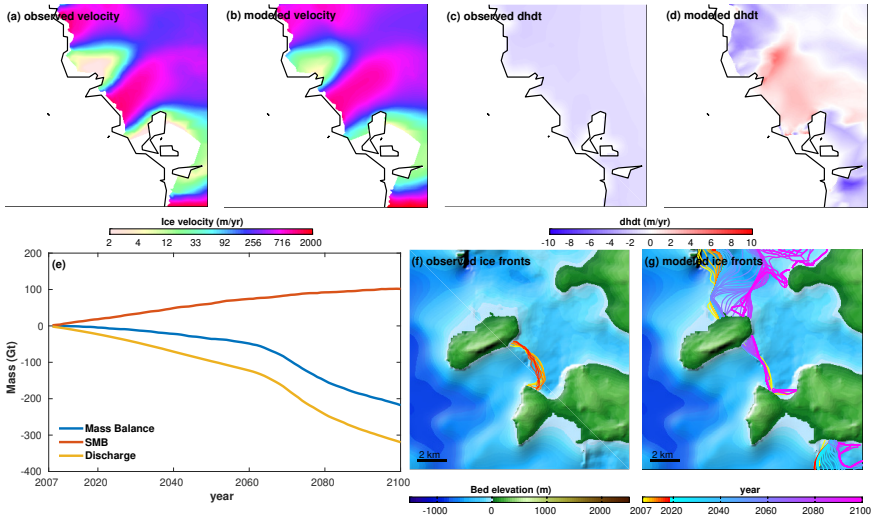

HayesNN

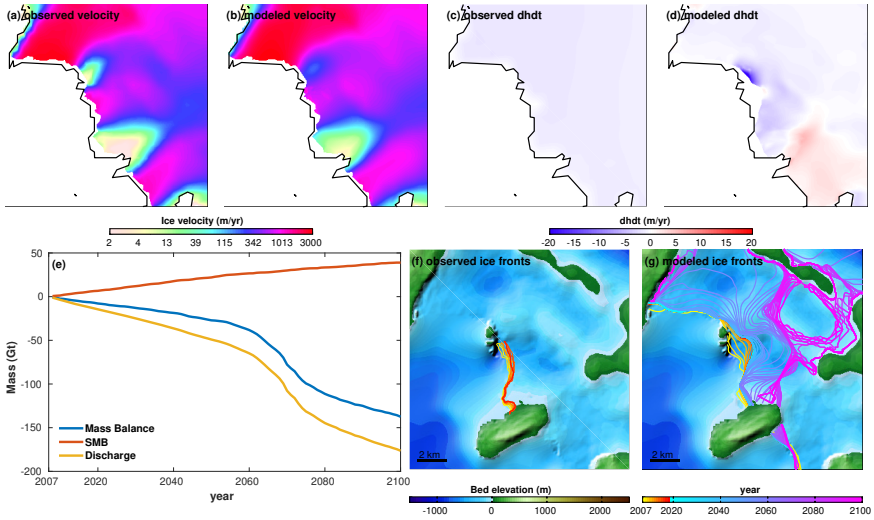

HayesNorth

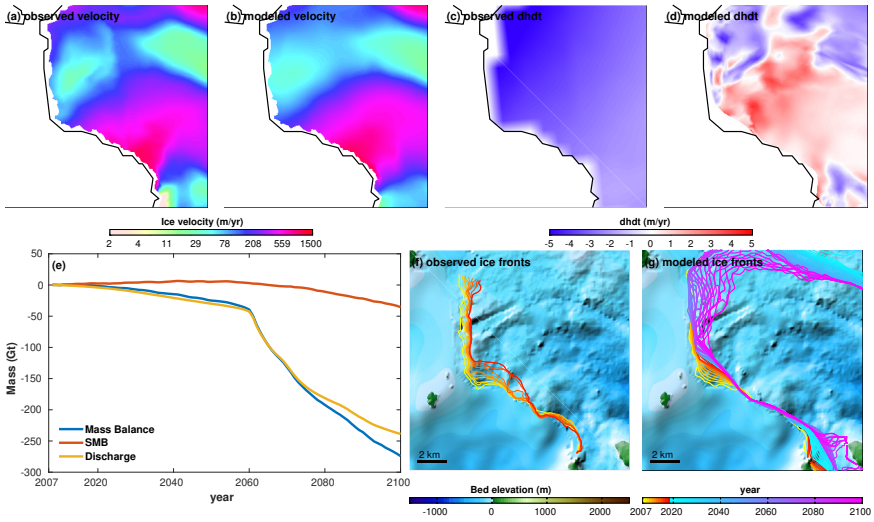

HayesSS

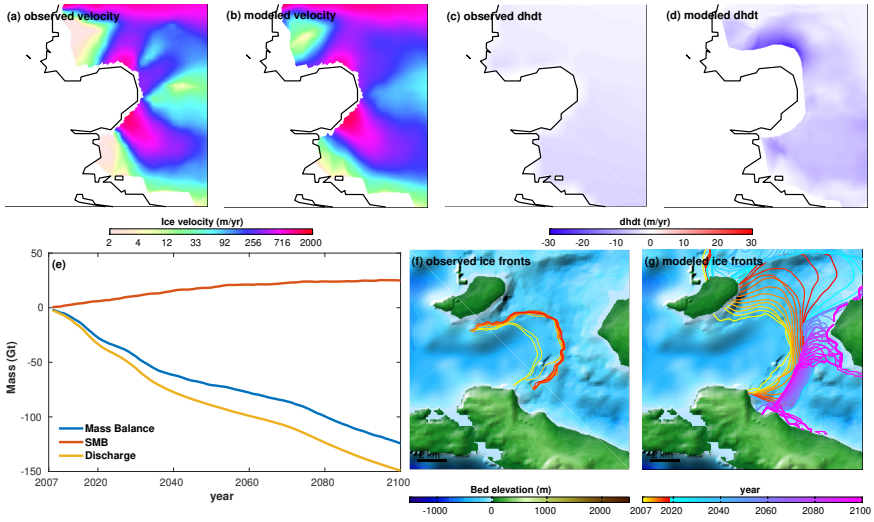

HellandE

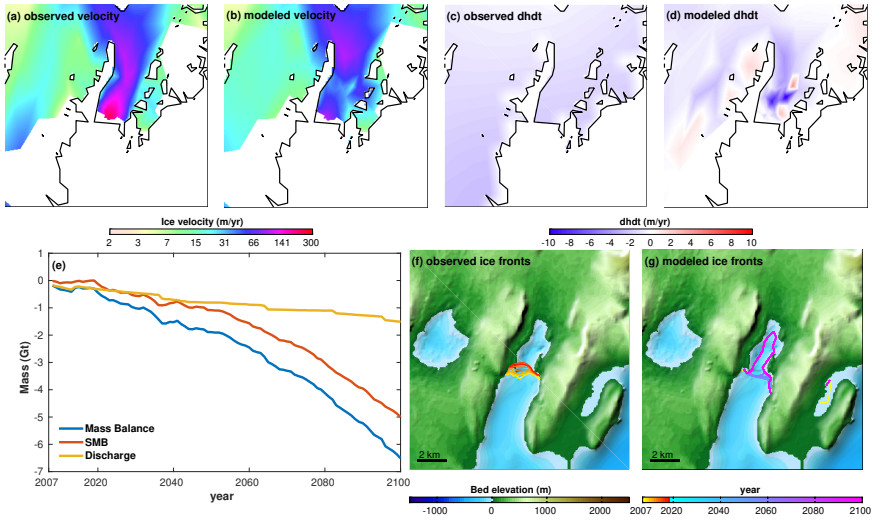

Illullip

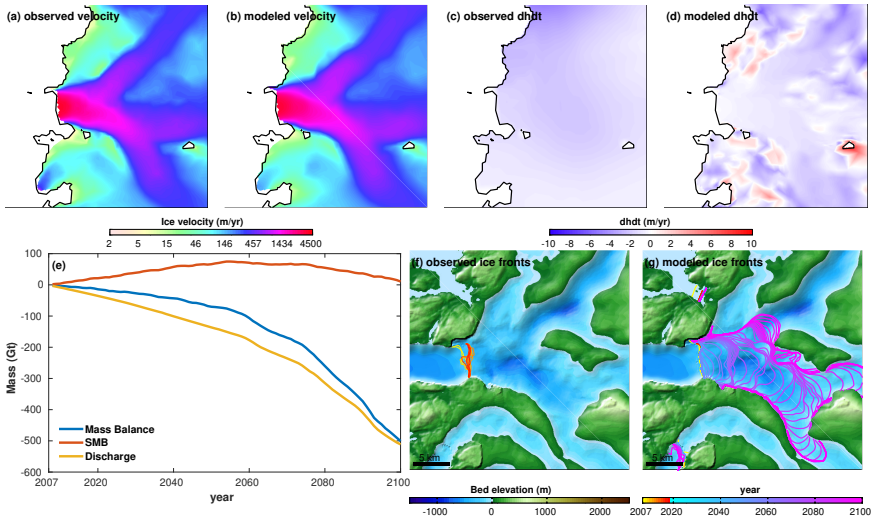

Issuusarsuit

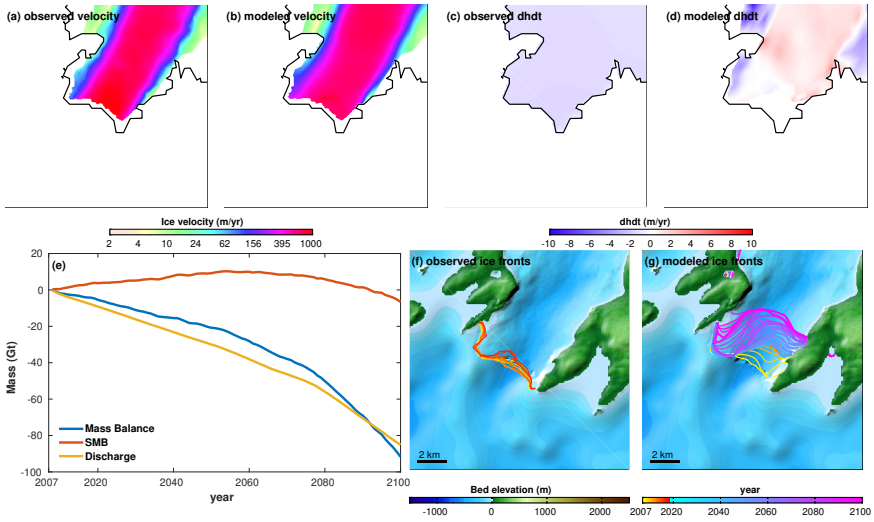

Kakivfaat

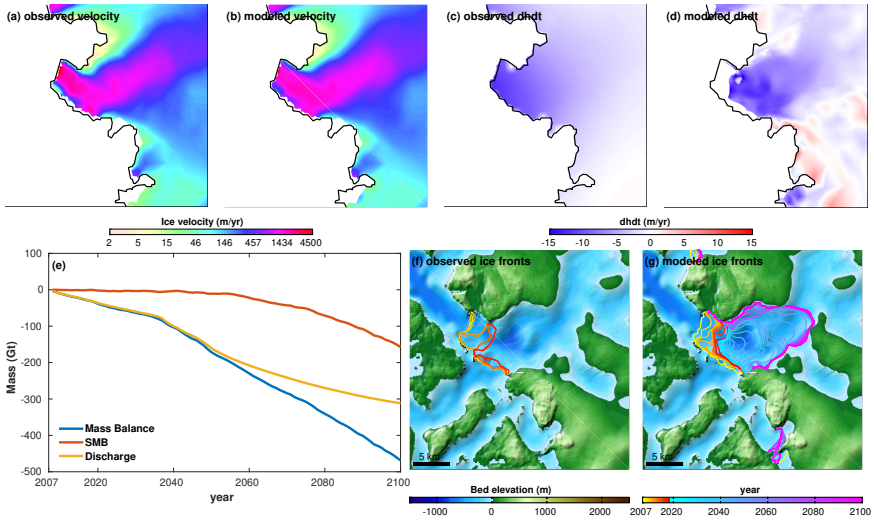

Kjer

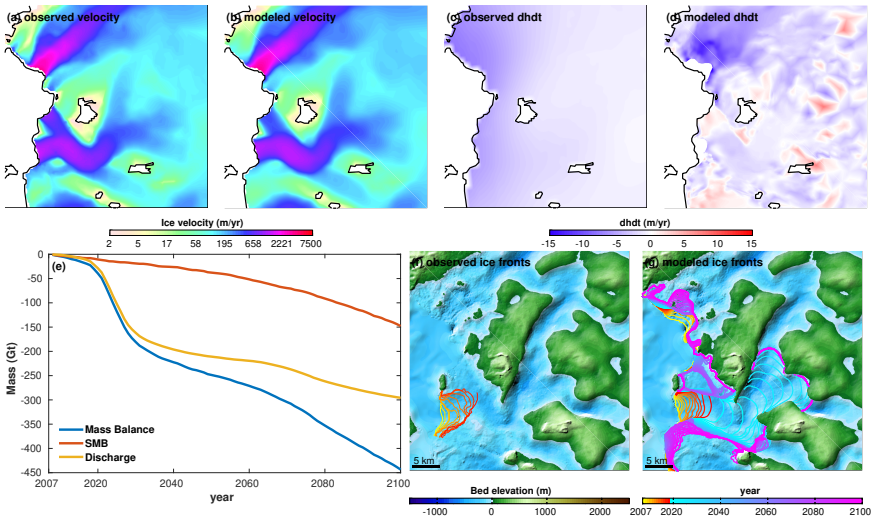

KjerN

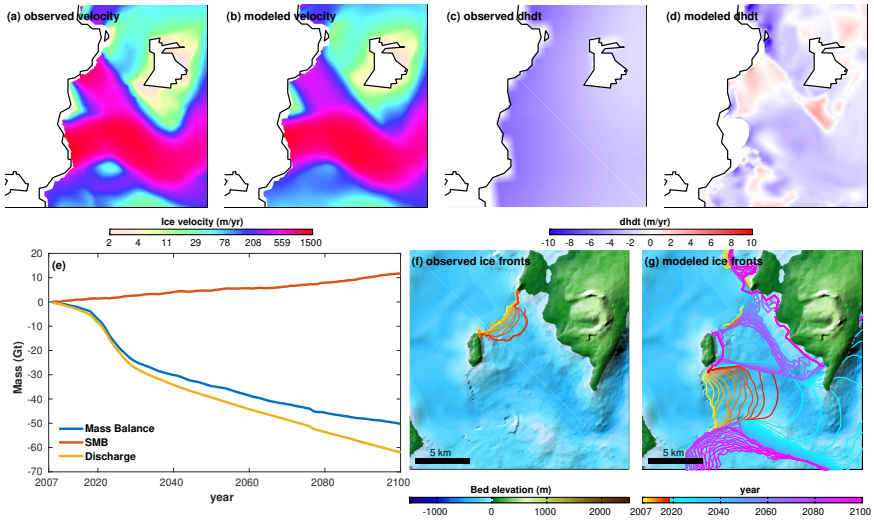

KongOscar

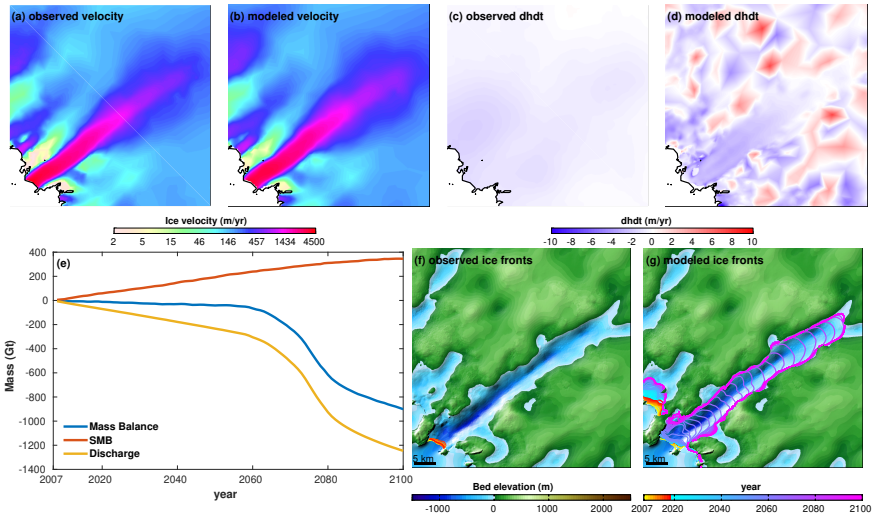

Nansen

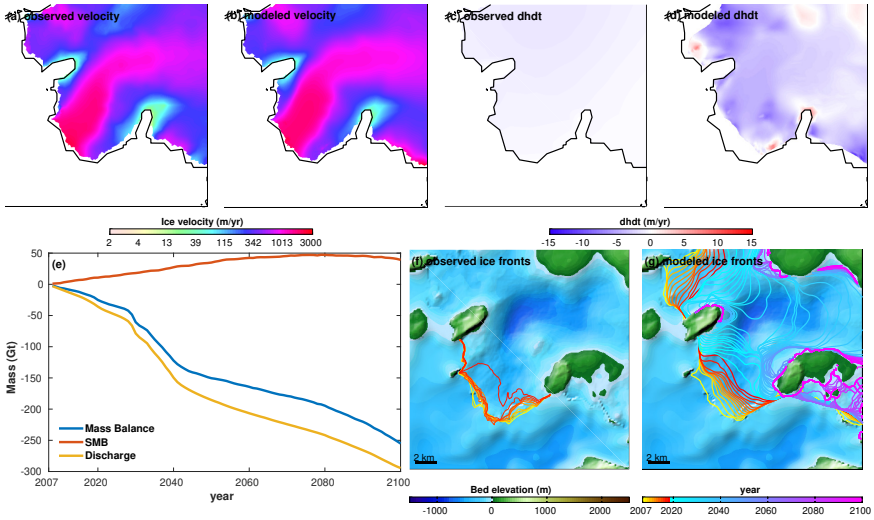

NansenS

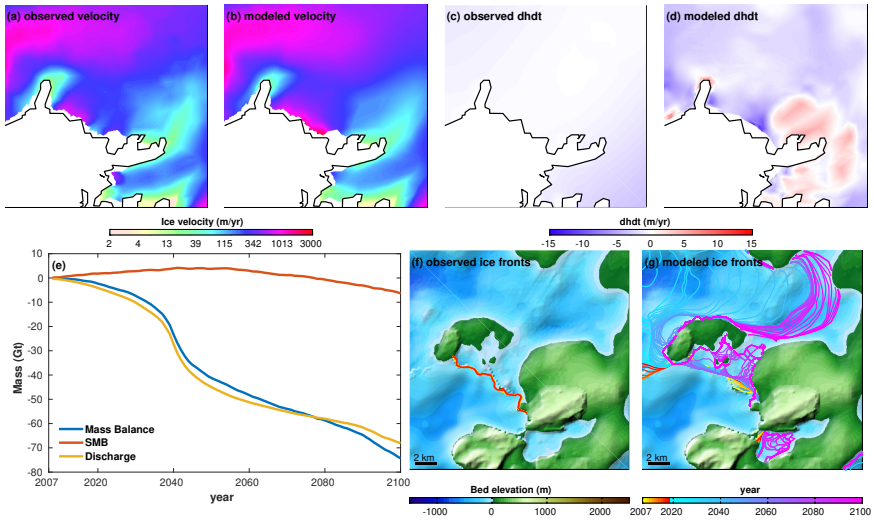

Nordenskiold

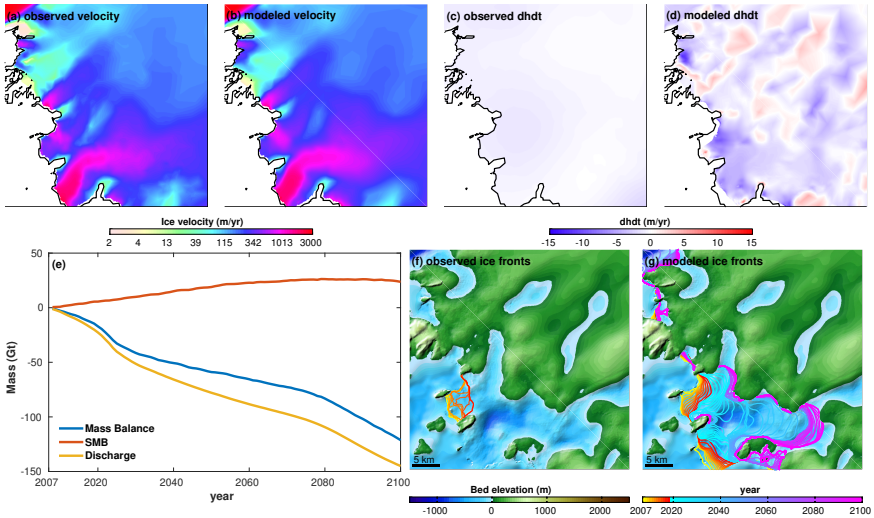

NordenskioldN

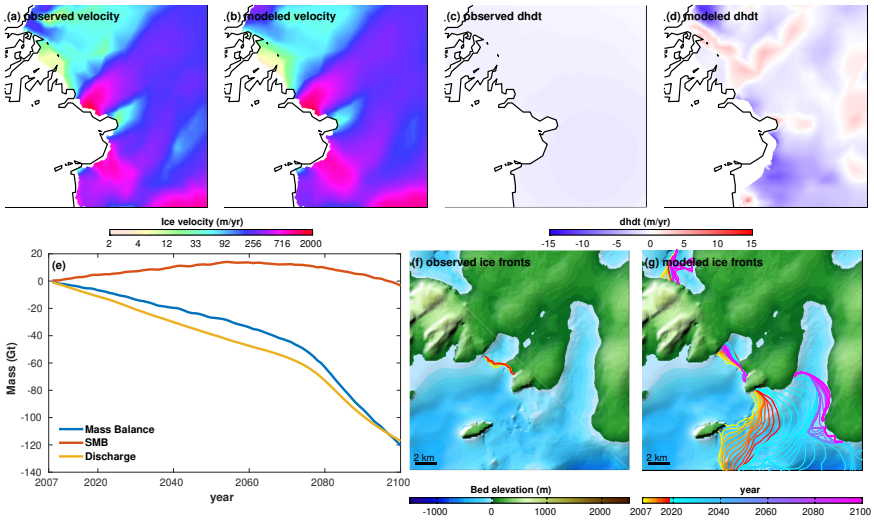

Nunatakassaap

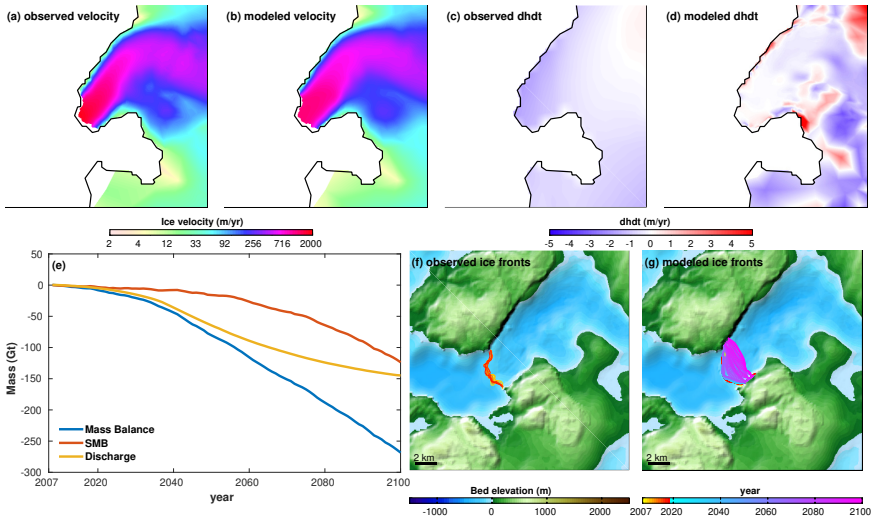

OscarN

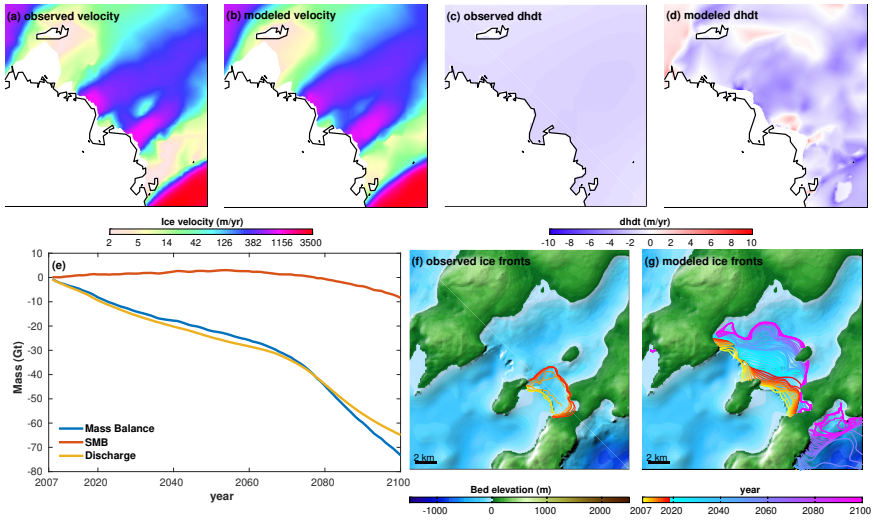

OscarNN

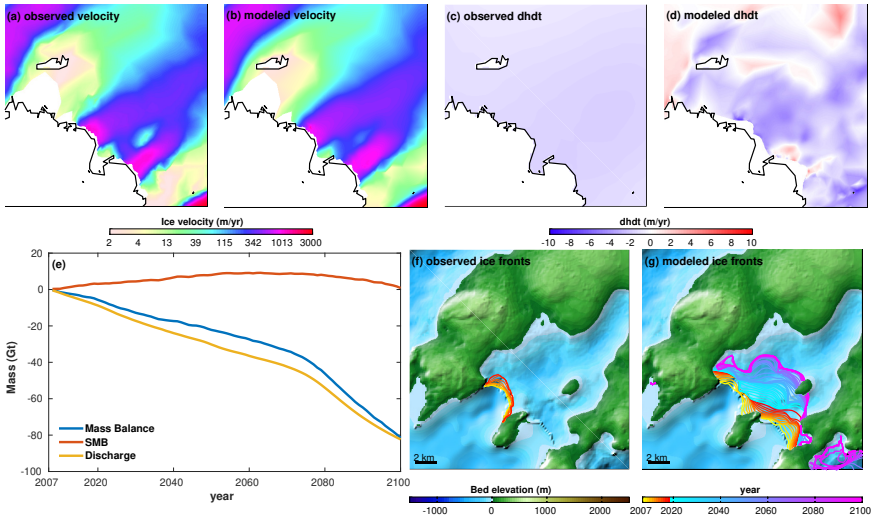

Qeqertarsuup

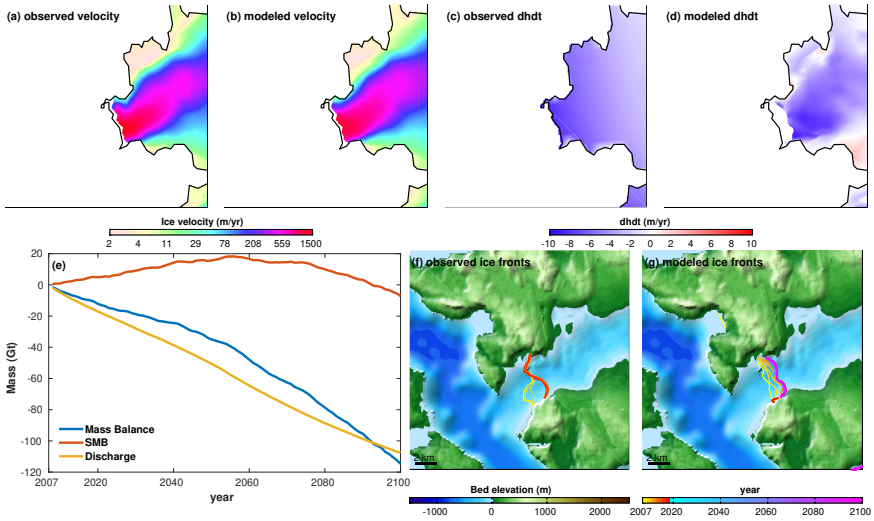

RinkGletscher

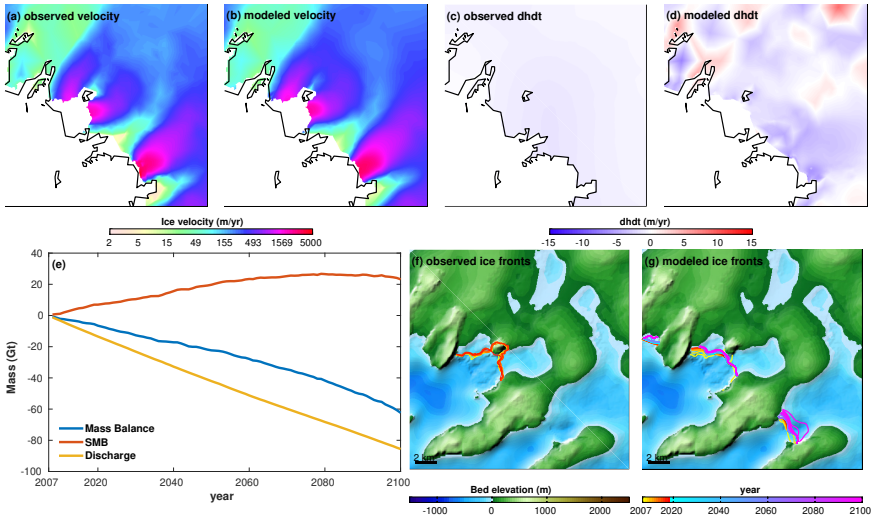

RinkGletscherS

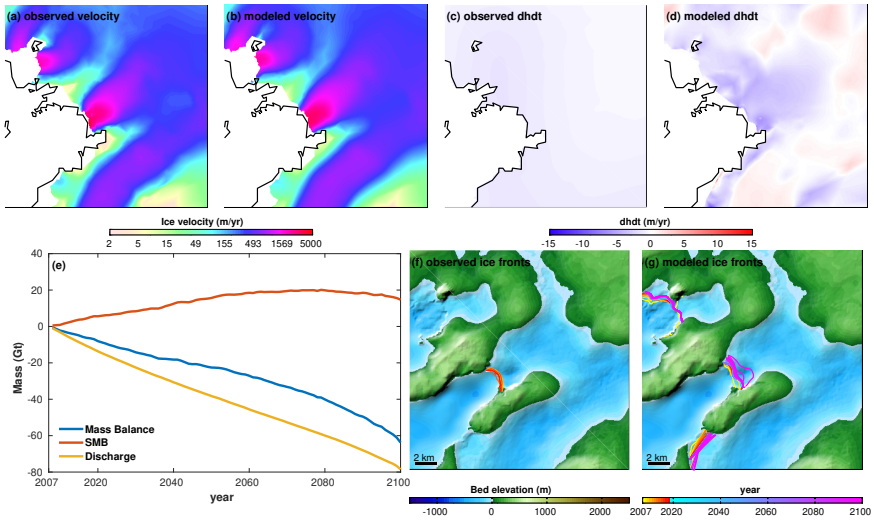

Savissuaq

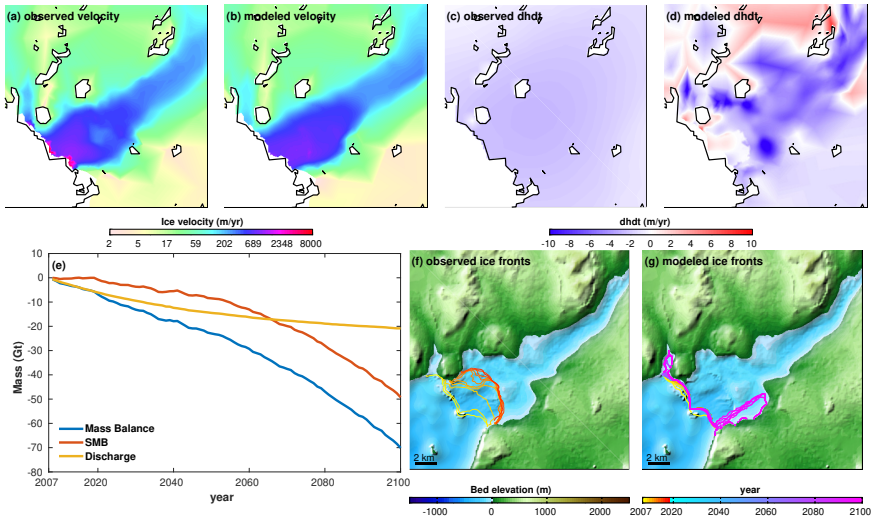

SavissuaqW

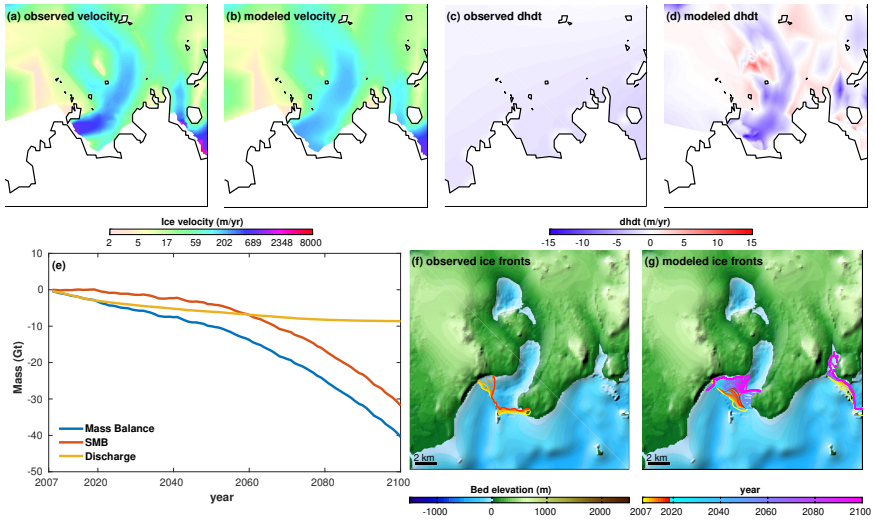

SavissuaqWW

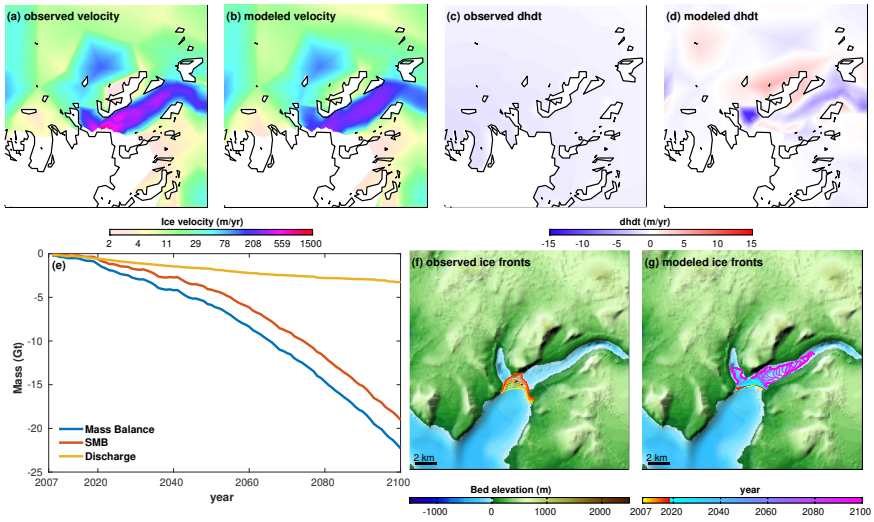

SavissuaqWWW

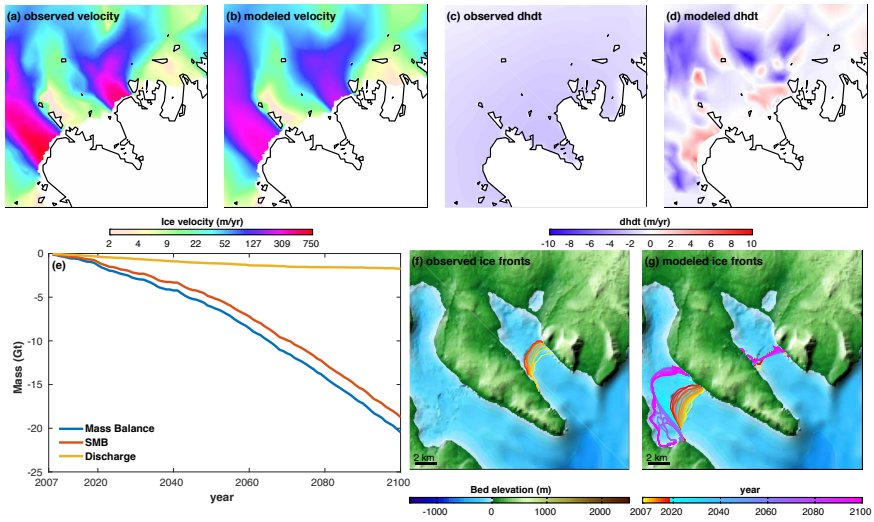

SavissuaqWWWW

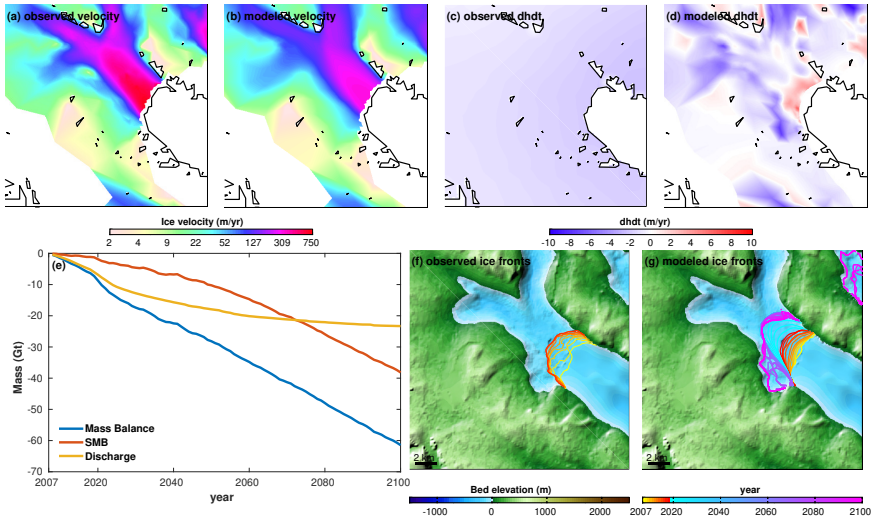

Steenstrup

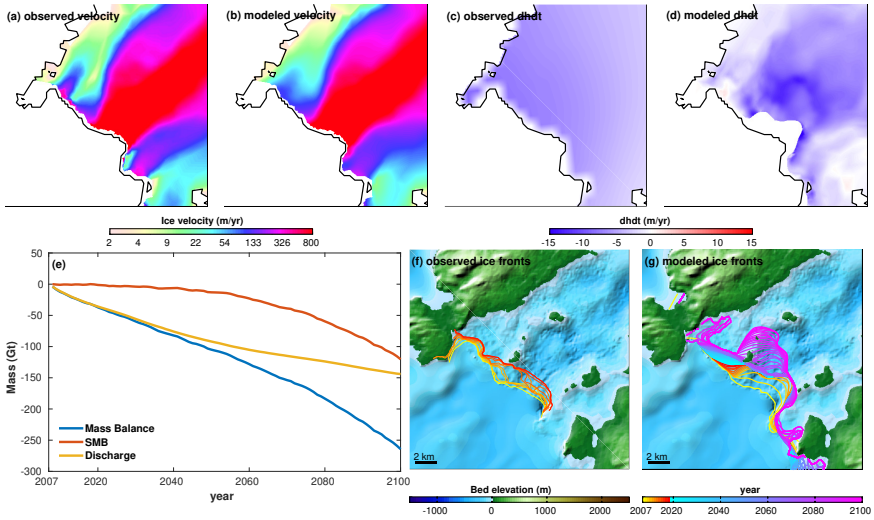

Sverdrup

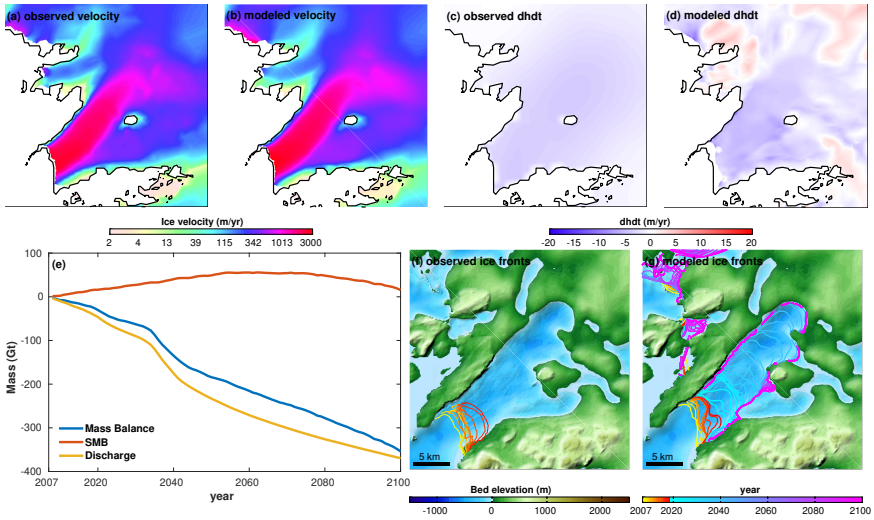

UpernavikIsstromC

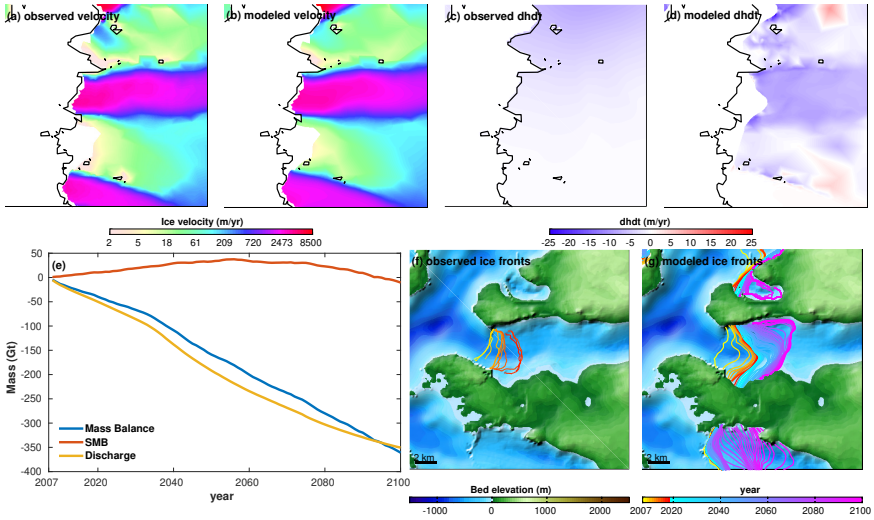

UpernavikIsstromN

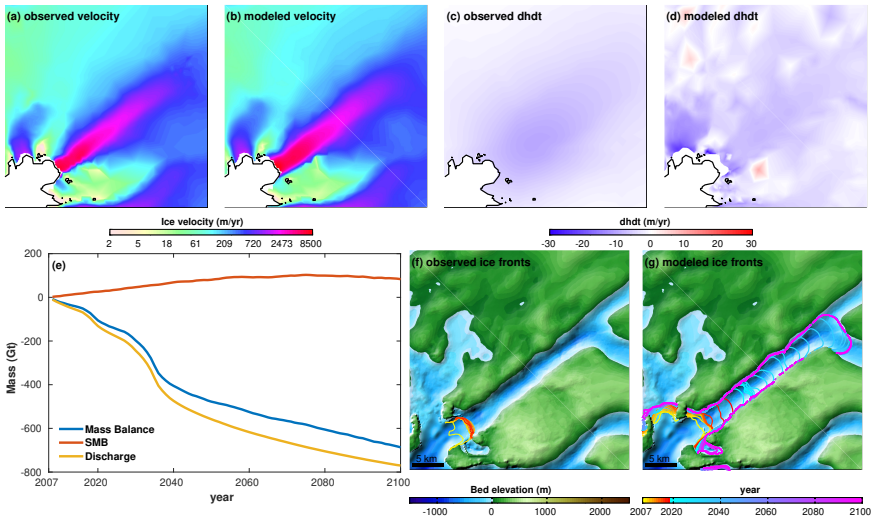

UpernavikIsstromNW

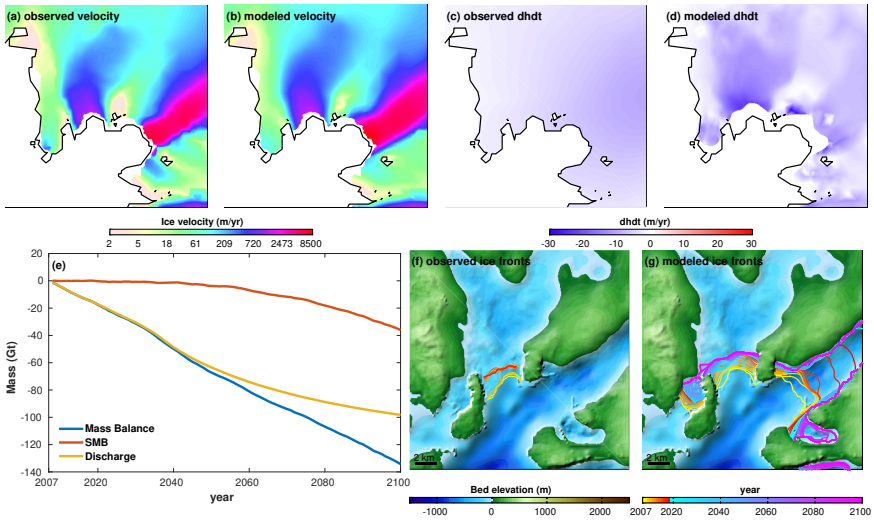

UpernavikIsstromS

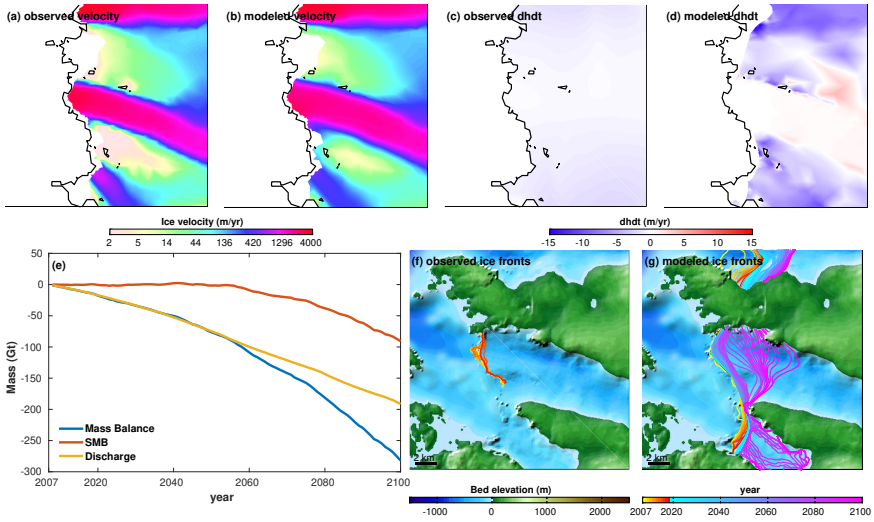

UpernavikIsstromSS

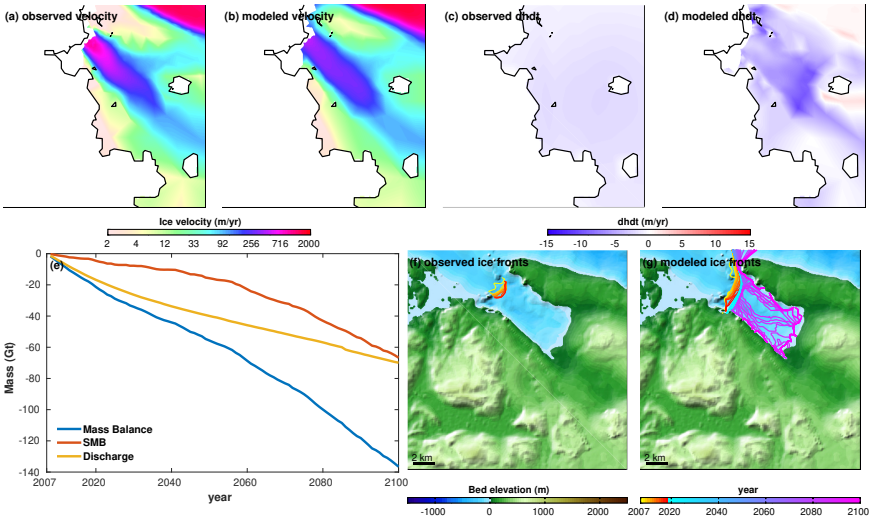

UssingBraeer

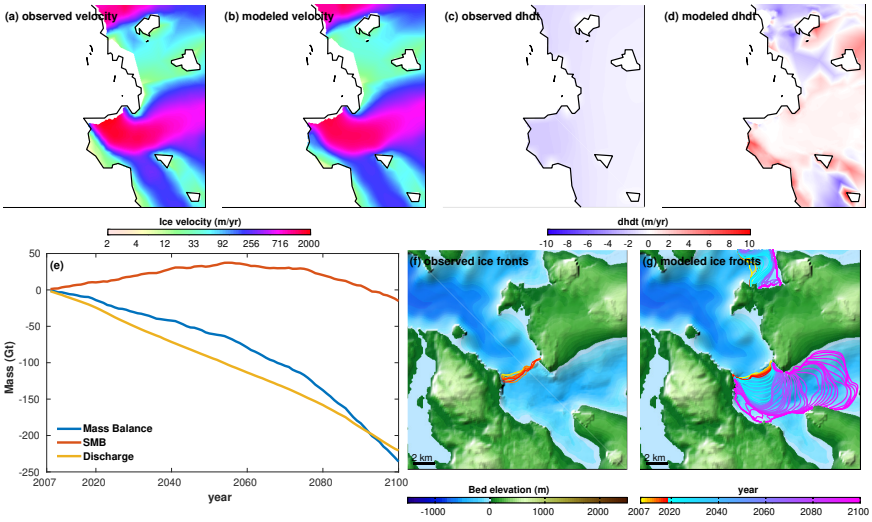

UssingBraeerN

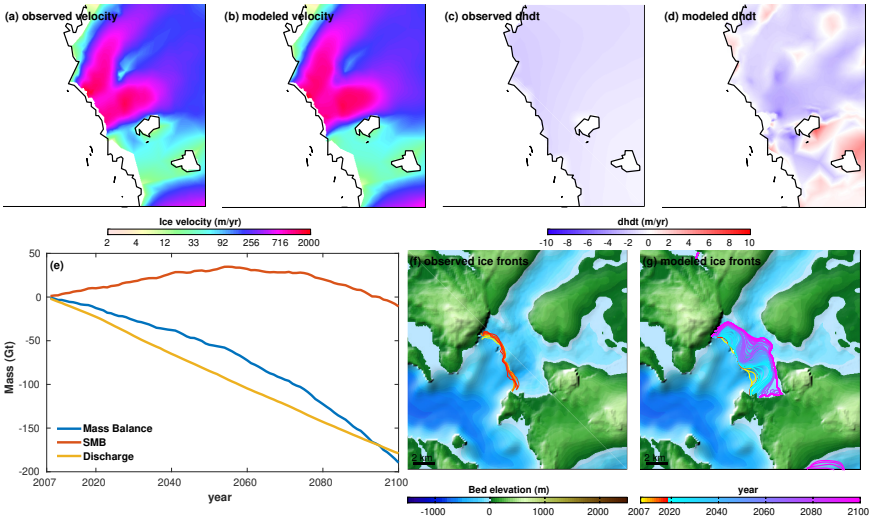

YngvarNielsen

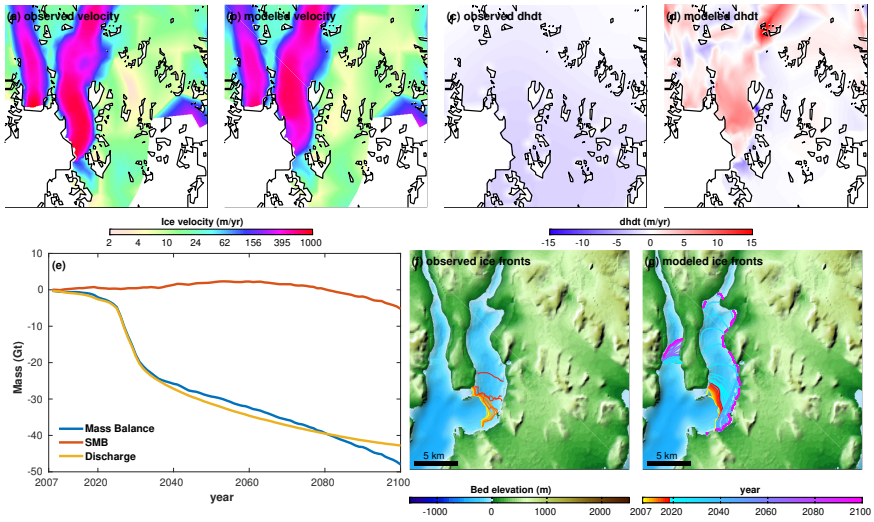

YngvarNielsenW

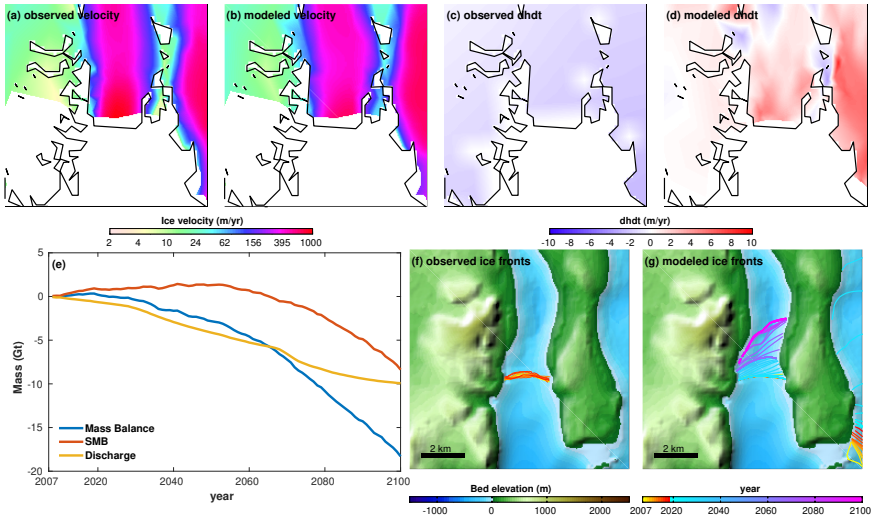

Academy

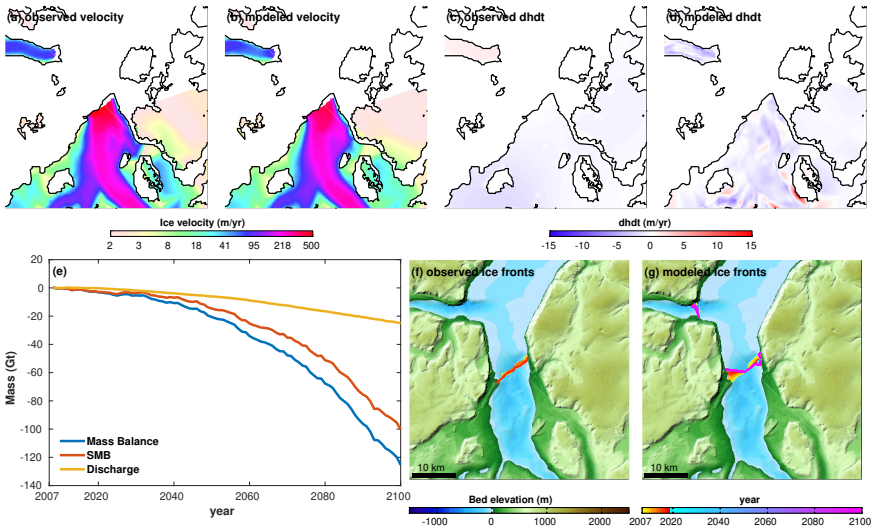

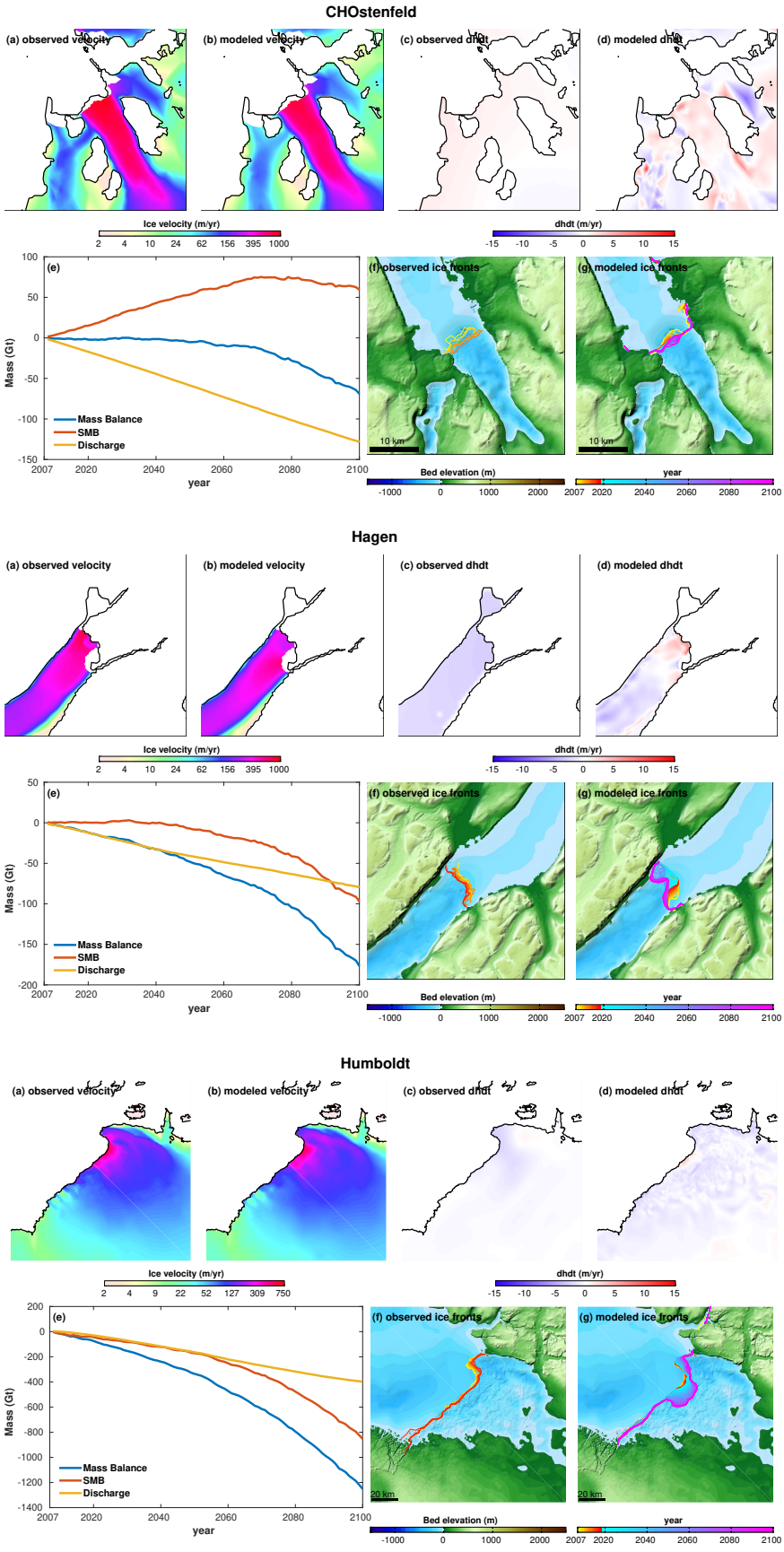
CHOstenfeld
(a) observed velocity
(b) modeled velocity
(c) observed dhdt
(d) modeled dhdt
Ice velocity (m/yr)
2 4 10 24 62 156 395 1000
dhdt (m/yr)
-15 -10 -5 0 5 10 15
(e)
Mass (Gt)
Mass Balance
SMB
Discharge
year
(f) observed ice fronts
(g) modeled ice fronts
10 km
Bed elevation (m)
-1000 0 1000 2000
year
2007 2020 2040 2060 2080 2100
Hagen
(a) observed velocity
(b) modeled velocity
(c) observed dhdt
(d) modeled dhdt
Ice velocity (m/yr)
2 4 10 24 62 156 395 1000
dhdt (m/yr)
-15 -10 -5 0 5 10 15
(e)
Mass (Gt)
Mass Balance
SMB
Discharge
year
(f) observed ice fronts
(g) modeled ice fronts
Bed elevation (m)
-1000 0 1000 2000
year
2007 2020 2040 2060 2080 2100
Humboldt
(a) observed velocity
(b) modeled velocity
(c) observed dhdt
(d) modeled dhdt
Ice velocity (m/yr)
2 4 9 22 52 127 309 750
dhdt (m/yr)
-15 -10 -5 0 5 10 15
(e)
Mass (Gt)
Mass Balance
SMB
Discharge
year
(f) observed ice fronts
(g) modeled ice fronts
20 km
Bed elevation (m)
-1000 0 1000 2000
year
2007 2020 2040 2060 2080 2100

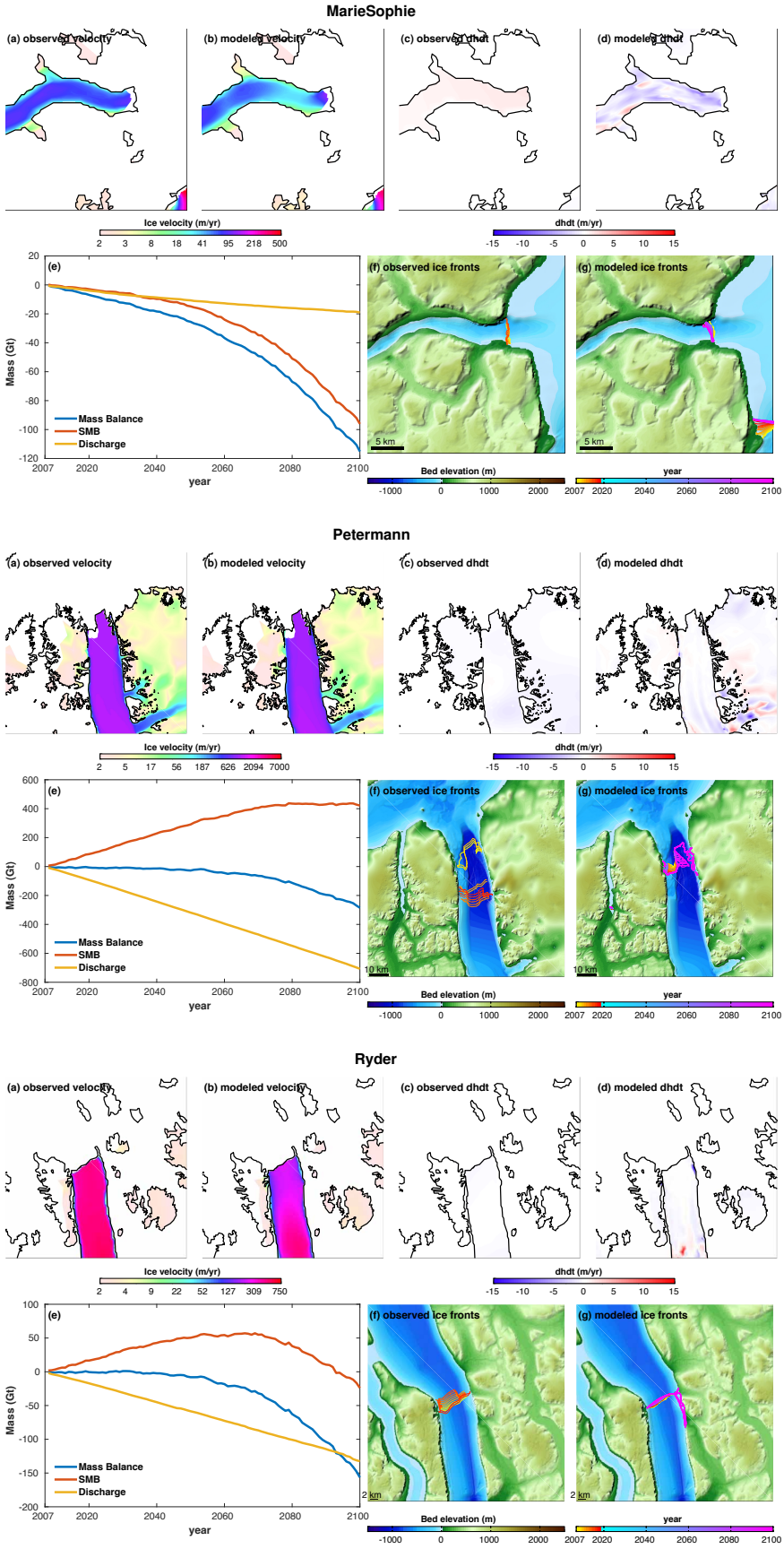
MarieSophie
(a) observed velocity
(b) modeled velocity
(c) observed dhdt
(d) modeled dhdt
Ice velocity (m/yr)
2 3 8 18 41 95 218 500
dhdt (m/yr)
-15 -10 -5 0 5 10 15
(e)
Mass (Gt)
Mass Balance
SMB
Discharge
year
(f) observed ice fronts
(g) modeled ice fronts
5 km
Bed elevation (m)
-1000 0 1000 2000
year
2007 2020 2040 2060 2080 2100
Petermann
(a) observed velocity
(b) modeled velocity
(c) observed dhdt
(d) modeled dhdt
Ice velocity (m/yr)
2 5 17 56 187 626 2094 7000
dhdt (m/yr)
-15 -10 -5 0 5 10 15
(e)
Mass (Gt)
Mass Balance
SMB
Discharge
year
(f) observed ice fronts
(g) modeled ice fronts
10 km
Bed elevation (m)
-1000 0 1000 2000
year
2007 2020 2040 2060 2080 2100
Ryder
(a) observed velocity
(b) modeled velocity
(c) observed dhdt
(d) modeled dhdt
Ice velocity (m/yr)
2 4 9 22 52 127 309 750
dhdt (m/yr)
-15 -10 -5 0 5 10 15
(e)
Mass (Gt)
Mass Balance
SMB
Discharge
year
(f) observed ice fronts
(g) modeled ice fronts
2 km
Bed elevation (m)
-1000 0 1000 2000
year
2007 2020 2040 2060 2080 2100

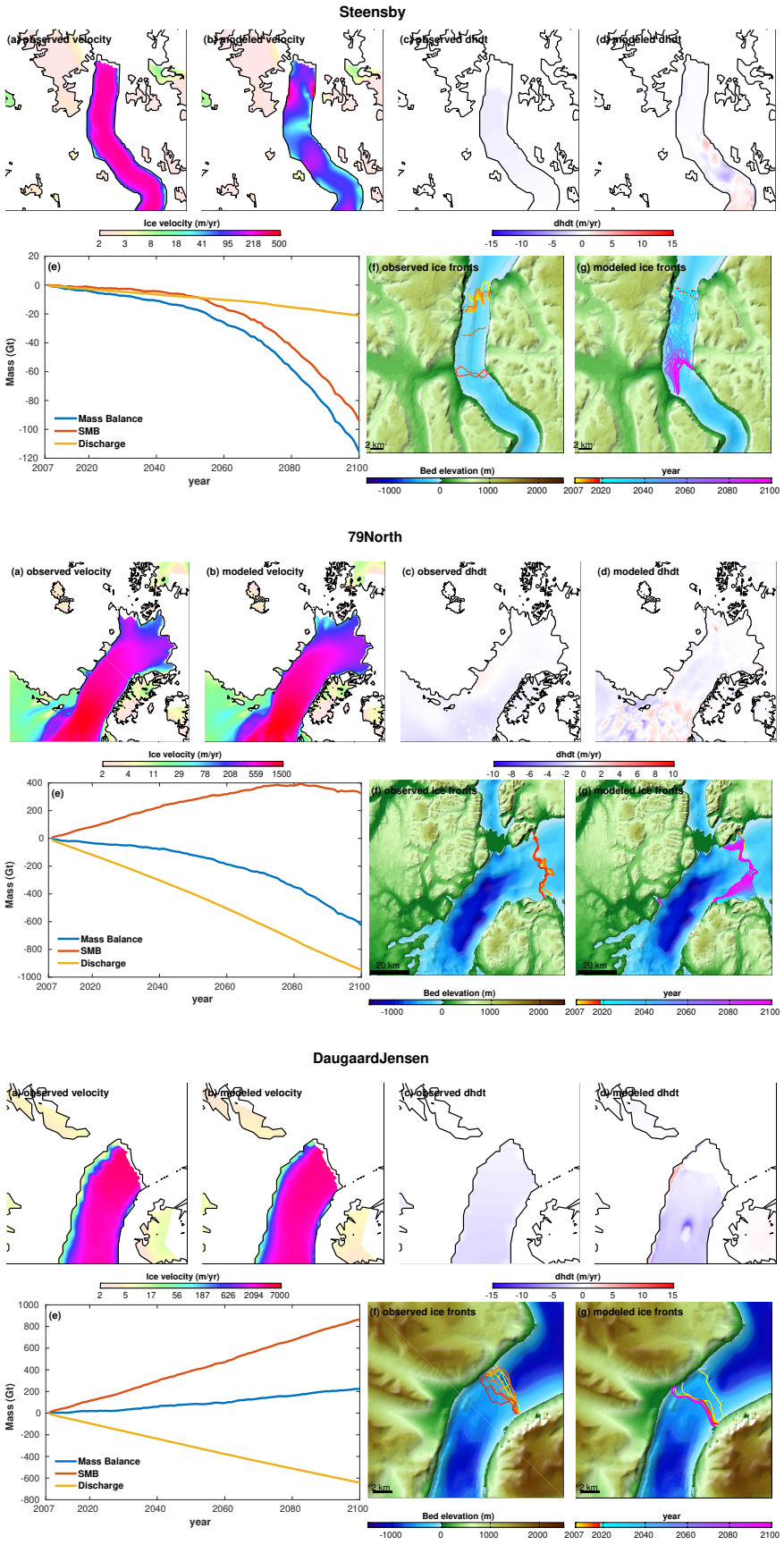
Steensby
(a) observed velocity
(b) modeled velocity
(c) observed dhdt
(d) modeled dhdt
Ice velocity (m/yr)
2 3 8 18 41 95 218 500
dhdt (m/yr)
-15 -10 -5 0 5 10 15
(e)
Mass (Gt)
year
Mass Balance
SMB
Discharge
(f) observed ice fronts
(g) modeled ice fronts
2 km
Bed elevation (m)
-1000 0 1000 2000
year
2007 2020 2040 2060 2080 2100
79North
(a) observed velocity
(b) modeled velocity
(c) observed dhdt
(d) modeled dhdt
Ice velocity (m/yr)
2 4 11 29 78 208 559 1500
dhdt (m/yr)
-10 -8 -6 -4 -2 0 2 4 6 8 10
(e)
Mass (Gt)
year
Mass Balance
SMB
Discharge
(f) observed ice fronts
(g) modeled ice fronts
20 km
Bed elevation (m)
-1000 0 1000 2000
year
2007 2020 2040 2060 2080 2100
DaugaardJensen
(a) observed velocity
(b) modeled velocity
(c) observed dhdt
(d) modeled dhdt
Ice velocity (m/yr)
2 5 17 56 187 626 2094 7000
dhdt (m/yr)
-15 -10 -5 0 5 10 15
(e)
Mass (Gt)
year
Mass Balance
SMB
Discharge
(f) observed ice fronts
(g) modeled ice fronts
2 km
Bed elevation (m)
-1000 0 1000 2000
year
2007 2020 2040 2060 2080 2100

FGraae

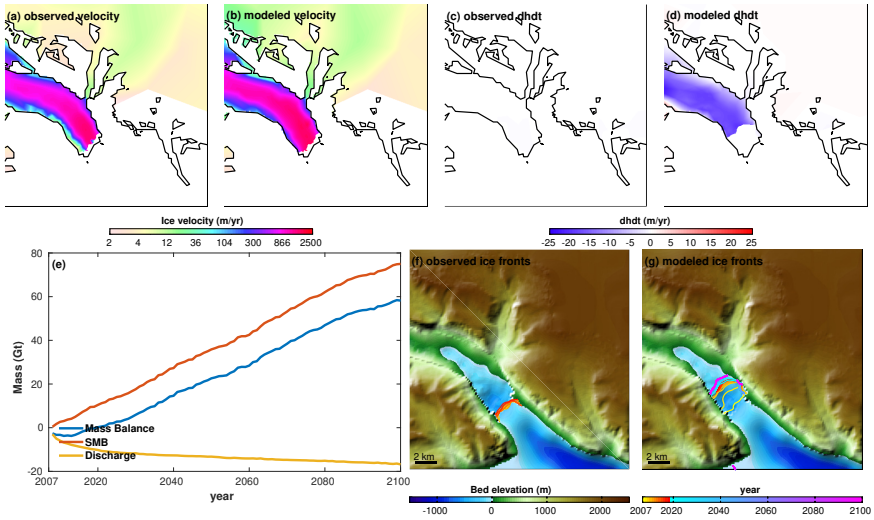

Kofoed

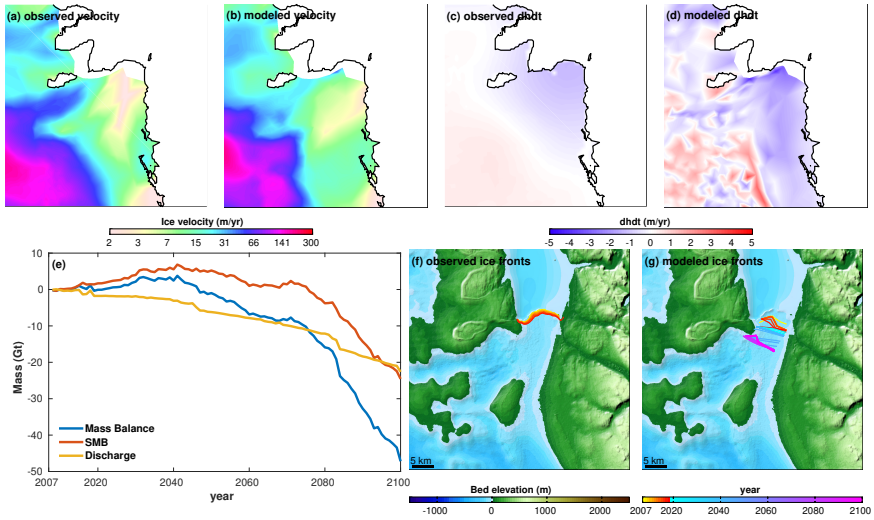

Rolige

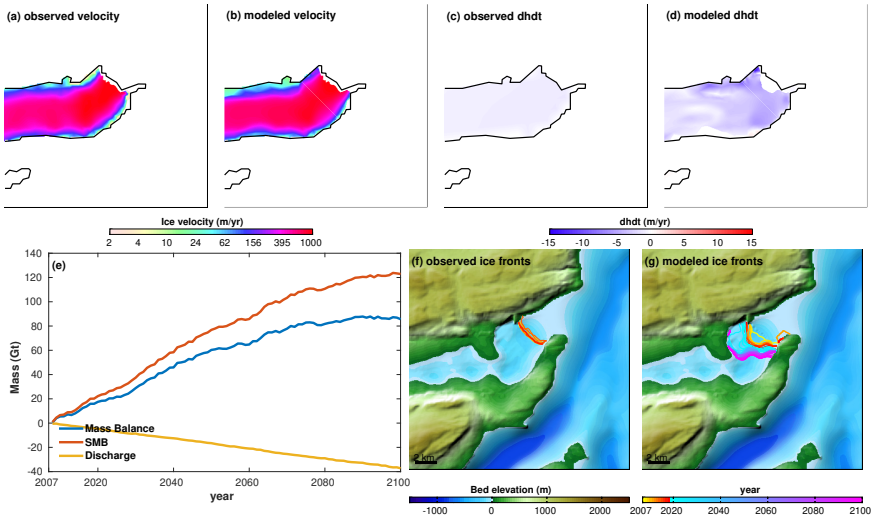

Storstrommen

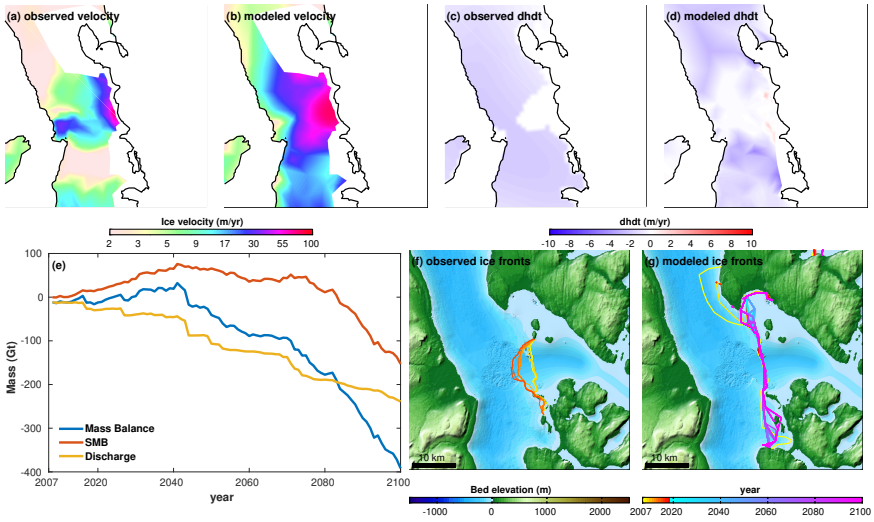

Vestfjord

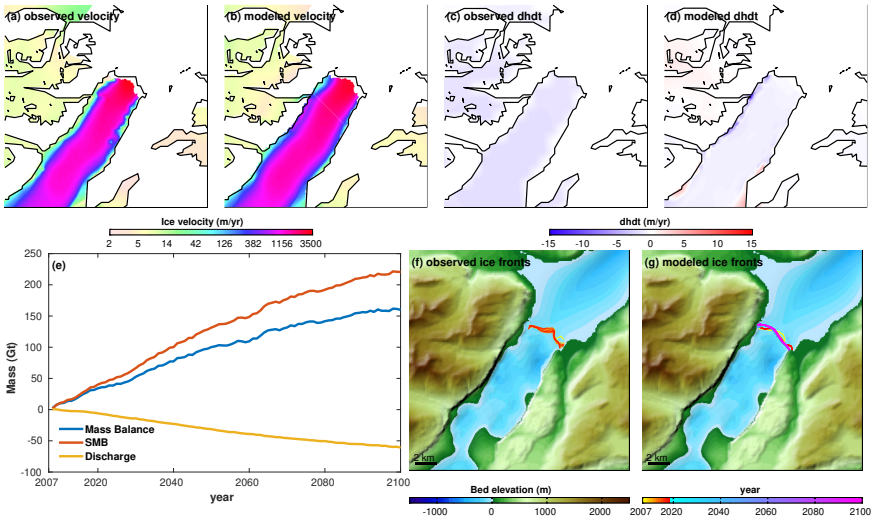

Zachariae

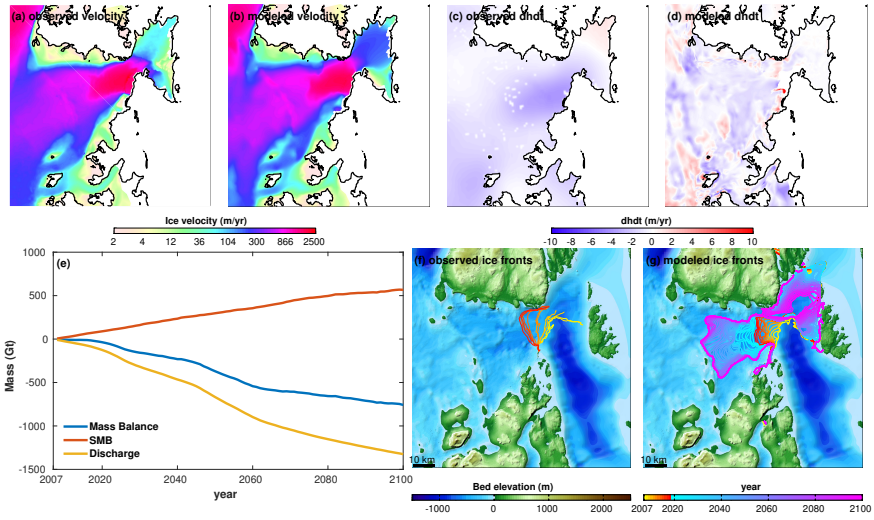

AnorituupKangerlua

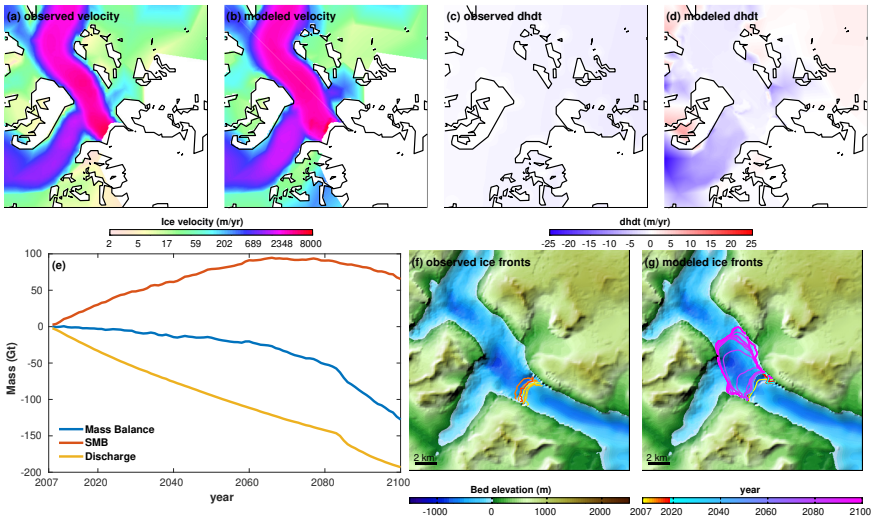

APBernstorff

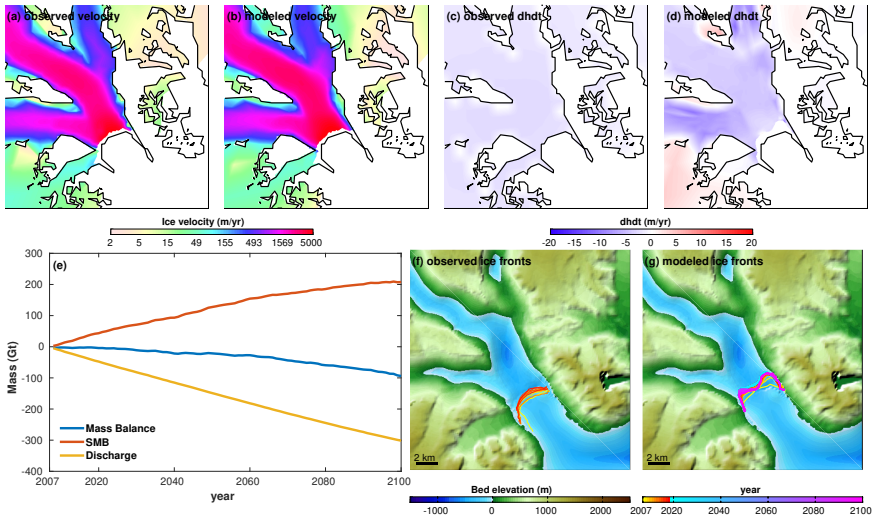

Danell

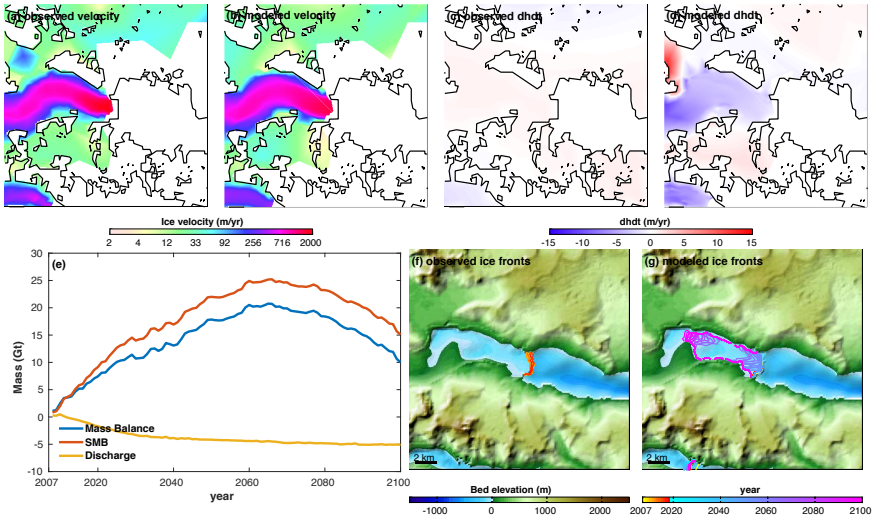

DanellS

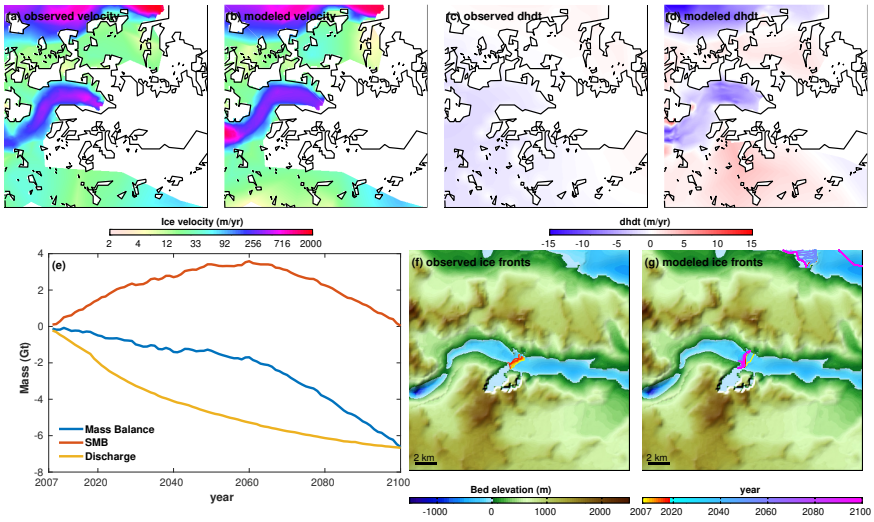

DeceptionOCN

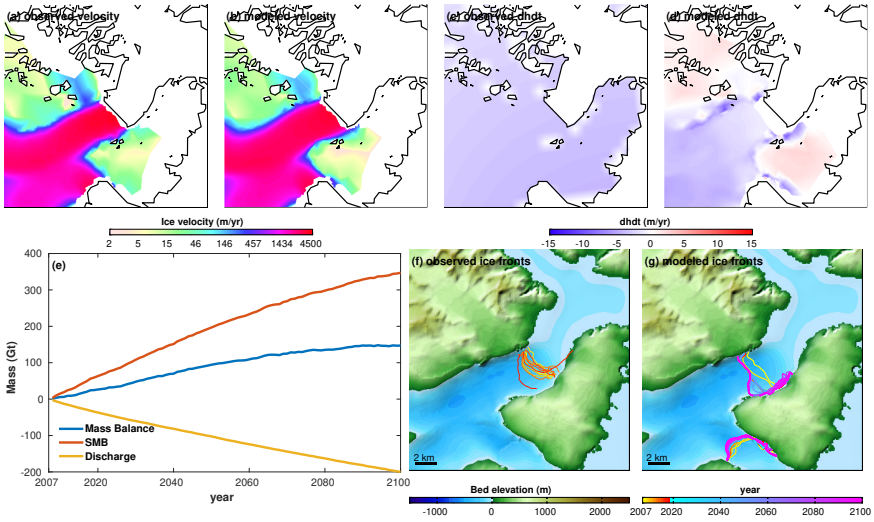

DeceptionOCS

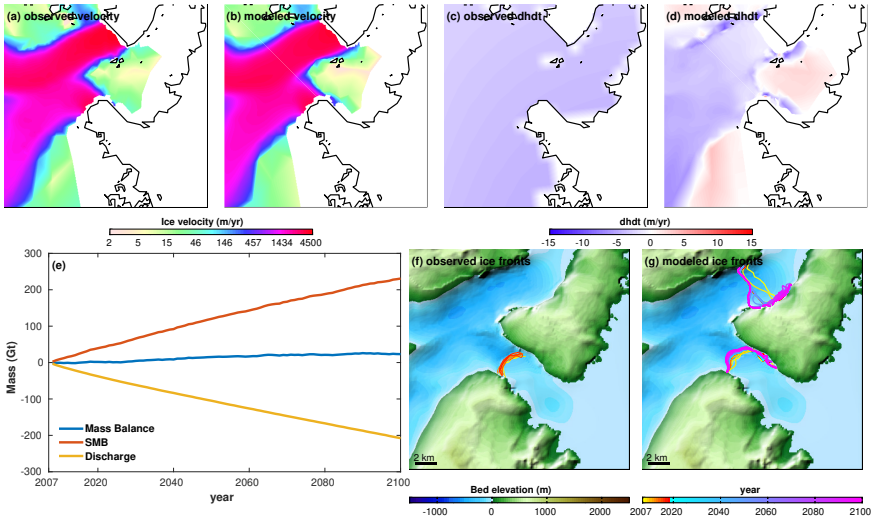

Graulv

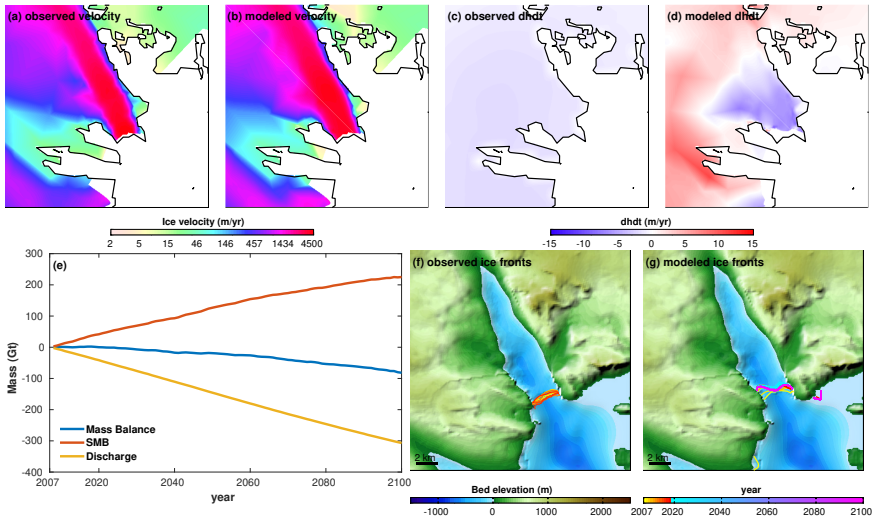

GyldenloveN

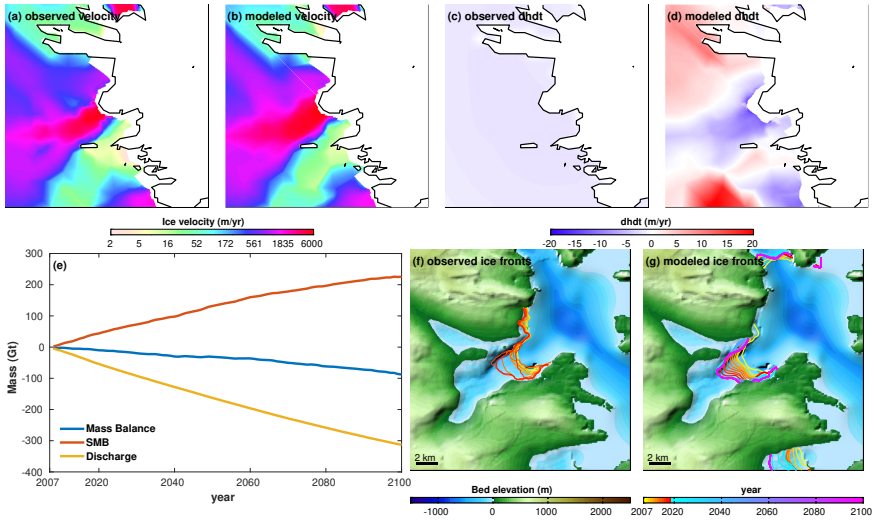

GyldenloveS

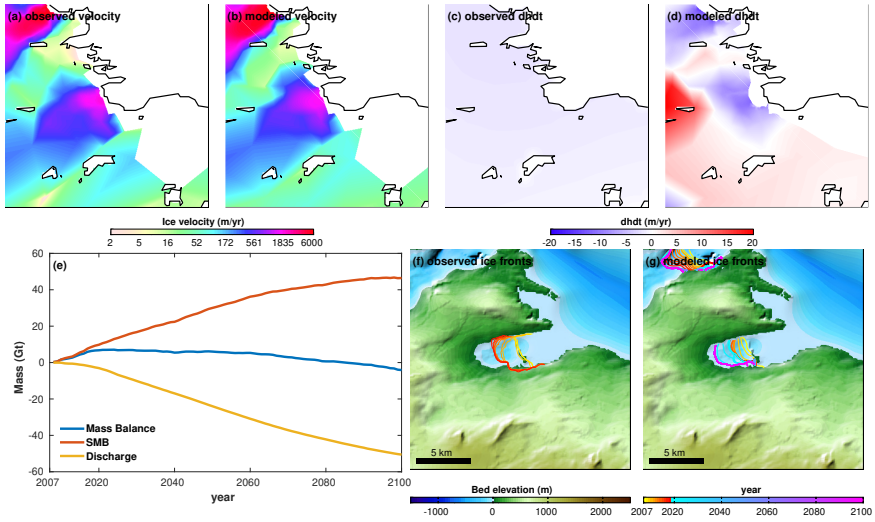

Heimdal

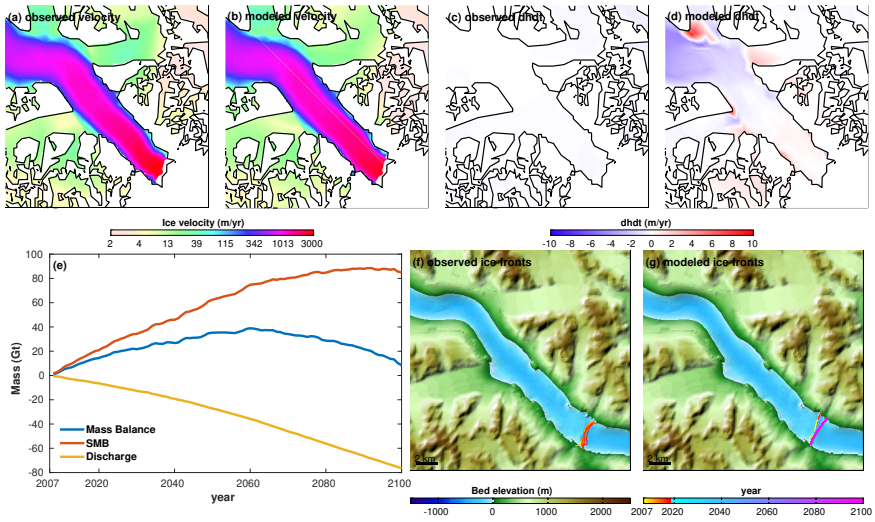

Helheim

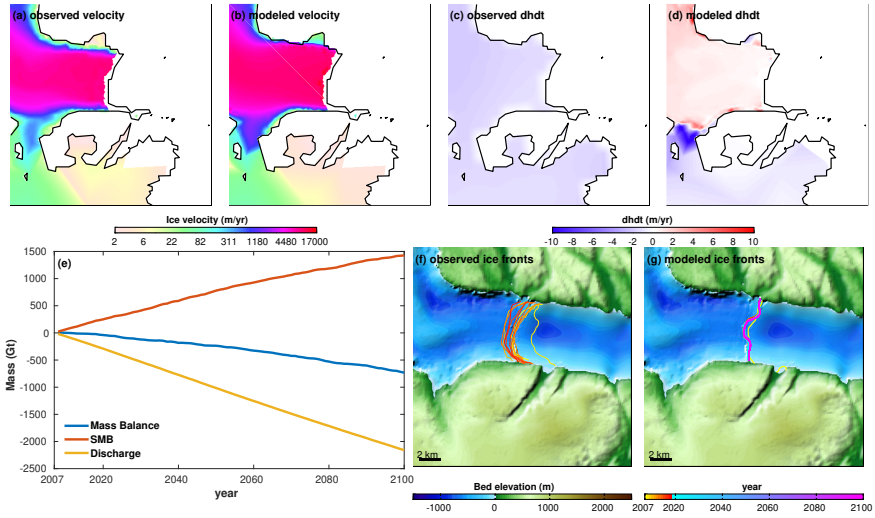

HerlufTrolleN

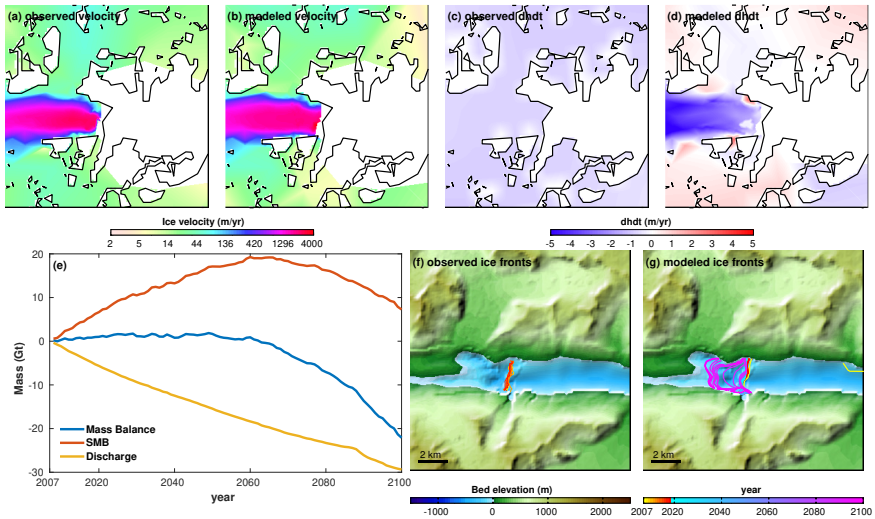

HerlufTrolleS

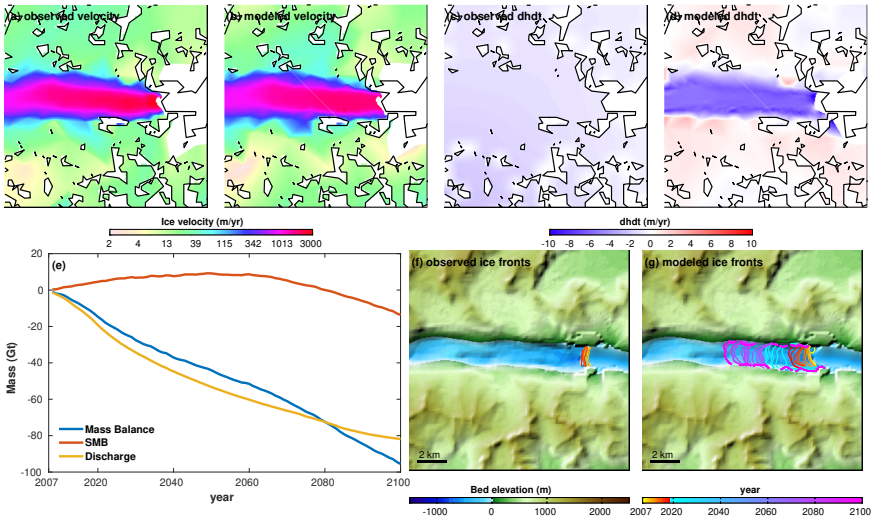

IkertivaqM

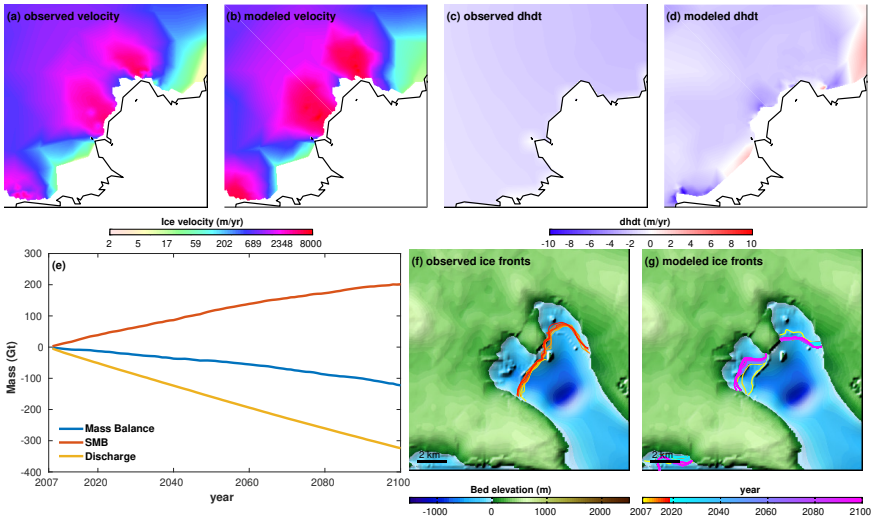

IkertivaqN

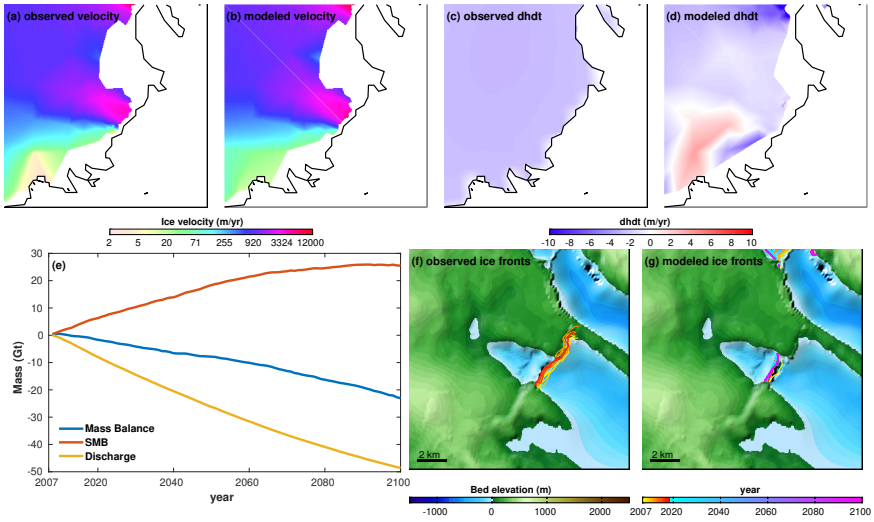

IkertivaqNN

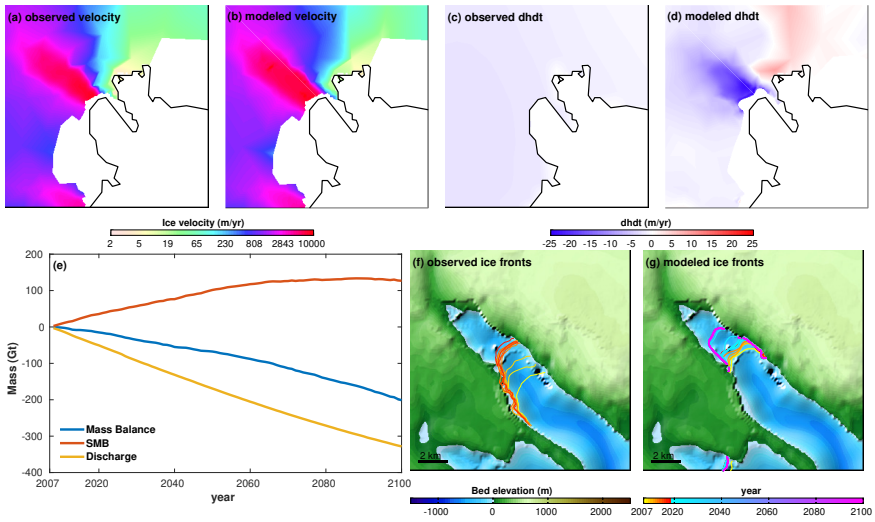

IkertivaqS

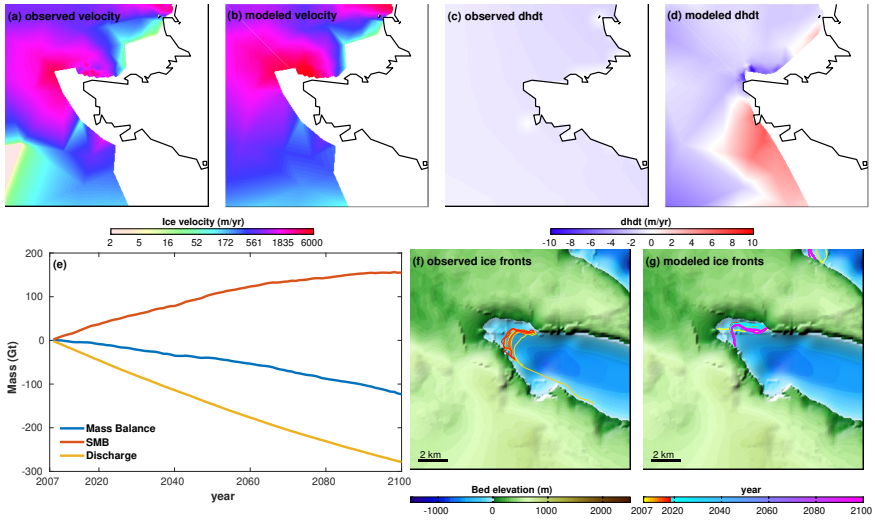

Kangerlussuaq

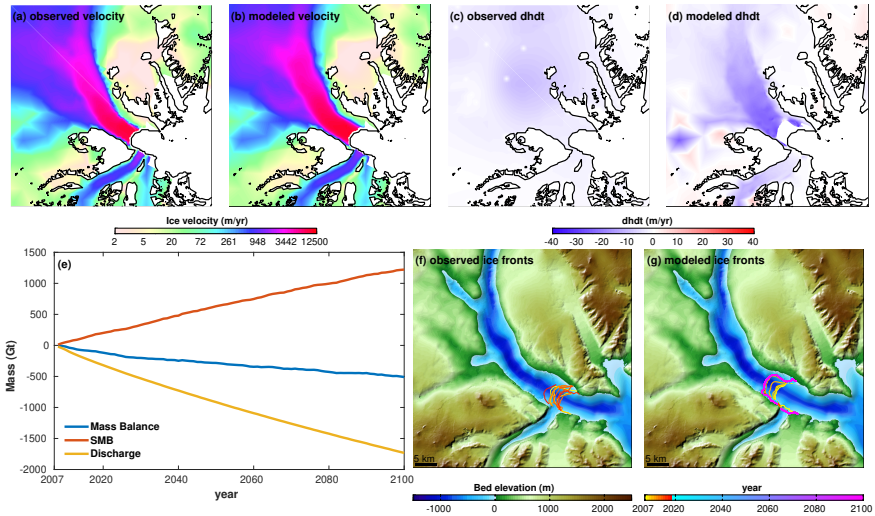

KIVSteenstrup

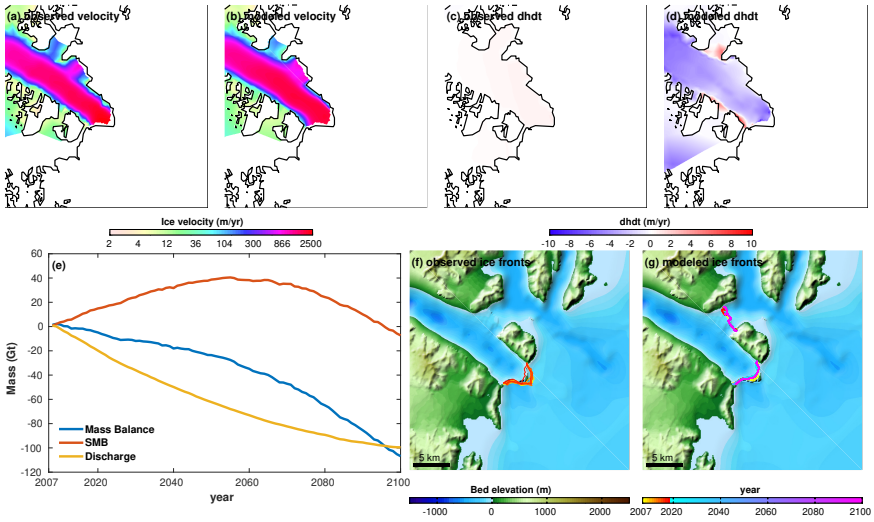

KogeBugtC

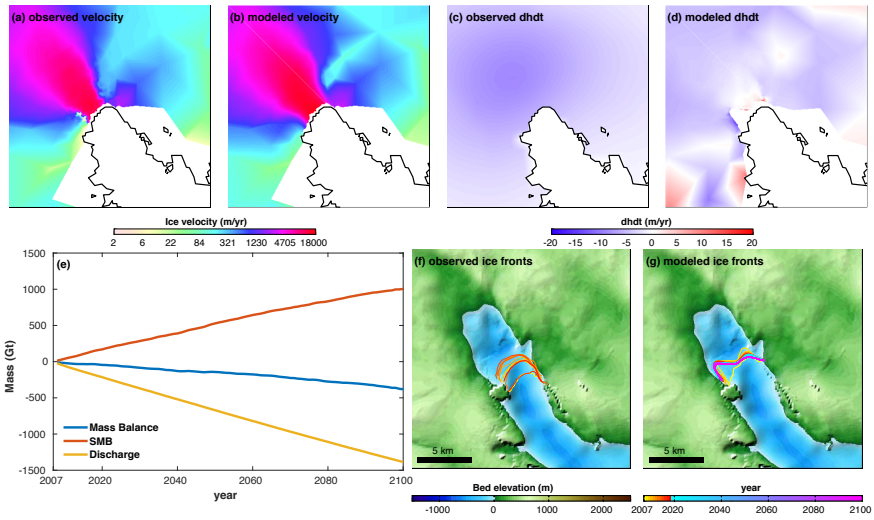

KogeBugtN

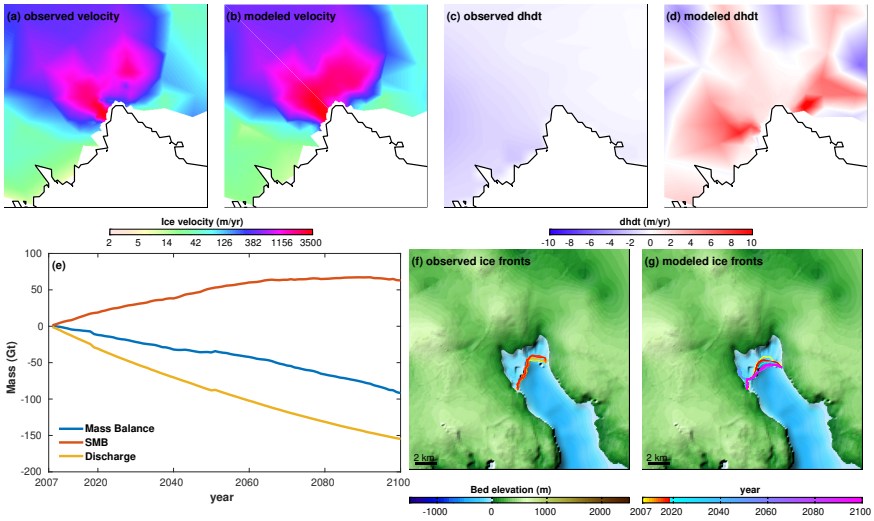

KogeBugtS

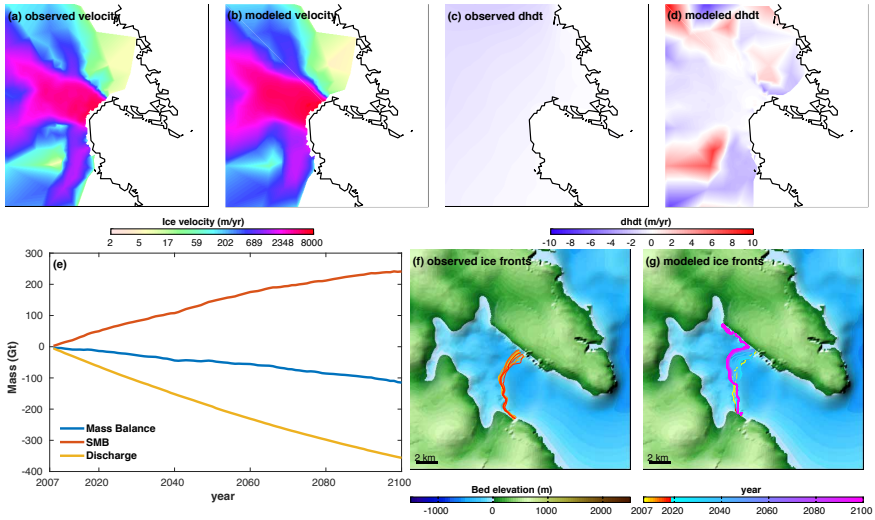

KongChristianIV

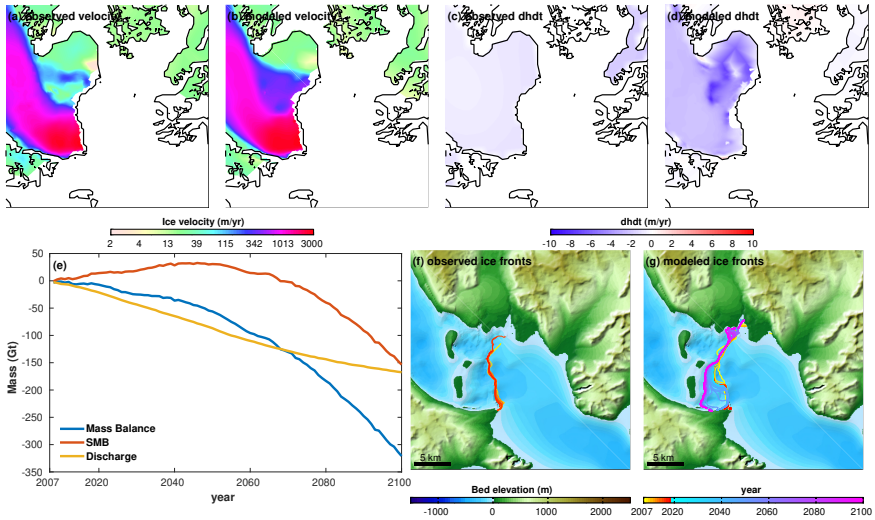

Kruuse

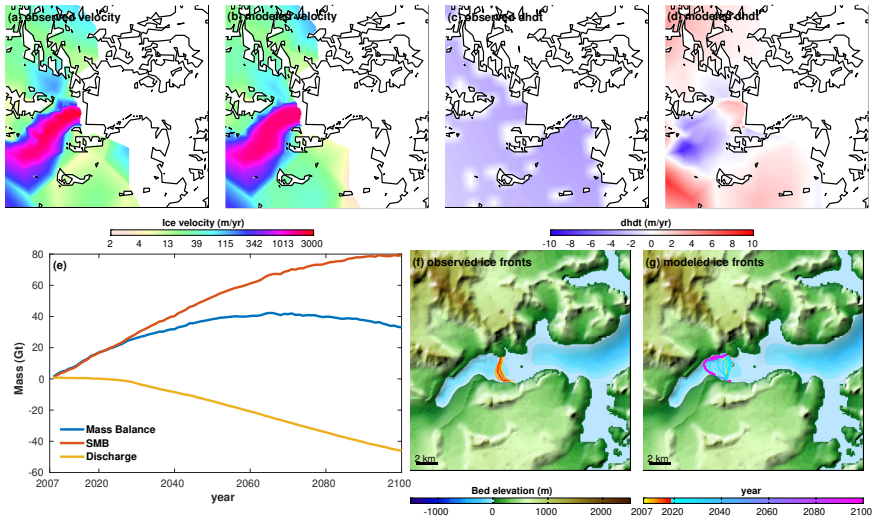

MogensHeinesenC

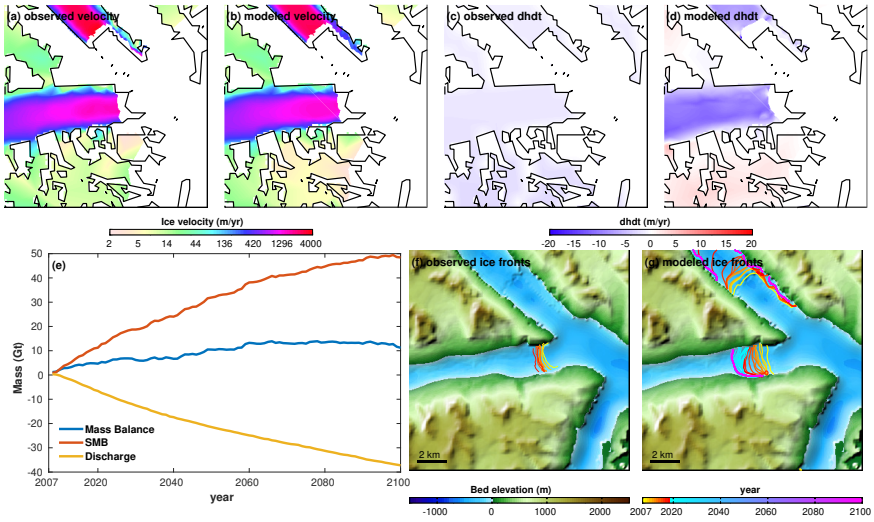

MogensHeinesenN

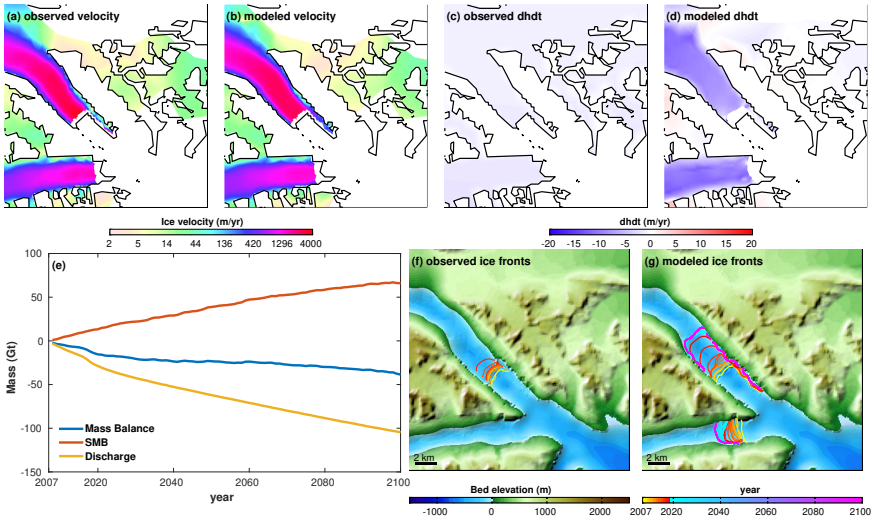

MogensHeinesenS

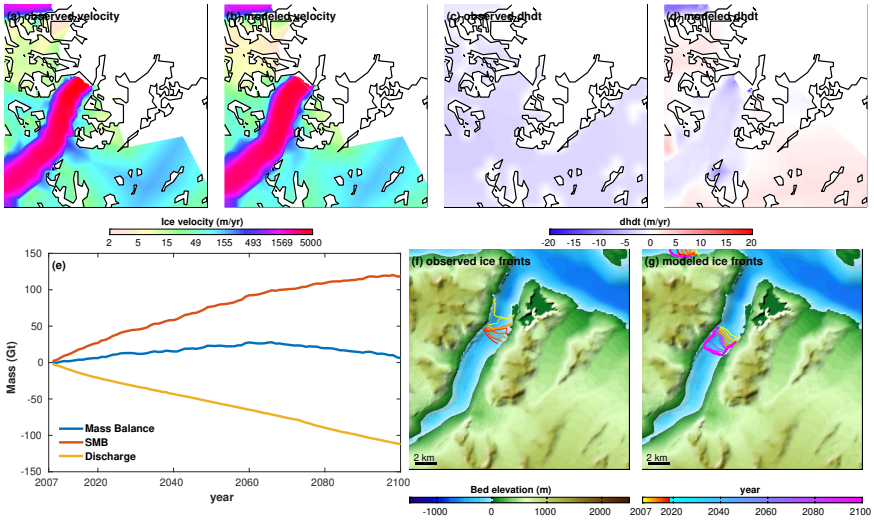

NapasorsuaqN

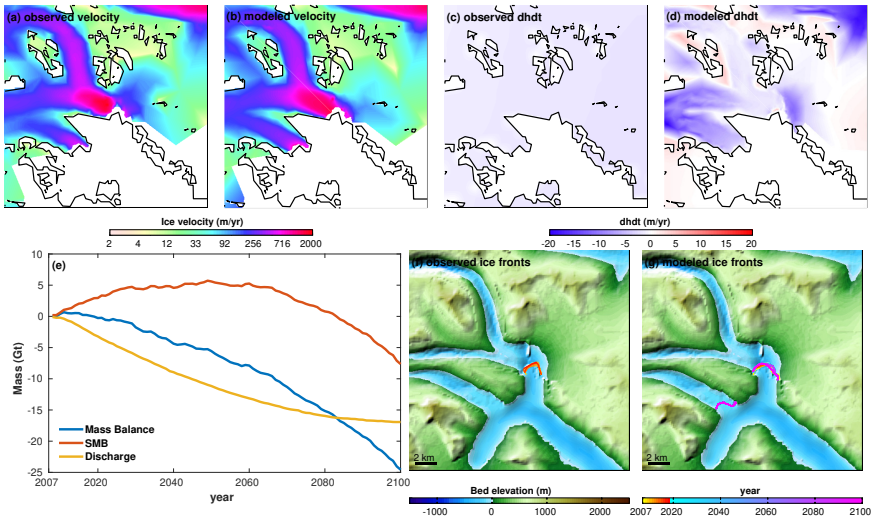

Polaric

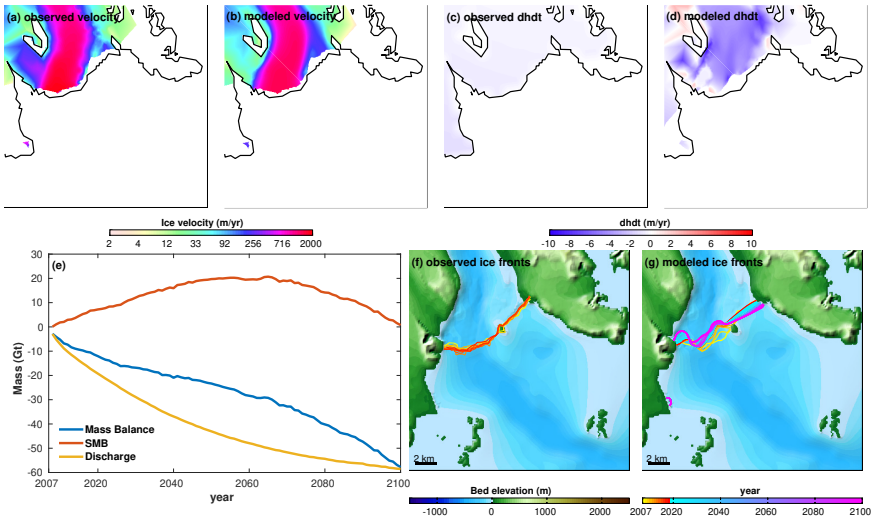

PuisortoqN

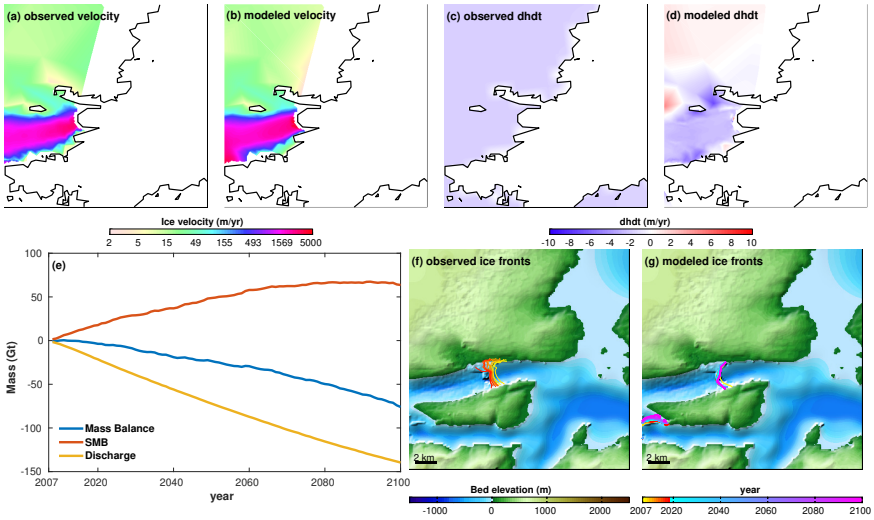

PuisortoqS

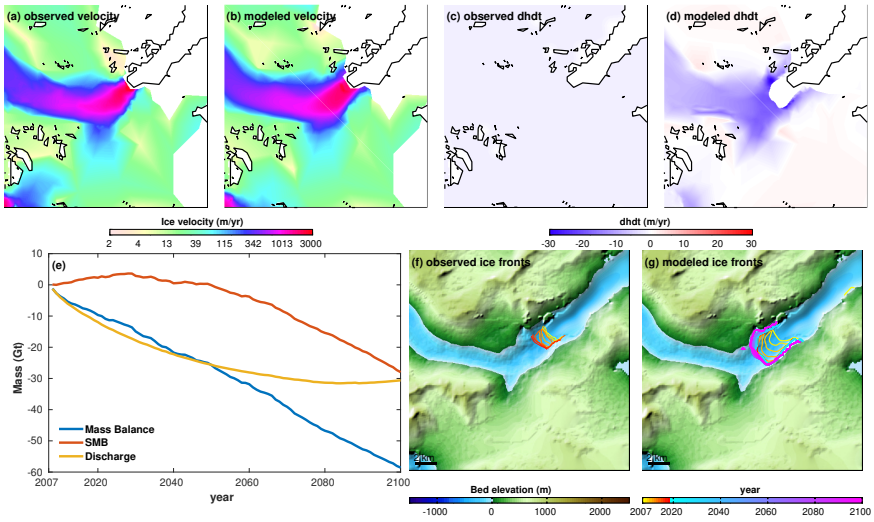

Rimfaxe

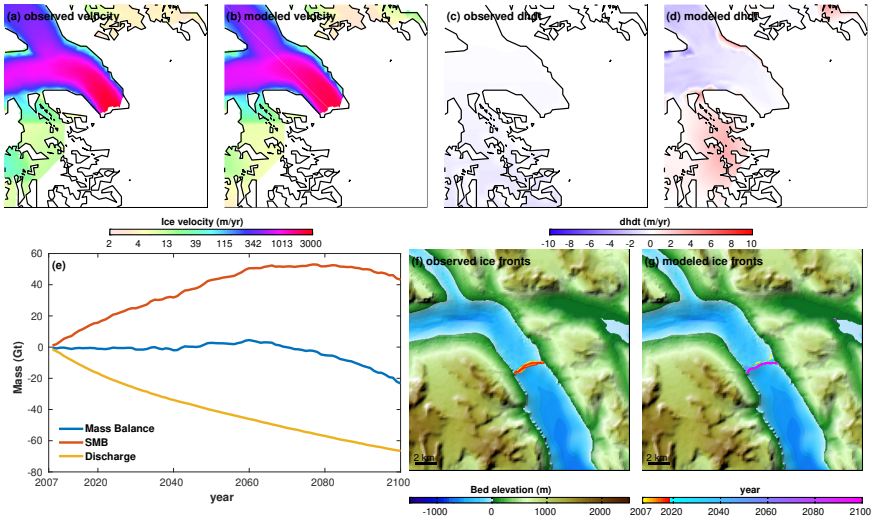

Skinfaxe

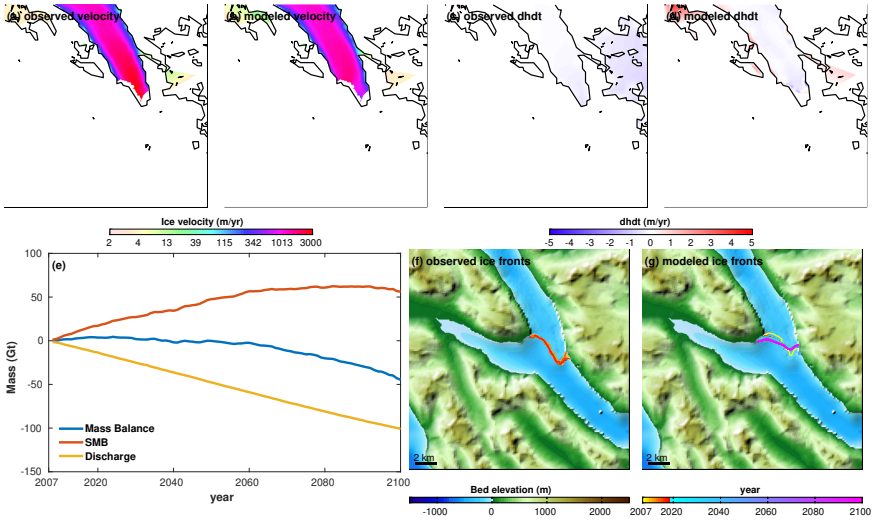

Tingmiarmiut

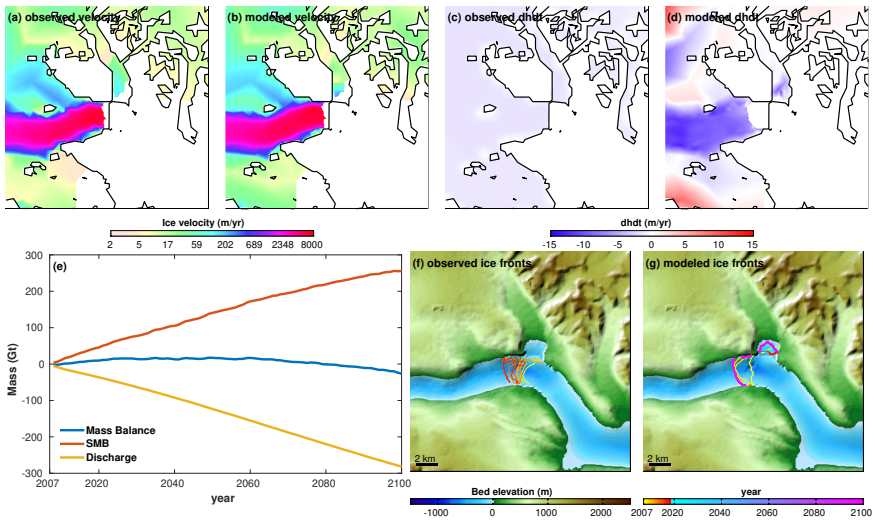

Uunartit